Universiteit
Leiden
The Netherlands

Unveiling the nature of giant radio galaxies

Dabhade, P.

Citation
Dabhade, P. (2021, May 25). *Unveiling the nature of giant radio galaxies*. Retrieved from https://hdl.handle.net/1887/3179453

Version:	Publisher's Version
License:	Licence agreement concerning inclusion of doctoral thesis in the Institutional Repository of the University of Leiden
Downloaded from:	https://hdl.handle.net/1887/3179453

Note: To cite this publication please use the final published version (if applicable).

Cover Page

Universiteit Leiden

The handle https://hdl.handle.net/1887/3179453 holds various files of this Leiden University dissertation.

Author: Dabhade, P.
Title: Unveiling the nature of giant radio galaxies
Issue Date: 2021-05-25

Unveiling the nature of giant radio galaxies

Pratik Dabhade

Unveiling the nature of giant radio galaxies

Proefschrift

ter verkrijging van

de graad van doctor aan de Universiteit Leiden,

op gezag van rector magnificus prof.dr.ir H. Bijl,

volgens besluit van het college voor promoties

te verdedigen op dinsdag 25 mei 2021

klokke 10:00 uur

door

Pratik Dabhade
Born in Jalna, India
June 1989

Promotores:	Prof. dr. H. J. A. Röttgering
	Prof. dr. Joydeep Bagchi (IUCAA & CHRIST University, India)

Promotiecommissie:

Secretaris:	Prof.dr. Paul van der Werf
Overige leden:	Prof.dr. Frank Israel
	Prof.dr. Peter Barthel (Groningen University)
	Prof.dr. Raffaella Morganti (Groningen University)
	Prof.dr. Somak Raychaudhury (IUCAA, India)
	Prof.dr. Dhruba Jyoti Saikia (IUCAA, India)
	Dr. Reinout van Weeren

© 2021 Pratik Dabhade

Dit proefschrift werd ondersteund door de Universiteit Leiden en IUCAA (India).

Cover: The front side shows the radio sky with giant radio galaxies with LOFAR on the ground. The back side shows GMRT and IRAM telescope investigating a special giant radio galaxy.

Dedicated to
my parents

``If you want to shine like the sun, first burn like the sun"
- Dr. A. P. J. Abdul Kalam

Contents

1 Introduction 1
1.1 Active Galactic Nuclei 3
1.2 Radio-loud Galaxies and Quasars 5
1.3 Giant radio galaxies 11
1.4 Work in this thesis 15
1.5 Future scope 19

2 Discovery of Giant Radio Galaxies from NVSS: Radio & Infrared Properties 25
2.1 Introduction 26
2.2 Multi-frequency Properties of GRG Sample 30
2.2.1 Identification of New GRGs and Radio Analysis . . 30
2.2.2 Optical Analysis 32
2.2.3 Infrared Analysis 33
2.2.4 Black Hole Mass Estimation 34
2.3 Results 35
2.3.1 GRG1 (J001604+042024) 35
2.3.2 GRG2 (J002224.96-081845) 35
2.3.3 GRG3 (J031536-074338) 35
2.3.4 GRG4 (J042925+003304): A Giant Radio Quasar? . 35
2.3.5 GRG5 (J044932-302638): A Giant Radio Quasar . . 36
2.3.6 GRG6 (J080248+492723) 45
2.3.7 GRG7 (J085701.76+013130.9) 45
2.3.8 GRG8 (J105838.66+244535) 45
2.3.9 GRG9 (J105920-170920) 46
2.3.10 GRG10 (J132741+574943) 46
2.3.11 GRG11 (J132743.50+174837) 46

2.3.12 GRG12 (J200843+004918): An Extremely Large Radio Source? . . . 46
2.3.13 GRG13 (J203449-263036) . . . 49
2.3.14 GRG14 (J205939+243423) . . . 49
2.3.15 GRG15 (J223301+131502): A GRG hosted by a BCG 49
2.3.16 GRG16 (J225039.15+284445.5) . . . 52
2.3.17 GRG17 (J225615.1-361759) . . . 52
2.3.18 GRG18 (J230444-105048) . . . 53
2.3.19 GRG19 (J231201.27+135655.9) . . . 53
2.3.20 GRG20 (J231620-010207) . . . 53
2.3.21 GRG21 (J232623+245840) . . . 53
2.3.22 GRG22 (J232849.99-082512.7) . . . 54
2.3.23 GRG23 (J233552.1+521539) . . . 54
2.3.24 GRG24 (J234929-000305) . . . 54
2.3.25 GRG25 (J235531+025607) . . . 55
2.4 Discussion . . . 55
2.4.1 Black Hole Mass of GRG . . . 55
2.4.2 Demographics of GRGs . . . 57
2.4.3 WISE mid-IR studies of GRGs . . . 58
2.4.4 P-D Diagram . . . 61
2.5 Conclusions and Summary . . . 63
2.6 Supplementary material . . . 66

3 Giant radio galaxies in the LOFAR Two-metre Sky Survey-I: Radio and environmental properties 69
3.1 Introduction . . . 70
3.2 Identifying new GRGs in LoTSS . . . 73
3.2.1 The LoTSS first data release . . . 73
3.2.2 Semi-automated search for GRGs . . . 75
3.2.3 Manual Visual Search from LoTSS DR1 . . . 76
3.2.4 Final catalogue: VAC+MVS . . . 78
3.3 Results : The LoTSS catalogue of GRGs . . . 78
3.3.1 Optical host properties . . . 78
3.3.2 Spectral Index (α_{144}^{1400}) . . . 79
3.3.3 Notes on individual objects . . . 82
3.3.4 Giant radio quasars . . . 84
3.3.5 Environment analysis of GRGs . . . 87
3.4 Discussion . . . 88
3.4.1 GRGs with sizes $>$ 2 Mpc . . . 88

3.4.2 Morphology of GRGs . . . 88
3.4.3 GRGs in dense environments . . . 91
3.5 Summary . . . 93
3.6 Supplementary material . . . 107

4 Chapter 4 : SAGAN. I. New sample and multi-wavelength studies 117
4.1 Introduction . . . 118
4.2 Project SAGAN . . . 122
4.2.1 New sample of GRGs from NVSS . . . 123
4.2.2 The GRG catalogue . . . 128
4.3 Analysis . . . 128
4.3.1 Size . . . 128
4.3.2 Flux density and radio power . . . 129
4.3.3 Jet kinetic power . . . 129
4.3.4 Spectral index . . . 130
4.3.5 Absolute r-band magnitude . . . 131
4.3.6 Black hole mass . . . 131
4.3.7 Eddington ratio . . . 131
4.3.8 Black hole spin . . . 132
4.3.9 WISE mid-IR properties . . . 133
4.4 SAGAN GRG sample: Results . . . 135
4.4.1 Spectral index distribution of the SGS . . . 135
4.4.2 PD$z\alpha$ parameters of GRGs . . . 137
4.4.3 Morphology of GRGs . . . 141
4.4.4 Environmental analysis of the SGS . . . 142
4.5 GRG catalogue: Properties and correlations . . . 142
4.5.1 Comparison of the properties of GRGs and GRQs . . . 143
4.5.2 Comparison of the properties of HEGRGs and LEGRGs 150
4.5.3 How similar are GRGs and RGs ? . . . 155
4.5.4 Astrophysical processes near accreting black holes in GRGs . . . 158
4.5.5 Environment analysis . . . 165
4.6 Discussion . . . 166
4.7 Summary . . . 169
4.8 Tables . . . 170
4.9 Notes on individual sources from SGS . . . 181
4.10 Radio maps of all GRGs from the SGS. . . . 183

5 SAGAN. II : Molecular gas content of giant radio galaxies- Based on observations carried out with IRAM-30m 191
5.1 Introduction . . . 192
5.2 The sample . . . 193
5.2.1 R1-1: 2MASX J23453268−0449256 . . . 196
5.2.2 R1-2: CGCG 245−031 . . . 196
5.2.3 R1-3: B2 1029+28 . . . 196
5.2.4 R2-1: WNB0313+683 . . . 197
5.2.5 R2-2: LCRS B132559.3−025215 . . . 197
5.2.6 R2-3: 2MASX J14504940+1006497 . . . 197
5.2.7 R2-4: NGC 6251 . . . 197
5.2.8 R2-8: Speca . . . 198
5.2.9 Other GRGs . . . 198
5.2.10 Non-GRGs . . . 198
5.3 Observations . . . 198
5.4 Results . . . 202
5.4.1 Molecular masses . . . 205
5.4.2 Deconvolving the two-horn spectra . . . 205
5.5 Discussion . . . 207
5.5.1 Star formation and gas mass . . . 208
5.5.2 Radio power and fueling . . . 211
5.6 Summary . . . 214

6 Chapter 6 : Barbell shaped giant radio galaxy with ~100 kpc kink in jet 217
6.1 Introduction . . . 218
6.2 Observations and data analysis . . . 219
6.2.1 Optical . . . 219
6.2.2 Radio Observations and data analysis . . . 224
6.3 Results & Discussion . . . 228
6.3.1 Redshift . . . 228
6.3.2 Size, radio power and jet kinetic power . . . 228
6.3.3 Radio morphology . . . 228
6.3.4 Spectral index (α) . . . 233
6.3.5 Spectral ageing and magnetic field . . . 233
6.3.6 Jet and the kink . . . 237
6.3.7 Environment Studies . . . 240
6.4 Summary . . . 242
Bibliography . . . 243

Summary 261
Samenvatting in het Nederlands 267
List of publications 273
Curriculum Vitae 277
Acknowledgements 279

1 Introduction

"Science is a way of thinking much more than it is a body of knowledge."

- Carl Sagan

The scientific framework explaining the growth and evolution of the Universe is referred to as the standard model* of cosmology or the standard Λ cold dark matter (ΛCDM) model (Peebles 2012, 2017). It successfully describes the formation and growth of structures starting from the first second to the present epoch. The ΛCDM model is widely supported by numerous high precision observations, like the measurement of the 'Cosmic microwave background radiation' (CMBR or CMB) using space based missions (e.g., Planck Collaboration et al. 2016). For the early Universe, prior to the hot Big Bang phase, the 'Cosmic Inflation' (Gorbunov & Rubakov 2011; Baumann 2009) emerges as the leading scenario and sets natural finely tuned initial conditions for the standard model. It explains the large scale observed homogeneity as a result of the rapid growth the inflation caused. There were fluctuations in the energy densities (matter) which were possibly caused by the quantum fluctuations in the early Universe. These fluctuations grew under the influence of gravity, and as the Universe expanded and cooled, it led to the formation of smaller over-densities or irregularities in the primordial Universe (after 3,80,000 years), which are observed in the CMB as anisotropies. Upon further expansion of the Universe, dark matter haloes grew, providing essential potential well for the gas clouds to settle in. The over-densities, along with gravity, triggered the collapse of dense gas clouds into the formation of very high-mass stars due to rapid adiabatic heating of gas, condensation and high accretion rate. This set the stage for the formation of the first galaxies, and the theories (Rees 1993; Barkana & Loeb 2001) suggest that these were around 100 million years after the big

*https://pdg.lbl.gov/2020/astrophysics-cosmology/astro-cosmo.html

bang phase. The most sensitive observations to date have found galaxies at redshifts (z) of 10 to 11 (Bouwens et al. 2015; Oesch et al. 2016), which is ~400 million years after the Big bang phase.

Stars, dust, and gas held together by the interplay of gravity and dark matter in a system is called a galaxy. Galaxies weigh around $\sim 10^9$ to 10^{12} $M_\odot$, and are often part of a bigger systems like galaxy groups or galaxy clusters. As per the standard ΛCDM cosmological model, structure formation is hierarchical, where smaller dark matter (DM) halos merge to form bigger ones, which led to the formation of the first galaxies in the Universe (Springel et al. 2005). Decades of observations combined with complex simulations in the recent years have enriched our understanding of the formation and evolution of galaxies, however, it continues to be an on-going endeavour (Loeb 2010). The physics involved in galaxy formation is quite complex as it needs to encompass thermodynamics of gas, production energy for stars and the dynamics of stars. Galaxies are classified on the basis of their structure, and hence we have three broad categories like the elliptical, spiral and irregular type of galaxies.

As per the Hubble classification scheme, the elliptical and spiral galaxies are further sub-classified (Hubble 1926; de Vaucouleurs 1963). The elliptical galaxies are subdivided into several categories based on their ellipticity level ranging from E0 (almost spherical) to E7 (elongated). These are the largest galaxies seen at optical/infrared wavelengths, which are formed as a result of mergers over a period of giga years (Gyr). In comparison to our own galaxy - the Milky Way, ellipticals can be ten times larger and host trillion stars. Also, the giant ellipticals are often located at the centres of galaxy clusters, and quite a lot of their population emits dominantly at radio wavelengths (Valentijn & Bijleveld 1983; Bagchi & Kapahi 1994; Best et al. 2007; Hogan et al. 2015). Spiral galaxies, on the other hand exhibit spiral arms attached to the central bulge of the galaxy with a rotating disk with enhanced star formation. Under the Hubble classification scheme, the spiral galaxies were assigned a, b, and c classification based on their compactness of the spiral arms. Furthermore, spiral galaxies were sub-classified into barred spiral galaxies which show a central bar-shaped structure comprising of stars. The most abundant type of galaxy known in the Universe is the Dwarf galaxy, which owing to their low size, luminosity, and mass are difficult to observe. Galaxies with no well defined shapes are referred to as the irregular type whose masses are in the range of $\sim 10^8$ to 10^{10} $M_\odot$. They are thought to be the end products of galaxy mergers or tidal interactions, leading to their peculiar shape.

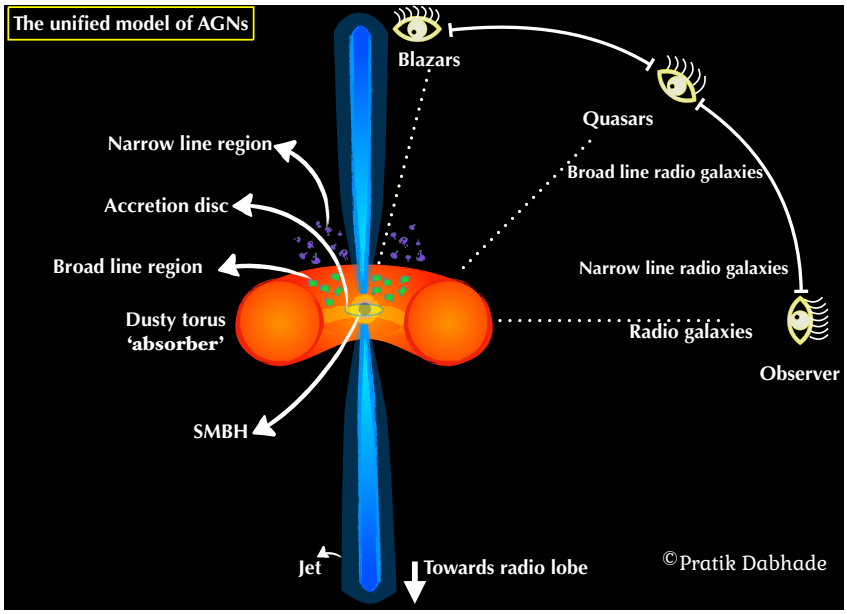

Figure 1.1: The modified version of the unified AGN model presented here in context of the radio galaxies.

1.1 Active Galactic Nuclei

Based on observational evidence, backed with theory, the mergers driving the galaxy formation is the favoured model. The model explains that the galaxy mergers initiate a sequence of events where the gas clouds collide upon mergers, triggering star formation. This, in turn, causes the gas to be pushed towards the galaxy centre, creating an active galactic nucleus (AGN) (Hopkins et al. 2008). Almost all galaxies harbour a super-massive black hole (SMBH) at their centres (Kormendy & Richstone 1995; Magorrian et al. 1998), and their masses correlate with the velocity dispersions of stars (Gebhardt et al. 2000; Kormendy & Ho 2013). Hence, the observed correlation with the central bulges and the SMBH (Ferrarese & Merritt 2000; Marconi & Hunt 2003; Gültekin et al. 2009). Therefore, it became clear that there exists a co-evolution of galaxies and AGN (Silk & Rees 1998; Kauffmann & Haehnelt 2000; Volonteri et al. 2003).

The field of AGN studies was started with the findings of broad and strong emission lines in the nuclei of spiral galaxies Seyfert (1943). These spiral galaxies were observed to show strong nuclear emission (non-stellar)

as compared to other normal galaxies. Extensive studies over the years have gathered convincing proof that the AGN centre comprises of an active super-massive black hole ($\geqslant 10^6$ $M_\odot$). AGNs emit over broad electromagnetic spectrum ranging from radio to gamma-rays with 10^{48} erg s^{-1} bolometric luminosities (L_{bol}). The AGN is covered in an axisymmetric dusty structure called the 'dusty torus' as illustrated in Fig. 1.1, which is quite luminous at mid-infrared wavelengths. It has dimensions of 0.1-10 parsecs which are luminosity-dependent.

Over the years AGN have been classified into several types but essentially are characterised based on a) orientation (Antonucci 1993; Urry & Padovani 1995), and b) their accretion states (Heckman & Best 2014). The updated orientation based unification scheme of AGN (Netzer 2015) comprises of two parts, the first one unifies AGN properties observed from infrared, optical, ultraviolet and X-ray unification, and the other is exclusively about radio unification. The former unification deals with the dusty torus and explains the distinctions between type-I and type-II AGNs. The later unification of radio unifies the radio relativistic jets with the torus. Over the years these models have been constantly updated with more multi-wavelength observations of the AGNs, and it has been realized that the AGNs could differ from one another based on the properties beyond their luminosities and torus inclination. It is suggested that the AGN could differ based on the nature of the central engine and its state (e.g. RIAF or high-efficiency accretion flow) or due to absence of certain components in AGN, e.g. the broad line region (BLR) or narrow line region (NLR).

Currently, the two broad categories of AGNs which are widely accepted are the radiative-mode and jet-mode, whose properties are briefly discussed below-

1. Radiative-mode AGNs - These are efficient accretors and as a result most of their energy output is in the form of electromagnetic radiation arising from accretion through geometrically thin and optically thick accretion disk. The accretion disk emits thermal continuum emission from extreme UV to optical regime of electromagnetic spectrum. A hot corona surrounds the accretion disk which Compton up-scatters soft seed photons to high energy X-rays. This system of corona and accretion disk produces ionizing radiation which heats and photoionises dense gas clouds located close to the SMBH, and in turn produces the observed permitted emission lines in UV, optical and near IR regimes. Some gas at larger distances also produces forbidden and permitted lines with narrow widths. This mode is further

subdivided into different types (Netzer 2015) which are as follows-

- Type I AGNs : Show presence of bright central nuclei (unobscured) and broad (1000 to 20,000 km/s) permitted and semi-forbidden emission lines (as shown in Fig. 1.1). Type-I AGNs with low to intermediate luminosities have narrow emission lines of high ionization, and some population also exhibit forbidden lines. These are also referred to as Seyfert 1 galaxies or quasars.
- Type II AGNs: Show presence of strong narrow (300 to 1000 km/s) lines in near-infrared to optical regime with clear signs of photoionisation. The central region is hidden due to line of sight being near to the equatorial plane of the torus.
- LINERs (low-ionization nuclear emission-line regions) : They are characterised by low-ionization and presence of narrow emission lines from ionized gas. LINERs are further sub-divided into two classes of type-I (having broad emission lines) and type-II (having narrow emission lines). LINERs also show variation in their UV and X-ray fluxes.

2. Jet-mode AGNs- As the name indicates these AGNs produce two sided relativistic jets in which bulk kinetic energy is transported. The Eddington ratio for such AGN is much smaller than the radiative mode and the jets are likely to be produced via RIAFs. The low accretion rate and inefficient flow has been attributed to either the absence of geometrically thin accretion disk or its truncation in inner regions. It may possibly be replaced by geometrically thick disk as well, which has shorter inflow time compared to radiative cooling time (e.g., Narayan & Yi 1994; Ho 2008. Hence these are referred to as advection-dominated or radiatively inefficient accretion flows (ADAFs/RIAFs), which possibly favour launch of relativistic jets. It is further discussed in Sec. 1.2 in context of radio galaxies.

1.2 Radio-loud Galaxies and Quasars

About 90 years ago, efforts of Karl Jansky* led to the discovery (Jansky 1933) of radio waves from the Milky Way and beyond, which opened a

*Flux unit in radio astronomy is Jansky (Jy) in honour of Karl Jansky, where 1 Jy $= 10^{-26}$ W m^{-2} Hz^{-1}.

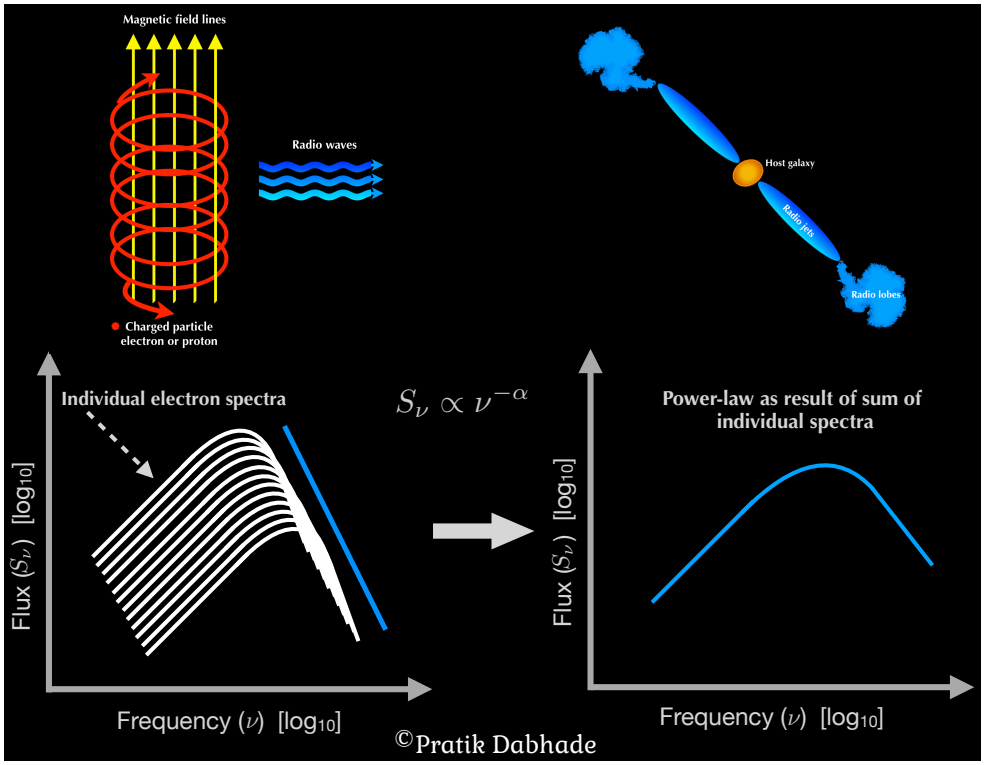

Figure 1.2: The figure illustrates the concept of Synchrotron radiation. The synchrotron emission spectrum follows a power-law decay and is constructed by adding the contributions from individual electrons, where the flux is observed to decline at higher frequencies. The slope of this distribution is called the spectral index α which usually ranges from -3 to 2 for radio sources in general and for RGs it is ~ 0.75.

new branch of astronomy, called radio astronomy. This paved the way for the discovery of several new objects and creation of sub-fields within astronomy, thereby enriching our knowledge of the Universe. The discovery of radio waves from outer space was taken up by Grote Reber in the 1930s, who with his meticulous work and ingenuity performed landmark research (Reber 1940, 1944, 1946, 1949) and established this field.

Following up on the work of Reber and other advancements in the field by Ryle (1952), works of Smith (1951), Jennison & Das Gupta (1953), and Baade & Minkowski (1954) established the association of radio emission from galaxies (e.g., Cygnus A) and thus, a new class of objects called 'radio galaxies' (RGs) came into existence. Works of Shklovskii (1955), Baade (1956) Burbidge (1956) based on radio spectrum and polarisation properties showed that the observed radio emission from these galaxies is produced by the process of synchrotron radiation (Ginzburg & Syrovatskii 1965, 1969). The production of this radiation is from charged particles (commonly electrons) helically moving or spiralling around magnetic field (as seen in top left of Fig. 1.2) lines at relativistic speeds (Rybicki & Lightman 1986; Shu 1991). The velocity of the charged particle directly influences the frequency of the emission. The spiralling of the charged particle in the magnetic field results in the release of energy in terms of emission of photons. Depending on the strength of the magnetic field, the charged particle loses more energy as it gyrates for a longer time. This results in the charged particle spiralling in the magnetic field at wider lengths leading it to emit radiation at low frequencies or longer wavelength (i.e. radio band of the electromagnetic spectrum). The lifetimes of the electrons in the cosmic radio sources (e.g., AGN) can range from thousands to millions of years before losing their energies via various different processes (see Longair 2011). It is evident from the shape (power law distribution, as seen in the bottom left of Fig. 1.2) of their spectra, which is obtained by observing the source at multiple frequencies covering a wide range. For an electron which is emitting via synchrotron process in a fixed magnetic field, the initial power law is given by $N(E) = N_0 E^{-\delta}$, where N_0 is normalization factor and δ is the power law index of the initially injected electron energy distribution. Such a power law distribution (bottom left of Fig. 1.2) is observed in astrophysical sources with the form $S_\nu \propto \nu^{-\alpha}$, where slope of the power law distribution is the spectral index α, which depends only on δ, with $\alpha = (\delta - 1)/2$.

The radio emission was observed to extend far beyond the optical extents ($\sim$ 20 to 70 kpc) of the galaxies ranging from few to hundreds of

kiloparsec* scales and beyond. Such objects like RGs also later came to be known as 'radio-loud'.

In the 1960s, radio bright objects at large distances called quasars were discovered (Schmidt 1963; Greenstein & Schmidt 1964) which are the incredibly bright nuclei of distant galaxies. This opened a window to test cosmological models (Rowan-Robinson 1967; Longair & Pooley 1969; Kapahi 1975; Condon 1984; Daly 1994a; Barai & Wiita 2006). Later on, 'radio-quiet' quasars too were found which radiated dominantly at other wavelengths than radio (Sandage 1965).

Based on the observational development then, a theoretical framework (Salpeter 1964; Lynden-Bell 1969; Bardeen 1970) was put forth that the centres of the galaxies host a supermassive black hole of 10^6 - 10^{10} $M_\odot$ mass, which produces twin collimated relativistic jets (Blandford & Rees 1974; Scheuer 1974) observed at radio wavelengths. The idea of the central compact object powering the RGs shrouded in the ion torus was proposed by Rees et al. (1982), which explained their observed lower core power in radio sources compared to the power of their extended components. This model also suggested that the ion tori plays a vital role in supporting the magnetic field, leading to extracting rotational energy from the SMBH to produce the bipolar relativistic jets. Several observations have now shown the evidence of the dusty torus in AGNs (e.g., Jaffe et al. 2004, Koshida et al. 2014, and Carilli et al. 2019). Also, studies involving continuous monitoring of powerful AGNs at multiple wavelengths (especially at higher energies like X-rays and gamma rays) have established the jet connection to the accretion disk (Marscher et al. 2002; Chatterjee et al. 2009). Very recent studies of the powerful radio source M87 with earth size radio telescope called the event horizon telescope have achieved unprecedented resolution and sensitivity. Their observations, for the first time, have resolved closest possible regions near the SMBH, well inside the radio core, proving beyond doubt the existence of black holes and them powering the radio jets (Doeleman et al. 2012; Event Horizon Telescope Collaboration et al. 2019).

Studies (e.g. Marconi et al. 2004; Best et al. 2005; Saikia & Jamrozy 2009) have shown that the SMBH residing in the AGN of the galaxy is active for a limited period when compared to the galaxy's lifetime and is often re-activated or remains in a dormant phase of low activity. Factors responsible for the reactivation or restart of such AGN can be dependent on its environment and availability of accreting fuel (e.g. gas). However, it is difficult to exactly understand these factors due the different AGN

*1 Parsec $\approx 3.08 \times 10^{16}$ metres

modes (radiative and jet mode). The radiative mode AGNs are thought accrete via dense cold gas (Hardcastle et al. 2007) or which may be arising from a merger, whereas for the jet mode driven by radiatively inefficient AGN it has been suggested it needs hot accretion. However, some recent studies have suggested (Gaspari et al. 2013) that for jet mode AGN is driven by chaotic cold accretion. Radio-loud AGN studies (Schoenmakers et al. 2000a; Best et al. 2005; Stanghellini et al. 2005; Saikia & Jamrozy 2009) using optical and radio data have shown that the SMBH activity period is quite less compared to the lifetime of the galaxy and hence, the observations can only be explained by restarted activity of SMBH. This renewal of AGN is dependent on the modes of its nuclear activity and the galaxy's environment (Hardcastle et al. 2007; Heckman & Best 2014; Hardcastle 2018a).

The 'jet-mode' AGN are also known as low-excitation type or low-excitation radio galaxy (LERG), which are mostly prevalent in the radio domain or in RG population (Heckman & Best 2014). Despite having active relativistic jets, they do not show evidence of a luminous accretion disk as they are quite weak at X-ray energies. This possibly could be due to a presence of truncated accretion disk, where accretion could be happening with the help of a geometrically thick structure. The gas is thought to be accreted via radiatively in-efficient flows (RIAFs) or in other words advection dominated flows (ADAFs). As a possible consequence of the above scenario, observationally they do not show strong emission lines in the spectrum of their respective AGNs. These RI type AGNs are the dominant population in the local Universe as compared to the RE type (Best & Heckman 2012a), and studies (Best et al. 2005) have shown that galaxies hosting RI type AGN are quite distinct and that they occur in more dense environments with higher mass and redder colour.

RGs come in many shapes and sizes as seen in Fig. 1.3, and are also referred to as 'DRAGNS', which stands for 'double radio source associated with galactic nucleus'. RGs have been mainly divided into two classes, namely, Fanaroff-Riley type-I (FR-I) and Fanaroff-Riley type-II (FR-II) as described in Fanaroff & Riley (1974), which was mainly done on the basis of radio morphology. Around the same time, the work of Northover (1973), Turland (1975), and van Breugel & Miley (1977) provided great evidence for the existence of extragalactic AGN radio jets emanating from the central region of galaxies. This led to the understanding of the overall structure of RGs, which consists of a radio core (coinciding with the host galaxy) shooting out bipolar jets, which often ended up in cloud like structure

called lobes (FR-II) as seen in the top right side of Fig. 1.2. Often high concentration of radio emission was found farther from the host galaxy, transported by jets into lobes to a region called as 'hotspot', the existence of which was shown by Mitton & Ryle 1969 first and then further confirmed by Miley & Wade 1971; Hargrave & Ryle 1974 in the famous radio source Cygnus A. The radio jets and lobes are optically thin in nature, with jets having spectral index $\alpha \sim 0.5$ to 0.8 and ~ 0.7 to 1.5 for the lobes. For the radio core which is compact and optically thick, the spectral index is flat (0 to 0.5) or inverted in some cases. The current interpretation based on the decades of observations and models (Scheuer 1974; Gopal-Krishna & Wiita 1987; Falle 1991; Kaiser & Alexander 1997; Blundell et al. 1999; Hardcastle 2018b) is that the radio jets emanating from the central region of the galaxy propagates through the interstellar medium to outer intergalactic medium for FR-I type. In FR-II type, the jet material encounters and smashes into the ambient medium and creates 'hotspots', which is a shock front with lot of particle acceleration. The region where the jet ends and impacts with external medium, a 'working surface' is developed which maintains high pressure (Blandford & Rees 1974). Here, the bulk kinetic energy of the jet converts into relativistic particles via first-order Fermi acceleration and magnetic fields through shock compression. This process results in emission of large amount of radio synchrotron radiation from high surface brightness 'hotspots'.

Jets are the collimated streams of plasma containing relativistic electrons trapped in a magnetic field, and they primarily radiate via radio synchrotron emission. The jets scaling from parsec to megaparsec scales are powered by the black holes sitting at the heart of the AGN. The leading models explaining the launching and collimation of jets are the mechanisms by Blandford & Znajek 1977 (B-Z) and Blandford & Payne 1982 (B-P). It is outlined in the former model that the jets are powered via extraction of the rotational energy of the black hole, and in the latter case, the jets are anchored by the poloidal component of the magnetic field in the accretion disc surrounding the black hole. Another interesting model is the magneto-hydrodynamic (MHD) model which requires a gravitational potential hub i.e. a black hole surrounded by differentially rotating accretion disc with a poloidal magnetic field threading it (Meier et al. 2001). The complexity of the process of jet collimation and confinement increases with different processes contributing at different radii. At the very start, the jet is confined by the gas dynamical disc around the black hole. This region lies within $\sim$ 10-10^5 Schwarzschild radii (r_s) from the black hole (10^8 $M_\odot$ at $z < 0.1$)

(Junor et al. 1999; Hada 2020). If the wind happens to be hydromagnetic then the jet carries an axial current (Blandford et al. 2019) of toroidal magnetic field which is in turn balanced by gas pressure (Begelman et al. 1984). Thus, relativistic jets are mainly confined by gas pressure, and at the lobes by the backflow of particles coming from hotspots for FR-II sources. Study of AGN jets using VLBI along with other multi-wavelength facilities has enhanced our knowledge about the intricate configuration of jet magnetic fields and helped us to constrain the ejection site of highly energetic flares. Recent studies of M87 jet-base with high sensitivity arrays and Very long baseline array support the magnetically-driven (Livio 1999) jet launching model in the presence of spinning black holes.

The works of Scheuer & Readhead (1979); Kapahi & Saikia (1981); Orr & Browne (1982); Kapahi & Saikia (1982) on the relativistic beaming of quasars created the essential foundation for the standard unification scheme proposed for radio quasars and radio galaxies (Scheuer 1987; Barthel 1987, 1989) based on orientation. Under this scheme, it is proposed that (radiatively-efficient) radio-loud quasars, broad line radio galaxies (BLRGs) and narrow line radio galaxies (NLRGs) intrinsically belong to the same population (see Fig. 1.1). This model suggests that closer to the central super-massive black hole is the broad emission-line region which is shrouded in the dusty torus and further out lies the narrow-line emission region. As illustrated in Fig. 1.1, objects viewed closer to the plane of the sky are classified as NLRGs, whereas BLRGs and quasars are viewed at an angle by the observer. The low excitation radio galaxies (LERGs) are thought to be deviant to this proposed model (Barthel 1994). More details can be found in the review article of Urry & Padovani (1995) and further studies (e.g., Ishwara-Chandra & Saikia 2000 and Mullin et al. 2008) tested this model with larger samples, and their results largely support the unification scheme.

1.3 Giant radio galaxies

When the overall size of RGs grows to megaparsec (Mpc) scales, then they are referred to as Giant Radio Galaxies (GRGs). Originally, they were defined by Willis et al. (1974) as per the cosmology commonly used in those days, with the Hubble constant (H_0) ~ 50 km s^{-1} Mpc^{-1}. These structures of unfathomable scales (Mpc) are relatively rarer than their smaller sized counterparts, i.e., the RGs. To perceive the giant scale better, a Mpc is the distance covered by ~ 33 Milky Way galaxies (extent observed at

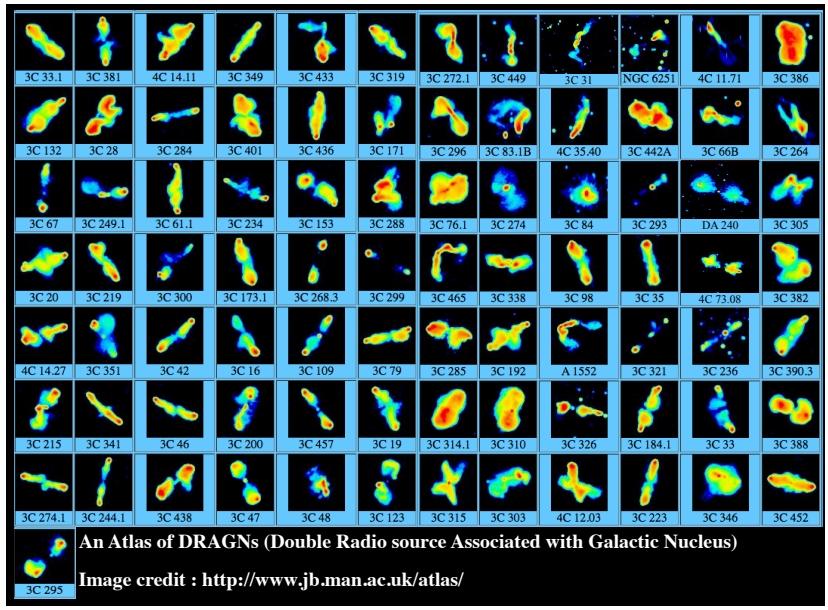

Figure 1.3: Radio images of famous radio galaxies and radio quasars from the 3C and 4C radio survey sample mapped with VLA and WSRT.

optical wavelengths ∼30 kpc) stacked in a row (see Fig. 1.5). Sizes of the GRGs are often comparable to the sizes of the galaxy clusters, and hence they can possibly influence large scale structures, seeding magnetic fields (Kronberg et al. 2004), particle acceleration (O'Sullivan et al. 2009), and probing the intergalactic medium (Strom & Willis 1980; Gopal-Krishna et al. 1989; Subrahmanyan & Saripalli 1993). Few environmental studies (intergalactic medium or IGM) of GRGs (e.g. Malarecki et al. 2013, 2015; Peng et al. 2015) have attempted to probe the Warm-Hot Intergalactic Medium (WHIM). The study of WHIM is of particular importance with respect to the 'missing baryonic problem' (Cen & Ostriker 1999; Davé et al. 2001; Nicastro et al. 2008), which refers to the discrepancy between observed and predicted baryonic budget of the Universe. The missing baryons were then conjectured to be hiding in the low density hot plasma permeating through the Universe, whose detection has recently been claimed (Eckert et al. 2015; Nicastro et al. 2018). Also, Xu et al. (2006) used GRGs as tools to estimate magnetic field in large scale structure with the help of the Faraday rotation measurement.

In the 1970s, with the development of the aperture synthesis telescope

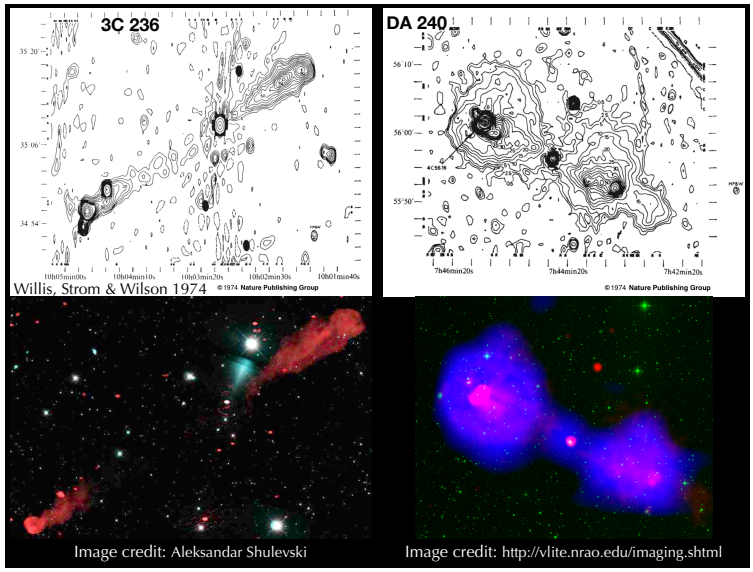

Figure 1.4: The top panel shows radio images of the first two GRGs discovered by Willis et al. (1974) made using the WSRT. The bottom panel shows improved images made recently using LOFAR for 3C 236) and combination of WSRT and VLA for DA 240.

like the Westerbork Synthesis Radio Telescope (WSRT; Baars & Hooghoudt 1974; Hogbom & Brouw 1974), the first two GRGs (3C 236 and DA240) were identified by Willis et al. (1974) using Bridle et al. (1972) ∼98% complete 1400 MHz radio sample. Owing to the large angular sizes (>30′) and large fluxes (>5 Jy) of the two sources, Willis et al. (1974) were able to sufficiently resolve them at 610 MHz with arcminute (′) resolution (top panel of Fig. 1.4). After this, radio astronomers using aperture synthesis telescopes like the WSRT and the Very Large Array (VLA; Thompson et al. 1980; Napier et al. 1983) continued to map bright radio sources from radio catalogues like the third Cambridge radio survey (3CR; Bennett 1962; Laing et al. 1983) and Bologna radio survey (B2; Colla et al. 1970) and continued to find more GRGs. Despite this, only about 50 GRGs were found till the ∼1990s (Ishwara-Chandra & Saikia 1999). All GRG discoveries were made using radio interferometers at high frequency, which equipped them with better resolution, with the exception of GRG 0503-286. It was identified and studied first using the Ooty Synthesis Radio telescope (OSRT; Swarup 1984) at 327 MHz by Saripalli et al. (1986).

It was only in the mid-1990s when the WSRT, the VLA, and the Molonglo Observatory Synthesis Telescope (MOST; Mills 1981) started their

respective large area radio surveys, a larger number of GRGs were discovered. Therefore, it will be fair to present their work briefly:

- Schoenmakers et al. (1998, 2001) using the advantage of low-frequency survey (more sensitive to steep spectrum emission from lobes) like the Westerbork Northern Sky Survey (WENSS; Rengelink et al. 1997) at 325 MHz discovered large sample (~ 30) of GRGs and performed systematic studies (Schoenmakers et al. 2000b). Here, they created a sample of 49 GRGs from WENSS and found a sharp cut off of sources above 2 Mpc in size and that no GRG exists above 10^{27} W Hz^{-1} radio power at 325 MHz in the given survey area. Studies by Schoenmakers et al. 2000b also defined a complete sub-sample of 18 GRGs, and based on their observations between 325 MHz to 10 GHz radio frequencies with acrminute resolution, they estimated the average spectral age of ~ 80 Myr, advance velocities of 0.4c and particle densities of 10^{-5} cm^{-3}. These findings were similar to that of Mack et al. 1998, who studied five GRGs in their work. The work of Schoenmakers et al. 2000b concluded that the morphology of GRGs is slightly more asymmetric than the low size RGs from the 3CRR, with their over-pressured radio lobes and GRGs are older with respect to their spectral ages. They also observed that GRGs are located in relatively sparser environments. Furthermore, their work also focused on the emission line properties of their host AGN for a small sample of 22 sources and found no differences between the properties of GRGs and RGs.

- Similarly, a radio survey at higher frequency was carried out with the VLA at 1400 MHz, which is called the NRAO* VLA Sky Survey (NVSS; Condon et al. 1998). Using the NVSS, Lara et al. (2001a) and Machalski et al. (2001) found 31 and 22 new GRGs, respectively. These were followed up with radio observations to decipher their morphology and study other radio properties (Lara et al. 2001b, 2004; Machalski et al. 2004a,c, 2006a; Machalski & Jamrozy 2006; Machalski et al. 2007a,b).

- Using the MOST, Bock et al. (1999); Mauch et al. (2003) carried out a survey called Sydney University Molonglo Sky Survey (SUMSS) at 843 MHz. Subsequently, it was used by Saripalli et al. (2005) to find more GRGs especially in the unexplored southern sky ($< -30^\circ$

*National Radio Astronomy Observatory

declination) which was covered by SUMSS for the first time at ∼1 GHz frequencies. They defined a complete sample of 18 GRGs and observed it with other radio telescopes to study their morphology and asymmetry parameters. A subset of Saripalli et al. (2005) sample was followed up by Subrahmanyan et al. (2006) and Malarecki et al. (2013) for their respective studies on the radio morphology and probing of the IGM.

The above-mentioned dedicated searches from respective surveys still did not reveal a large population of GRGs due to lack of enough radio sensitivity and resolution (coarser resolution of WENSS: ∼ 54″, NVSS: 45″, and SUMSS: ∼ 45″) to resolve the morphologies sufficiently. Also, another reason was the lack of large sky area optical spectroscopic surveys. In order to identify GRGs, the radio images must have enough sensitivity and resolution to detect and identify the radio core, which must coincide with an optical galaxy or quasar whose redshift is needed to estimate the projected linear size.

The GRGs discovered were followed up by others, e.g. Konar et al. 2004, who studied a sample of 17 GRGs (some hosted by quasars too) at multiple radio frequencies from 240 MHz to 8 GHz to study their morphology and other radio properties. Magnetic field and spectral age estimates were also obtained by Konar et al. 2008 and Jamrozy et al. 2008 for a sample of 10 GRGs. The spectral ages of GRGs in their sample were in the range of 6 to 36 Myr with an average injection index of 0.6.

Based on the tools (telescopes+data+computational infrastructure) available at the time, above-mentioned works found a few hundred GRGs since 1974 along with their radio and associated properties. Now, with the advent of large sky area surveys in radio as well as in optical along with simulations, it is now possible to take this field further towards understanding the origin and evolution of these giant sources. The induction of several new radio telescopes which are equipped with cutting edge technology like the Jansky VLA (JVLA) and LOFAR have already shown unprecedented results (see bottom panel of Fig. 1.4).

1.4 Work in this thesis

The study of GRGs is essential with respect to understanding the growth and evolution of RGs, and their possible contributions to other processes in the Universe.

The goal of the thesis is to answer some of the following questions :

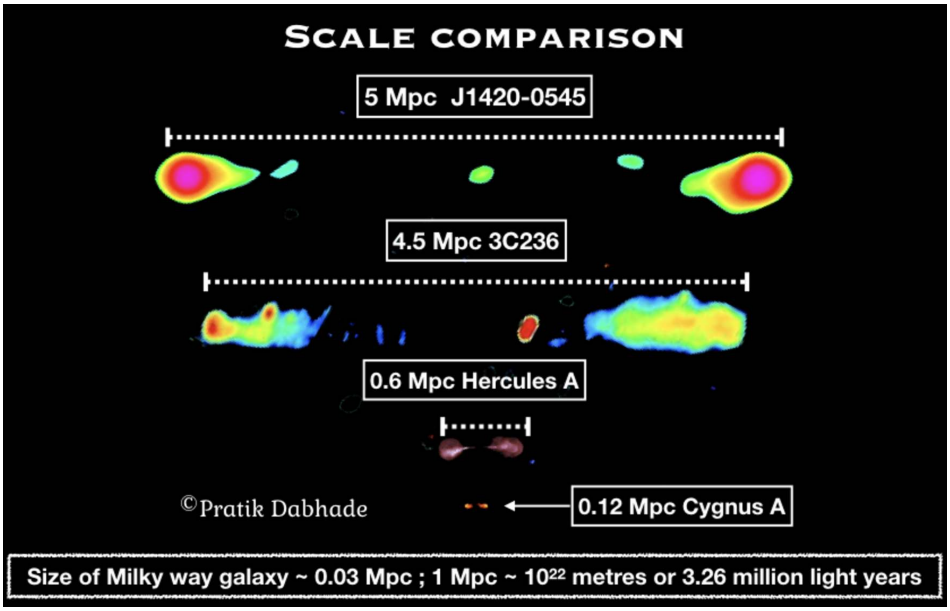

Figure 1.5: The figure shows radio images of some of the biggest GRGs and most famous RGs oriented horizontally with their respective size scales for the sake of comparison.

- What is the space density of GRGs ?
- What are the causes for their megaparsec scale sizes ?
- Do GRGs have a preferred AGN excitation state - high or low ?
- How do the radio properties of GRGs and RGs compare ?
- Are GRGs older than RGs ?
- Does the mass of GRG's SMBH outweigh the mass of RG's SMBH ?
- What fraction of the giants are powered by quasars (GRQs) ?
- Do GRGs only grow in the sparse environment ?

The work in this thesis comprises of three main broad parts-

1. Search for new samples of GRGs from existing and new radio surveys with the added help of large optical spectroscopic surveys.
2. Creating a complete and uniform database of GRGs known till date, which will be the basis of future studies for the community at large.
3. Using the newly created large database of GRGs, studying their host AGN properties systematically with statistically significant samples and exploring their environmental properties.

Below is the summary of each chapter comprising of above-mentioned work which was essentially done using data from different radio telescopes (see Fig. 1.6) and archival optical/mid-infrared data.

- Chapter 2: A dedicated project was initiated for the studies of GRGs called SAGAN, which stands for Search and Analysis of Giant radio galaxies with Associated Nuclei. In this chapter, the pilot results of the project are presented based on the initial searches from the NVSS. A total of 25 new GRGs are reported along with the mid-infrared properties of their host AGN and AGN excitation types.
- Chapter 3: Before the arrival of high sensitive low-frequency instruments like the LOFAR, very few attempts (Perley & Erickson 1979; Artyukh & Ogannisyan 1988; McGilchrist et al. 1990; Cotter et al. 1996; Nandi et al. 2010) were made to observe GRGs at low frequencies (< 200 MHz) mainly because of the lack of resolution at these frequencies provided by the telescopes before, necessary technology

and the difficulties in dealing with the turbulent ionosphere affecting the radio waves. Using the LOFAR's unique capabilities of mapping low-frequency sky at unprecedented sensitivity and high resolution, the LOFAR Two-metre Sky Survey (LoTSS; Shimwell et al. 2019) was conducted in the Hobby-Eberly Telescope Dark Energy Experiment Spring field region (HETDEX). It covered 424 deg^2 sky area with 6″ and 20″ resolutions, having noise levels of ~100 μJy beam^{-1}. Based on manual and semi-automated techniques, the largest sample of GRGs (225) was discovered from the LoTSS, of which 40 are hosted by quasars. The chapter explains the procedures used for searches and the properties of the new sample. The sample also enabled to show for the first time that the spectral index of RGs and GRGs is similar.

- Chapter 4: Here, the first major results of project SAGAN are described which are as follows: hitherto creation of the largest and uniform GRG catalogue comprising of 820 objects, reported between 1974 to March 2020 (see Fig. 1.7). This was done using all the publicly available data. Another new 162 GRGs were also reported for the first time in this study. Using the GRG catalogue, the radio properties and host AGN properties were studied in detail. Also, a comparative study of properties between RGs and GRGs was carried out. The results backed by significant statistics show that the distributions of the radio spectral index and the black hole mass of GRGs do not differ from RGs. Other key physical properties like black hole mass, spin, Eddington ratio, jet kinetic power, total radio power, magnetic field, and size were compared for GRGs with low excitation AGN and GRGs with high excitation AGN. Our findings strongly suggest that statistically, the GRGs with high excitation AGN have larger sizes, stronger radio power, jet kinetic power, and higher Eddington ratio than those GRGs with low excitation AGN. We also find ~ 10% of all GRGs reside in centres of galaxy clusters and that they tend to avoid massive clusters.

- Chapter 5: Here, we explore the millimetre wave properties of the host AGNs of GRGs by attempting to detect molecular gas, which may shed more light on their accretion properties, star formation rate and stellar mass properties. Also, how these properties compare with other objects to determine the factors making these objects giants. Such studies are very scarce, and it is thought that GRGs may not contain enough molecular and atomic gas to fuel star formation.

Using the large GRG catalogue from the SAGAN project, 12 GRGs were selected based on their mid-infrared properties to observe with the IRAM-30m millimetre telescope. Molecular gas content, star formation efficiency and depletion time information were obtained for few sources. In all, we obtained detection in three of the twelve objects with upper limits in the rest and combined the results with other GRGs from literature. The results suggests that the GRGs, in general, seem to have much longer depletion time than that of their radio emission.

- Chapter 6: As part of project SAGAN, hundreds of new GRGs were found, and a sub-sample of GRGs was observed with the Giant Metrewave Radio Telescope at multiple frequencies to obtain high resolution images to decipher their morphologies and to estimate magnetic field along with their spectral ages. Here, the study of one of the most peculiar GRGs is presented which is hosted by a galaxy in a dense cluster like environment, and exhibits $\sim$200 kpc linear jet terminating into a $\sim$100 kpc 'kink' like structure. Along with three frequency GMRT data (325 MHz to 1400 MHz), the study also benefited from the LOFAR 144 MHz low-frequency data, which allowed us to probe the source at very low frequencies with high resolution and good sensitivity. We observe that the GMRT 325 MHz and LOFAR 144 MHz maps show the maximum emission from the GRG, and also the counter jet on the eastern side is seen feeding the lobe. The detection of counter-jets (especially of such large sizes) in FR-II GRGs is not common and hence, this object provides an unique opportunity to study the large scale MHD processes. The 'kink' structure is quite bright and shows a shock front whose Mach number also has been estimated, and the possible process giving rise to it have been extensively discussed. Owing to its peculiar morphology and uncanny resemblance, it has been named as 'Barbell GRG'.

1.5 Future scope

Recently, the LoTSS, owing to its unprecedented sensitivity to low surface brightness diffuse emission has produced very interesting results as evident from the series of papers in the *Astronomy & Astrophysics* journal's special issue*. This enabled to the discovery of the largest GRG sample (225) to

*LOFAR Surveys: a new window on the Universe

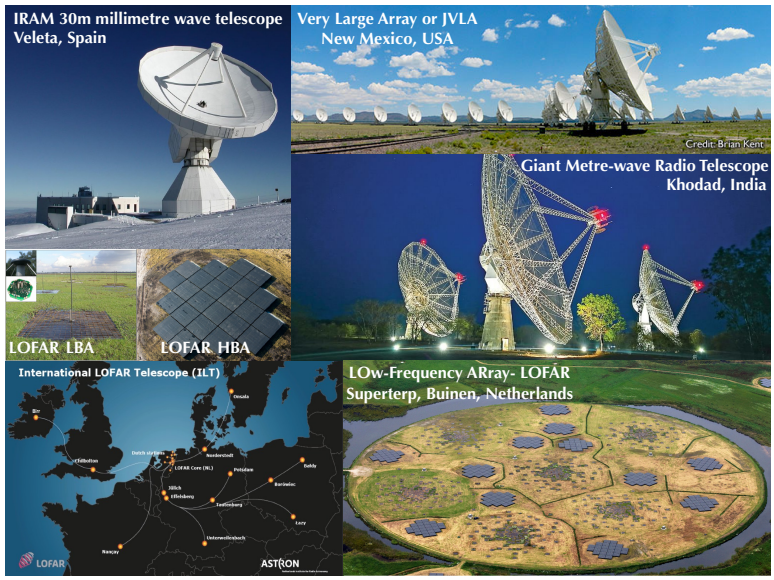

Figure 1.6: The figure shows a montage of the radio telescopes (and one millimetre-wave: IRAM) like the VLA, GMRT, and LOFAR whose data have been extensively used in the work presented in this thesis.

date from a relatively smaller part of the sky (HETDEX field of ~ 424 deg^2) and unveiled (Chapter 3 of this thesis) the hidden GRG population (Dabhade et al. 2020b). The LoTSS, which is an ongoing survey of the northern sky ($\sim 2\pi$ steradians) is expected to find at least ~ 12000 GRGs, implying that GRGs are not as rare as previously thought. It will be complemented with the ongoing optical-spectroscopic survey like the WEAVE-LOFAR survey (Smith et al. 2016). The above number is far higher than what was predicted few years back with the future survey of the Square Kilometre Survey called the SKA1$_{SUR}$, which is poised to cover $\sim 80\%$ of sky upto $+48^\circ$ declination at L band. Based on predicted calculations of Peng et al. 2015, the SKA1$_{SUR}$ survey should detect about 12000 GRGs from the total sky area, which is larger than what the LoTSS is going to cover.

All the above mentioned work were greatly benefited from the surge in the improvement in imaging techniques and new software packages. In the coming years, radio telescopes with their respective surveys are expected to produce data on the astronomical scale. While the challenging task of data reduction via automated pipelines has been accomplished, the task of sorting and examining the final images in an automated fashion still remains

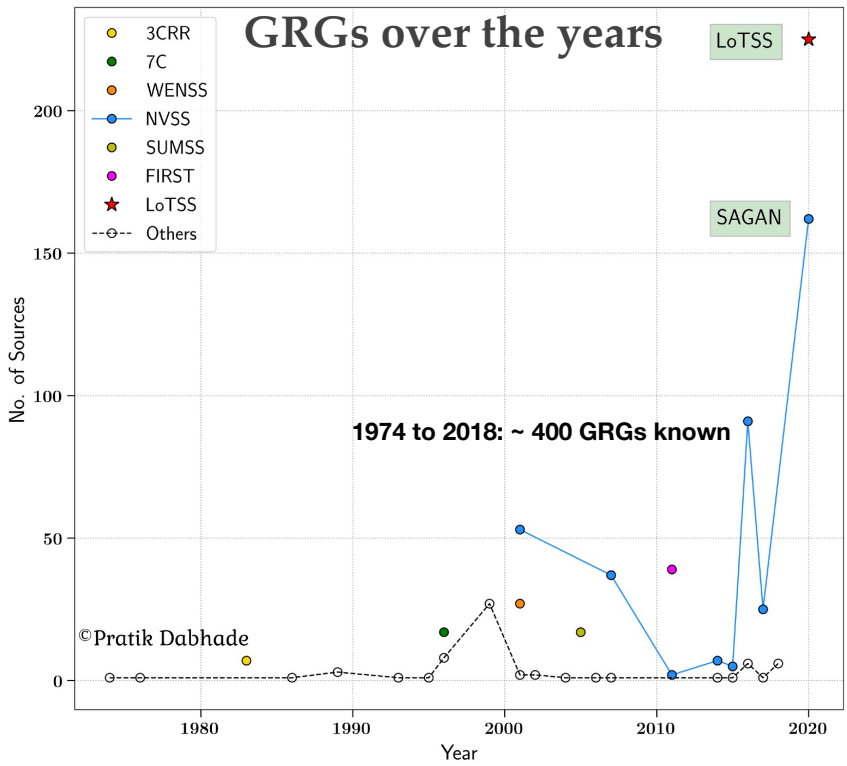

Figure 1.7: The plot shows discoveries of GRGs over the years starting from 1974 to 2020 via different radio surveys. Work done in this thesis has led to the doubling of the known population of GRGs, which in turn has enabled studies with statistically significant samples. Details of the work related to the LoTSS sample is presented in Chapter 3, followed by chapter 4, which is dedicated to the SAGAN sample.

a work in progress. Recently, there have been some promising results in this area obtained using machine learning techniques (Galvin et al. 2020).

The existence of the giant radio lobes depends on the external medium (thermal or ram pressure) which can confine them or provide a working surface. Therefore, in case of GRGs with hundreds of kpc large lobes, the external pressure on large scales can be probed. It is possible to estimate the pressure of the lobes of GRGs using X-ray observation of inverse-Compton process, where the electrons in the lobe scatter photons of the Cosmic microwave background radiation (CMB). This enables us to directly measure the electron energy density, and sheds more light on the particle content and magnetic field strength. The demonstration of the above technique has been done in the past two decades (e.g. Hardcastle et al. 2002; Croston et al. 2005) for FR-II type radio sources, which has helped constrain source dynamics by comparison of lobe internal pressure and external pressure arising from X-ray emitting hot gas. Very few GRGs till date have been studied (e.g. Konar et al. 2009; Isobe & Koyama 2015; Mirakhor et al. 2021) using this technique, and for the better understanding of GRGs and their environments it is essential to study their X-ray properties. Hence, dedicated study with Chandra and XMM-Newton X-ray telescopes of large samples of GRGs residing in cluster environment is needed. This effort will also largely be benefited from the near future data release of all sky X-ray survey of eROSITA (Basu-Zych et al. 2020).

The ongoing and the upcoming surveys at radio and other wavelengths, will not only find more GRGs but also possibly will provide definite answers related to the questions posed by their enormous sizes. There is also quite a vast scope of using GRGs as tools to probe other problems like the study of WHIM (Malarecki et al. 2013, 2015) for the 'missing baryons' problem. Old relic GRGs owing to their large sizes could also be responsible for providing necessary seed particles for giant radio relics (Rottgering et al. 1997; Bagchi et al. 2006; van Weeren et al. 2019) found near the galaxy clusters and can help in understanding their origins better.

As briefly discussed in Sec. 1.2, the RGs have been used in the past for cosmological studies and in the 1990s, brave and exciting attempts (alternative to the supernova studies) were also made to use RGs as standard candles (Daly 1994b; Gurvits et al. 1999; Sahni & Starobinsky 2000) to measure the acceleration parameter of the Universe. Now, with more data on RGs and in particular GRGs, these techniques (Daly et al. 2008; Weinberg et al. 2013) could be revisited and improved (e.g., see Turner & Shabala 2019) to use these objects as independent cosmological probes for measuring

the Hubble constant and in the quest for understanding dark energy.

The respective radio surveys from LOFAR, uGMRT, ASKAP, JVLA and MeerKAT are already reaching unprecedented sensitivities and their surveys have already unearthed hundreds of objects with no optical identifications. This implies that these are mostly high redshift objects which are not visible or detected in the currently available optical and infrared surveys. Hence, optical surveys from upcoming facilities like the Large Synoptic Survey Telescope (LSST) or Vera Rubin Observatory (Ivezić et al. 2019) and EUCLID space mission (Amendola et al. 2013) will provide us optical identification for all over high redshift radio source candidates and thereby allowing us to study the high redshift Universe.

2 | Discovery of Giant Radio Galaxies from NVSS: Radio & Infrared Properties

Giant radio galaxies (GRGs) are one of the largest astrophysical sources in the Universe with an overall projected linear size of ∼0.7 Mpc or more. Last six decades of radio astronomy research has led to the detection of thousands of radio galaxies. But only ∼300 of them can be classified as GRGs. The reasons behind their large size and rarity are unknown. We carried out a systematic search for these radio giants and found a large sample of GRGs. In this paper, we report the discovery of 25 GRGs from NVSS, in the redshift range (z) ∼0.07 to 0.67. Their physical sizes range from ∼0.8 Mpc to ∼4 Mpc. Eight of these GRGs have sizes $\geqslant$ 2 Mpc which is a rarity. Here, for the first time, we investigate the mid-IR properties of the optical hosts of the GRGs and classify them securely into various AGN types using the WISE mid-IR colours. Using radio and IR data, four of the hosts of GRGs were observed to be radio loud quasars that extend up to 2 Mpc in radio size. These GRGs missed detection in earlier searches possibly because of their highly diffuse nature, low surface brightness and lack of optical data. The new GRGs are a significant addition to the existing sample that will contribute to better understanding of the physical properties of radio giants.

Pratik Dabhade, Madhuri Gaikwad, Joydeep Bagchi, Mamta Pandey-Pommier and Somak Raychaudhury
Monthly Notices of Royal Astronomical Society,469, 2886, (2017)
DOI:10.1093/mnras/stx860

2.1 Introduction

Giant Radio Galaxies (hereafter GRGs) represent an extreme class of active galaxies which have their linear sizes from ∼ 0.7 to 5 Mpc thus placing them amongst the largest single astrophysical objects known to us. The first GRG 3C236 was discovered about 40 years ago by Willis et al. (1974), is ∼ 4.62 Mpc in size and still ranks among the largest known GRGs. Since then only a few other GRGs have been reported. The largest known GRG till date is J1420-0545 which spans 4.95 Mpc (Machalski et al. 2008). Despite various studies on GRGs, no unified model has emerged that can explain the immense physical scale and other physical properties of these extreme class of radio sources. With the advent of large area sky surveys like NVSS (NRAO VLA Sky Survey) (Condon et al. 1998), WENSS (Westerbork Northern Sky Survey) (Rengelink et al. 1997) and SUMSS (Sydney University Molonglo Sky Survey) (Mauch et al. 2003) several more GRGs have been found and many more await discovery through dedicated searches. Morphologically, most of the GRGs show bright hot spots at the end of their radio lobes and are hence classified as edge-brightened Fanaroff-Riley class II (FR-II) objects (Fanaroff & Riley 1974). These radio sources are born in the active nuclei at the galactic centre. It is believed that their so called 'central engine' is a mass accreting super massive black hole (SMBH) of mass $10^8 - 10^{10}$ $M_\odot$, which is responsible for the ejection of the collimated, bipolar relativistic jets orthogonal to an accretion disc (Lynden-Bell 1969; Begelman et al. 1984). In common with normal radio galaxies, GRGs are usually hosted by bright elliptical galaxies. However, revealing an exceedingly rare phenomenon, recently two extremely massive and fast rotating spiral galaxies have been found that host relativistic jets and lobes that extend to megaparsec scales (Hota et al. 2011; Bagchi et al. 2014). These extraordinary objects demonstrate that given the right conditions, the central engine of the spiral galaxies can launch megaparsec scale radio jets and form lobes around them.

Since the inception of radio astronomy thousands of radio galaxies have been discovered, but only a tiny fraction of them (∼ 300 so far) are GRGs (Subrahmanyan et al. 1996; Ishwara-Chandra & Saikia 1999; Lara et al. 2001a; Schoenmakers et al. 2001; Machalski et al. 2001; Saripalli et al. 2005; Machalski et al. 2006b, 2007c; Kuźmicz & Jamrozy 2012). Of these, only GRGs have been studied in sufficient detail in multiple wavebands for achieving a good understanding of their unusual nature. This puts a restriction on carrying out any statistical study of their properties. Understanding

their birth & evolution, the duty cycle of radio activity, and the influence of the surrounding intergalactic medium (IGM), which confines the lobes far away from the host galaxy and provides a 'working-surface' for the jets to act, are among the most important problems in this field. Since the GRGs are known to extend to such large sizes, they are believed to be the last stop of radio galaxy evolution. Hence their study may help us impose important constraints on the various evolutionary models of radio galaxies. For the existence of radio lobes and hot spots at large distances from the AGN (Active Galactic Nuclei), a low density, ambient IGM is implied in which the lobes expand and eventually diffuse out at the end of their lives. It was shown by Safouris et al. (2009) that GRGs can serve as outstanding probes of the IGM via the relationship between morphology of a radio galaxy and the properties of surrounding material which is part of the large-scale cosmic-web. GRGs can also transport enriched material from the host galaxy to large distances and pollute the IGM with non-thermal particles and magnetic fields (Kronberg 1994). This non-thermal magnetized plasma may lurk in the IGM for billions of years, and become a promising source for injection of high energy "seed" particles in the turbulent intra-cluster medium (ICM) and in energetic shock waves associated with megaparsec scale central radio halos and peripheral radio relics, which are observed in some merging galaxy clusters (Enßlin & Gopal-Krishna 2001; Bagchi et al. 2006; van Weeren et al. 2010). Thus, GRGs may also play an important role in the high energy processes related to large-scale structure formation in the Universe.

Despite many observations and various theoretical models proposed, the mechanisms by which the relativistic jets are launched from the accretion discs around massive black holes in AGNs are very poorly understood (Blandford & Znajek 1977; Blandford & Payne 1982). Till date, few theoretical models have been proposed to explain the growth of GRGs to such enormous sizes. One of the common explanation for their gigantic size is attributed to the less dense IGM around them, which allows them to expand and grow unhindered (Jamrozy et al. 2008; Subrahmanyan et al. 2008; Safouris et al. 2009; Malarecki et al. 2015). This implies that GRGs are preferentially born in sparser galactic environment. Another theory proposes that GRGs are very old radio galaxies (Kaiser et al. 1997) that have grown to their current sizes over a long timescales. Detailed multi-frequency studies of larger sample of GRGs is required to validate or challenge these models in addition to discovering more GRGs in diverse galactic environments.

It is also interesting to note that megaparsec scale radio emitting plasma lobes of GRGs are the largest known natural reservoirs of magnetic field and non-thermal relativistic particles associated with a single galactic system. This makes GRGs excellent 'calorimeters' for measuring the energy output of the central black holes (BHs), because the giant radio lobes are believed to store most of the released energy of black holes for a very long time interval and may also reveal multiple radio episodes of black hole activity (Kronberg et al. 2001a). Moreover, because the extended lobes of GRGs can contain charged particles long enough for them to be accelerated to extremely high energies (Hillas 1984), it has been suggested (Kronberg 2004; Hardcastle et al. 2009) that shocks within the energetic jets and radio lobes of GRGs can be the possible sites for the acceleration of ultra high energy cosmic rays (UHECRs) whose origin is still unknown and a subject of world-wide research (Hörandel 2008; Bauleo & Rodríguez Martino 2009; Hooper 2016).

In this paper, we present a new sample of GRGs, of linear sizes in the range of 0.8 Mpc to 3.7 Mpc which were discovered during our extensive search in the 1.4 GHz radio images available in the NVSS. In the forthcoming papers, we will present more samples of GRGs along with results of statistical analysis and multi-wavelength studies of their properties. The upcoming sections are organised as follows: in section 2 we present the optical, radio and near infrared analysis of GRG sample along with the estimation of the mass of the central black hole in the AGN. In section 3, we discuss the individual GRGs and their physical properties. In Section 4, we describe their collective properties and discuss important results and their wider astrophysical implications. Finally, in Section 5, we summarize our work and discuss the future possibilities. Throughout the paper we adopt the flat ΛCDM cosmological model based on the latest Planck results (H_o = 67.8 km s^{-1} Mpc^{-1}, Ω_m =0.308) (Planck Collaboration et al. 2016). We use it to determine the linear sizes, luminosities and other relevant physical parameters of the GRGs. The Ned Wright cosmology calculator (Wright 2006) was used to obtain parameters like comoving distance (D_c), luminosity distance (D_L) and scale (kpc/ ″).

Table 2.1: Basic GRG information: $z^{\dagger}$ indicates spectroscopic redshifts.The linear projected size (Mpc) is computed using Eq.2.1. $S_{i(1.4GHz)}$ is integrated flux of the source. The $P_{1.4GHz}$ is the Radio power computed using Eq.2.2.

No.	RA (J2000)	Dec (J2000)	Angular Size (′)arcmins	z	Linear Size (Mpc)	$S_{i(1.4GHz)}$ (mJy)	$P_{1.4GHz}$ $10^{25}WHz^{-1}$
GRG1	00:16:04.3	+04:20:24.1	6.9	$0.43281 \pm 0.00009^{\dagger}$	2.40	50 ± 5	1.7 ± 0.2
GRG2	00:22:24.9	−08:18:45.7	6.2	$0.57147 \pm 0.00011^{\dagger}$	2.50	259 ± 24	14.6 ± 1.3
GRG3	03:15:36.2	−07:43:38.8	3.3	0.269 ± 0.033	0.86	151 ± 16	2.2 ± 0.2
GRG4	04:29:25.8	+00:33:04.8	6.6	0.468 ± 0.092	2.40	111 ± 10	4.5 ± 0.7
GRG5	04:49:32.3	−30:26:37.8	7.5	$0.31496 \pm 0.00015^{\dagger}$	2.14	94 ± 9	1.8 ± 0.2
GRG6	08:02:48.8	+49:27:23.8	4.3	0.678 ± 0.053	1.88	52 ± 7	3.9 ± 0.5
GRG7	08:57:01.7	+01:31:30.9	6.2	$0.27336 \pm 0.00007^{\dagger}$	1.58	99 ± 9	1.5 ± 0.1
GRG8	10:58:38.6	+24:45:35.1	10.4	0.201 ± 0.016	2.13	147 ± 12	1.3 ± 0.1
GRG9	10:59:20.1	−17:09:20.8	11.5	$0.1027 \pm 0.0005^{\dagger}$	1.33	154 ± 7	0.4 ± 0.01
GRG10	13:27:41.3	+57:49:43.4	12.1	$0.12018 \pm 0.00001^{\dagger}$	1.61	89 ± 4	0.3 ± 0.009
GRG11	13:27:43.5	+17:48:37.3	3.1	$0.65688 \pm 0.00025^{\dagger}$	1.33	70 ± 12	4.9 ± 0.8
GRG12	20:08:43.3	+00:49:18.9	11	0.412 ± 0.094	3.71	81 ± 3	2.6 ± 0.4
GRG13	20:34:49.2	−26:30:36.4	6.7	$0.10329 \pm 0.00015^{\dagger}$	0.78	76 ± 6	0.2 ± 0.01
GRG14	20:59:39.8	+24:34:23.9	8.2	0.116 ± 0.019	1.06	149 ± 8	0.4 ± 0.02
GRG15	22:33:01.3	+13:15:02.5	16	0.093 ± 0.011	1.71	125 ± 4	0.24 ± 0.008
GRG16	22:50:39.1	+28:44:45.5	8.4	0.097 ± 0.009	0.93	120 ± 9	0.2 ± 0.01
GRG17	22:56:15.1	−36:17:59.1	14.5	$0.090252 \pm 0.00015^{\dagger}$	1.51	195 ± 11	0.3 ± 0.02
GRG18	23:04:44.8	−10:50:48.2	4.3	$0.21026 \pm 0.00018^{\dagger}$	0.91	58 ± 8	0.5 ± 0.07
GRG19	23:12:01.3	+13:56:55.9	11.4	$0.14041 \pm 0.00001^{\dagger}$	1.74	338 ± 26	1.4 ± 0.1
GRG20	23:16:20.1	−01:02:07.3	6.8	0.221 ± 0.029	1.50	90 ± 5	0.9 ± 0.07
GRG21	23:26:23.2	+24:58:40.4	11.7	$0.25497 \pm 0.00002^{\dagger}$	2.88	274 ± 27	3.6 ± 0.3
GRG22	23:28:49.9	−08:25:12.7	4.7	0.555 ± 0.056	1.87	63 ± 7	3.4 ± 0.3
GRG23	23:35:52.1	+52:15:39.9	10.2	$0.070649 \pm 0.00015^{\dagger}$	0.85	95 ± 8	0.10 ± 0.008
GRG24	23:49:29.7	−00:03:05.8	4.3	0.187 ± 0.049	0.84	28 ± 3	0.20 ± 0.02
GRG25	23:55:31.6	+02:56:07.1	8.1	0.657 ± 0.235	3.48	80 ± 9	5.7 ± 1.7

2.2 Multi-frequency Properties of GRG Sample

In Table 1, we report the multi-frequency properties of our GRG sample. Henceforth, the GRGs are identified with labels GRG1, GRG2, GRG3, etc. Eight of the reported 25 GRGs have projected linear size $\geqslant$ 2 Mpc with the largest extending to $\sim$ 3.7 Mpc which places them among the largest radio galaxies known so far. The basic information like sky position of optical host galaxy (RA and DEC), redshift, the angular (arcminutes) sizes, physical sizes (Mpc), radio flux density $S_{i(1.4GHz)}$ and power is tabulated in Table 2.1. Angular size of the GRGs was estimated using the available radio maps. The angular extent was taken to be the separation between the peaks (radio brightness) of the outermost lobe components and only sources with angular size $\geqslant 3'$ were selected. The linear projected sizes of the GRGs in Table 2.1 were then computed using the formula :

$$d = \frac{\theta \times D_c}{1+z} \times \frac{\pi}{10800} \tag{2.1}$$

where
θ = Angle subtended by the source in sky in arcminutes.
z= Redshift.
D_c = Comoving distance (Mpc).
d = Projected linear size of the source in Mpc.
(Kellermann & Verschuur 1988).

2.2.1 Identification of New GRGs and Radio Analysis

All the 25 new GRGs were discovered in the 1.4 GHz NVSS images via extensive search for large scale double radio sources. This was done manually by careful visual inspection of NVSS radio maps. Search for more GRGs from NVSS is being carried out under our project SAGAN *. SAGAN stands for Search & Analysis of GRGs with Associated Nuclei. In this project, for the first time, we aim to make a sample of all known GRGs and find new GRGs from the existing survey data. Our search has yielded more than 150 new giant radio galaxy candidates and we present only those confirmed as a GRG in this paper. The criteria to form the sample of 25 GRGs reported in this paper are:

1. Double radio sources with angular size $\geqslant 3'$.
2. Confirming the coincidence of radio core and host galaxy (as seen in optical) by overlaying radio and optical maps.

*https://sites.google.com/site/anantasakyatta/sagan

3. Availability of reliable redshift (spectroscopic or photometric) information of the host galaxy from various optical surveys.

Recently similar work with different methods was carried out by Proctor (2016) where the author identified radio sources $\geqslant 4'$ as giant radio source candidates via automated pattern recognition algorithms. Information such as host galaxy identification and redshift, which is imperative for confirming actual giant radio nature of a galaxy, is not supplemented in Proctor (2016).

NVSS is a 1.4 GHz continuum survey covering the entire sky north of −40 deg declination (Condon et al. 1998). NVSS images are made with a relatively large restoring beam (45 ″ FWHM) to yield the high surface-brightness sensitivity needed for completeness and photometric accuracy. Their rms brightness fluctuations are about 0.45 mJy/beam = 0.14 K (Stokes I) and 0.29 mJy/beam = 0.09 K (Stokes Q and U). The rms uncertainties in right ascension and declination vary from < 1 ″ for relatively strong (S > 15 mJy) point sources to 7 ″ for the faintest (S = 2.3 mJy) detectable sources. The completeness limit is about 2.5 mJy.

For a more detailed morphology of the GRGs and identification of AGN core, the VLA high resolution FIRST (Faint Images of the Radio Sky at Twenty-cm) (Becker et al. 1995) survey data was employed. The FIRST survey at 1.4 GHz was done using NRAO Very Large Array (VLA) in its B-configuration, using 2×7, 3 MHz frequency channels centered at 1365 and 1435 MHz. FIRST survey maps have 1.8″ pixels, restoring beam of 5 ″ and a typical rms of 0.15 mJy. FIRST data for GRG2, GRG3, GRG7, GRG8, GRG9, GRG20, GRG22, GRG24 and GRG25 is available. In addition, we searched the SUMSS data and obtained the flux density of few GRGs at 843 MHz. SUMSS is an imaging survey (Mauch et al. 2003) of the sky south of declination, $\delta = -30$ degrees at 843 MHz. The survey has a resolution of 45×45 cosec$|\ \delta\ |$ arcsec^2. SUMSS is similar in sensitivity and resolution to the northern VLA NVSS. The SUMSS data is available only for GRG5 and GRG17, thereby providing their flux density at 843 MHz. The integrated flux densities (S_i) of GRGs were computed using NVSS maps in Common Astronomy Software Applications (CASA) using the task "CASA-VIEWER". The radio colour maps overlaid with contours shown in Figure 2.1 for GRGs were produced using the NVSS images. For this purpose Cubehelix colour scheme was used to make colour maps using task "CASA-VIEWER"in CASA. The Cubehelix colour scheme gives more weightage to green and yellow colours where human eye is more sensitive thereby bringing out essential details better in the radio images (Green 2011).

Radio powers for GRGs were calculated using the formula: (Donoso et al. 2009)

$$P_{1.4} = 4\pi D_L^2 S_{1.4}(1+z)^{\alpha-1} \tag{2.2}$$

where D_L is the luminosity distance, $S_{1.4}$ is the measured radio flux at 1.4 GHz, $(1+z)^{\alpha-1}$ is the standard k-correction used in radio astronomy and α is the radio spectral index ($S_\nu \propto \nu^{-\alpha}$) for which we adopt a universal value of 1 which is usually observed for radio galaxies. This value of α also takes care of the steepness for some sources.

2.2.2 Optical Analysis

The central regions of the GRGs were searched in the optical band for host galaxies and the brightest galaxy found within 1′ of the central peak was identified as a host galaxy. In many cases the host galaxies were found to overlap with the compact radio cores detected in NVSS and in some cases in the VLA FIRST survey. For optical images and spectroscopic redshifts we used the Sloan Digital Sky Survey (SDSS) (York et al. 2000), a major multi-filter imaging and spectroscopic redshift survey using a dedicated 2.5-m wide-angle optical telescope at Apache Point Observatory. SDSS Data Release 12 (DR12) is the final data release of the SDSS-III, containing all SDSS observations till July 2014. The SDSS also provides CCD images in five filters (u, g, r, i and z) and estimated photometric redshifts (photoZ), which were used if spectroscopic redshifts were unavailable. The photoZ redshifts are quoted for the host galaxies of GRG3, GRG4, GRG6, GRG8, GRG12, GRG14, GRG15, GRG16, GRG20, GRG22, GRG24 and GRG25. The SDSS optical colour images of host galaxies are shown in Figure 2.9. The spectroscopic redshifts of GRG1, GRG2, GRG7, GRG10, GRG11, GRG19 and GRG21 were obtained from SDSS DR12 (Alam et al. 2015). Host galaxies with spectroscopic information from SDSS also have velocity dispersion information which is described in detail in Bolton et al. (2012).

For GRGs (GRG1, GRG2, GRG5, GRG7, GRG10 and GRG21) we adopted Best & Heckman (2012b) classification criteria to classify the hosts into HERGs (High Excitation Radio Galaxies) and LERGs (Low Excitation Radio Galaxies). If the host galaxy has [OIII] (5507 Å) line equivalent width > 5Å, it is classified as HERG else it is classified as LERG. This is the first time that such a study of hosts of GRGs has been attempted.

For some of the optical hosts (GRG5, GRG9, GRG13, GRG17 and GRG18) the redshifts were obtained from the 6dF galaxy survey (Jones

et al. 2009). The 6dF refers to the Six Degree Field instrument survey that uses optical fibers and robotic positioning technology on the Anglo-Australian 3.9m telescope. Host spectrum of GRG23 was obtained from 2MASS (Two Micron All Sky Survey) redshift survey (Skrutskie et al. 2006; Huchra et al. 2012). For GRGs with spectroscopic host information not available in SDSS, computation of excitation index (EI) and corresponding classification was not attempted due to either incomplete information or lower SNR.

2.2.3 Infrared Analysis

In order to study and classify the AGN types for the GRGs we used the Wide-field Infrared Survey Explorer (WISE) (Wright et al. 2010) mid-IR magnitudes and colours and AGN hosts of the GRGs. Colour-colour plots were used to complete this study and classification. The WISE survey is an all sky survey in four mid-IR bands [W1 (3.4μm), W2 (4.6μm), W3 (12μm), W4 (22μm)] with an angular resolution of 6.1, 6.4, 6.5 and 12″ respectively. The WISE all-sky catalog was searched for all the host galaxies of the GRGs in our sample within a search radius of 5″ to obtain their magnitudes in the four mid-IR bands. The mid-IR magnitudes allowed us to compute the luminosities in the four respective bands (Table 2.4).

Mid Infrared: WISE COLOUR-COLOUR PLOT

We used the mid-IR colours to obtain the properties of a possibly dust obscured galactic nucleus and determine the radiative efficiency of the AGN. Mid-IR data is highly suitable for this purpose because the optical-UV radiation from the AGN accretion disc is absorbed by the putative dusty torus and re-radiated in mid-IR bands. It has been shown that WISE colours can effectively distinguish AGNs from star-forming and passive galaxies. Moreover, within the AGN subset itself, HERGs and LERGs stand out clearly on the mid-IR colour-colour and mid-IR-radio plots (Lacy et al. 2004; Stern et al. 2005; Assef et al. 2010; Yang et al. 2015). For the first time in this paper, using mid-IR colours we classify the GRGs into HERG, LERG, BLRG (Broad Line Radio Galaxy) and QSO (quasar) categories. Gürkan et al. (2014) have shown that W1-W2 versus W2-W4 plots display a better separation between LERGs and NLRGs (Narrow Line Radio Galaxies) than the W1-W2 versus W2-W3 plot. This in turn implies that the infrared emission from the dusty torus around an AGN is possibly stronger in W4 (22 μm) band. We have produced the WISE mid-IR colour-colour plots

(similar to Gürkan et al. (2014)) of radio loud AGN associated with all our newly discovered GRGs.

Near Infrared : Two Micron All Sky Survey (2MASS)

The J (1.25 μm), H (1.65 μm) and K (2.17 μm) bands near infrared magnitudes (Table 2.2) of all hosts of GRGs were obtained from the 2MASS catalog (Skrutskie et al. 2006). The K band luminosities of the hosts of the GRGs were calculated using the K band magnitudes and redshifts. However, no data was available in 2MASS for GRG2, GRG6, GRG11, GR12, GRG15, GRG19, GRG20, GRG21, GRG22 and GRG25.

2.2.4 Black Hole Mass Estimation

The central black hole mass of the host of the GRGs was computed using two methods which are as follows:

M_{BH}-$L_{K,bulge}$ relation

The central black hole mass of GRGs as listed in Table 2.2 was computed using the K band magnitude of the (bulge dominated) elliptical host galaxy ($L_{K,bulge}$) and using the M_{BH}-$L_{K,bulge}$ correlation (Marconi & Hunt 2003; Graham 2007). Absolute K band magnitude for the Sun of $M_{K\odot} = 3.28$ was used to compute the K band bulge luminosity.

$$\log(M_{BH}/M_{\odot}) = 0.95(\pm 0.15)\log \times \frac{L_{K,sph}}{10^{10.91} L_{K\odot}} + 8.26(\pm 0.11) \tag{2.3}$$

where $L_{K,sph}/L_{K,\odot}$ is the K band luminosity of the spheroid component of the galaxy (i.e., the bulge or the elliptical galaxy itself) in solar units.

M_{BH}-σ relation

Information on central velocity dispersion for optical hosts of GRG1, GRG2, GRG7, GRG10, GRG11, GRG19 and GRG21 is available via fiber spectroscopy in SDSS DR12 which (also listed in Table 2.3) further enabled us to compute the central black hole mass using the well known M_{BH}-σ relation (McConnell & Ma 2013)

$$\log(M_{BH}/M_{\odot}) = \alpha + \beta \log(\sigma/200 \mathrm{kms}^{-1}) \tag{2.4}$$

where $\alpha = 8.32 \pm 0.05$ and $\beta = 5.64 \pm 0.32$.

2.3 Results

In this section we provide notes on individual GRGs and discuss their optical, mid-IR and radio properties in detail.

2.3.1 GRG1 (J001604+042024)

GRG1 is a very low surface brightness radio source ($\sim$ 50 mJy) with a projected linear size of about 2.4 Mpc. The radio maps from NVSS show two radio lobes on both sides of the faint core. The host galaxy is at redshift of 0.433 and is one of the distant GRGs in our sample. Based on the criteria suggested by Best & Heckman (2012b), as mentioned in Section 2.2 we classify the host of GRG1 as LERG.

2.3.2 GRG2 (J002224.96-081845)

GRG2 is the fourth most distant GRG in our reporting sample with a spectroscopic redshift of 0.571. This results in an overall projected linear size of $\sim$ 2.5 Mpc. A fewer fraction of GRGs with overall size greater than 2 Mpc are known and even fewer at higher redshifts. It is the most powerful source from our sample as shown in Table 2.1. The FIRST map clearly resolves the faint radio core and the two radio lobes. GRG2 can clearly be classified as a FR-II type radio galaxy. Based on the criteria suggested by Best & Heckman (2012b) as mentioned in Section 2.2 we classify the host of GRG2 as LERG. This GRG is also mentioned in Bankowicz et al. (2015) where they have obtained the spectroscopic redshift of the host galaxy which is similar to that of SDSS as quoted above.

2.3.3 GRG3 (J031536-074338)

GRG3 is one of the smallest GRGs in our sample with an overall projected linear size of about 0.86 Mpc. The FIRST map clearly resolves the radio core and lobes thereby confirming its FR-II type nature.

2.3.4 GRG4 (J042925+003304): A Giant Radio Quasar?

We observe GRG4 to have a very high infrared luminosity as seen in Table 2.4. GRG4 is located at a moderately high redshift of $z\sim$ 0.47 (SDSS-photoZ). Figure 2.9 shows the host galaxy exhibiting a prominent red colour which could be attributed to obscuration from dust. This could be a possible reason why this galaxy has acquired such a large infrared luminosity.

Using the 2MASS K-band bulge luminosity we computed the mass of the central black hole to be massive at $\sim 3.5{\times}10^9$ $M_\odot$. Based on the high mass of the central black hole and high luminosities in radio and infrared bands, we infer GRG4 to be a quasar; however high sensitivity optical spectrum is still needed to confirm its quasar nature. Our claim is further supported by its position on the WISE mid-IR colour-colour plots as seen in Figure 2.6. The AGN clearly lies in a region on the plot which is populated mostly by radio loud quasars. The host galaxy also could be an ultra luminous infrared galaxy with its far infrared luminosity above the value of 10^{12} $L_\odot$ as seen in Table 2.4.

2.3.5 GRG5 (J044932-302638): A Giant Radio Quasar

GRG5 has a strong core dominated feature along with a double lobe structure as seen in Figure 2.1e. The southern lobe is possibly contaminated by another unrelated radio source as it shows an apparent extension towards the western side. This object is also observed in the SUMSS which is slightly poorer in resolution and sensitivity when compared to NVSS. The spectroscopic redshift of ~ 0.315 was obtained from Jones et al. (2009) from which the projected linear size is ~ 2.1 Mpc. We infer the central black hole to be massive at $1.7{\times}10^9$ $M_\odot$ (Table 2.2). On the wise mid-IR colour-colour plots (Figure 2.6) GRG5 lies in the region of high excitation radio loud quasars which possibly makes it a giant radio quasar. The following properties further support the hypothesis of GRG5 being a giant radio quasar (GRQ):

1. Host galaxy of GRG5 shows excess emission in near and far UV (GALEX) Bianchi & GALEX Team (1999).

2. It shows very high total and core ($3.8{\times}10^{24}$ W Hz^{-1}) radio luminosities along with high infrared luminosity which is consistent with the nature of a quasar.

3. The optical spectrum (Figure 2.2) available in 6dF Galaxy Survey (6dFGS; Jones et al. 2009) shows a very broad Hβ line width (~ 2000 km/s) which is commonly observed in quasars. A gaussian fit routine was used using IRAF (Image Reduction and Analysis Facility) and IDL (Interactive Data Language) on the lines of Hβ and [OIII] doublet of the same spectrum to obtain the widths as shown in Figure 2.3.

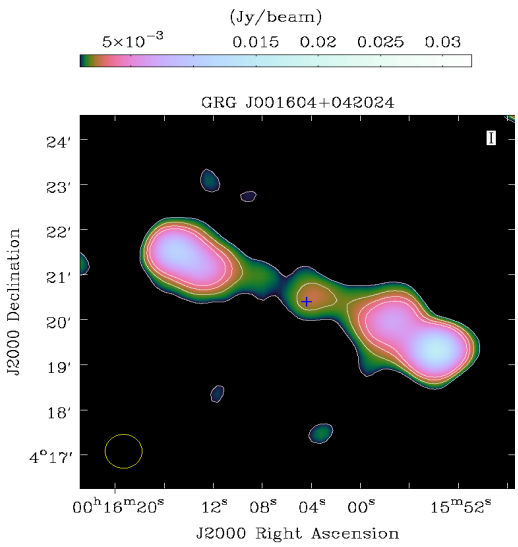

(a) GRG1 (Linear size = 2.40 Mpc)

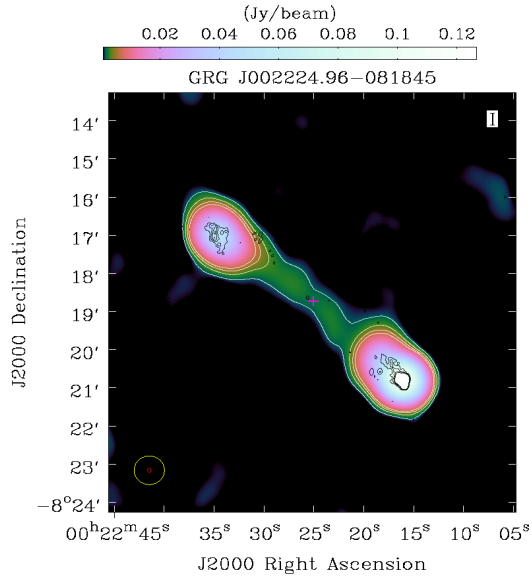

(b) GRG2 (Linear size = 2.50 Mpc)

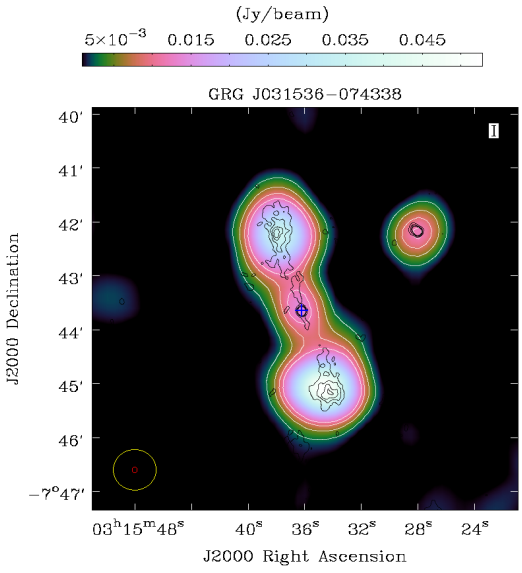

(c) GRG3 (Linear size = 0.86 Mpc)

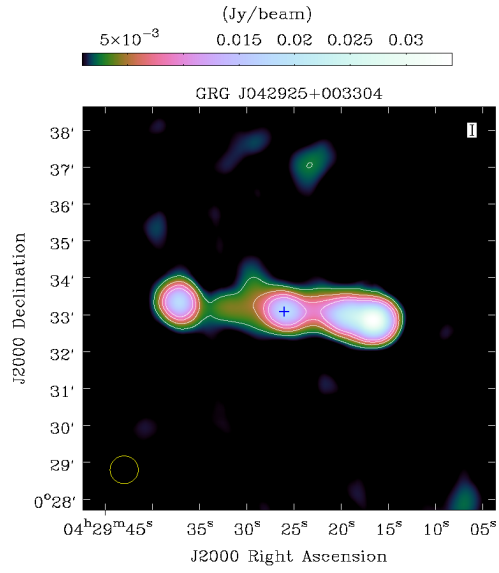

(d) GRG4 (Linear size = 2.40 Mpc)

Figure 2.1

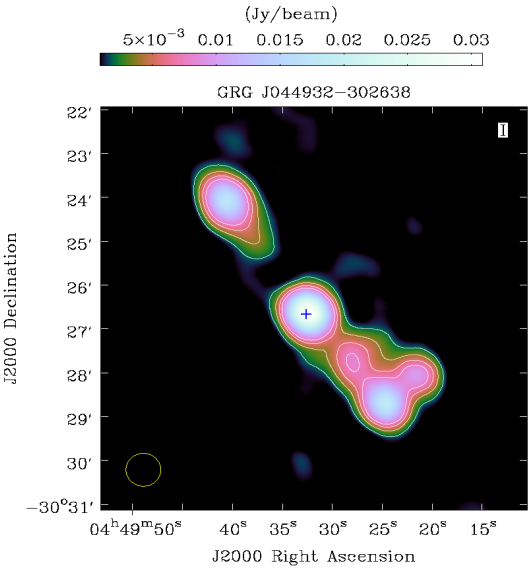

(e) GRG5 (Linear size = 2.14 Mpc)

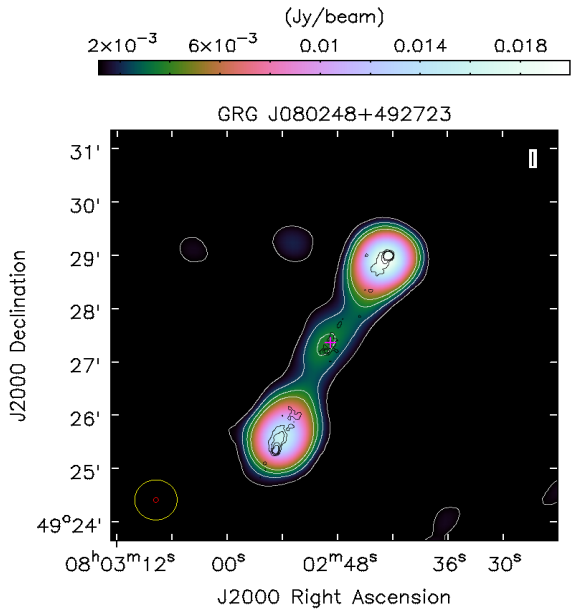

(f) GRG6 (Linear size = 1.88 Mpc)

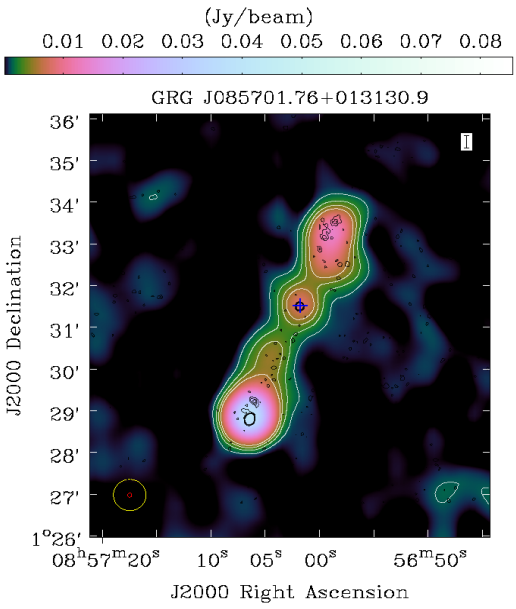

(g) GRG7 (Linear size = 1.58 Mpc)

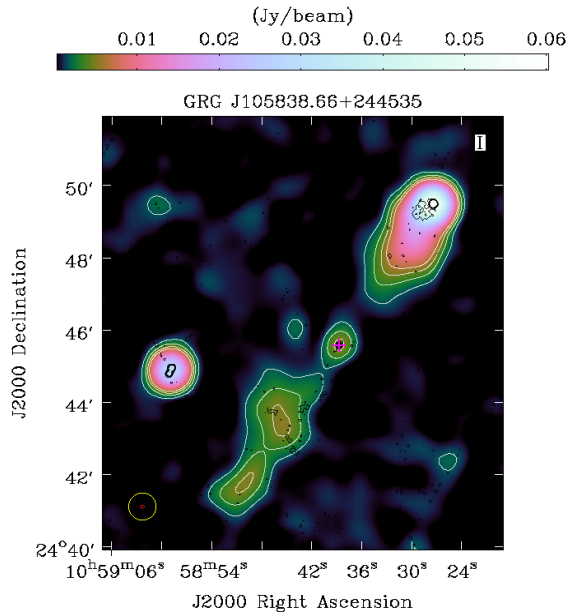

(h) GRG8 (Linear size = 2.13 Mpc)

Figure 2.1

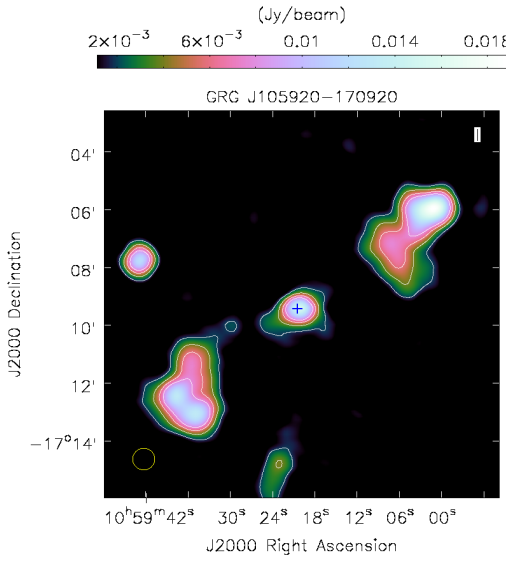

(i) GRG9 (Linear size = 1.33 Mpc)

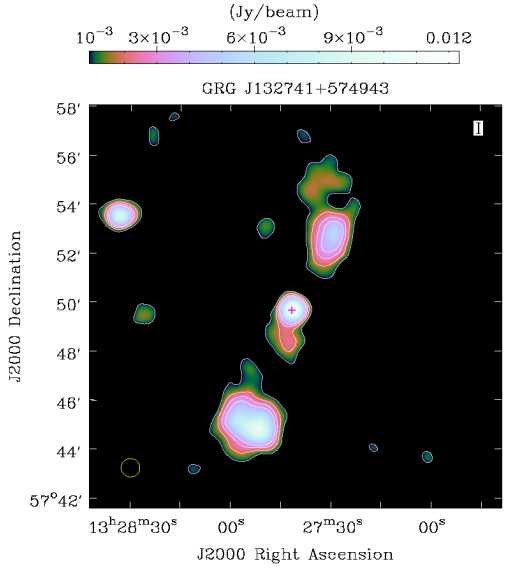

(j) GRG10 (Linear size = 1.61 Mpc)

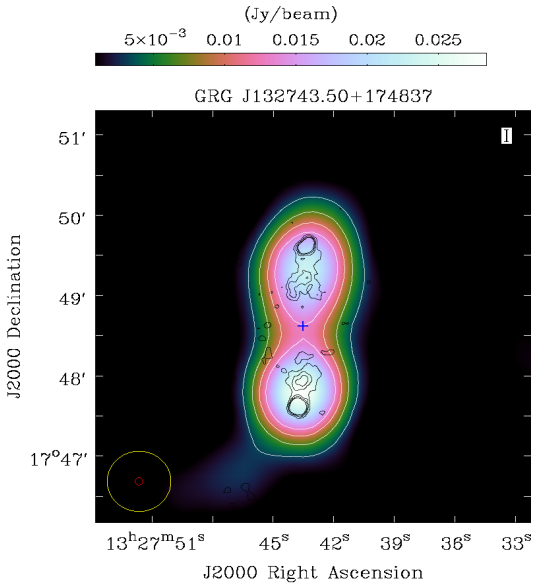

(k) GRG11 (Linear size = 1.33 Mpc)

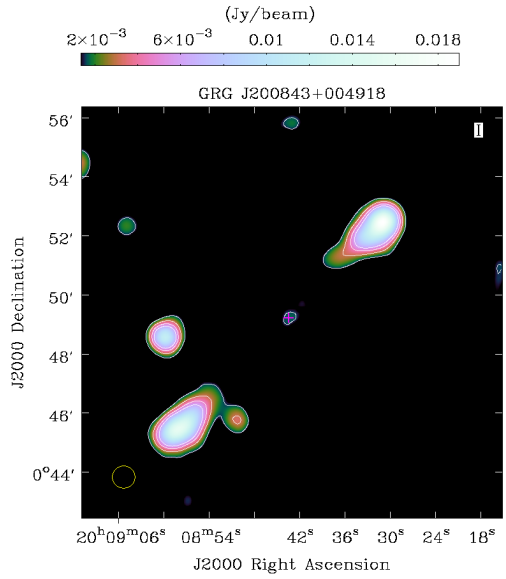

(l) GRG12 (Linear size = 3.71 Mpc)

Figure 2.1

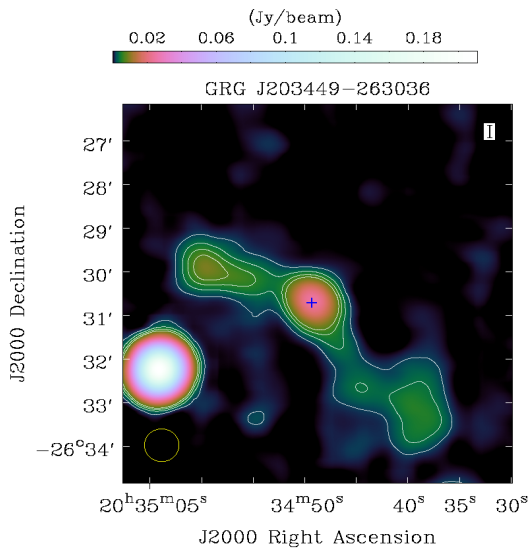

(m) GRG13 (Linear size = 0.78 Mpc)

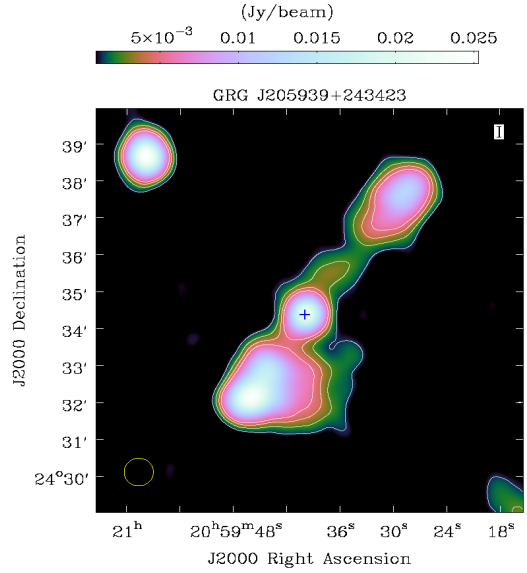

(n) GRG14 (Linear size = 1.06 Mpc)

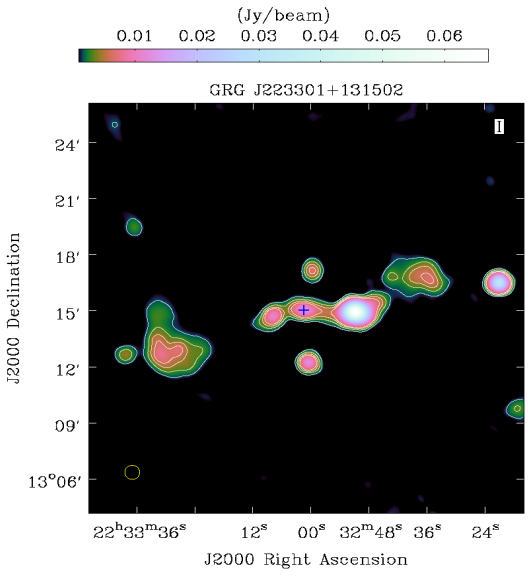

(o) GRG15 (Linear size = 1.71 Mpc)

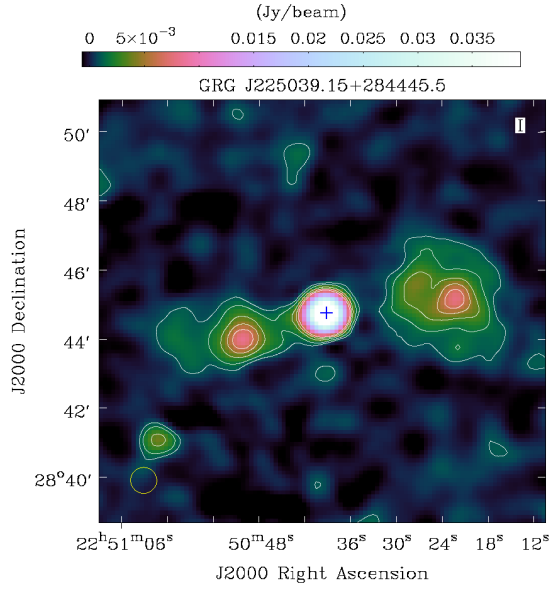

(p) GRG16 (Linear size = 0.93 Mpc)

Figure 2.1

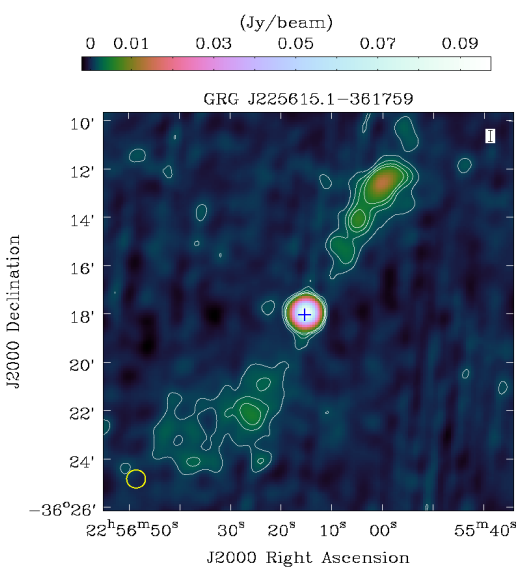

(q) GRG17 (Linear size = 1.51 Mpc)

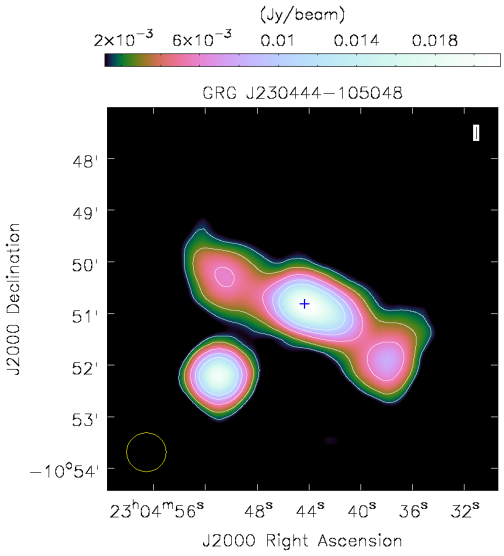

(r) GRG18 (Linear size = 0.91 Mpc)

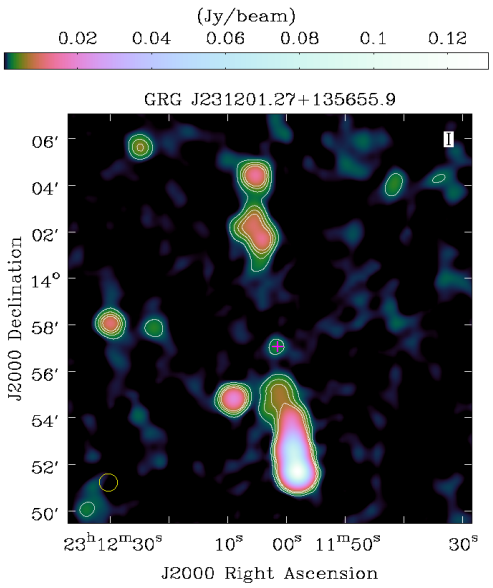

(s) GRG19 (Linear size = 1.74 Mpc)

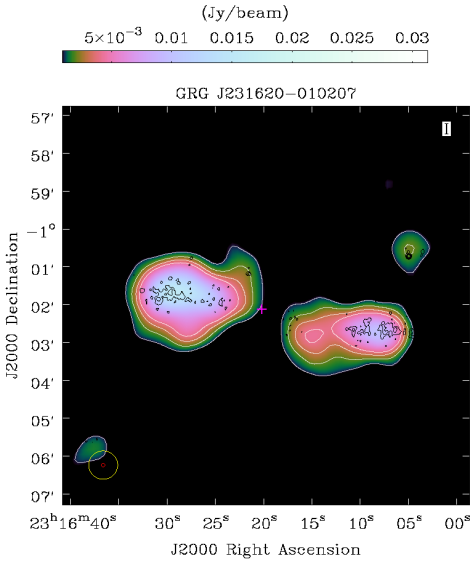

(t) GRG20 (Linear size = 1.50 Mpc)

Figure 2.1

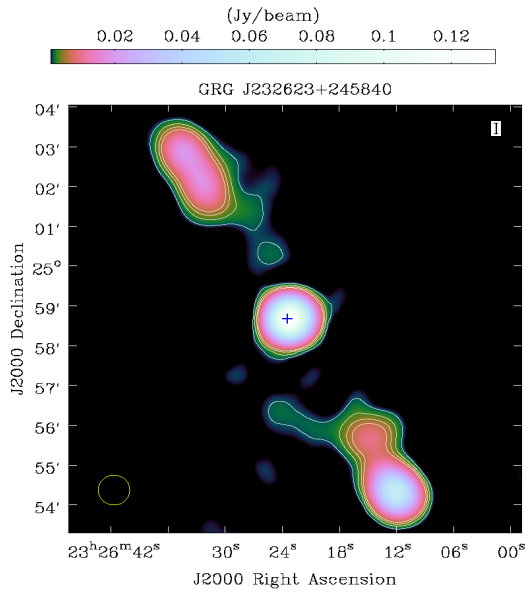

(u) GRG21 (Linear size = 2.88 Mpc)

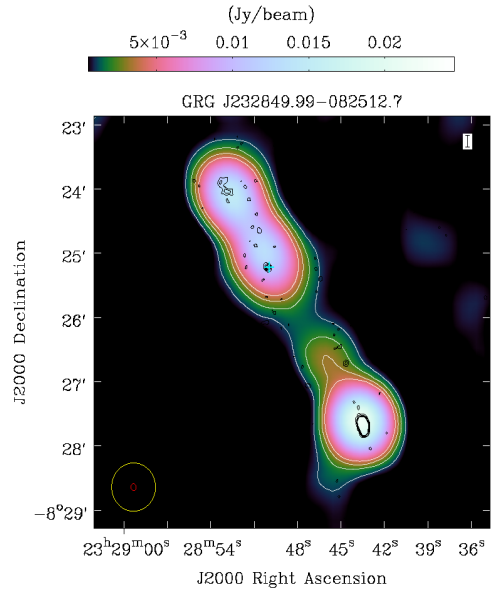

(v) GRG22 (Linear size = 1.87 Mpc)

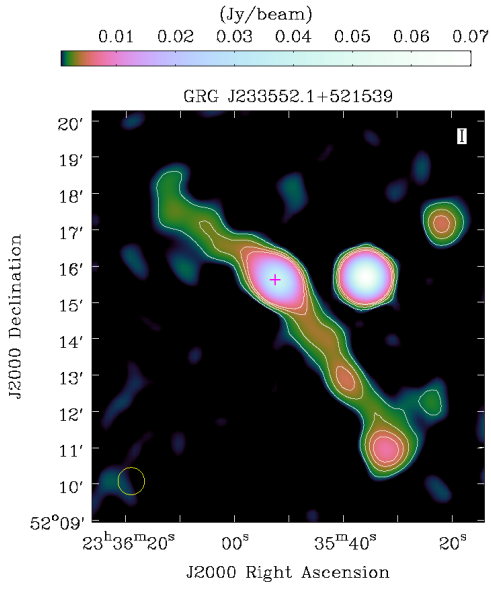

(w) GRG23 (Linear size = 0.85 Mpc)

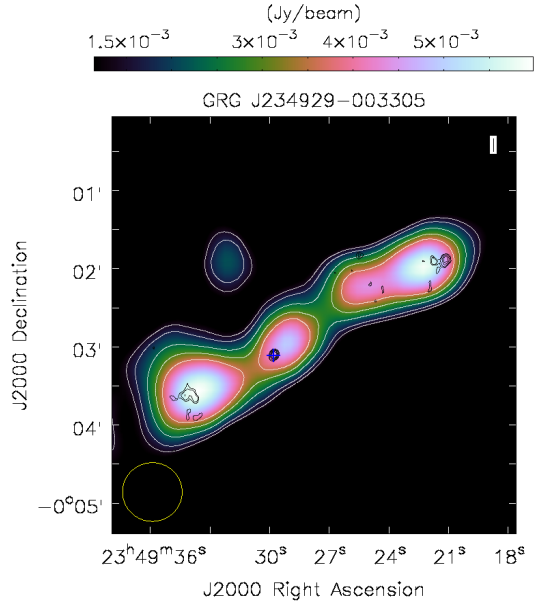

(x) GRG24 (Linear size = 0.84 Mpc)

Figure 2.1

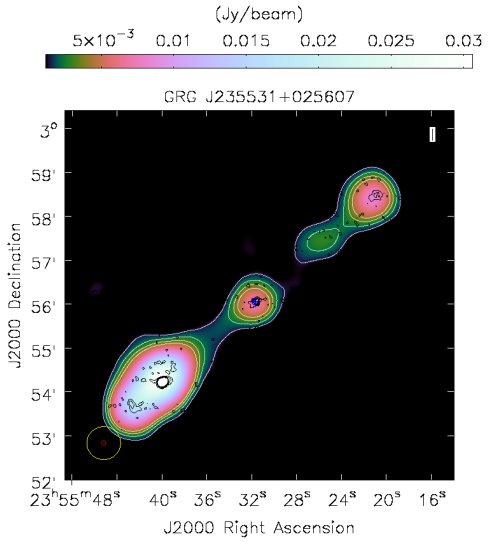

(y) GRG25 (Linear size = 3.48 Mpc)

Figure 2.1: NVSS colour (Cube-Helix) & contour maps of GRG1 - GRG25 made using task "viewer" in CASA with relative contour levels as [0.2, 0.4, 0.6, 0.8] mJy/beam. The beam size ($45'' \times 45''$ FWHM) for NVSS is represented in yellow colour and in red for FIRST ($5'' \times 5''$ FWHM) at the bottom left corner of each image. The white contours are of NVSS and the black contours (relative contour levels as [0.2, 0.4, 0.6, 0.8] mJy/beam) are of FIRST survey. The host galaxy (optical) position is marked with '+' symbol.

Table 2.2: The J, H & K band magnitudes along with their respective errors are presented in this table. M_{BH} is the mass of the black hole determined by using M_{BH}-$L_{K,bulge}$ correlation as given in Eq.2.3.

GRG No.	J	J_{Error}	H	H_{Error}	K	K_{Error}	M_{BH} ($10^8 M_\odot$)	$M_{BH-error}$ ($10^8 M_\odot$)
1	17.31	0.23	16.25	0.17	15.64	0.2	13.8	2.4
3	17.12	0.22	16.52	0.25	15.39	0.21	6	1.1
4	16.62	-	16.58	-	14.79	0.13	34.6	3.8
5	16.18	0.1	15.69	0.15	14.59	0.11	17	1.7
7	17.03	0.23	16.02	0.19	15.35	0.19	6.3	1.0
8	16.46	0.11	15.8	0.13	15.18	0.13	3.8	0.5
9	14.32	0.08	13.69	0.11	13.11	0.07	5.8	0.4
10	14.45	0.06	13.9	0.07	13.33	0.06	6.6	0.3
13	14.14	0.05	13.54	0.06	13.1	0.06	5.9	0.3
14	15.34	0.07	14.6	0.08	14.24	0.09	2.8	0.2
16	14.62	0.05	14.1	0.06	13.56	0.06	3.5	0.2
17	14.19	0.05	13.48	0.06	12.98	0.05	5.0	0.2
18	15.51	0.08	14.69	0.1	13.99	0.09	12	0.9
23	14.18	0.07	13.28	0.08	12.97	0.08	3.1	0.2
24	16.95	0.14	15.89	0.15	15.3	0.17	2.9	0.4

Table 2.3: The following table provides information about central velocity dispersion for hosts of GRGs whose data was available from SDSS. The velocity dispersion values were used to compute the black hole mass of the hosts of the following GRGs using M_{BH}-σ relation.

No.	Velocity Dispersion (kms^{-1})	M_{BH} (10^9 $M_\odot$)
GRG1	169.65 ± 35.02	0.08 ± 0.09
GRG2	250.18 ± 48.54	0.73 ± 0.80
GRG7	280.21 ± 30.28	1.39 ± 0.85
GRG10	309.58 ± 07.41	2.45 ± 0.33
GRG11	286.46 ± 70.63	1.59 ± 2.2
GRG19	247.28 ± 07.35	0.69 ± 0.11
GRG21	202.82 ± 14.13	0.22 ± 0.08

2.3.6 GRG6 (J080248+492723)

GRG6 is about 1.88 Mpc in projected linear size with its host galaxy at a redshift of ∼ 0.678. This is the most distant GRG in our sample. Not many GRGs of this size are known at higher redshifts. The FIRST map clearly resolves the radio core and lobes. The black hole mass of the host is unknown due to non-availability of K band and SDSS data. The FIRST map clearly resolves this GRG depicting its FR-II nature.

2.3.7 GRG7 (J085701.76+013130.9)

GRG7 has a very low surface brightness with an overall linear size of ∼ 1.6 Mpc. The FIRST map clearly resolves the radio core and the two radio lobes thus confirming its FR-II type nature. Also, the host galaxy is located ∼ 3.5′ away from the GMBCG J134.30444+01.56066 galaxy cluster (which is at similar redshift as that of the GRG) as listed in the GMBCG catalog of galaxy clusters (Hao et al. 2010) .

2.3.8 GRG8 (J105838.66+244535)

GRG8 shows a peculiar morphology extending over 2.1 Mpc. The southern lobe is highly diffuse with an integrated flux (S_i) of just ∼30 mJy at 1.4 GHz. In contrast to the southern lobe, the northern lobe shows a typical edge brightened lobe with an integrated flux (S_i) of ∼ 120 mJy.

2.3.9 GRG9 (J105920-170920)

GRG9 shows clear FR-II type morphology extending over 1 Mpc. The overall integrated flux (S_i) of GRG9 is only about 150 mJy at 1.4 GHz and has traces of diffuse emission.

2.3.10 GRG10 (J132741+574943)

The radio core of GRG10 shows an extension towards the southern lobe which could be attributed to an unresolved radio jet. Interestingly, from Figure 2.1j, we observe diffuse emission beyond the hotspot of the northern lobe. The radio core as detected in FIRST coincides with the galaxy (SDSS J132741.32+574943.4) thus confirming it as a host. It is at a spectroscopic redshift of 0.1202 which makes its projected linear size to be 1.6 Mpc.

2.3.11 GRG11 (J132743.50+174837)

GRG11 is one of the more distant GRGs in our reporting sample with a redshift of $\sim$ 0.657. The FIRST map (Figure 2.1k) resolves GRG11 to be FR-II type with distinctive lobes. The host galaxy appears highly reddened (Figure 2.9). We obtain a massive $\sim 10^9 M_\odot$ black hole mass via M_{BH}-σ, but it should be treated with caution due to high error, as seen in Table 2.3.

2.3.12 GRG12 (J200843+004918): An Extremely Large Radio Source?

GRG12 has angular size of 11′ showing a strong edge brightened FR-II structure. A faint galaxy SDSS J200843.37+004918.8 (m_r = 20.76) coincides with the faint radio core as seen in Figure 2.1l, indicating it to be the host galaxy of GRG12. The host galaxy has a photometric redshift of 0.412 (SDSS-photoZ) which results in $\sim$ 3.7 Mpc as its linear size. This would make GRG12 the largest GRG in the present sample as well as one of the largest radio sources known till date, after GRG J0422+1512 ($\sim$4 Mpc) (Amirkhanyan et al. 2015), 3C236 ($\sim$4.6 Mpc) (Willis et al. 1974) and GRG J1420-0545, the biggest with a projected linear size of $\sim$4.9 Mpc. (Machalski et al. 2008). The sizes of these GRGs (GRG J0422+1512, GRG 3C236 & GRG J1420-0545) were re-computed based on the cosmology adopted in this paper. Radio galaxies of such extreme physical sizes are extremely rare. GRG12 shows a clear FR-II morphology and is quite similar to GRG J1420-0545. The mass of the central black hole could not be determined via M_{BH}-$L_{K,bulge}$ correlation as the host galaxy is not detected in 2MASS survey. It was also not detected in WISE survey in any bands,

suggesting the galaxy to be quite far away. We need spectroscopic redshift data and detailed radio imaging observations to further probe this suspected extremely large radio galaxy.

Table 2.4: This table essentially shows mid-IR band magnitudes of GRGs. SNR is the profile-fit measurement signal-to-noise ratio in that band. This value is the ratio of the flux (of the band) to flux uncertainty in the W1 profile-fit photometry measurement. 10^{th} column shows the classification of GRGs using mid-IR WISE scheme, whereas the 11^{th} column shows GRG classification based on optical line flux ratios from SDSS spectrum. The WISE mid-IR luminosities (L_{W1}, L_{W2}, L_{W3} & L_{W4}) of GRGs in W1, W2, W3 and W4 bands as expressed in $L_{\odot}$.

GRG No.	W1	W1snr	W2	W2snr	W3	W3snr	W4	W4snr	IR	Optical	L_{W1} (10^9)	L_{W2} (10^9)	L_{W3} (10^{10})	L_{W4} (10^{11})
1	14.9	31.6	14.7	16.2	12.3	2.6	8.5	1	LERG	LERG	3.38	3.84	3.68	1.2
2	14.9	31.9	14.8	16.5	12.4	-2	8.9	0.1	LERG	LERG	6.51	7.37	6.62	1.6
3	14.7	35.7	14.2	26.1	11.4	5.9	8.2	3.5	LERG	-	1.28	2.08	2.69	0.53
4	12.6	45.5	11.2	51.7	8.3	41.1	5.9	24	QSO	-	32.98	122.18	169.27	15.89
5	13.8	42.4	12.5	47.5	9.6	30.3	7.2	12.7	QSO	QSO	4.36	13.82	21.68	1.99
6	15.5	25.1	14.8	18.4	10.9	8.8	7.7	7.1	LERG	-	5.82	10.03	36.4	7.68
7	14.8	32.4	14.6	18.1	12.4	2.3	8.9	-0.3	LERG	LERG	1.27	1.53	1.19	0.27
8	14.4	39.2	13.7	30.4	11.6	3.3	8.1	1.3	HERG	-	0.92	1.77	1.17	0.3
9	12.2	47.2	12.1	47.6	11.3	6.6	8.7	0.5	LERG	-	1.59	1.71	0.35	0.04
10	12.5	47.9	12.4	48.7	11.2	9.1	8.5	3.7	LERG	LERG	1.62	1.86	0.56	0.07
11	15.4	29.3	15.2	12.6	12.4	1.1	9.1	0.6	LERG	-	5.65	6.66	9.08	1.87
12	16.9	9.3	16.4	3.9	12.5	-0.7	8.9	-0.6	LERG	-	0.47	0.76	2.59	0.75
13	12.3	47.8	12.3	42.1	11.5	4.7	8.5	0.5	LERG	-	1.37	1.43	0.3	0.05
14	13.6	44.1	13.4	38.6	11.5	6	8.8	0.4	LERG	-	0.57	0.67	0.41	0.05
16	12.7	44.6	12.6	43.1	11.0	8.7	8.7	2.7	LERG	-	0.84	0.97	0.41	0.03
17	12.5	46.9	12.3	48.7	10.6	12.6	8.9	0.5	LERG	-	0.93	1.04	0.55	0.03
18	13.4	38.6	13.2	29.9	11.6	1.1	7.8	1.8	LERG	-	2.58	3.16	1.31	0.45
20	14.9	31.5	13.9	25.8	11.0	7.2	8.1	1.4	QSO	-	0.69	1.74	2.52	0.36
21	14.5	35.5	13.9	30.5	11.4	7.3	8.6	3.4	HERG	HERG	1.41	2.38	2.47	0.33
22	14.4	36.9	12.9	39.7	9.6	20.6	6.7	14.2	QSO	-	10.07	37.02	81.36	11.19
23	12.1	36.8	12.0	38	11.1	7	8.5	0.4	LERG	-	0.81	0.84	0.19	0.02
24	14.7	32.6	14.2	19.6	11.3	5.2	8.0	1.5	LERG	-	0.57	0.94	1.3	0.27
25	16.1	16.7	15.9	5.9	12.2	2.9	8.7	2.6	LERG	-	2.92	3.31	11.39	2.75

2.3.13 GRG13 (J203449-263036)

As seen in Figure 2.1m, GRG13 does not display clear lobe hotspots. The emission around the core is more of diffuse nature. The radio core is very bright which coincides with the host galaxy (6dF J203449-263036) and has a spectroscopic redshift of 0.103 as obtained from Jones et al. (2009). GRG13 shows highly bent nature in the south-western lobe as compared to the north-eastern lobe. Due to presence of another strong radio source close to north-eastern lobe, the weak diffuse emission in this region is not very clearly seen in the NVSS map. From Figure 2.6, we observe GRG13 to lie in the LERG region.

2.3.14 GRG14 (J205939+243423)

GRG14 shows an asymmetric morphology as evidenced in Figure 2.1n. The southern lobe (S_i=58 mJy) shows a strong hotspot surrounded by some extended diffuse emission and is closer to the radio core than the northern lobe (S_i=23 mJy). This asymmetry could be attributed to the existence of varied IGM near the southern lobe. The host galaxy, as seen in Figure 2.9, shows slight elongated morphology. Spectrum and spectroscopic redshifts are not available for the host (SDSS J205939.82+243423.9) of GRG14. However, SDSS photoZ is about 0.116 which results in its projected linear size to be $\sim$1.1 Mpc. Based on Figure 2.6 and a low black hole mass (Table 2.2), we infer GRG14 to be a LERG.

2.3.15 GRG15 (J223301+131502): A GRG hosted by a BCG

The radio morphology of this GRG is non-linear and peculiar. We observe the host galaxy SDSS J223301.30+131502.5 in optical band (Figure 2.9) to coincide with the radio core whose position is marked '+' on the NVSS colour contour map (Figure 2.1o). On the western side of the core, we observe a bright unresolved peak which we conjecture to be a bright knot structure on the jet. A similar but fainter knot is also observed on the eastern jet closer to the radio core. Beyond these two close hotspot/knots on either side of the radio core are the outer lobes of GRG15 which appear quite diffuse. The distance between outer lobes is measured to be $\sim 16'$, while the host galaxy has a photometric redshift of 0.093 which makes the projected linear size of the source as 1.71 Mpc. No FIRST data is available for this source therefore a higher resolution image is required to extract a clear picture of its fairly complicated morphology.

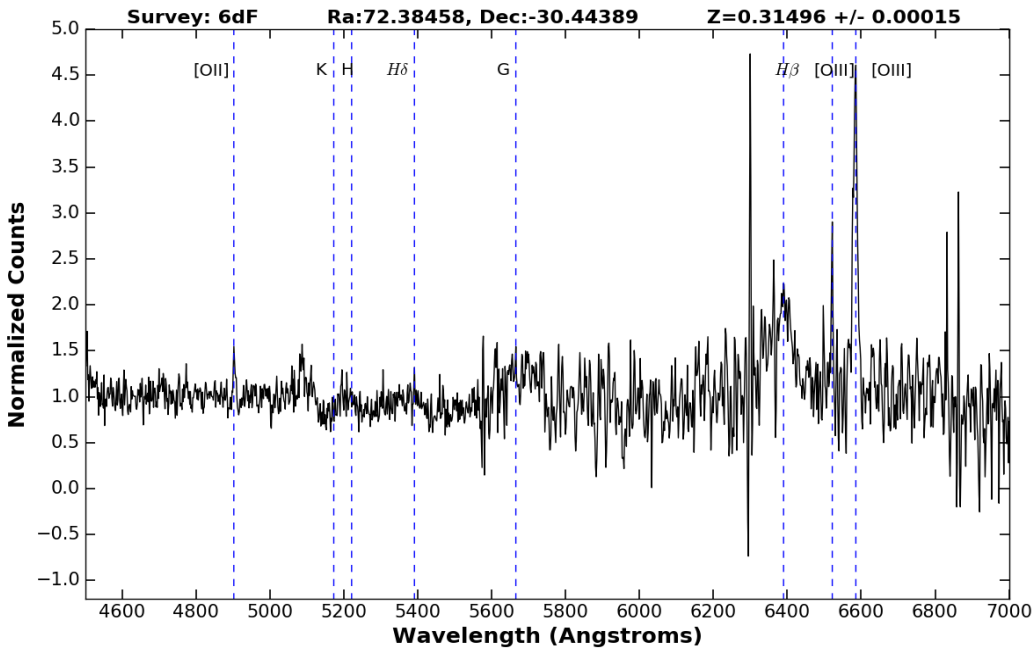

Figure 2.2: Re-plotted optical spectrum of GRG5 using 6dFGS data.

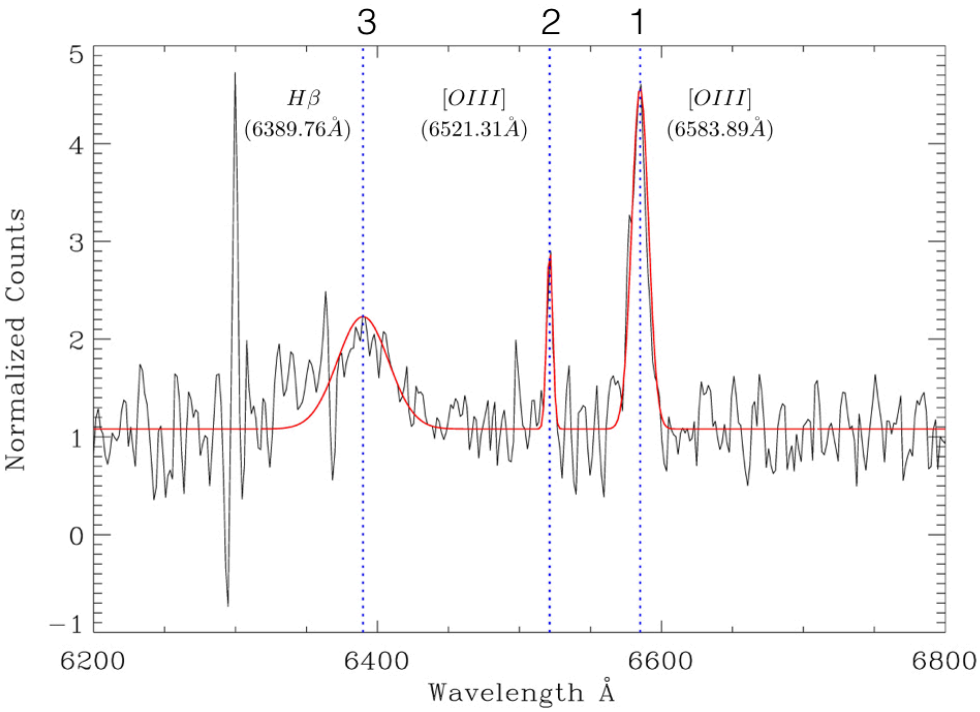

Figure 2.3: The above figure shows zoomed in version of optical spectrum of host of GRG5 (J044932-302638) obtained from 6dFGS. A gaussian was fit to spectral lines Hβ and [OIII] doublet to obtain the widths. The widths are as follows: (1)$[OIII]$: $\triangle\lambda$ = 13.77Å, $\triangle$v= 627.3km/s, (2)[OIII] : $\triangle\lambda$ = 4.91Å, $\triangle$v= 226.3km/s, (3)Hβ : $\triangle\lambda$ = 42.39Å, $\triangle$v= 1990.2km/s. The broad nature of Hβ line is clear indicator of its quasar nature.

Interestingly, in the GMBCG catalog of galaxy clusters (Hao et al. 2010), we find the host of GRG15 listed as the brightest cluster galaxy (BCG) in cluster GMBCG J338.25544+13.25070. This is a bright cD galaxy (SDSS m_r = 15.21) near the cluster center. The host is also listed as BCG in maxBCG galaxy cluster catalog (Koester et al. 2007) and the WHL galaxy cluster catalog (Wen et al. 2012). The SDSS shows the redshift of the cluster is near to 0.102, close to the photometric redshift (0.093) of host cD galaxy. Having a peculiar radio morphology and residing in a dense cluster environment, we find GRG15 to be very unusual and thus important for understanding the evolution of GRGs in dense cluster environments. Further studies are required to understand the physical and spectral evolution of this galaxy which has attained projected linear size of 1.71 Mpc inspite being in a dense cluster environment (Figure 2.5). This GRG challenges one of the common beliefs that GRGs grow to their gigantic sizes due to their preferential location in the sparse galactic environment. This GRG also demonstrates that environment alone may not play a primary role in growth of the GRGs, as commonly believed in earlier works. Rather, a powerful AGN is at work here. While it is well known that BCGs preferentially have radio loud AGN (Bagchi & Kapahi 1994; Best et al. 2007), observations so far imply that very small fraction of BCGs have large scale radio structures. This result highlights the need for more detailed studies of the external environments for other GRGs as well as the physical conditions for the BHs powering these massive objects such as their mass, spin and mass accretion rate. This can be achieved via future high resolution X-ray, optical and IR spectroscopic studies of the host galaxies of these GRGs.

2.3.16 GRG16 (J225039.15+284445.5)

The radio core coincides with the optical host (SDSS J225039.15+284445.5) perfectly which is at a redshift of ∼0.097 thus making its projected linear size as 0.9 Mpc. In Figure 2.1p, we see the evidence of the source showing hotspots which are asymmetric. We also observe diffuse emission beyond the hotspots.

2.3.17 GRG17 (J225615.1-361759)

GRG17 shows highly diffuse nature with its southern lobe more diffuse than the northern one (Figure 2.1q). The northern lobe has some hint of a hotspot while the southern one is highly diffuse and has a very low surface brightness. The redshift as obtained from Jones et al. (2009), is 0.09 which makes its projected linear size as 1.5 Mpc. Only the core is significantly

observed in the SUMSS.

2.3.18 GRG18 (J230444-105048)

GRG18 has low surface brightness and does not show clear hotspots, as seen from Figure 2.1r. Its radio core is seen to coincide with optical host (2MASX J23044483-1050474). The redshift, as obtained from Jones et al. (2009), is about 0.21 which results in its linear projected size to be ∼0.9 Mpc. With no clear lobes or hotspots observed, it is more likely to be of FR-I nature.

2.3.19 GRG19 (J231201.27+135655.9)

The radio core is seen to coincide with the optical host (SDSS J231201.27+135655.9) and is at a redshift of ∼0.140 which results in its projected linear size of ∼1.7 Mpc. In Figure 2.1s, we observe the southern lobe to be brighter than the northern lobe. The northern lobe shows a hotspot towards the far end. Based on the criteria mentioned in Section 2.2, we classify the host of GRG19 as LERG.

2.3.20 GRG20 (J231620-010207)

In Figure 2.1t, we see the distinct lobes of GRG20 with the radio core off centered towards the eastern lobe. The radio core, as seen in FIRST, coincides with the optical host (SDSS J231620.15-010207.3). At a redshift of 0.221 (SDSS photoZ) gives its projected linear size is 1.5 Mpc. Through the WISE colour-colour diagram we observe it to lie in the QSO region. Further optical studies are required to confirm the true nature of the host galaxy.

2.3.21 GRG21 (J232623+245840)

Having an extremely large size of 2.9 Mpc, GRG21 is the third largest in our reporting sample. We obtained the spectroscopic redshift (0.2549) and velocity dispersion (σ = 202.82±14.14 km/s) from SDSS DR12 spectrum. Using the M_{BH}-σ relation we computed the mass (Table 2.3) of the central black hole to be $0.22\pm0.08\times10^9$ $M_\odot$. It has a high core radio luminosity (L_c) = 2×10^{25} W Hz^{-1} computed from the NVSS maps. Based on the criteria mentioned in Section 2.2 and mid-IR colour-colour (Figure 2.6) plot, we classify it to be a HERG. GRG21 is highly core-dominated radio galaxy

having a bright double structure with the southern lobe (having a hotspot) being brighter (S_i=89 mJy) than the northern lobe (S_i=44 mJy), as seen in Figure 2.1u.

2.3.22 GRG22 (J232849.99-082512.7)

At a redshift ∼0.555 its measured projected linear size is 1.9 Mpc, where the host galaxy (SDSS J232849.99-082512.7) coincides with the radio core perfectly. From Figure 2.1v we observe that GRG 22 is highly asymmetric and the radio core lies towards the northern lobe. The core is clearly resolved in FIRST and can be seen from the black contours plotted in Figure 2.1v. The black contours seen in Figure 2.1v are from FIRST where the core is clearly resolved. This GRG is also mentioned in Bankowicz et al. (2015) where they have obtained the spectroscopic redshift of the host galaxy which is lesser than that of SDSS as quoted above. Taking Bankowicz et al. (2015) redshift for the host J232849.99-082512.7 as 0.3839± 0.0073 we obtain slightly lesser projected linear size ∼1.5 Mpc and $P_{1.4GHz}$ $\sim 1.8 \times 10^{25}$ W Hz^{-1}.

2.3.23 GRG23 (J233552.1+521539)

The host 2MASX J233552.14+521538.7 coincides with the radio core and is observed to be towards the north-eastern lobe. With a redshift of ∼0.07 (Huchra et al. 2012), its projected linear size measures 0.85 Mpc. From Figure 2.1w, we observe GRG23 to be an asymmetric GRG with the south-western lobe being very elongated and showing a hotspot. But there is no indication of hotspot in the north-eastern lobe and the jets terminates abruptly without a lobe or hotspot.

2.3.24 GRG24 (J234929-000305)

The host galaxy (SDSS J234929.77-000305.8) for GRG24 is seen to coincide with the radio core which is prominently seen in FIRST. With a redshift of ∼0.187 its projected linear size measures 0.84 Mpc. From Figure 2.1x, we observe the eastern lobe to show further diffuse emission while the western lobe is elongated. The black contours seen in Figure 2.1x are from FIRST where the core is clearly resolved.

2.3.25 GRG25 (J235531+025607)

GRG25 is the second largest GRG and one of the more distant from our reporting sample. The SDSS photoZ is of redshift ∼0.657 thus giving the projected linear size as ∼3.5 Mpc. There are scarcely any GRGs known at this redshift with sizes greater than ∼ 2 Mpc. We observe the host galaxy (SDSS J235531.63+025607.1) to coincide with the radio core. This GRG shows a double lobed morphology, as evidenced from Figure 2.1y. The black contours as seen in Figure 2.1y are from FIRST where the core is clearly resolved.

2.4 Discussion

2.4.1 Black Hole Mass of GRG

It is commonly observed that megaparsec scale radio galaxies are hosted by bright elliptical galaxies, with a few rare exceptions recently discovered where the host galaxies are clearly spirals (Hota et al. 2011; Bagchi et al. 2014). It is conjectured that GRG hosts contain super massive black holes of masses $10^8 - 10^9 M_\odot$ in their galactic centres which are responsible for powering their large-scale jets and terminal lobes (Begelman et al. 1984). It still remains a mystery as to how this system of jets and lobes grew to their current gigantic sizes. Our knowledge about the physics of black hole growth in AGN, and the impact of the energetic relativistic jets on the surrounding medium is very limited and not yet fully understood. Several papers have pointed out (e.g. Laor (2000); McLure et al. (2004); Sikora et al. (2007)), that AGNs harboring black holes of masses above a few $\times 10^8$ $M_\odot$ in elliptical galaxies only are capable of launching large scale (> 100 kpc) radio jets.

In our present sample, almost all the GRGs are hosted by elliptical galaxies and we show that almost all of them host SMBHs (super massive black holes) of mass range 10^8-10^9 $M_\odot$ as computed in Table 2.2 and 2.3. The mass of SMBH of all the GRGs except GRG2, GRG10, GRG11, GRG12, GRG15, GRG19 to GRG22 and GRG25 was computed using the M_{BH}-$L_{K,bulge}$ correlation (Graham 2007) as seen in Table 2.2. Interestingly, none of the black hole masses estimated by us fall below 10^8 $M_\odot$ thus supporting the earlier results suggesting that there is possibly a minimum BH mass that separates radio-loud galaxies from radio-quiet ones. Amongst our sample of 25, the mass of central BH of GRG1, GRG4, GRG5 and GRG18 (Table 2.2) is exceptionally high, all above 10^9 $M_\odot$.

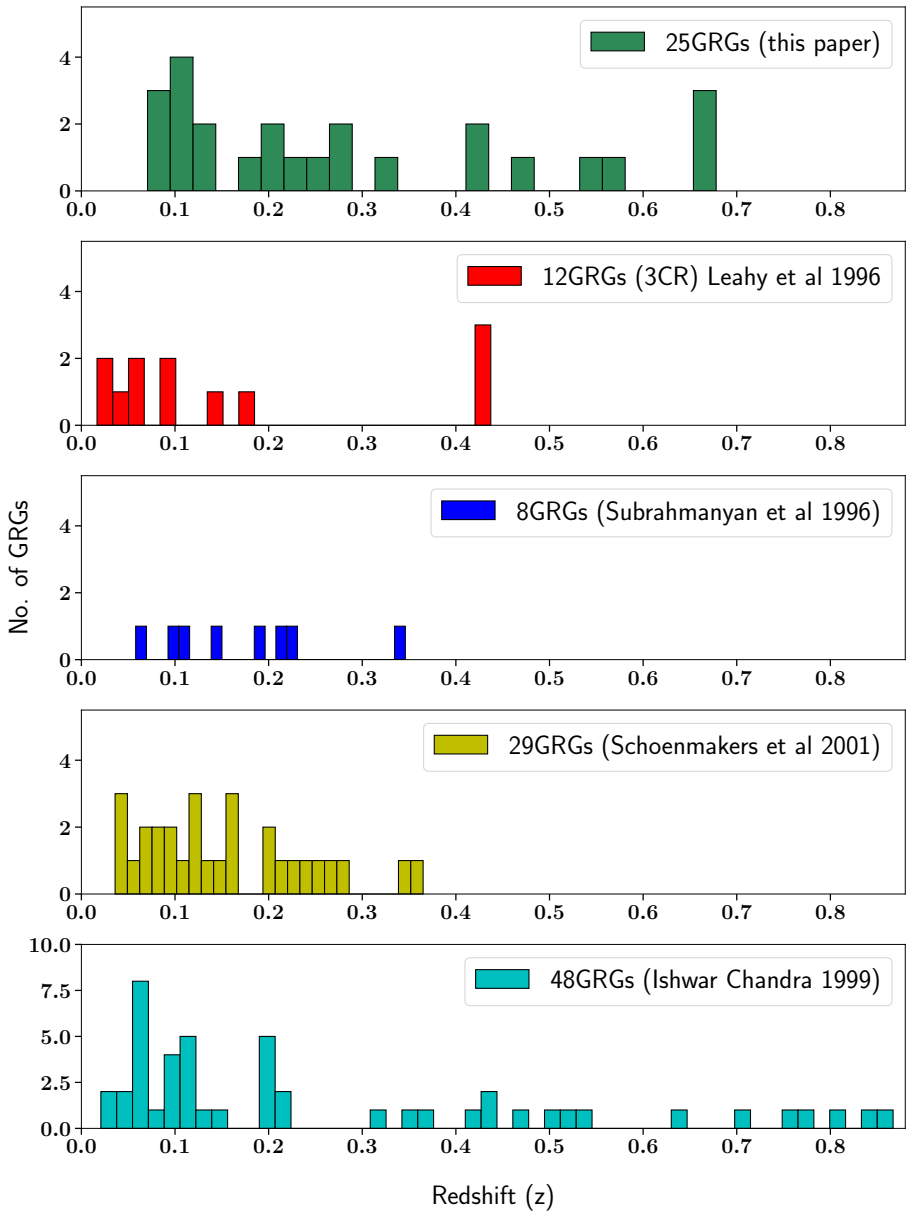

Figure 2.4: A comparison of redshift distribution of GRGs of linear sizes $\geqslant$ 700 kpc, both from our present sample as well as from other samples of GRGs in the literature.

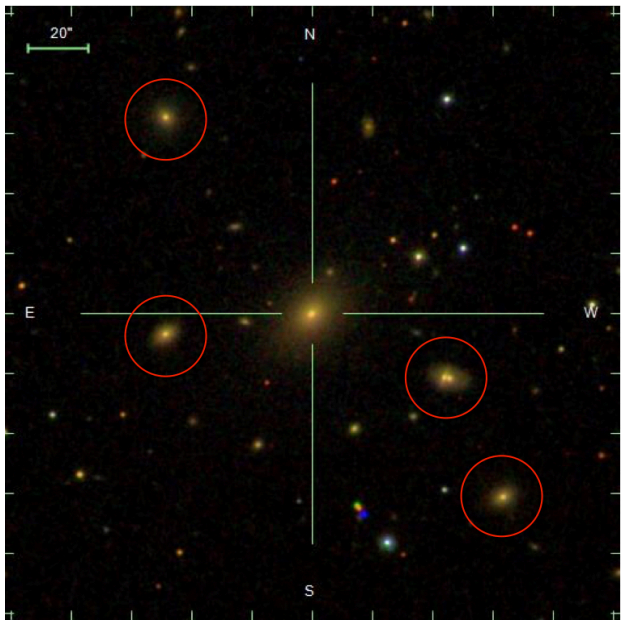

Figure 2.5: 3.3' × 3.3' optical SDSS image of environment of GRG15. Red circles are other galaxies of same cluster and at the center is the host galaxy of GRG15.

2.4.2 Demographics of GRGs

From literature, we know that very few GRGs are known till date (~300) relative to normal radio galaxies and even a small subset of GRGs are known to be at high redshifts ($z > 0.8$). The effect of inverse compton losses on the ageing of the particles in radio lobes rapidly increases with redshift as the energy density of the cosmic microwave background increases as $(1+z)^4$ (Peebles 1993) which when combined with adiabatic expansion and synchrotron losses diminishes the luminosity of an object rapidly thus making it difficult to be detected in flux limited surveys. Therefore, it indicates that the detected high redshift GRGs are intrinsically very powerful. This is reflected in our sample of 25 where we have seven GRGs having their redshift $\geqslant 0.3$. In Figure 2.4, we can see a comparison of redshift distributions of our GRGs (25) with other samples of known GRGs. These samples of known GRGs (Leahy et al. 1996; Subrahmanyan et al. 1996; Ishwara-Chandra & Saikia 1999; Schoenmakers et al. 2001) were chosen for uniformity and their characteristics, like linear sizes and redshift, were recomputed and reconfirmed according to the cosmology adopted in this paper. Our sample of 25 GRGs clearly show a wide range of redshifts from 0.07 to ~0.68. Due to

the faint nature of GRGs it is extremely difficult to detect such large sized distant sources at much higher redshifts ($z > 0.5$) and needs high sensitivity deep images at fairly low radio frequencies ($\nu < 100$ MHz) with sufficiently high resolutions where these extended lobe structures shine more prominently. Upcoming low frequency surveys from uGMRT *, LOFAR (van Haarlem et al. 2013), MWA (Tingay et al. 2013) and future surveys like SKA-LOW will be able to discover many GRGs at very high redshifts. Increasing the number of such more rare distant GRGs will help us constrain the evolutionary models in cosmic time.

Based on the intensity ratios of the optical emission lines, radio-loud AGN can be classified in two distinct populations namely the low-excitation radio galaxies (LERG) and high-excitation radio galaxies (HERG). Best & Heckman (2012b) differentiated between the LERG and the HERG by the efficiency of matter being accreted onto the central black hole. It is observed that LERGs are radiatively inefficient accretors with most of the energy from the accretion being channeled into the radio jet. On the other hand, HERGs are radiatively efficient and show strong evidence of nuclear activity in the optical band. LERGs show high black hole mass along with low accretion rate which is exactly opposite for HERGs. It is clear that jets can be generated both with and without a radiatively efficient disc. As seen from Table 2.4 (11th column - 'optical'), we have classified 6 GRGs using SDSS line flux ratios and equivalent widths into HERGs and LERGs. We do not observe any trend in the hosts of the GRGs being preferentially high excitation or low excitation. Such a classification of large sample of GRGs will perhaps reveal the underlying dichotomy or any other trends for GRGs.

2.4.3 WISE mid-IR studies of GRGs

Gürkan et al. (2014) differentiated between LERG, HERG, NLRG, BLRG and radio loud quasars with the help of WISE (mid-IR) colour-colour plots using the Cambridge radio surveys (3C, 4C etc). We place our GRGs on the WISE mid-IR colour-colour plots (Figure 2.6) to classify their AGN using the four mid-infrared bands. To our knowledge this kind of classification is being done for the first time for GRGs. Gürkan et al. (2014) have shown that LERGs have redder colours and lie at the bottom-left region of the WISE colour-colour plots. From Figure 2.6, we observe that majority of the GRGs in our reporting sample lie in the LERG region ([W1] - [W2]

*http://www.gmrt.ncra.tifr.res.in/gmrt_hpage/Upgrade/index.html

< 0.8). In Figure 2.6, we plot the excitation type of nearly 100 AGN of GRGs and it is evident from this plot that GRGs do not show a preference towards high excitation or low excitation types. However the GRQs are all of high excitation type (see discussion below).

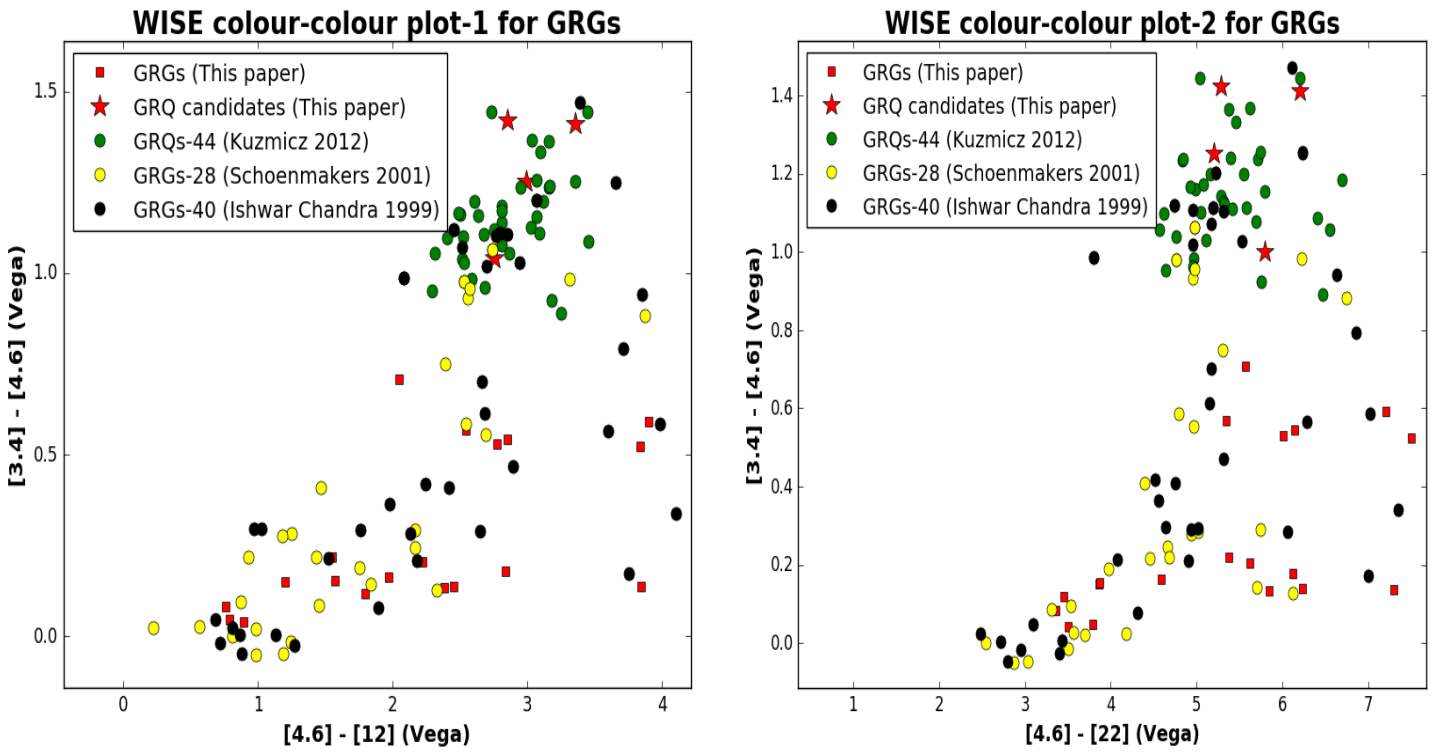

Figure 2.6: The above plots illustrate where our GRGs lie on the mid-IR colour-colour plots made using WISE mid-IR magnitudes W1, W2, W3 and W4 (3.4, 4.6, 12, 22-μm Vega magnitudes). Left plot: The region of star-forming galaxies is [W2] - [W3] > 2 (Wright et al. 2010) and LERGs are concentrated mostly in the region: [W1]-[W2] < 0.8 and [W2]-[W3] < 2.5. Right plot: The x-axis here is [W2] - [W4]. Gürkan et al. (2014) have shown that in both plots, quasars and BLRGs have similar colours.

An efficient method for quasar identification

From standard AGN models we know that optical or UV emission obscured by dusty structures around the accretion disc is re-radiated in the mid-IR. Thus, hidden quasars can be found by means of mid-IR observations such as WISE. Gürkan et al. (2014) have shown that quasars have higher mid-IR luminosities compared to other AGN types and it is also observed to be holding for vast range of redshifts. The re-radiated optical or UV emission from AGN dominates in 22μm flux (W4). Wu et al. (2012) have also shown using SDSS quasars that WISE bands are efficient in finding quasars. From Gürkan et al. (2014) colour-colour plots, we observed that radio loud quasars cluster in one particular region of the plots defined by [W1] - [W2] > 0.85 and [W2] - [W3] > 2. We further validated it by putting known GRQs (44) from Kuźmicz & Jamrozy (2012) on the colour-colour plot and find that all the GRQs lie in the QSO region of the plot as mentioned above. Further, we observe that GRG4, GRG5, GRG20 and GRG22 from our new sample lie in QSO region of the plots (Figure 2.6) which indicates that they are possibly radio loud quasars. Radio loud quasars are known to have a very high core radio luminosity as well as high infrared luminosity which is indeed very well exhibited by GRG4 and GRG5 of our reporting sample. They also show high black hole mass (> 10^9 $M_\odot$) which is another indicator of their quasar nature. This claim is further validated by the optical spectrum of GRG5 (Figures 2.2 & 2.3). GRQs B0750+434 ~2.45 Mpc (Schoenmakers et al. 2001) & HE1127-1304 ~2.1 Mpc (Bhatnagar et al. 1998) are two of the largest GRQs known till date. This places GRG4 and GRG5 (also 2.4 Mpc and 2.1 Mpc respectively) from our sample amongst the largest known GRQs. These giant radio quasars are very important for the ongoing studies on AGN unification schemes. Therefore, we show that in absence of an optical spectrum, the WISE mid-IR colour-colour plots along with the radio and infrared luminosities provide a good alternative method to identify GRQs and classify GRGs into different AGN types.

2.4.4 P-D Diagram

Traditionally, a P-D diagram (Baldwin 1982) is a plot between radio power (P) at some fixed frequency and the linear size (D) of radio galaxies. Using tools such as the P-D diagram, we can study the evolution of radio sources (Kaiser et al. 1997; Ishwara-Chandra & Saikia 2000; Manolakou & Kirk 2002; Machalski et al. 2004b). In Figure 2.7, we plot the P-D diagram for our new sample GRGs (25) along with a sample of known GRGs from literature (Laing et al. 1983; Lara et al. 2001a). This is one of the biggest

(82) sample (new and previously known) of GRGs ever to be compared in a P-D diagram. For sources from 3CR*, flux at 1.4 GHz was obtained using the given spectral index. This enabled us to compute the radio power at 1.4 GHz using Eq 2.2. The 3CR sample has a total of 85 sources (DRAGNs : Double Radio source Associated with Galactic Nucleus) of which only 70 were above 100 kpc in total size. Only these 70 sources were plotted on the P-D diagram. Based on our definition ($D \geqslant 700$kpc) of GRGs, only 12 sources are giants from the 3CR sample of 70 radio galaxies (RGs). The second chosen sample for comparison study in this plot is from Lara et al. (2001a) where the total number of sources are 70 (45GRGs & 25RGs). The sample in Lara et al. (2001a) is also constructed from NVSS (similar to our sample) and it provided us the 1.4 GHz flux in mJy with total source size in arcminutes. The linear sizes and radio power were recomputed for all the objects (on the plot) using the updated cosmological parameters (as stated in section 1) so as to maintain uniformity and avoid biases in comparison.

It is well evident from the P-D diagram that large sized radio sources tend to be less radio luminous at 1.4 GHz frequency. This perhaps indicates that as these radio galaxies grow in size (megaparsec scales), they become less luminous. The diminishing luminosity is possibly due to adiabatic expansion and radiative energy losses. In some cases, it might also be because the radio-loud phase is turned off. Based on the evolutionary models by Blundell & Rawlings (1999), after an initial rapid increment, the luminosity of the radio lobes decreases rapidly as the source grows to a larger extent. The sources evolve towards lower power and larger size as they age. This is suggested by the absence of radio sources in the upper right corner of the P-D diagram (large sizes and high powers). Assuming that the sample used is a reasonable representation of the population, we support our claim through the results of the Mann-Whitney U test (Mann & Whitney 1947) which is a non-parametric test for equality of sample medians. Galaxy size of 700 kpc is used to segregate the sample into two - those lower than 700 kpc are refered as RGs while the others as GRGs. We test the null hypothesis of the median power of RGs and GRGs being equal against the alternative hypothesis of radio power of GRGs being lower than that of RGs.

With the test statistic $W = 2779$ and a p-value $= 0.0277$, we have sufficient evidence to reject the null hypothesis.

Interestingly, no sources are seen in the extreme lower right corner of the P-D diagram either, i.e. of very large sizes and very low powers. The

*http://www.jb.man.ac.uk/atlas/

existing surveys which have discovered most of the known GRGs so far are unable to detect these extreme GRGs due to sensitivity limitation of the surveys. The models predict that these yet unobserved sources are possibly the final stage of evolution of a radio galaxy before it fades away. Therefore, future low frequency radio surveys (Kapinska et al. 2015) (below 100 MHz) with LOFAR, SKA-low etc. will be able to uncover the hitherto undetected population of giant radio sources in the bottom right part of the P-D diagram. These sources will provide vital information on the evolution of radio galaxies to such extreme limits and on duty cycle of accreting massive black holes in host galaxies.

Such studies of GRGs are of vital importance for making progress in understanding the unusual nature of these extreme galaxies. The multi-frequency observations will allow us to obtain sensitive maps of the low surface brightness diffuse emission, spectral index maps, break frequency, and spectral ages of GRGs. Under project SAGAN, reporting and analysis of more new GRGs from our discovery sample will form part of our next paper in this series which is under preparation currently. Some very interesting results from multi-wavelength analysis of larger sample of GRGs shall be discussed in our consecutive papers of this same series. Recent unique work carried by others like Proctor (2016) will be quite useful for forming a bigger and complete sample of GRGs after supplementing it with existing and new optical data. We would like to highlight that all the studies carried out in the present paper were done using the archival data from various surveys in radio, optical and infrared bands.

2.5 Conclusions and Summary

In this paper, we present the discovery of 25 new GRGs from the NVSS survey and their multiwavelength studies. This reporting sample of GRGs is not a complete sample of search in NVSS. Efforts to make a complete sample from these searches in NVSS is under progress and will be presented in the forthcoming papers. The NVSS was completed more than 15 years ago and these new discoveries signify its continued importance and confirm that it is far from becoming obsolete. Large size and relatively low surface brightness of GRGs makes it difficult to detect them via automated detection in various radio surveys. Combining NVSS images with optical data from SDSS as well as archival data from FIRST and SUMSS, we provide a complete study of the morphology of these sources. Further, using WISE colours, we could classify the hosts of GRGs into different accretion types (HERGs, LERGs, etc.). Using 2MASS K band and SDSS spectroscopic data, we estimate

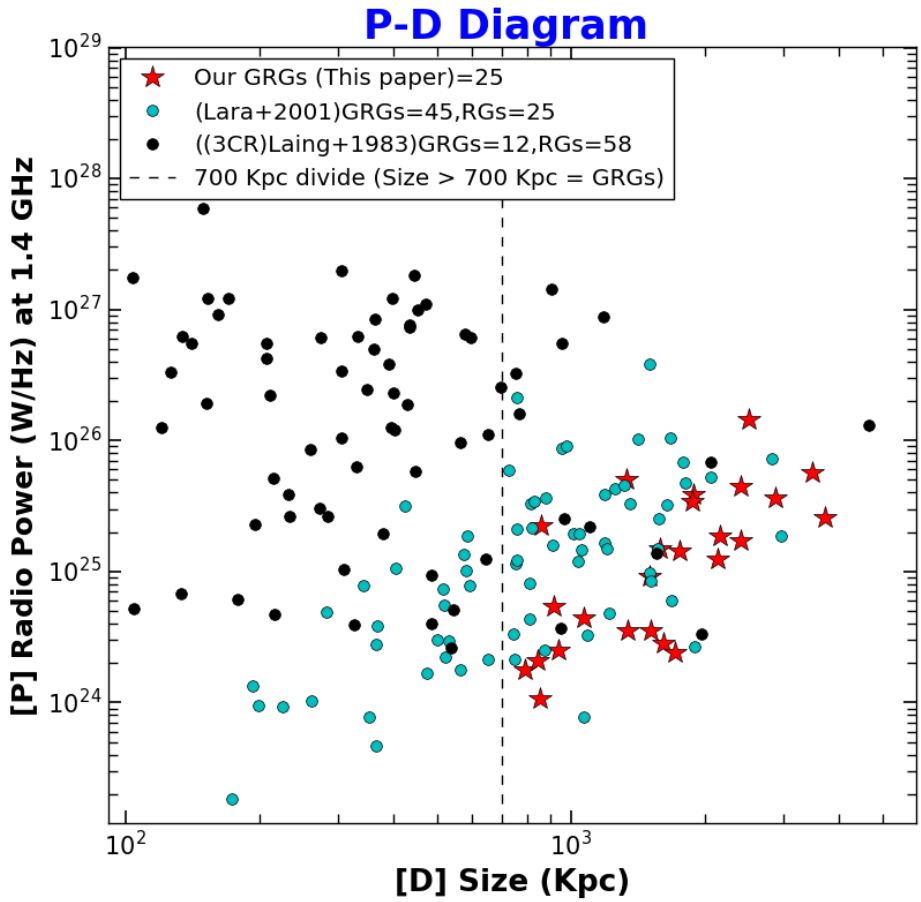

Figure 2.7: Above figure shows the newly discovered 25 GRGs plotted on the P-D diagram along with other known RGs and GRGs from different papers. Sizes and powers of known RGs and GRGs were recomputed for uniformity.

the mass of the central black hole in ∼ 50 % of hosts of these GRGs. The estimated black hole masses are in the range of $10^8 - 10^9$ M⊙.
A brief summary of our results is as follows:

1. Considering that only ∼ 300 GRGs are known till date, our contribution of 25 new GRGs enhances the sample by ∼ 9%. Furthermore, all the GRGs in our sample have radio power above 10^{24} W Hz^{-1} at 1.4 GHz.

2. Optical spectra for 13 GRGs were available from the archive. Almost all the optical spectra presented in this paper show detection of Hα, Hβ, [O II], [O III], NII, SII thus confirming their AGN nature. We also classified a few GRGs into HERGs and LERGs using the SDSS line flux ratios.

3. We proposed a new method for identifying radio loud quasars without an optical spectrum. This was done by estimating its mid-IR luminosity from WISE, radio luminosity and its location on the WISE colour-colour plots. We find that the radio loud quasars cluster in one particular region of the plots defined by [W1] - [W2] > 0.85 and [W2] - [W3] > 2. We find that GRG4, GRG5, GRG20 and GRG22 show very high radio core luminosities as well as high mid-IR luminosities which are strong indications of their quasar nature. This was further confirmed with the optical spectrum of GRG5.

4. We show, for the first time, the classification of GRGs into QSOs, LERGs, HERGs, etc. using the WISE mid-IR colour-colour plots. From this classification, we notice that nearly half of GRGs in our reporting sample are LERGs.

5. None of the host galaxies of GRGs in our sample fall on the star forming (SF) region ([W2]-[W3] $\geqslant$ 2.5 and [W1]-[W2] $\leqslant$ 1) of the WISE mid-IR colour-colour plots, from which we infer that host galaxies of GRGs are mostly passive, red ellipticals without significant star-forming activity at the present moment. However, more studies are required to investigate this with a larger sample.

6. GRG15 clearly challenges the common belief that GRGs grow in sparse, non-cluster environment. The optical observation of the environment of this GRG host clearly shows that it is a cD-like brightest cluster galaxy which lies in a dense central region of the cluster. This

shows that the environment alone does not play a major role in their exceptional large sizes.

7. The P-D diagram suggests that GRGs (>0.7 Mpc), in comparison to normal radio galaxies, are less luminous and less powerful, indicating the end stage (de-energising) of radio galaxy life-time. Moreover, we observe a lack of extremely large and powerful sources in the top right corner of the P-D diagram.

8. Also, the P-D diagram suggests a cutoff in the GRG radio power at $\sim 10^{26}$ WHz^{-1} with a drastic drop-off in linear size beyond 3 Mpc. This indicates that GRGs are large, low surface brightness sources that show a decrease in radio power with the increase in size, as expected for luminosity evolution in active radio galaxies (Kaiser et al. 1997; Blundell & Rawlings 1999). Furthermore, this cut-off is possibly limited by instrumental sensitivity.

9. The occurrence of GRGs with respect to redshift also shows (Figure 2.4) a decrease thereby indicating limitation in detection of distant GRGs with current surveys. It also highlights the need for high sensitivity, low frequency radio surveys in the near future with telescopes like uGMRT, LOFAR and SKA.

2.6 Supplementary material

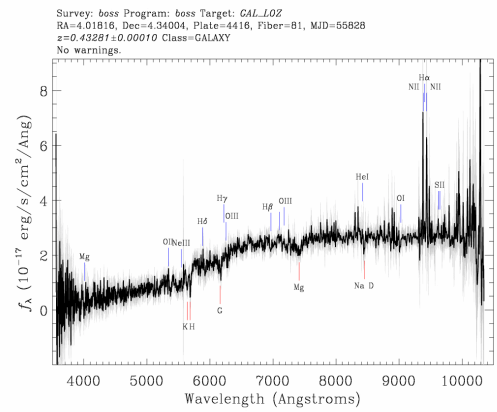

(a) GRG1 spectrum

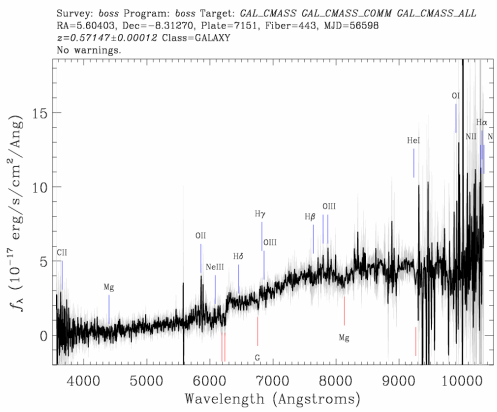

(b) GRG2 spectrum

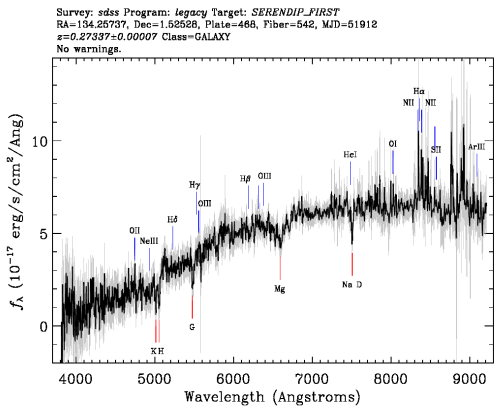

(c) GRG7 spectrum

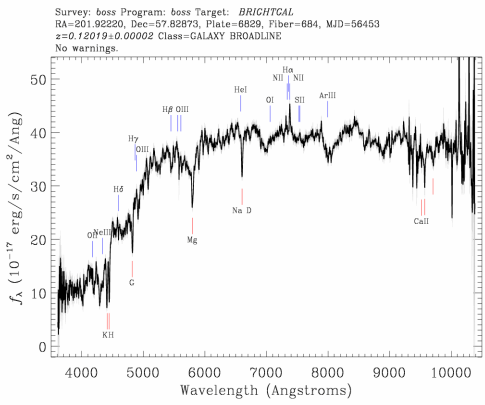

(d) GRG10 spectrum

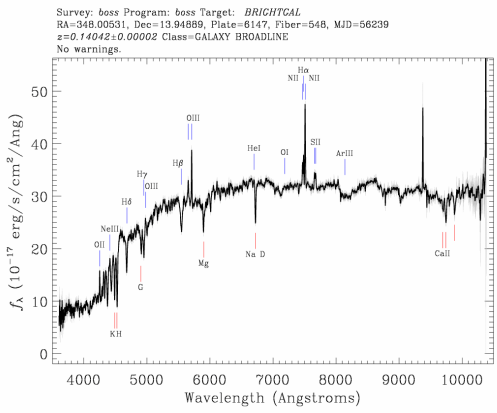

(e) GRG19 spectrum

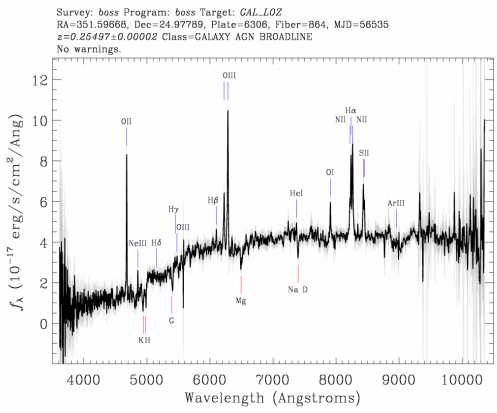

(f) GRG21 spectrum

Figure 2.8: Spectra of hosts of GRG1, GRG2, GRG7, GRG10, GRG19 and GRG21 obtained from SDSS DR12 sky server.

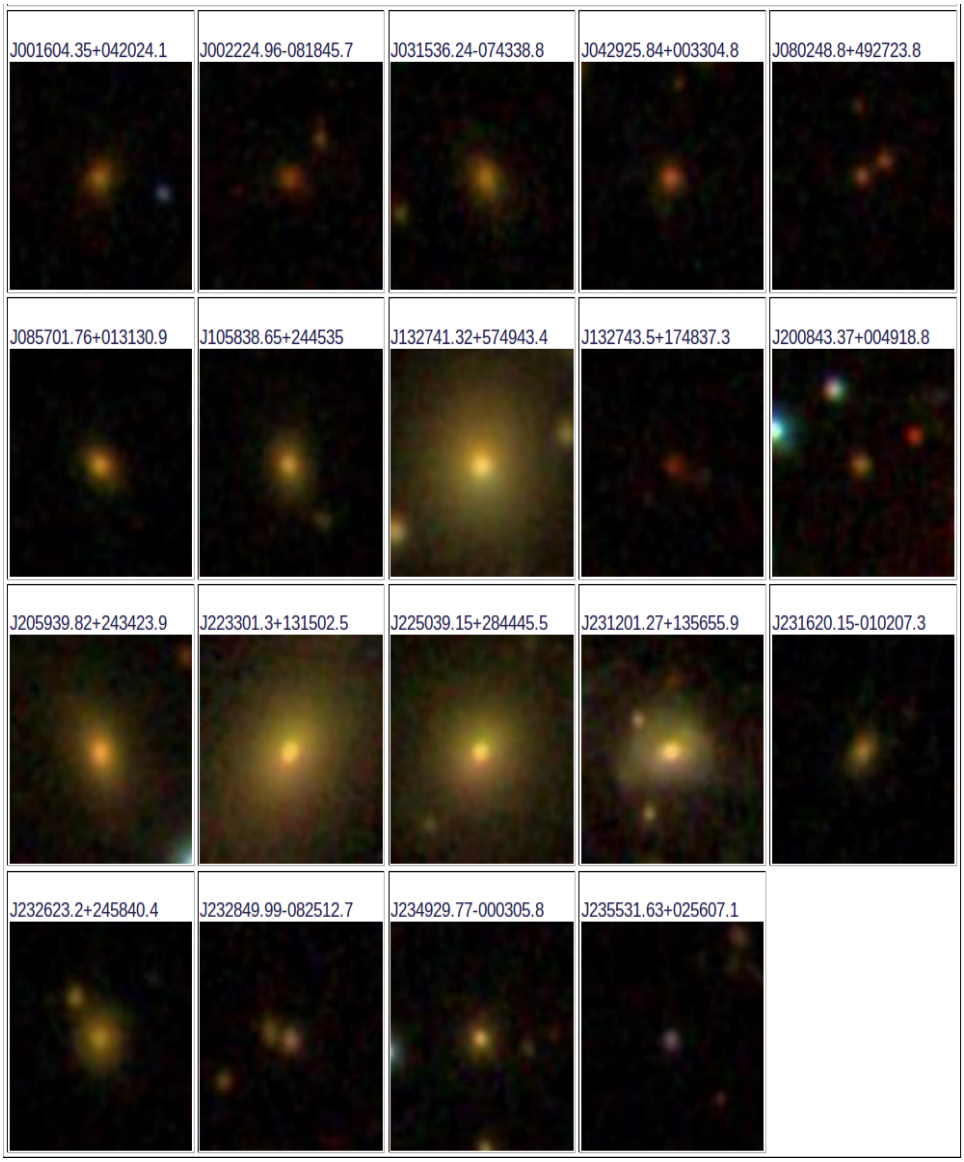

Figure 2.9: Optical images of host galaxies of GRGs from SDSS.

3 | Giant radio galaxies in the LOFAR Two-metre Sky Survey-I: Radio and environmental properties

Giant radio galaxies (GRGs) are a subclass of radio galaxies which have grown to megaparsec scales. GRGs are much rarer than normal sized radio galaxies (< 0.7 Mpc) and the reason for their gigantic sizes is still debated. Here, we report the biggest sample of GRGs identified to date. These objects were found in the LOFAR Two-metre Sky Survey (LoTSS) first data release images, which cover a 424 deg^2 region. Of the 239 GRGs found, 225 are new discoveries. The GRGs in our sample have sizes ranging from 0.7 to 3.5 Mpc and have redshifts (z) between 0.1 and 2.3. Seven GRGs have sizes above 2 Mpc and one has a size of $\sim$3.5 Mpc. The sample contains 40 GRGs hosted by spectroscopically confirmed quasars. Here, we present the search techniques employed and the resulting catalogue of the newly discovered large sample of GRGs along with their radio properties. We, here also show for the first time that the spectral index of GRGs is similar to that of normal sized radio galaxies, indicating that most of the GRG population is not dead or is not like remnant type radio galaxy. We find 20/239 GRGs in our sample are located at the centres of clusters and present our analysis on their cluster environment and radio morphology.

P. Dabhade, H. J. A. Röttgering, J . Bagchi, T. W. Shimwell ,M. J. Hardcastle, S. Sankhyayan, R. Morganti, M. Jamrozy, A. Shulevski, and K. J. Duncan
A&A,635,27,(2020)
DOI: 10.1051/0004-6361/201935589

3.1 Introduction

A radio galaxy normally contains a radio core, jets and lobes powered by an active galactic nucleus (AGN). A radio galaxy that has grown to Mpc scales is traditionally defined as a giant radio galaxy (GRG) (Willis et al. 1974; Ishwara-Chandra & Saikia 1999). Here, the total size is defined as the largest angular separation between the end of the two radio lobes. This subclass of radio galaxies is among the largest single structures known in the universe along with the cluster radio relics (Rottgering et al. 1997; Bagchi et al. 2006; van Weeren et al. 2011). Born in the active nucleus of a galaxy or a quasar, radio galaxies/quasars eject collimated and bipolar relativistic jets (Lynden-Bell 1969; Begelman et al. 1984). The driving engine for these jets is an accreting supermassive black hole (SMBH) with a typical mass of $10^8 - 10^{10}$ $M_\odot$. SMBHs that drive powerful jets reside in elliptical galaxies and only a handful are found in spiral galaxies (Hota et al. 2011; Bagchi et al. 2014).

Morphologically, radio galaxies have been historically divided into two classes, Fanaroff-Riley type I (FR-I) and Fanaroff-Riley type II (FR-II). The lower radio luminosity FR-I sources have their brightest regions closer to the nucleus and their jets fade with distance from core. For the more powerful Fanaroff-Riley type II (FR-II) radio galaxies (Fanaroff & Riley 1974), the jet remains relativistic all the way from the central AGN to the hotspots in lobes.

For all radio galaxies the ejection of a collimated jet is dependent on the availability of fuel. Assuming GRGs grow to an enormous size due to a prolonged period activity, this would require either an unusually large reservoir of fuel or a very efficient jet formation mechanism.

Radio galaxies were first discovered about six decades ago (Jennison & Das Gupta 1953) and since then hundreds of thousands of radio galaxies have been found. In contrast to the large number of radio galaxies, only ~ 350 (Dabhade et al. (2017); Kuźmicz et al. (2018) & references therein) or so GRGs have been found of which only a small fraction has been studied in detail. These giants, when associated with quasars as their AGN, are called giant radio quasars (GRQs) and only around 70 GRQs are known so far (Kuźmicz et al. 2018). The term 'GRQ' is used here to emphasize the fact that the GRG has quasar as the powering AGN.

The hypotheses proposed (which are not mutually exclusive) to explain the enormous sizes of GRGs include:

1. GRGs possess exceptionally powerful radio jets when compared to

normal radio galaxies and these provide the necessary thrust to reach Mpc scales (Wiita et al. 1989).

2. GRGs are very old radio galaxies and have had sufficient time to expand over large distances (Subrahmanyan et al. 1996).

3. GRGs grow in low density environments, (Mack et al. 1998; Malarecki et al. 2015; Saripalli & Malarecki 2015) enabling them to grow comparatively fast.

None of the above hypotheses have been tested using large uniform samples of GRGs. In smaller samples, contradictory results have been found. For example, Mack et al. (1998) found evidence that the ages of GRGs in their sample are similar to that of normal sized radio galaxies which is contradictory to the above mentioned second point. Also, point three has been contradicted by findings of Komberg & Pashchenko 2009; Dabhade et al. 2017, where they have reported a number of GRGs to be located in cluster environments.

The exceptionally large lobes of GRGs makes them excellent laboratories for studying the evolution of the particle and magnetic field energy density, acceleration of high energy cosmic rays and can also be used to probe large scale environments (Kronberg et al. 2004; Safouris et al. 2009; Malarecki et al. 2015; Isobe & Koyama 2015).

Until the mid-1990s, GRGs were mostly discovered serendipitously. Only after the advent of deep and large sky radio surveys like Faint Images of the Radio Sky at Twenty-cm (FIRST) (Becker et al. 1995), NRAO VLA Sky Survey (NVSS) (Condon et al. 1998), Westerbork Northern Sky Survey (WENSS) (Rengelink et al. 1997) and Sydney University Molonglo Sky Survey (SUMSS) (Bock et al. 1999) were systematic searches for GRGs carried out. Lara et al. (2001a), Machalski et al. (2001) and Dabhade et al. (2017) searched the higher frequency survey such as NVSS (1400 MHz) for GRGs, and Saripalli et al. (2005) used SUMSS, whereas Schoenmakers et al. (2001) used lower frequency surveys such as WENSS (327 MHz).

The lobes of the GRGs have steep spectral indices and hence are bright at low radio frequencies. Cotter et al. (1996) made a sample of GRGs using the 151 MHz 7C survey (McGilchrist et al. 1990). The 7C survey has a low resolution of 70×70 cosec (δ) arcsec^2 and a noise level ~ 15 mJy beam^{-1} $(1\ \sigma)$ and as a consequence contained only a few GRGs. The WENSS has better resolution (54×54 cosec (δ) arcsec^2) and better sensitivity (RMS noise $(1\ \sigma) \sim 3$ mJy beam^{-1}) and also covers a somewhat larger area ~ 8100

deg^2 (7C survey $\sim$5580 deg^2). This enabled Schoenmakers et al. (2001) to compile a large sample of 47 GRGs from the WENSS.

In recent years, four large low frequency surveys have been carried out, namely :

- 119-158 MHz Multifrequency Snapshot Sky Survey (MSSS) (Heald et al. 2015).
- 150 MHz TIFR GMRT SKY SURVEY- Alternative data release-1 (TGSS-ADR1) (Intema et al. 2017).
- 72-231 MHz GaLactic and Extragalactic All-sky Murchison Widefield Array (GLEAM) survey (Hurley-Walker et al. 2017).
- 120 - 168 MHz LOFAR Two-metre Sky Survey (LoTSS) (Shimwell et al. 2017, 2019).

In the past 20 years, large surveys have also been carried out at optical wavelengths. These surveys include the Sloan Digital Sky Survey (SDSS) (York et al. 2000), the 2 degree Field Galaxy Redshift Survey (2dFGRS) (Colless et al. 2001), the 2MASS Redshift Survey (2MRS) (Huchra et al. 2012), the 6 degree Field Galaxy Survey (6dFGS) (Jones et al. 2009) and most recently the deep photometric survey called Panoramic Survey Telescope and Rapid Response System (Pan-STARRS; Kaiser et al. 2002, 2010; Chambers et al. 2016). The data from these surveys has allowed the identification of many new GRGs, as shown in Dabhade et al. (2017).

High sensitivity to low surface brightness features and high spatial resolution to decipher the morphologies are key requirements in identifying GRGs. LoTSS provides a combination of both these properties for the first time and hence, combining it with the SDSS/Pan-STARRS optical surveys, we use it to search for new GRGs in order to form a statistically significant sample. Our study of GRGs will be presented in 2 papers:

1. Paper I (this paper) reports the methodology used for the systematic search scheme implemented for the discovery of new GRGs/GRQs from the LoTSS and presents the sample's radio properties.
2. Paper II will focus on studying the host AGN and galaxy properties of the GRGs/GRQs sample and comparing them with another sample (also from LoTSS) of normal sized radio galaxies (NRGs) matched in redshift and optical/radio luminosity to the GRG sample.

Throughout the paper, we adopt the flat ΛCDM cosmological model based on the latest Planck results (H_o = 67.8 km s^{-1} Mpc^{-1}, Ω_m =0.308) (Planck Collaboration et al. 2016), which gives a scale of 4.6 kpc/″for the redshift of 0.3. In this paper, radio galaxies with projected linear sizes $\geqslant$ 0.7 Mpc, computed using the above mentioned cosmological parameters are called GRGs. All images are in the J2000 coordinate system. We use the convention $S_\nu \propto \nu^{-\alpha}$, where S_ν is flux at frequency ν and α is the spectral index.

3.2 Identifying new GRGs in LoTSS

3.2.1 The LoTSS first data release

LoTSS is a 120-168 MHz survey that is being conducted with the high-band antennas (HBA) of LOFAR and will eventually cover the whole northern sky. Hardcastle et al. (2016) have already demonstrated the potential of LoTSS deep observations for discovering GRGs and found seven in the Herschel ATLAS North Galactic Pole survey area (142 deg^2). Here, we focus on the LoTSS first data release (LoTSS DR1; Shimwell et al. 2019). The LoTSS DR1 spans (J2000.0 epoch) right ascension 10h45m to 15h30m and declination 45°00′ to 57°00′ (HETDEX:Hobby-Eberly Telescope Dark Energy Experiment Spring field region) covering an area of 424 deg^2 with a median noise level across the mosaic of 71 μJy $beam^{-1}$ and ∼6″resolution. In Fig. 3.1, we see a comparison between the LoTSS and other radio surveys like NVSS and FIRST for a GRG from our sample. The top image (a) is an optical-radio overlay with blue colour indicating LoTSS low frequency 6″resolution map on the optical SDSS tri-colour image. In the bottom image (b), the same source is shown as it is observed in NVSS and FIRST. NVSS, though highly sensitive to large scale diffuse emission, fails to reveal the finer details across the source and cannot properly resolve the core due to it coarser resolution of 45″. FIRST survey on the other hand has high resolution, which manages to resolve the core and hence help in identifying the host AGN/galaxy but misses out on almost all the diffuse emission of the lobes and hence it alone cannot be used to identify RGs. The LoTSS data provides with both high resolution as well as high sensitivity and does not resolve out structures revealing finer details of the emission of large scale jets. Both images (Fig. 3.1 and source 7 of Fig. 3.15) show clearly the radio core and jets feeding the giant radio lobes and the hotspots. This clearly illustrates the excellence of LoTSS and its great potential in

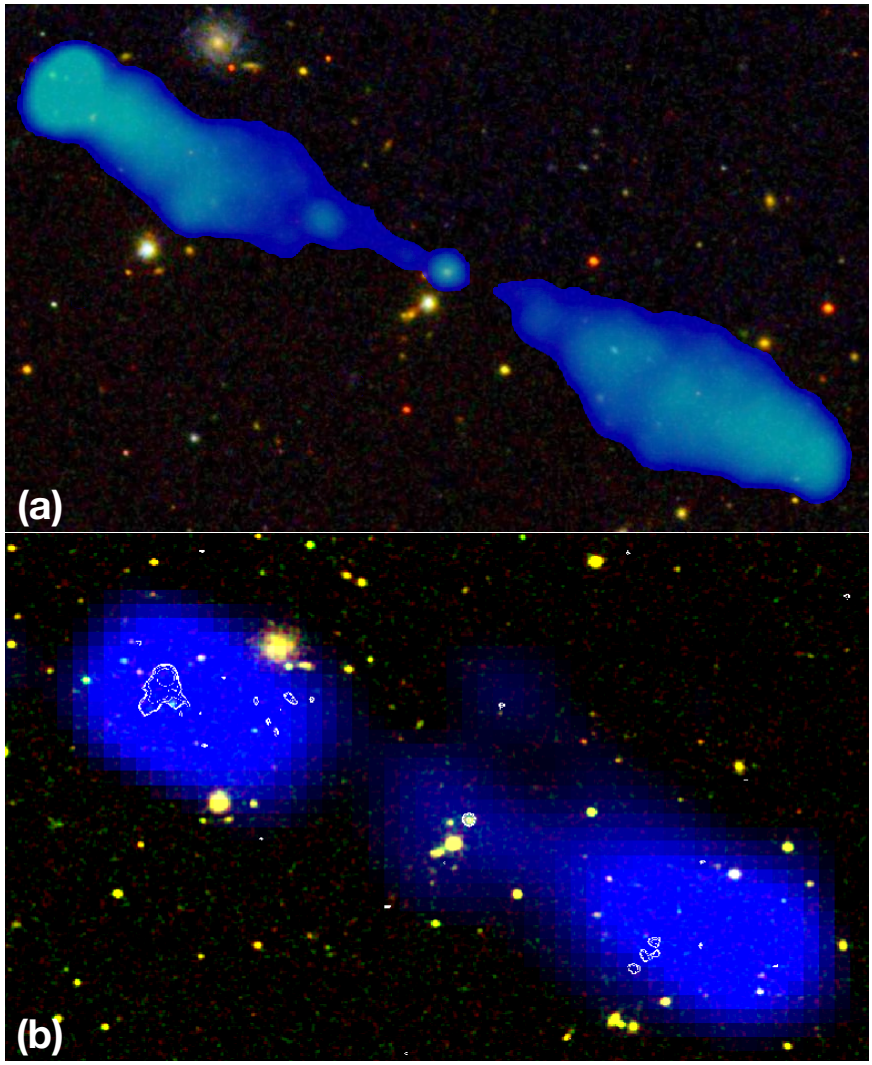

Figure 3.1: (a)A colour composite image of 1.86 Mpc long GRG J105817.90+514017.70 made using LoTSS-DR1 144 MHz radio and optical SDSS image. (b) A colour composite image of the same object with optical and radio overlay, where blue represents 1400 MHz NVSS image with 45″resolution and white contours from 1400 MHz FIRST survey having 5″resolution superimposed on optical SDSS image. The LoTSS 144 MHz 6″ resolution image shown in top panel clearly resolves the core and jet and also highlights the diffuse parts of the lobes, which is missed by the FIRST and unresolved in NVSS.

unveiling interesting sources.

Using the LoTSS DR1 radio data and optical-infrared data, a Value Added Catalogue* (VAC) of 318520 radio sources has been created (Williams et al. (2019); DR1-II). The host galaxies/quasars were identified using the Pan-STARRS and Wide-field Infrared Survey Explorer (WISE; (Wright et al. 2010)). The Pan-STARRS-AllWISE catalogue was cross matched with LoTSS survey using a likelihood ratio method. Furthermore, human visual inspection was used for the final classification of complex radio sources using the LOFAR Galaxy Zoo (LGZ), the details of which are given in Williams et al. (2019) (DR1-II). The photometric redshift and rest-frame colour estimates for all hosts (galaxies/quasars) of the matched radio sources are presented in Duncan et al. (2019) (DR1-III). The VAC lists the radio properties, identification methods and optical properties where available.

3.2.2 Semi-automated search for GRGs

The methodology of identifying GRGs and forming the final catalogue is presented in flow chart as seen in Fig. 3.2 and is described below:

1. The VAC of 318520 radio sources was at first refined based on the point source completeness, which is 90% at an integrated flux density of 0.5 mJy for LoTSS DR1 (Shimwell et al. 2019). We apply a flux density cut at this level. This results in the total number of sources reducing to 239845.

2. Secondly, only objects with optical identification and redshift estimates were selected, resulting in 162249 sources.

3. The redshift information in the VAC is compiled mainly using the SDSS spectroscopic data. For the sources which do not have spectroscopic redshift information from the SDSS or any other spectroscopic survey, Duncan et al. (2019) have estimated photometric redshifts using multi-band photometry. For our work, we have imposed a further photometric quality cut on the estimated photometric redshifts. Only sources satisfying the condition $\Delta z/(1+z) < 0.1$ were selected, where Δz is the half-width of the 80% credible interval. This results in reduction of the sample from 162249 sources to 89671 sources.

*https://www.lofar-surveys.org/

4. Williams et al. (2019) inspected all the extended complex radio sources visually via the LGZ program and estimated the angular size for them. A semi-automated way was adopted for this work by Williams et al. (2019). This resulted in angular size estimation of total 13222 sources in the VAC.

   We find that, of the 89671 sources (which have reliable redshifts), only 4808 sources have angular size estimates by the above mentioned method (LGZ). Or, in other words, 4808 sources have angular size estimates as well have passed the photometric quality cut (point 3).

5. For all the 4808 sources, we computed the projected linear size (kpc) and only those that had an extension above 700 kpc were considered for further analysis. This resulted in a sample of 398 candidate GRGs.

6. Further, the candidate GRGs were visually inspected by us to identify and remove those with uncertainty in the host, large asymmetry or a high degree of bending or narrow angle tailed morphology. The angular size measurement was refined by taking the distance between the farthest points of the 3σ contours of the source and the projected linear size was recomputed. We have measured the sizes of the sources using the LoTSS DR1- low resolution maps ($20''$) as it shows the entire structure of the GRGs and also does not miss any diffuse emission. . The final sample size of GRGs from the VAC is 186 GRGs.

3.2.3 Manual Visual Search from LoTSS DR1

An independent manual visual search (MVS) was also carried out to search for GRGs in LoTSS DR1 to look for additional GRGs that were missed in the semi-automated method employed on the VAC. In this approach, all mosaics from LoTSS DR1 were scanned for extended double lobed structures (candidate GRGs). The radio core of the candidate GRGs were searched in the optical band (SDSS and PAN-STARRS) and IR band (WISE) for counterparts (host galaxies). We also used other radio surveys like FIRST, TGSS and WENSS for additional information and consistency checks. This method (MVS) yielded 53 additional GRGs. These 53 GRGs were missed by the selection criteria because of the photometric redshift cuts we imposed or because the complex nature of the source structures lead them to being not fully characterised in the VAC.

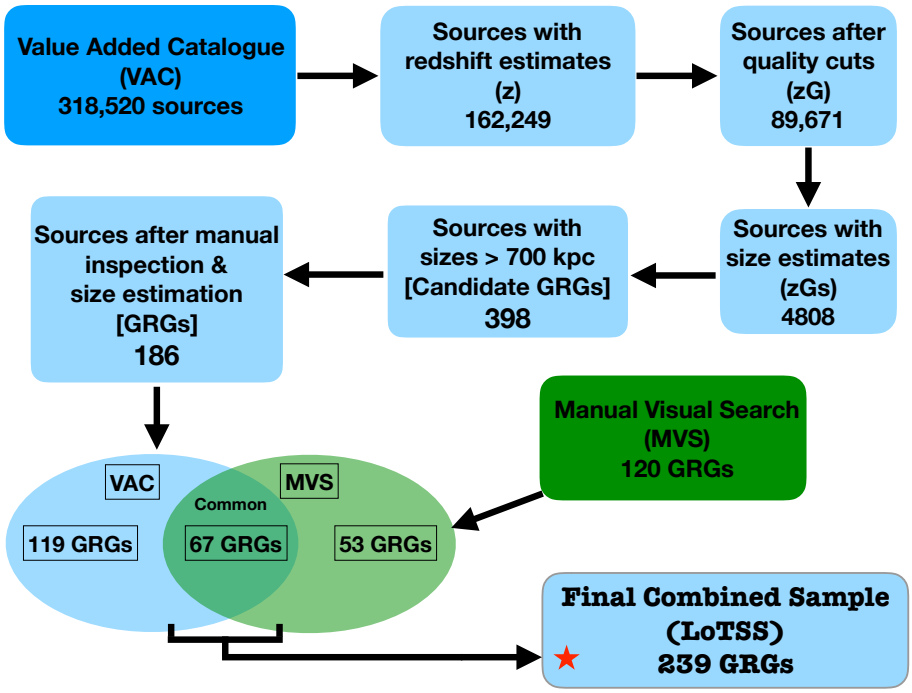

Figure 3.2: The above figure shows schematics for finding GRGs from LoTSS DR1 using VAC and MVS in steps. More details are presented in Sect. 3.2.

3.2.4 Final catalogue: VAC+MVS

We combined both GRG samples (VAC and MVS) to form the final GRG catalogue of 239 GRGs (Table. 3.2). The final catalogue of 239 GRGs was cross matched with the GRG catalogue of Kuźmicz et al. (2018), which is a complete compendium of GRGs published till 2018 along with other literature search, and we find 13 of our 239 GRGs to be already known (listed in 13$^{\text{th}}$ column of Table 3.2). The high-resolution 6″ LoTSS images at 144 MHz of GRGs can be found in the appendix 3.6 from Fig. 3.15 to Fig. 3.22, where the white contours represent emission seen in the LoTSS low resolution 20″ map at 144 MHz. The position of host galaxy is marked with a white cross '+'.

3.3 Results : The LoTSS catalogue of GRGs

Our search of LoTSS DR1 has enabled us to construct a catalogue* of 239 GRGs. With the high sensitivity of LoTSS, we are able to detect GRGs as faint as ~ 2.5 mJy in total flux at 144 MHz. Using the available optical data and radio data, we have computed the radio powers, spectral indices and classified the morphological types for the sample of 239 GRGs (Table. 3.2). The GRGs from our sample have sizes in the range of 0.7 Mpc to ~ 3.5 Mpc (Fig. 3.3) with median size of 0.89 Mpc and mean size of 1.02 Mpc. GRGs with sizes greater than 2 Mpc are very rare within the GRG population and in our sample we find 7/239 GRGs having sizes $\geqslant$ 2 Mpc.

3.3.1 Optical host properties

The GRGs in our sample span a wide redshift range from 0.1 to 2.3 (Fig. 3.4). GRGs that are hosted by galaxies are not selected beyond $z \sim 1$ due to sensitivity limits of the optical surveys. We use the SDSS DR14 Quasar catalogue (Pâris et al. 2018) and SDSS to identify the GRGs hosted by quasars in our sample. 151/239 GRGs have optical spectroscopic redshifts from SDSS. Of the 151 GRGs with optical spectroscopic redshifts 40 are hosted by quasars (GRQs). Interestingly, based on the available optical data (SDSS and Pan-STARRS) and the Galaxy Zoo catalogue of spiral

*Before the precise measurement of H_o, originally GRGs were defined as RGs with projected linear sizes $\geqslant$ 1 Mpc using $\mathrm{H_o} = 50$ km s^{-1} Mpc^{-1}. If we convert the original definition with the latest precise measurement of $\mathrm{H_o} = 67.8$ km s^{-1} Mpc^{-1} with $\Omega_\mathrm{m} = 0.308$, then the lower limit of projected linear size of GRGs is ~ 0.74 Mpc. In our sample, 28 GRGs have projected linear sizes between 0.7 Mpc to 0.74 Mpc.

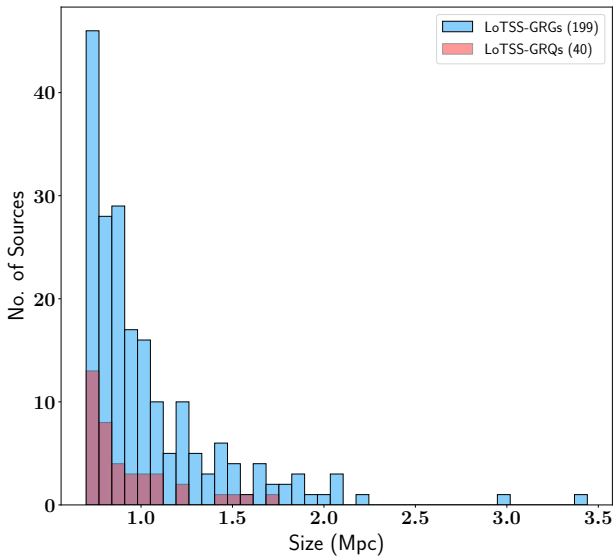

Figure 3.3: Histogram for sizes of GRGs and GRQs from the LoTSS sample.

galaxies (Hart et al. 2016), we find that none of the GRGs is hosted by a spiral galaxy.

Most of the redshifts of the hosts of GRGs were obtained from the VAC, which has made use of the spectroscopic data from the SDSS and has estimated photometric redshifts for the sources which do not have spectroscopic data in SDSS or in other literature. The uncertainties in the photometric redshifts are explained in section 3 (especially section 3.5) of Duncan et al. 2019.

3.3.2 Spectral Index (α_{144}^{1400})

The LoTSS DR1 provides maps of the radio sky (centered at 144 MHz) at two resolutions, high (6″) and low (20″) which enables us to identify compact cores, jets and hotspots as well as see the extent of diffuse emission. To compute the flux at 144 MHz, we use the 20″ low resolution maps of LoTSS DR 1 (column 8 of Table 3.2). Measurement in the flux errors is done taking a 20% calibration error for LoTSS DR1 (Shimwell et al. 2019). By combining high frequency (1400 MHz) NVSS and low frequency (144 MHz) LoTSS, we have computed the integrated spectral index (α_{144}^{1400}) for GRGs in our sample (column 10 of Table 3.2). The NVSS radio map cutouts for

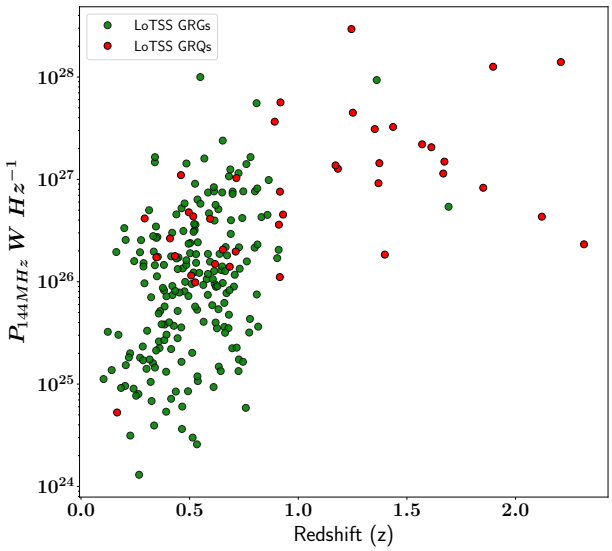

Figure 3.4: Radio power and redshift distribution for GRGs and GRQs from LoTSS. The two galaxies marked in green colour with $z \geqslant 1$ are quasar candidates as explaind in Sec. 3.3.4.

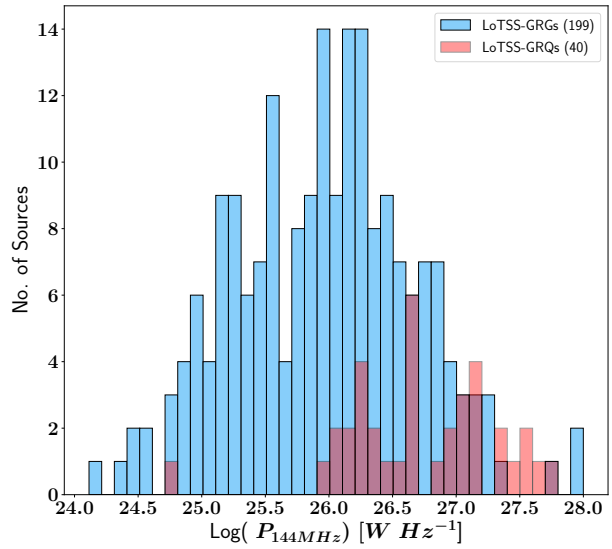

Figure 3.5: Histogram of radio power at 144 MHz of GRGs and GRQs.

GRGs were obtained from its server*, from which we have measured the flux of the source.

Following steps were adopted to obtain spectral index:

- Convolve the LoTSS low resolution images (cutouts of GRGs from main mosaics) to the same resolution of NVSS (45″) and regrid the LoTSS images to match with NVSS.
- Make automated masks (regions to extract flux) using the package PyBDSF† (Python Blob Detection and Source Finder) of Mohan & Rafferty (2015).
- The 45″ convolved LoTSS maps were manually inspected for possible contamination (using the high resolution LoTSS maps (6″) and FIRST's 5″ maps) from other sources in the field and manual masks were made. The flux was obtained by considering only the region in manual masks from the automated masks.
- Finally, using the fluxes obtained from NVSS and LoTSS, the integrated spectral index was computed for the whole source.

A total of 37/239 sources were contaminated by other nearby radio sources in the low resolution convolved LoTSS maps and NVSS maps, for these sources (marked with '-' in column 10 of Table 3.2) a spectral index was not computed. For sources with no detection in NVSS, upper limits on the flux were computed, and a spectral index limit was obtained (indicated with < sign in column 10 of Table 3.2).

Fig. 3.6 shows the spectral index (α_{144}^{1400}) distribution of 171 GRGs and 31 GRQs. The median and mean values for spectral index of GRGs are 0.77 and 0.79, respectively. Similarly, for GRQs, the median and mean values are 0.78 and 0.76, respectively. These mean spectral index values of GRGs and GRQs are similar to those of normal sized radio galaxies (Oort et al. 1988; Gruppioni et al. 1997; Kapahi et al. 1998; Ishwara-Chandra et al. 2010; Mahony et al. 2016). In the work of Oort et al. (1988), they have surveyed the Lynx field with the Westerbork Synthesis Radio Telescope (WSRT) at 325 MHz and 1400 MHz. Gruppioni et al. (1997) surveyed the Marano field using the Australia Telescope Compact Array (ATCA) at 1.4 GHz and 2.4 GHz. Kapahi et al. (1998) surveyed the Molonglo Radio Catalogue sources with the VLA at L and S bands. Ishwara-Chandra et al. (2010)

*https://www.cv.nrao.edu/nvss/postage.shtml
†http://www.astron.nl/citt/pybdsf/

surveyed the LBDS-Lynx field (LBDS: Leiden-Berkeley Deep Survey) using the 150-MHz band of Giant Metrewave Radio Telescope and other archival data from GMRT at 610 MHz and 325 MHz along with data from other surveys like WENSS, FIRST and NVSS. Mahony et al. (2016) surveyed the Lockman Hole field using LOFAR 150 MHz and WSRT 1.4 GHz. All the above work obtained spectral index values in the range of ∼0.7 to 0.8 and therefore 0.75 value is often assumed as the average spectral index value for radio galaxies in the absence of any multi-frequency observations.

The above mentioned result implies that RGs and GRGs do not differ in terms of their spectral index properties, and most of the GRG population are active radio galaxies and not dead or remnant radio galaxies. The values for the spectral index of GRGs given by us are integrated values for the whole source and not just one component of GRGs (like core or lobes). It is found that for some GRGs, the lobes come out to be steeper than usual- which is obtained by multi-frequency (observations at 3 to 4 radio bands) observations of individual sources. There are examples (source number 16,17 and 193) in our sample where the sources are core dominated (maximum flux observed in radio core) and it hence influences sources to have flatter (less than 0.5) overall spectral index.

3.3.3 Notes on individual objects

Below, we present brief notes on a selection of some of the most interesting objects in our sample.

- Source 5- GRG J105725.96+492900.31: The host galaxy does not perfectly coincide with the bight core like feature which is separated by ∼5″distance from one another. It is most likely a knot in the jet, which is located right next to a faint radio core. There is no other galaxy present in the immediate vicinity and no other alternate compact radio emission along with axis of the source, which could possibly be an alternate host of this source.

- Source 10- GRG J110433.11+464225.76: This unusual source has a well detected radio core but does not exhibit any jets or well formed lobes. It has diffuse emission on either side of the radio core and has been reported by Thwala et al. (2019) as a relic radio galaxy with a size of 0.86 Mpc, thereby making it a GRG. Towards north western side of the source, there exists an independent FR-II type radio galaxy. Using the higher resolution maps the independent source's flux was

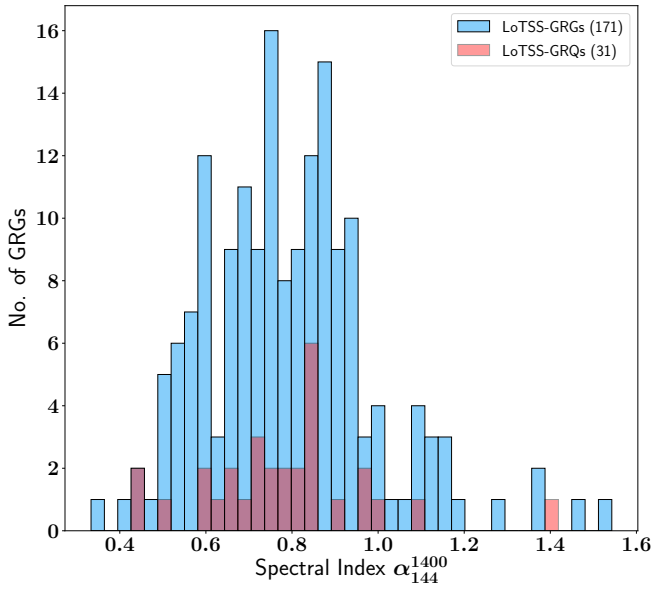

Figure 3.6: Histogram of Spectral index (α_{144}^{1400}) of GRGs and GRQs in LoTSS DR1 sample made using LoTSS and NVSS.

measured and then subtracted from the LoTSS's low resolution maps to avoid contamination of source fluxes.

- Source 44- GRG J113931.77+472124.3: As seen in Fig. 3.16, there is compact radio source north of the '+' marker (host galaxy-radio core), which is an independent source. Also, the bright compact source seen towards south eastern side is independent of the GRG J113931.77+472124.3.

- Source 61- GRG J121555.53+512416.41 and
  Source 162- GRG J135628.50+524219.23: These sources are core dominated objects at both low and high frequencies. The lobes of both sources are not detected in NVSS. These are possibly candidates of revived/rejuvenated GRGs as we only observe the diffuse lobes at low frequencies (LoTSS), which could be from the previous epoch. The presence of the bright core may indicate restarting activity.

- Source 136- GRG J133322.79+533250.94: This source displays a peculiar morphology and is possibly residing in a unique environment. The VAC estimates its photometric redshift (z) to be 0.3539± 0.0344.

Lopes (2007) estimates its photometric redshift based on SDSS data to be 0.39301 ± 0.02578. GRG J133322.79+533250.94 is close to two galaxy clusters, namely WHL J133322.0+5333490 at redshift of 0.3938 and WHL J133316.5+533333 at a redshift of 0.3834. Based on Lopes (2007) photometric redshift, GRG J133322.79+533250.94 is plausibly to be associated with the galaxy cluster WHL J133322.0+5333490 as they are at similar redshifts and is separated by $\sim 1'$. This GRG appears to be residing in an environment of a possible merger of two galaxy clusters and the associated radio relic can be seen towards north of the GRG (Fig 3.7).

- Source 161- GRG J135414.72+491315.2: The radio core coinciding with a faint galaxy is detected only in the FIRST survey.
- Source 221- GRG J145002.36+540528.27: The radio core is well detected in the FIRST survey, which coincides with a galaxy. The source is sufficiently resolved only in the LoTSS high resolution map as it is located right next to a bright source. The spectral index was computed by estimating an upper limit for the flux from NVSS.
- Source 222- GRG J145057.28+530007.76: The radio core is only resolved in the FIRST survey. It is not symmetrically placed between the two lobes and is closer to the eastern lobe.
- Source 237- GRG J151835.37+510410.70: The radio core is not symmetrically placed between the two lobes and is closer to the northern lobe. It is also well detected in the FIRST survey. The southern lobe shows a prominent hotspot.

3.3.4 Giant radio quasars

GRGs with quasars as their AGN (GRQs) are even rarer than the GRGs with non quasar AGN. Based on the catalogue of Kuźmicz et al. (2018) and candidates presented by Kuligowska & Kuźmicz (2018), there are only about ~ 70 GRQs known till date and less than ~ 10 GRQs known at $z \geqslant 2$. From our LoTSS sample of 239 GRGs, 40 are confirmed GRQs and 2 are candidates GRQs (Q_c). A total of only six GRQs of the 40 confirmed GRQs were previously reported (column 13 in Table 3.2) and rest are all new findings. Our sample of ~ 40 GRQs significantly increase the sample of total GRQs known till date from 70 (Kuźmicz et al. 2018) to more than

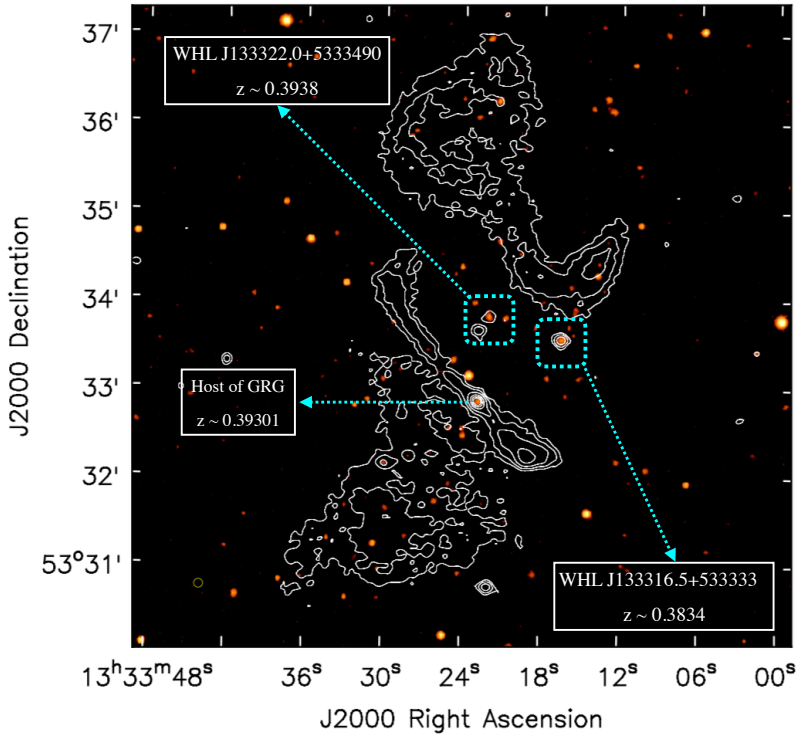

Figure 3.7: The figure shows GRG J133322.79+533250.94 amidst possibly galaxy cluster relics. The background image in orange colour is SDSS I band optical image which is superimposed with LoTSS DR1 high resolution (6″) contours.

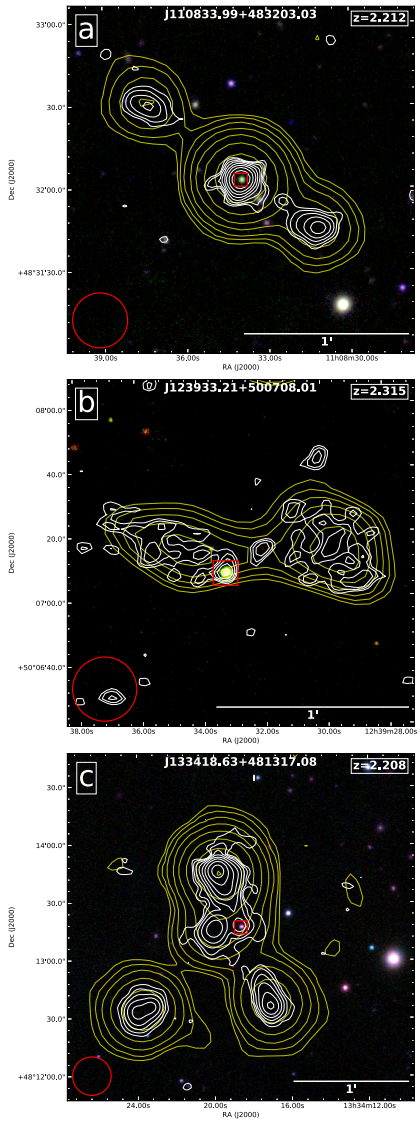

Figure 3.8: The above three images are optical-radio overlay of high redshift ($z > 2$) GRGs, where the optical images colour composite of three bands of PanSTARRS and radio is from the LoTSS DR-1 at two resolutions. The red square indicates the host of the three GRQs. The white and yellow colour contours represents LoTSS high (6″×6″) and low (20″×20″; red circles at bottom left) resolution maps respectively, which have eight equally spaced relative contour levels starting from three times σ, where σ denotes the local RMS noise.

100. The GRQs in our sample have median and mean radio powers of 6.2×10^{26} W Hz^{-1} and 2.4×10^{27} W Hz^{-1} at 144 MHz respectively as seen in the histogram distribution of radio powers (Fig. 3.5).

Below we present some brief notes on individual objects-

- GRQs J110833.99+483203.03, J123933.21+500708.01 and J133418.63+481317.08 are the three GRQs which we have found at very high redshift of $z \geqslant 2$ and are shown in Fig. 3.8.
- GRG J110833.99+483203.03 (16 in Table 3.2) is a highly core dominated object at both high as well as low frequencies and hence exhibits a very flat spectral index of ~ 0.2.
- GRGs J132554.31+551936.23 and J141408.45+484156.11 (126 and 178 in Table 3.2) which have high redshifts and are the two quasar candidates (Q_c) as indicated by Richards et al. 2009, 2015. These objects have all the properties of a radio loud quasars but still are candidates because of absence of an optical spectra. Therefore they are not labeled as quasars (not marked in red colour) in any of the figures.

3.3.5 Environment analysis of GRGs

We use two optically selected galaxy cluster catalogues to identify host of GRGs with Brightest Cluster Galaxies (BCGs), which are found to be at the centers of galaxy clusters. We chose the following two catalogues as they are made using SDSS and have an overlap with HETDEX region which is common for LoTSS DR1.

Firstly, we used the galaxy cluster catalogue of Wen et al. (2012) (here after WHL cluster catalogue), which consists of 132,684 clusters. They have used photometric data from SDSS-III to find the clusters. This is the biggest galaxy cluster catalogue made using SDSS in the redshift range of $0.05 < z < 0.8$ and is $\sim 95\%$ complete for clusters with a mass of $M_{200} > 10^{14} M_\odot$ in the redshift range of $0.05 < z < 0.42$. A total of 71 GRGs from our sample fall in this redshift range.

We find 17 GRGs to be BCGs based on the WHL cluster catalogue. We also used the Gaussian Mixture Brightest Cluster Galaxy (GMBCG) catalogue (Hao et al. 2010) consisting of 55,880 galaxy clusters which is more than 90% complete within the redshift range of $0.1 < z < 0.55$. We find 3 extra GRGs to be BCGs from the GMBCG catalogue. Therefore, we find a total of 20 GRGs (Table 3.3) from our sample of 239 to be BCGs

residing in dense cluster environments and hosted by BCGs of the clusters. The mass and radius (obtained from Wen et al. 2012) of the 17 clusters are listed in Table 3.3.

3.4 Discussion

3.4.1 GRGs with sizes > 2 Mpc

GRGs with projected linear sizes > 2 Mpc are quite rare and as observed from Fig. 3.3, there are only 7 GRGs with sizes greater than 2 Mpc in our sample of 239. Based on sample compilation (incomplete) of all the known GRGs till date of ~400 sources, only ~62 GRGs (~15%) have sizes greater than 2 Mpc (Willis et al. 1974; Laing et al. 1983; Lacy et al. 1993; Ishwara-Chandra & Saikia 1999; Schoenmakers et al. 2001; Machalski et al. 2001; Lara et al. 2001a; Saripalli et al. 2005; Machalski et al. 2007c; Koziel-Wierzbowska & Stasinska 2012; Solovyov & Verkhodanov 2014; Amirkhanyan et al. 2015; Amirkhanyan 2016; Dabhade et al. 2017; Clarke et al. 2017; Prescott et al. 2018; Sebastian et al. 2018).

If we take a complete radio sample like 3CRR (Laing et al. 1983), then we have only 12 GRGs from the total sample of 173, which is only ~7% of the total population. Considering this sample of 12 GRGs from 3CRR*, there are only 2 sources with sizes greater than 2 Mpc, which constitutes ~ 17% of the total GRG population in 3CRR complete sample. The conditions under which a radio galaxies grows to become are a GRG is not very well understood and studies so far based on the observations and theory seems to suggest that the gigantic size could be due to an interplay between the jet power and the environment.

3.4.2 Morphology of GRGs

Most known GRGs exhibit FR-II type of morphology and we very rarely see radio galaxies with Mpc scale size with FR I type of morphology. Based on their morphologies we classify 18 GRGs as FR I type and 215 GRGs as FR II type. GRG J121900.76+505254.41 is the only FR-I GRG residing at cluster centre and hosted by a BCG (Table 3.3).

The total radio power of FR-I sources on average is less than that of the FRII sources (Ledlow & Owen 1996; Lara et al. 2004). As seen in Fig. 3.9, the FR-I type of GRGs have a limited range in radio power $10^{24} \sim 10^{26}$

*http://www.jb.man.ac.uk/atlas/

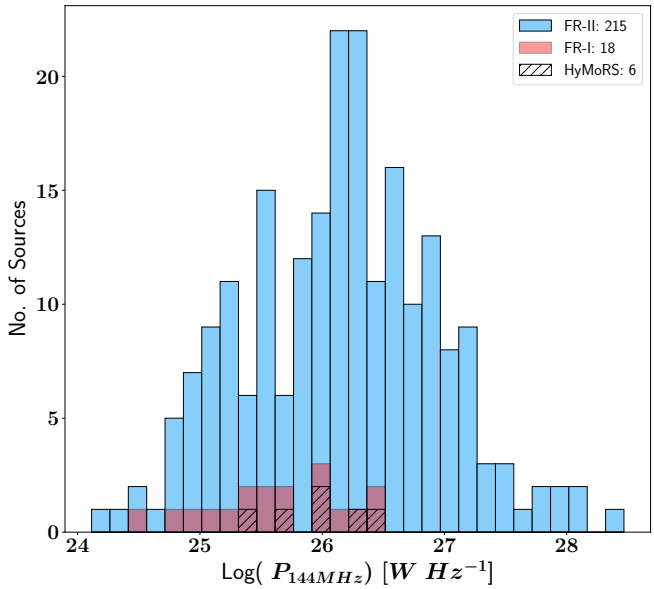

Figure 3.9: Radio power (144 MHz) distribution of of FR-I, FR-II and HyMoRS souces in LoTSS DR1 sample of giants.

W Hz^{-1}, whereas the FR-II exhibits a wide range of radio powers from 10^{24} $\sim 10^{28}$ W Hz^{-1} at 144 MHz.

GRGs with Hybrid morphology

Radio galaxies which show FR-I morphology on one side and FR-II morphology on other side are referred as HyMoRS (Gopal-Krishna & Wiita 2002). The earliest example of such morphology was presented and studied by Saikia et al. (1996), for the radio galaxy 4C +63.07. They attribute this to an intrinsic asymmetry in either the collimation of its jets or the supply of fuel from the central black hole to opposite sides.

Gawroński et al. (2006) have estimated the occurrence of HyMoRS to be as low as $\leqslant 1\%$ amongst the radio galaxy population. Recently, Kapinska et al. (2015) presented 25 new candidate HyMoRS, of which 5 are GRGs with one being at the centre of a galaxy cluster. Therefore, one of the possible scenarios for such hybrid morphology could be attributed to different environments on each side of the host galaxy (radio core).

In our sample of 239 GRGs, we find 6 examples of HyMoRS (identified via visual inspection) which are listed in column 11 (FR type) of Table 3.2,

indicated with roman numeral III, images of these sources are presented in Fig. 3.11. This is by far the largest HyMoRS GRG sample reported ever. Environment, as well as host AGN studies, are needed to understand this class of radio galaxies, which can also grow to megaparsec scales in size.

DDRGs: Double double radio galaxies

DDRG are FR-II type objects with two pairs of lobes, which is indicative of their restarted nature (Schoenmakers et al. 2000a; Saikia & Jamrozy 2009). The newly created jets in such sources travel outwards through the cocoon formed by the earlier cycle/episode of activity rather than the common intergalactic or intracluster medium, after moving through the interstellar medium of the host galaxy. In general, the outer double lobes are aligned with the inner ones and can extend from few kpc up to Mpc scales. It is likely that in DDRGs, due to an unknown mechanism or activity, the interruption of these bipolar relativistic jet flows has occurred leading to such morphologies.
In the last ∼20 years only about 140 DDRGs have been reported (Schoenmakers et al. 2000a; Nandi & Saikia 2012; Kuźmicz et al. 2017; Mahatma et al. 2019; Nandi et al. 2019). Recently, Mahatma et al. 2019 created a new sample of 33 DDRGs using the LoTSS DR1 and a follow up observations at higher frequency with the Jansky Very Large Array (JVLA), where they compared the optical and infrared magnitudes and colours of their host galaxies with a sample of normal radio galaxies. They find that the host galaxy properties of both DDRGs and normal radio galaxies are similar and suggest that the DDRG activity is a regular part of the life cycle of the radio galaxies. We have found only 14 GRGs (largest sample reported till date) in our entire sample with DDRG type morphology as seen in Fig. 3.12 and Fig. 3.13, indicating that megaparsec scale DDRGs are rare. Except J110457.07+480913, J110613.55+485748.29, J121900.76+505254.41, J123754.05+512201.28, J134313.31+560008.35 and J141504.70+463428.97, rest 8 were previously classified as DDRGs in the literature (7 in Mahatma et al. 2019 and GRGJ140718.48+513204.63 in Nandi & Saikia 2012).

We note that sources 28 (GRG JJ112130.35+494208.14) and 221 (GRG J145002.36+540528.27) show some signs of being DDRGs but based on the current radio maps available to us they cannot be confirmed as DDRGs and hence are candidate DDRGs.

These sources provide a unique opportunity to study timescales of AGN recurrent activity. As seen in Fig. 3.12, Fig. 3.13 and Fig. 3.14, some components of the giant DDRGs are very faint and it was only possible

with LoTSS's high sensitivity and resolution to detect and sufficiently resolve them. Further studies on host AGN/galaxy properties of DDRGs along with their local environments are needed to understand these peculiar sources better.

3.4.3 GRGs in dense environments

It has been hypothesised that the growth of GRGs to enormous size is favoured by their location in low density environments. Using our large new sample of GRGs, it is now possible to test this hypothesis for objects with low redshifts ($z < 0.55$). We find, at least 8.4% GRGs (Table 3.3) from our sample (20/239) are located in high density environments and are hosted by BCGs. This low number of BCG GRGs is possibly due to absence of data for high redshift clusters in the WHL cluster catalogue and GMBCG catalogue, which are more sensitive to clusters with redshift less than ~ 0.42 and ~ 0.55, respectively (see Sect. 3.3.5). We have 128 GRGs with $z \leqslant 0.55$, therefore at least $\sim 16\%$ (20/128) GRGs are in dense cluster environments. Based on the work of Paul et al. (2017), virialized structures of mass $M_{200} \geqslant 0.8 \times 10^{14}$ $M_{\odot}$ are classified as cluster of galaxies and non-virialized gravitionally bound structures consisting of few galaxies with $M_{200} < 0.8 \times 10^{14}$ $M_{\odot}$ are classified as group of galaxies. Using this classification there are 14 GRGs in clusters and 3 GRGs in groups of galaxies (see Table 3.3).

Croston et al. (2019) carried out a study of environments of ~ 8000 radio loud AGNs from the LoTSS, where they find that only 10% of AGNs are associated with high density environments like galaxy groups/clusters and AGNs with $L_{150} > 10^{25}$ W Hz^{-1} (where L_{150} is the radio power at 150 MHz) are more likely to be in cluster environments. Similarly our 20 BCG GRGs which are also radio loud AGNs in galaxy cluster, exhibit P_{144MHz} or $L_{150} > 10^{25}$WHz^{-1}.

To compare properties of galaxy clusters which have radio loud BCGs (also BCG-GRGs) and the galaxy clusters with radio quiet BCGs, we extracted all the galaxy clusters present in the LoTSS-DR1 HETDEX region from the WHL cluster catalogue. This resulted in total of 5027 galaxy clusters below redshift (z) of 0.55 (highest redshift of BCG-GRG in our sample). Next, we cross-matched the location of BCGs (5027) from the WHL cluster with the VAC and FIRST catalogue to determine all the radio loud BCGs in this region. The final number of galaxy clusters with radio loud BCGs is 1559 (unique sample after combining results from matches with VAC and FIRST). The 1559 radio loud BCGs also include our 17 BCG-GRGs (found

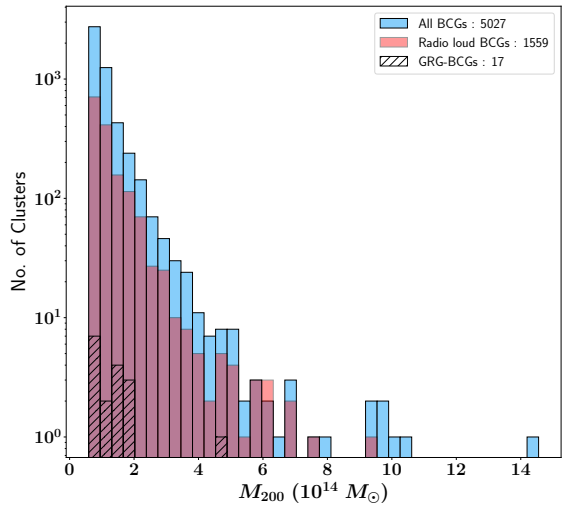

Figure 3.10: Distribution of M_{200} (mass of the cluster within r_{200}) of clusters of galaxies.

in WHL; see Table 3.3). In Fig. 3.10 we have shown the distribution of M_{200}, which is the mass of the cluster within r_{200}, of clusters of galaxies, where r_{200} is the radius within which the mean density of a cluster is 200 times of the critical density of the Universe. We note that about 30% (1541) clusters have radio loud BCGs which are not giants and only $\sim$0.34 % of the clusters in WHL cluster catalogue (HETDEX region) host a GRG (or have BCG GRG). Though the GRG sample is less here but more or less complete, it seems that GRGs which are BCGs tend to avoid very high mass clusters and prefer less dense clusters.

The BCG GRGs also can possibly trace the inhomogeneities in the intergalactic gas, which could be one of the determining factors for the growth and evolution of these giant sources. The forward propagation of jets as well as backflow from hotspots in the lobes of GRGs are influenced by the gas they encounter. Only 1/20 BCG GRGs in our sample have FR-I type radio morphology and rest 19 have FR-II type of radio morphology. Almost all these sources do not exhibit highly linear structures but are distorted or bent to certain extent, which indicates the effect of interaction between the cluster medium and the expanding radio jets of the BCG GRGs. Remarkably, despite the possible resistance presented by the cluster medium, these sources have managed to grow to megaparsec scales. This seems to suggest the presence of extraordinarily powerful AGN powering these sources.

Table 3.1: Short summary of classification of GRGs.

Classification	No. of objects
GRQs	40
BCGs	20
FR-II	215
FR-I	18
HyMoRS	6
DDRGs	14

3.5 Summary

A total of 239 GRGs (Table. 3.1) were found in ~424 deg^2 area using LoTSS, which is just ~2% area of the total survey that is planned to cover the northern sky. Our sample of 239 GRGs represents a lower number estimate due to limitation of optical data, which is essential for identifying host galaxy and its corresponding redshift. Assuming the isotropy and homogeneity of the Universe, if we extrapolate the number of GRGs expected to be found over the final sky coverage of LoTSS ($\sim 2\pi$ steradians), then we should be able to find at least ~12000 GRGs with LoTSS's sensitivity. Upcoming deep optical spectroscopic surveys like the WEAVE-LOFAR survey (Smith et al. 2016) will provide crucial data (redshifts) for identifying hundreds of more GRGs. The summary of the paper is as follows :

1. Our sample of 239 GRGs is in the redshift range of 0.1 to 2.3, out of which 225 are newly found. This makes it the largest sample discovered to date.

2. About 16% (40/239) of the sample are hosted by quasars, where three GRQs are above redshift of 2.

3. The depth and resolution of LoTSS images has enabled us to find GRGs with low powers of $\sim 10^{24}$ W Hz^{-1} at 144 MHz.

4. We show that the spectral index of GRGs and GRQs is similar to that of their low sized counterparts (NRGs).

5. Majority (90%) of our sample show FR-II type of morphology.

6. We have found 14 double-double GRGs, which is ∼5% of our sample. It is the largest reporting sample of giant DDRGs till date.

7. We have found 6 GRGs with HyMoRS morphology which are very rare.

8. Based on the optical data, we find that none of the GRGs in our sample are hosted by spiral galaxies.

9. At $z < 0.55$, at least ∼16% of GRGs lie at the centers (BCGs) of either big galaxy groups or galaxy clusters.

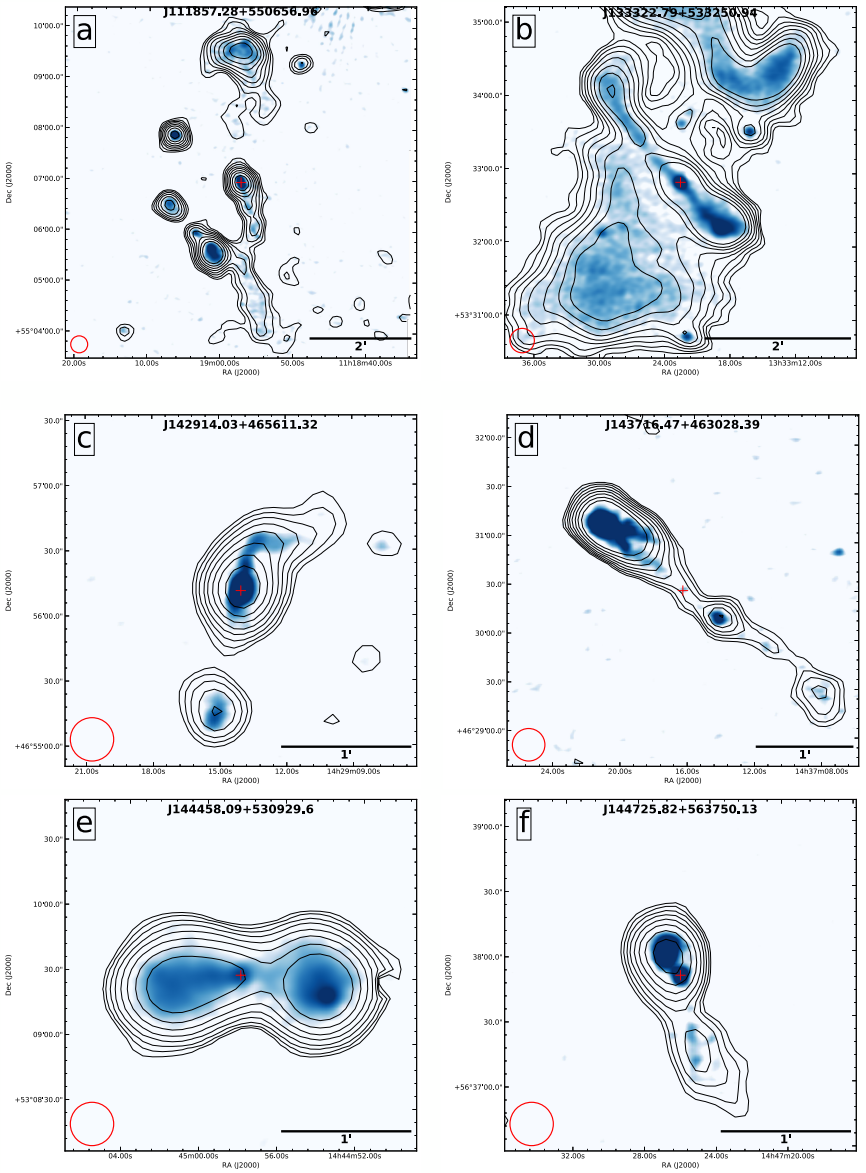

Figure 3.11: LoTSS DR1 (6″× 6″) maps of 6 HyMoRS in inverted blue colour scale with (20″× 20″) black contours (eight equally spaced relative contour levels starting from three times σ, where σ denotes the local RMS noise). The circles at bottom left corner represents the beam sizes of low resolution radio maps of LoTSS DR1. The red colour marker '+' indicates the location of the host galaxy.

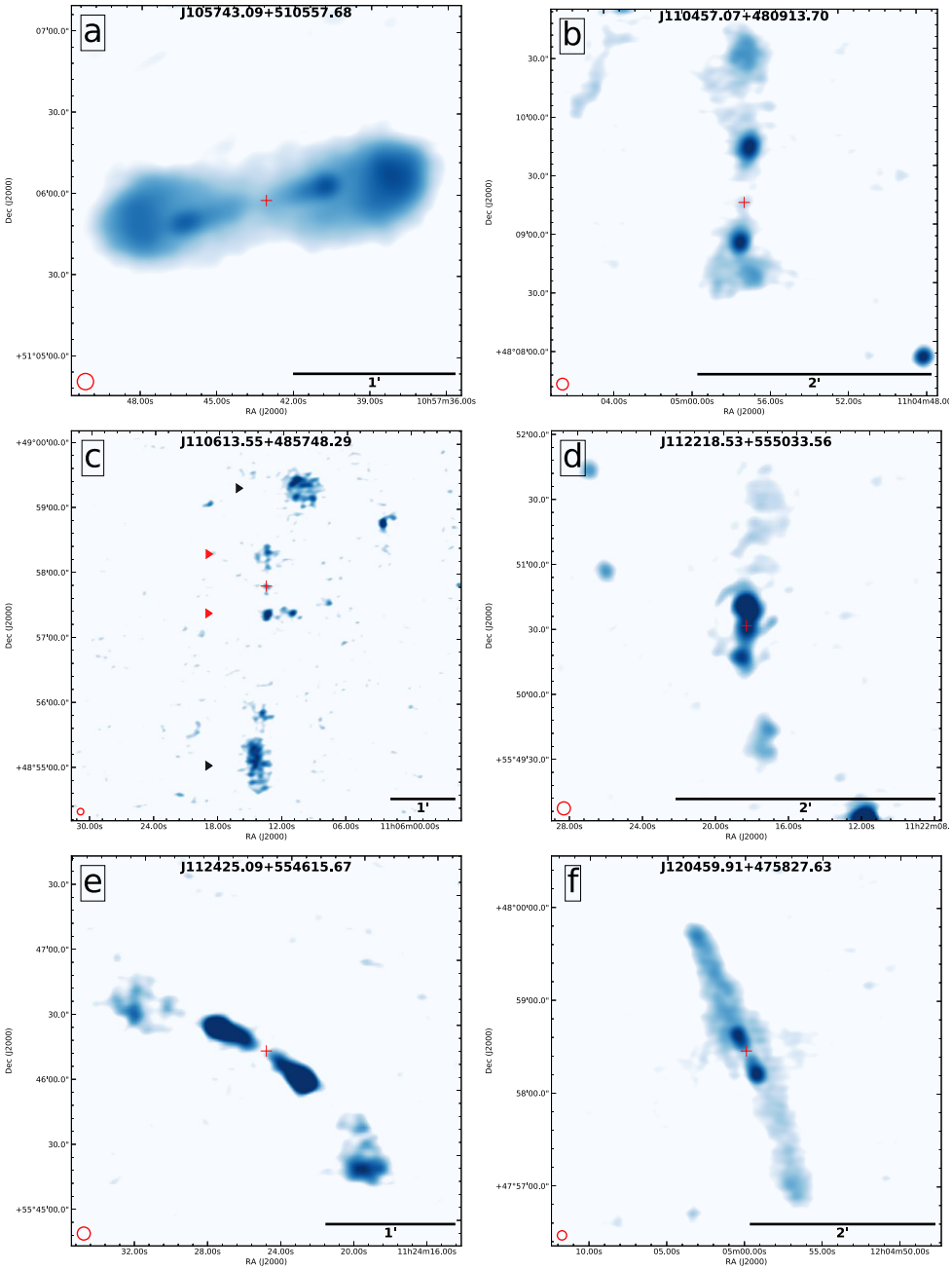

Figure 3.12: DDRGs postage-1 (1-6 DDRGs) made using LoTSS DR1 144 MHz radio image with $6'' \times 6''$ resolution in inverted blue colour scale. Refer to Sect. 3.4.2 for more details. The circle at bottom left corner represents the beam size. The red colour marker '+' indicates the location of the host galaxy. In source J110613.55+485748.29 (sub-image c) the two red markers indicate the inner pair of the DDRG and the black markers indicate the out pair of the DDRG.

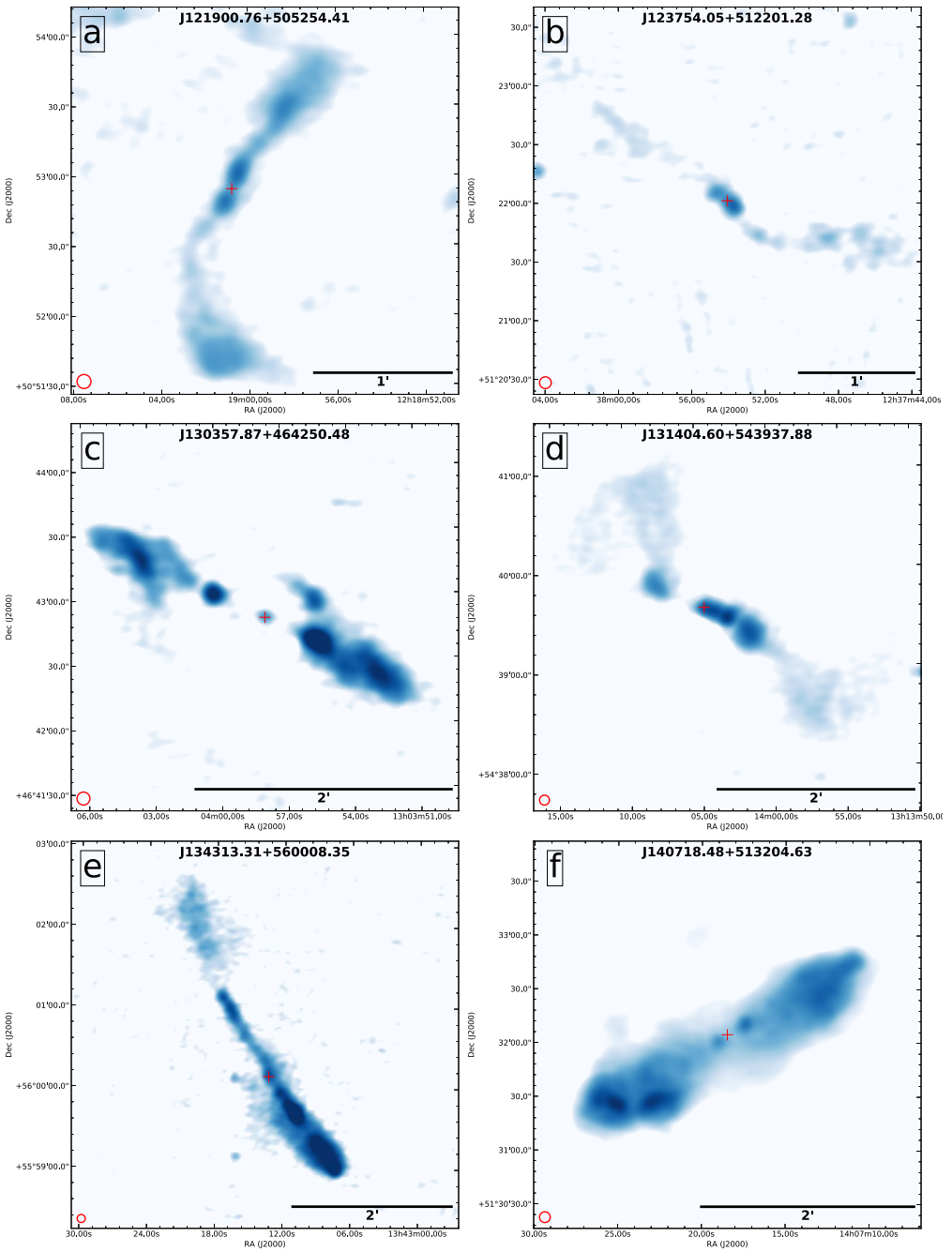

Figure 3.13: DDRGs postage-1 (7-12 DDRGs) made using LoTSS DR1 144 MHz radio image with $6'' \times 6''$ resolution in inverted blue colour scale. Refer to Sect. 3.4.2 for more details.

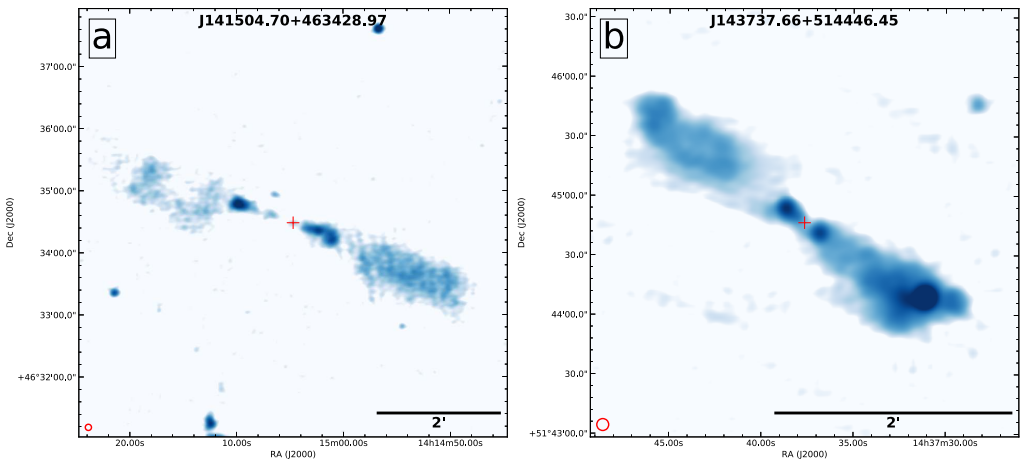

Figure 3.14: DDRGs postage-1 (13-14 DDRGs) made using LoTSS DR1 144 MHz radio image with $6'' \times 6''$ resolution in inverted blue colour scale. Refer to Sect. 3.4.2 for more details.

Table 3.2: Here, we list all the 239 GRGs found from the LoTSS. The Columns (2)-RA & (3)-Dec are the right ascension & declination (J2000.0 epoch) which indicate the center of the host galaxies of the GRG/GRQs from either SDSS or Pan-STARRS. Column (4) 'Class' represents the type of host of the GRG - G:galaxy, Q:quasar and Q_c: quasar candidate. In Column (5), z (redshift) marked with † represents spectroscopic redshift from SDSS, ⋆ represents photometric redshift from SDSS and § indicates redshifts from VAC. The one marked with superscript 'a' refers to redshift obtained from O'Sullivan et al. 2019 (spectroscopic) and 'b' from Lopes 2007 (photometric), owing to higher accuracy when compared to SDSS or VAC. Columns (6) & (7) are angular size and projected linear size of the source. Columns (8) & (9) are the integrated flux of sources at 144 MHz and its corresponding radio power. Column (10) α_{144}^{1400} is the integrated spectral index computed between 1400 MHz (NVSS) flux and 144 MHz (LoTSS) flux. Rows marked with '-' in Column (10) are blended sources for which we do not present a spectral index. Column (11) indicates the morphological type of the GRG: I represents FR-I type, II represents FR-II type and III represents HyMoRS. Column (12) represents the r band magnitude of the host galaxies of the GRGs obtained from SDSS. For sources 162 and 233, in the absence of reliable magnitudes from SDSS, we have given r band magnitudes from PAN-STARRS. The last column (Ref) shows references (see end of the table) for the GRGs already known in literature.

Sr.No	RA	Dec	Class	z	Size	Size	S_{144MHz}	P_{144MHz}	α_{144}^{1400}	FR	r	Ref
	(HMS)	(DMS)			($''$)	(Mpc)	(mJy)	(10^{26}W Hz^{-1})		Type	Mag	
(1)	(2)	(3)	(4)	(5)	(6)	(7)	(8)	(9)	(10)	(11)	(12)	(13)
1	10 57 05.43	+53 26 24.79	Q	0.45992 ± 0.00003†	153	0.92	1485 ± 297	11.00 ± 2.20	0.69 ± 0.09	II	19.48 ± 0.03	-
2	10 57 09.25	+48 40 41.03	G	0.27627 ± 0.00005†	439	1.90	1062 ± 212	2.55 ± 0.51	0.79 ± 0.09	II	18.01 ± 0.01	-
3	10 57 14.71	+55 48 56.02	Q	1.39830 ± 0.00166†	91	0.79	20 ± 4	1.84 ± 0.40	0.64 ± 0.11	II	18.86 ± 0.01	-
4	10 57 21.22	+53 14 22.42	G	0.33645 ± 0.00011†	145	0.72	11 ± 4	0.04 ± 0.02	<0.63	II	18.36 ± 0.02	-
5	10 57 25.96	+49 29 00.31	G	0.47614 ± 0.00022†	157	0.96	94 ± 19	0.81 ± 0.16	0.86 ± 0.10	II	19.76 ± 0.04	-
6	10 57 43.09	+51 05 57.68	G	0.46269 ± 0.00004†	126	0.76	657 ± 131	5.22 ± 1.05	0.85 ± 0.09	II	20.59 ± 0.05	-
7	10 58 17.90	+51 40 17.70	G	0.41497 ± 0.00003†	330	1.86	298 ± 88	1.77 ± 0.53	0.74 ± 0.22	II	19.62 ± 0.03	8
8	11 01 47.58	+46 49 11.20	G	0.68096 ± 0.00017†	150	1.09	532 ± 106	10.70 ± 2.15	0.88 ± 0.09	II	21.17 ± 0.12	3
9	11 01 59.17	+46 45 34.19	G	0.46877 ± 0.00019†	127	0.77	168 ± 34	1.35 ± 0.27	0.80 ± 0.09	II	19.49 ± 0.03	-
10	11 04 33.11	+46 42 25.76	G	0.14126 ± 0.00001†	305	0.78	253 ± 51	0.14 ± 0.03	0.68 ± 0.09	I	16.68 ± 0.01	9
11	11 04 57.07	+48 09 13.70	G	0.41471 ± 0.00011†	137	0.78	37 ± 7	0.22 ± 0.04	0.75 ± 0.12	II	19.84 ± 0.03	-
12	11 05 15.27	+54 41 09.30	G	0.28425 ± 0.00010†	169	0.75	89 ± 18	0.23 ± 0.05	0.90 ± 0.10	II	20.64 ± 0.05	-
13	11 06 13.55	+48 57 48.29	G	0.634 ± 0.108§	292	2.06	10 ± 2	0.15 ± 0.07	<0.63	II	20.25 ± 0.12	-
14	11 08 00.77	+51 20 28.64	G	0.801 ± 0.172§	157	1.21	192 ± 39	7.64 ± 4.33	1.38 ± 0.13	II	20.47 ± 0.10	-
15	11 08 15.18	+50 10 03.84	G	0.66956 ± 0.00023†	103	0.74	29 ± 6	0.77 ± 0.16	<1.54	II	21.49 ± 0.10	-
16	11 08 33.99	+48 32 03.03	Q	2.12100 ± 0.00026†	85	0.73	30 ± 6	4.32 ± 0.89	0.21 ± 0.09	II	19.64 ± 0.02	-
17	11 09 20.21	+48 15 00.51	G	0.39190 ± 0.00009†	183	1.00	12 ± 2	0.05 ± 0.01	0.33 ± 0.12	II	18.31 ± 0.02	-
18	11 09 35.40	+51 04 02.27	Q	1.18230 ± 0.00049†	106	0.90	186 ± 37	12.70 ± 2.58	-	II	19.13 ± 0.01	2
19	11 09 36.42	+53 13 48.13	G	0.288 ± 0.027§	230	1.03	583 ± 117	1.52 ± 0.45	-	II	18.16 ± 0.01	-
20	11 10 11.02	+53 30 58.74	G	0.58483 ± 0.00018†	142	0.96	565 ± 113	7.44 ± 1.50	-	II	20.64 ± 0.07	-
21	11 12 59.52	+49 42 27.11	G	0.502 ± 0.133§	244	1.54	223 ± 45	1.90 ± 1.26	0.55 ± 0.09	II	21.25 ± 0.09	-

Table 3.2: continued.

Sr.No	RA	Dec	Class	z	Size	Size	S_{144MHz}	P_{144MHz}	α_{144}^{1400}	FR	r	Ref
	(HMS)	(DMS)			($''$)	(Mpc)	(mJy)	(10^{26}W Hz^{-1})		Type	Mag	
(1)	(2)	(3)	(4)	(5)	(6)	(7)	(8)	(9)	(10)	(11)	(12)	(13)
22	11 13 31.45	+46 22 16.04	G	0.589 ± 0.145§	112	0.76	340 ± 68	4.66 ± 2.92	0.80 ± 0.09	II	21.84 ± 0.10	-
23	11 14 00.10	+53 22 16.57	G	0.727 ± 0.116§	125	0.93	6 ± 1	0.17 ± 0.08	<1.16	II	21.35 ± 0.15	-
24	11 15 29.60	+56 00 39.64	G	0.57880 ± 0.00007†	107	0.72	82 ± 16	1.06 ± 0.21	0.77 ± 0.09	II	20.33 ± 0.06	-
25	11 18 57.28	+55 06 56.96	G	0.35159 ± 0.00007†	347	1.77	669 ± 134	2.73 ± 0.55	-	III	19.23 ± 0.02	-
26	11 20 12.70	+51 32 56.34	G	0.72720 ± 0.00019†	103	0.77	94 ± 19	2.17 ± 0.44	0.86 ± 0.10	II	21.03 ± 0.10	-
27	11 21 26.44	+53 44 56.71	G	0.10378 ± 0.00002†	450	0.88	399 ± 80	0.11 ± 0.02	0.61 ± 0.09	II	15.11 ± 0.00	-
28	11 21 30.35	+49 42 08.14	G	0.494 ± 0.071§	132	0.82	86 ± 17	0.72 ± 0.29	0.61 ± 0.09	II	20.00 ± 0.04	-
29	11 22 18.53	+55 50 33.56	G	0.90962 ± 0.00047†	126	1.01	56 ± 11	2.05 ± 0.42	-	II	21.92 ± 0.18	-
30	11 24 25.09	+55 46 15.67	G	0.80902 ± 0.00042†	146	1.13	26 ± 5	0.75 ± 0.15	0.77 ± 0.13	II	22.14 ± 0.22	-
31	11 24 29.98	+46 35 23.68	Q	0.91500 ± 0.00013†	88	0.71	33 ± 7	1.11 ± 0.23	0.58 ± 0.10	II	20.12 ± 0.03	-
32	11 24 35.86	+49 03 25.92	G	0.47934 ± 0.00010†	121	0.74	120 ± 24	1.00 ± 0.20	-	II	20.10 ± 0.04	-
33	11 26 29.95	+49 01 37.16	G	0.660 ± 0.139§	111	0.80	35 ± 7	0.62 ± 0.34	0.76 ± 0.11	II	21.67 ± 0.12	-
34	11 26 39.89	+53 34 27.20	G	0.64523 ± 0.00024†	125	0.89	79 ± 16	1.30 ± 0.26	-	II	20.49 ± 0.08	-
35	11 27 13.18	+51 13 26.35	G	0.36132 ± 0.00007†	202	1.05	54 ± 11	0.23 ± 0.05	0.60 ± 0.10	I	18.12 ± 0.01	-
36	11 27 42.06	+52 19 44.68	G	0.72484 ± 0.00031†	114	0.85	6 ± 1	0.13 ± 0.03	<0.82	II	21.75 ± 0.12	-
37	11 28 54.65	+56 20 09.50	G	0.594 ± 0.067§	188	1.29	115 ± 23	1.57 ± 0.53	-	II	21.12 ± 0.10	-
38	11 29 43.41	+51 24 12.11	G	0.79923 ± 0.00008†	226	1.75	70 ± 14	2.15 ± 0.43	0.94 ± 0.11	II	21.53 ± 0.15	-
39	11 32 02.31	+47 28 24.14	G	0.26431 ± 0.00006†	205	0.86	38 ± 8	0.08 ± 0.02	0.61 ± 0.10	II	17.82 ± 0.01	-
40	11 32 50.67	+50 57 04.68	G	0.35857 ± 0.00010†	138	0.71	63 ± 13	0.26 ± 0.05	0.65 ± 0.10	II	18.53 ± 0.01	-
41	11 34 21.89	+56 34 13.28	G	0.626 ± 0.092§	227	1.59	21 ± 4	0.35 ± 0.14	0.92 ± 0.16	II	20.98 ± 0.08	-
42	11 34 35.48	+46 08 00.45	G	0.704 ± 0.163§	300	2.21	41 ± 8	0.90 ± 0.54	0.87 ± 0.16	II	21.39 ± 0.08	-
43	11 35 03.20	+48 26 12.12	G	0.22597 ± 0.00006†	202	0.76	131 ± 26	0.20 ± 0.04	0.78 ± 0.09	II	17.59 ± 0.01	-
44	11 39 31.77	+47 21 24.3	G	0.51791 ± 0.00012†	312	2.00	126 ± 25	1.23 ± 0.25	0.70 ± 0.09	II	20.32 ± 0.05	-
45	11 43 05.55	+52 27 26.89	Q	1.67249 ± 0.00082†	86	0.75	100 ± 20	14.90 ± 3.04	0.72 ± 0.09	II	20.23 ± 0.03	-
46	11 48 14.98	+54 57 16.49	G	0.22679 ± 0.00003†	202	0.76	22 ± 4	0.03 ± 0.01	0.51 ± 0.11	I	17.26 ± 0.01	-
47	11 51 59.9	+49 50 56.11	Q	0.89148 ± 0.00017†	96	0.77	1015 ± 203	36.60 ± 7.37	0.78 ± 0.09	II	18.38 ± 0.01	-
48	11 52 16.89	+46 24 51.37	G	0.44454 ± 0.02004★	148	0.87	43 ± 9	0.28 ± 0.06	0.56 ± 0.10	II	19.68 ± 0.03	-
49	11 58 39.12	+46 55 45.35	G	0.65974 ± 0.00023†	128	0.92	18 ± 4	0.36 ± 0.07	<1.08	II	21.61 ± 0.13	-
50	12 01 18.14	+46 32 41.98	G	0.638 ± 0.088§	129	0.91	111 ± 22	1.87 ± 0.73	0.83 ± 0.10	II	21.82 ± 0.15	-
51	12 01 22.84	+49 25 37.14	G	0.205 ± 0.045§	345	1.20	1946 ± 389	2.56 ± 1.35	1.09 ± 0.09	I	18.14 ± 0.01	-
52	12 02 06.86	+51 41 34.63	G	0.61278 ± 0.00028†	141	0.98	87 ± 17	1.27 ± 0.26	-	II	21.11 ± 0.10	-
53	12 04 59.91	+47 58 27.63	G	0.52963 ± 0.08487★	192	1.24	138 ± 28	1.53 ± 0.66	0.89 ± 0.09	II	20.96 ± 0.07	-
54	12 05 28.50	+56 13 42.32	G	0.681 ± 0.121§	118	0.86	26 ± 5	0.48 ± 0.23	<0.74	II	20.54 ± 0.13	-
55	12 05 46.98	+50 48 59.94	G	0.69799 ± 0.00021†	160	1.18	352 ± 70	7.60 ± 1.53	0.90 ± 0.09	II	21.02 ± 0.09	-
56	12 08 26.14	+47 15 25.03	G	0.56407 ± 0.00021†	113	0.75	34 ± 7	0.41 ± 0.08	-	II	20.76 ± 0.06	-
57	12 10 46.06	+53 29 22.90	G	0.44842 ± 0.00010†	119	0.71	234 ± 47	1.73 ± 0.35	0.85 ± 0.09	I	19.87 ± 0.03	-
58	12 10 55.67	+49 49 39.77	G	0.53442 ± 0.05992★	110	0.72	49 ± 10	0.53 ± 0.18	0.79 ± 0.10	I	20.57 ± 0.06	-
59	12 11 40.91	+50 10 15.11	G	0.33985 ± 0.14011★	143	0.71	372 ± 74	1.45 ± 1.42	0.86 ± 0.09	II	21.78 ± 0.13	-

Table 3.2: continued.

Sr.No	RA (HMS)	Dec (DMS)	Class	z	Size ($''$)	Size (Mpc)	S_{144MHz} (mJy)	P_{144MHz} (10^{26}W Hz^{-1})	α_{144}^{1400}	FR Type	r Mag	Ref
(1)	(2)	(3)	(4)	(5)	(6)	(7)	(8)	(9)	(10)	(11)	(12)	(13)
60	12 13 04.34	+51 18 26.38	Q	0.61680 ± 0.00013†	118	0.82	102 ± 20	1.49 ± 0.30	0.72 ± 0.09	II	19.78 ± 0.02	-
61	12 15 55.53	+51 24 16.41	G	0.44477 ± 0.00038†	277	1.63	74 ± 15	0.52 ± 0.10	-	I	19.17 ± 0.02	-
62	12 17 06.80	+51 47 34.33	G	0.616 ± 0.089§	183	1.28	57 ± 11	0.95 ± 0.39	0.99 ± 0.12	I	21.61 ± 0.10	-
63	12 17 07.40	+48 58 22.48	G	0.484 ± 0.029§	136	0.84	172 ± 34	1.46 ± 0.36	-	I	19.60 ± 0.03	-
64	12 18 18.15	+53 27 21.33	G	0.56754 ± 0.04447*	183	1.23	1270 ± 254	16.00 ± 4.41	0.81 ± 0.09	II	21.77 ± 0.17	-
65	12 18 49.88	+50 26 17.59	G	0.19920 ± 0.00002†	210	0.71	2942 ± 588	3.34 ± 0.67	0.67 ± 0.09	II	17.12 ± 0.01	6
66	12 19 00.76	+50 52 54.41	G	0.38509 ± 0.00008†	142	0.77	78 ± 16	0.38 ± 0.08	0.68 ± 0.10	I	18.35 ± 0.01	-
67	12 19 35.92	+46 59 29.88	G	0.67865 ± 0.00032†	114	0.83	19 ± 4	0.35 ± 0.07	-	II	21.14 ± 0.09	-
68	12 19 52.32	+47 20 58.49	Q	0.65310 ± 0.00009†	241	1.72	115 ± 23	2.06 ± 0.41	0.85 ± 0.10	II	19.10 ± 0.01	-
69	12 19 52.55	+46 54 25.74	Q	1.85116 ± 0.00041†	88	0.76	60 ± 12	8.28 ± 1.69	0.43 ± 0.09	II	18.62 ± 0.01	-
70	12 20 07.85	+47 05 19.65	G	0.689 ± 0.159§	149	1.09	109 ± 22	2.93 ± 1.75	1.37 ± 0.17	II	21.97 ± 0.12	-
71	12 20 28.13	+52 51 44.89	G	0.34583 ± 0.00008†	255	1.29	58 ± 12	0.21 ± 0.04	0.55 ± 0.09	II	18.09 ± 0.01	-
72	12 22 55.24	+49 26 42.32	G	0.20315 ± 0.00004†	354	1.22	84 ± 17	0.10 ± 0.02	0.48 ± 0.09	II	17.21 ± 0.01	-
73	12 23 27.25	+52 36 45.38	G	0.62112 ± 0.05830*	111	0.77	59 ± 12	0.89 ± 0.27	0.74 ± 0.10	I	21.19 ± 0.13	-
74	12 25 03.66	+47 23 36.40	G	0.774 ± 0.154§	95	0.73	14 ± 3	0.32 ± 0.17	0.51 ± 0.12	II	21.26 ± 0.09	-
75	12 25 31.36	+49 46 43.95	G	0.32488 ± 0.00009†	206	1.00	21 ± 4	0.07 ± 0.01	0.60 ± 0.12	I	18.32 ± 0.01	-
76	12 25 44.39	+49 49 42.93	G	0.63224 ± 0.08754*	164	1.16	286 ± 57	5.11 ± 2.00	1.00 ± 0.09	II	21.06 ± 0.06	-
77	12 25 58.20	+53 09 38.38	G	0.81100 ± 0.07937*	147	1.14	263 ± 53	8.15 ± 2.55	0.91 ± 0.09	II	20.25 ± 0.15	-
78	12 28 26.35	+52 31 01.10	G	0.453 ± 0.106§	157	0.93	106 ± 21	0.78 ± 0.46	0.80 ± 0.09	II	20.65 ± 0.06	-
79	12 29 36.25	+50 13 04.65	G	0.38357 ± 0.00007†	198	1.07	56 ± 11	0.27 ± 0.05	0.61 ± 0.10	I	18.53 ± 0.02	-
80	12 29 59.59	+53 32 47.04	G	0.52300 ± 0.05280*	137	0.88	296 ± 59	3.20 ± 1.01	0.90 ± 0.09	II	21.12 ± 0.11	-
81	12 30 14.05	+54 11 41.14	G	0.610 ± 0.087§	205	1.42	7 ± 1	0.09 ± 0.04	<0.57	II	20.96 ± 0.10	-
82	12 32 04.95	+53 06 27.31	G	0.20604 ± 0.00006†	274	0.95	120 ± 24	0.15 ± 0.03	0.90 ± 0.10	II	17.31 ± 0.01	-
83	12 32 50.45	+49 06 26.14	G	0.69015 ± 0.00013†	256	1.87	205 ± 41	3.99 ± 0.80	0.76 ± 0.09	II	20.92 ± 0.06	-
84	12 33 05.45	+49 02 51.93	Q	1.35200 ± 0.00107†	104	0.89	332 ± 66	31.00 ± 6.30	-	II	20.55 ± 0.03	-
85	12 35 01.52	+53 17 55.09	G	0.34480 ± 0.00030†	683	3.44	859 ± 172	3.46 ± 0.69	0.85 ± 0.09	II	19.24 ± 0.04	-
86	12 35 48.77	+50 50 36.30	G	0.650 ± 0.131§	105	0.75	84 ± 17	1.41 ± 0.75	-	II	21.49 ± 0.10	-
87	12 36 48.37	+46 04 05.91	G	0.615 ± 0.154§	125	0.87	268 ± 54	3.96 ± 2.53	0.75 ± 0.09	II	21.39 ± 0.10	-
88	12 37 54.05	+51 22 01.28	G	0.39184 ± 0.00018†	164	0.89	25 ± 5	0.13 ± 0.03	-	II	19.68 ± 0.03	-
89	12 38 07.78	+53 25 55.91	Q	0.34680 ± 0.00004†	157	0.80	455 ± 91	1.73 ± 0.35	0.61 ± 0.09	II	17.29 ± 0.01	-
90	12 39 33.21	+50 07 08.01	Q	2.31500 ± 0.00024†	89	0.75	3 ± 1	2.32 ± 0.52	<1.39	II	18.49 ± 0.01	-
91	12 40 12.46	+53 34 37.25	Q	0.29300 ± 0.00003†	164	0.74	1527 ± 305	4.15 ± 0.83	0.76 ± 0.09	II	18.52 ± 0.01	1
92	12 40 31.72	+48 59 36.89	G	0.53607 ± 0.04030*	136	0.89	605 ± 121	6.35 ± 1.72	0.70 ± 0.09	II	21.17 ± 0.08	-
93	12 41 42.34	+51 35 14.32	G	0.52951 ± 0.00011†	161	1.04	177 ± 36	1.86 ± 0.37	0.76 ± 0.09	II	19.57 ± 0.04	-
94	12 45 25.16	+47 07 10.11	G	0.51179 ± 0.00015†	111	0.70	22 ± 5	0.20 ± 0.04	0.60 ± 0.10	II	19.95 ± 0.03	-
95	12 45 31.06	+48 50 20.16	G	0.25359 ± 0.00010†	174	0.71	40 ± 8	0.08 ± 0.02	0.69 ± 0.11	I	17.99 ± 0.01	-
96	12 49 03.46	+52 40 05.29	G	0.663 ± 0.107§	135	0.97	66 ± 13	1.27 ± 0.56	0.93 ± 0.10	II	21.60 ± 0.13	-
97	12 49 13.20	+50 00 43.68	G	0.34956 ± 0.00010†	150	0.76	295 ± 59	1.13 ± 0.23	0.59 ± 0.09	I	18.82 ± 0.02	-

Table 3.2: continued.

Sr.No	RA	Dec	Class	z	Size	Size	S_{144MHz}	P_{144MHz}	α_{144}^{1400}	FR	r	Ref
	(HMS)	(DMS)			($''$)	(Mpc)	(mJy)	(10^{26}W Hz^{-1})		Type	Mag	
(1)	(2)	(3)	(4)	(5)	(6)	(7)	(8)	(9)	(10)	(11)	(12)	(13)
98	12 51 42.04	+50 34 24.65	G	0.54904 ± 0.00007†	150	0.99	8355 ± 1671	99.90 ± 20.10	0.86 ± 0.09	II	19.35 ± 0.03	5
99	12 56 24.74	+55 28 25.99	G	0.808 ± 0.179§	113	0.87	1765 ± 353	55.50 ± 32.10	0.94 ± 0.09	II	21.01 ± 0.12	-
100	12 57 16.35	+51 17 58.11	Q	0.52582 ± 0.00004†	170	1.09	96 ± 19	0.98 ± 0.20	0.74 ± 0.10	II	17.69 ± 0.01	-
101	12 58 21.37	+54 20 29.35	G	0.612 ± 0.099§	143	0.99	521 ± 104	7.64 ± 3.36	-	II	21.11 ± 0.09	-
102	12 59 50.83	+53 07 09.03	G	0.60663 ± 0.04364*	105	0.73	67 ± 13	1.06 ± 0.28	0.94 ± 0.11	II	20.93 ± 0.09	-
103	13 01 34.99	+54 08 09.21	G	0.313 ± 0.081§	168	0.79	1581 ± 316	5.00 ± 3.15	0.77 ± 0.09	II	19.23 ± 0.02	1
104	13 03 31.08	+53 59 48.65	G	0.24201 ± 0.00005†	248	0.97	50 ± 10	0.09 ± 0.02	0.84 ± 0.13	II	17.24 ± 0.01	-
105	13 03 32.19	+52 20 01.98	G	0.27200 ± 0.00007†	165	0.71	83 ± 17	0.18 ± 0.04	0.56 ± 0.09	I	17.98 ± 0.01	-
106	13 03 57.87	+46 42 50.48	G	0.58430 ± 0.00021†	159	1.08	137 ± 27	1.87 ± 0.38	0.83 ± 0.09	II	20.38 ± 0.06	-
107	13 04 30.80	+50 41 08.02	Q	0.93000 ± 0.00039†	122	0.98	119 ± 24	4.53 ± 0.92	0.71 ± 0.09	II	20.33 ± 0.03	-
108	13 05 21.32	+49 51 42.36	Q	1.25098 ± 0.00026†	88	0.75	544 ± 109	44.80 ± 9.07	0.82 ± 0.09	II	18.74 ± 0.01	-
109	13 06 35.08	+55 36 44.43	G	0.461 ± 0.031§	136	0.82	47 ± 9	0.36 ± 0.09	0.74 ± 0.11	II	20.17 ± 0.03	-
110	13 07 48.36	+56 11 46.96	G	0.83043 ± 0.08339*	120	0.94	143 ± 29	4.28 ± 1.37	-	II	22.23 ± 0.29	-
111	13 09 25.74	+53 48 17.26	G	0.81187 ± 0.00032†	118	0.92	75 ± 15	2.31 ± 0.47	0.89 ± 0.10	II	22.20 ± 0.26	-
112	13 10 28.87	+52 13 40.43	G	0.650 ± 0.094§	197	1.41	451 ± 90	7.45 ± 3.01	0.71 ± 0.09	II	20.28 ± 0.06	-
113	13 12 11.14	+48 09 25.26	Q	0.71510 ± 0.00003†	110	0.82	559 ± 112	10.30 ± 2.08	0.51 ± 0.09	II	17.13 ± 0.00	-
114	13 12 16.28	+48 47 45.40	G	0.36430 ± 0.00007†	210	1.09	122 ± 24	0.52 ± 0.10	0.60 ± 0.09	II	18.64 ± 0.01	-
115	13 13 55.21	+53 04 03.22	G	0.632 ± 0.088§	171	1.21	30 ± 6	0.54 ± 0.21	<1.03	II	21.76 ± 0.12	-
116	13 14 04.60	+54 39 37.88	G	0.34645 ± 0.00008†	210	1.06	678 ± 136	2.68 ± 0.54	-	II	17.80 ± 0.01	-
117	13 16 34.59	+49 32 39.67	G	0.563 ± 0.040§	126	0.84	84 ± 17	0.93 ± 0.24	0.57 ± 0.09	II	21.14 ± 0.05	-
118	13 17 22.25	+50 45 10.03	G	0.758 ± 0.134§	130	0.98	3 ± 1	0.06 ± 0.03	<0.58	II	21.67 ± 0.10	-
119	13 19 05.75	+47 46 39.23	G	0.90300 ± 0.00010†	262	2.10	44 ± 9	1.70 ± 0.34	0.83 ± 0.12	II	20.94 ± 0.04	-
120	13 20 29.67	+49 16 47.11	Q	0.68447 ± 0.00009†	113	0.82	74 ± 15	1.40 ± 0.28	-	II	19.08 ± 0.01	-
121	13 22 29.07	+50 48 44.53	G	0.18439 ± 0.00004†	326	1.04	94 ± 19	0.09 ± 0.02	-	II	17.23 ± 0.01	-
122	13 23 36.36	+47 29 49.68	G	0.440 ± 0.035§	180	1.05	249 ± 50	1.69 ± 0.46	-	II	19.36 ± 0.03	-
123	13 23 54.44	+46 31 42.89	G	0.35737 ± 0.00022†	136	0.70	118 ± 24	0.49 ± 0.10	0.69 ± 0.09	II	19.57 ± 0.03	-
124	13 24 35.19	+50 41 02.31	G	0.28711 ± 0.00006†	162	0.72	495 ± 99	1.41 ± 0.28	1.14 ± 0.09	II	18.17 ± 0.01	-
125	13 25 54.31	+55 19 36.23	G	1.692 ± 0.089§	87	0.75	31 ± 6	5.40 ± 1.32	0.85 ± 0.13	II	20.48 ± 0.03	-
126	13 26 14.35	+49 34 31.52	G	0.340 ± 0.044§	169	0.85	3885 ± 777	14.70 ± 5.35	0.76 ± 0.09	II	19.17 ± 0.02	7
127	13 26 15.35	+48 04 22.67	Q	0.59405 ± 0.00007†	103	0.71	287 ± 57	4.12 ± 0.83	0.85 ± 0.09	II	20.90 ± 0.08	-
128	13 26 46.56	+53 58 17.38	Q	0.40975 ± 0.00005†	178	1.00	444 ± 89	2.65 ± 0.53	0.84 ± 0.09	II	19.56 ± 0.03	-
129	13 27 13.33	+52 26 49.93	G	0.53770 ± 0.00015†	109	0.71	10 ± 3	0.11 ± 0.03	<0.80	II	20.31 ± 0.04	-
130	13 29 14.05	+52 09 38.80	G	0.620 ± 0.070§	118	0.82	25 ± 5	0.40 ± 0.14	0.86 ± 0.16	II	20.92 ± 0.09	-
131	13 29 24.63	+49 00 15.32	G	0.286 ± 0.081§	253	1.12	67 ± 13	0.17 ± 0.12	0.74 ± 0.11	II	19.08 ± 0.02	-
132	13 30 41.81	+48 27 54.88	G	0.33166 ± 0.00010†	153	0.75	47 ± 10	0.16 ± 0.03	0.53 ± 0.10	II	18.38 ± 0.01	-
133	13 31 35.25	+45 59 55.53	G	0.38482 ± 0.00009†	131	0.71	115 ± 23	0.57 ± 0.11	0.74 ± 0.09	II	18.06 ± 0.01	-
134	13 32 53.76	+48 45 32.05	G	0.73036 ± 0.00020†	122	0.91	65 ± 13	1.34 ± 0.27	0.61 ± 0.09	II	21.27 ± 0.11	-

Table 3.2: continued.

Sr.No	RA (HMS)	Dec (DMS)	Class	z	Size ($''$)	Size (Mpc)	S_{144MHz} (mJy)	P_{144MHz} (10^{26}W Hz^{-1})	α_{144}^{1400}	FR Type	r Mag	Ref
(1)	(2)	(3)	(4)	(5)	(6)	(7)	(8)	(9)	(10)	(11)	(12)	(13)
135	13 32 58.28	+53 53 55.60	G	0.32261 ± 0.00009†	174	0.84	199 ± 40	0.70 ± 0.14	0.94 ± 0.09	II	18.58 ± 0.01	-
136	13 33 22.79	+53 32 50.94	G	0.354 ± 0.034§	173	0.88	423 ± 86	1.75 ± 0.54	-	III	18.90 ± 0.02	-
137	13 34 11.70	+55 01 24.87	Q	1.24470 ± 0.00043†	91	0.78	3380 ± 676	294.00 ± 59.50	0.90 ± 0.09	II	17.97 ± 0.01	4
138	13 34 18.63	+48 13 17.08	Q	2.20849 ± 0.00009†	88	0.75	487 ± 97	140.00 ± 28.90	-	II	18.15 ± 0.01	-
139	13 35 12.01	+49 44 27.20	G	0.436 ± 0.041§	173	1.01	13 ± 3	0.08 ± 0.03	<0.71	II	19.32 ± 0.02	-
140	13 36 12.67	+54 47 42.24	Q	0.71180 ± 0.00012†	142	1.05	95 ± 19	1.97 ± 0.40	-	II	17.72 ± 0.01	-
141	13 36 18.75	+53 39 52.12	G	0.30138 ± 0.00006†	305	1.41	49 ± 10	0.14 ± 0.03	0.72 ± 0.11	II	17.91 ± 0.01	-
142	13 36 37.92	+55 40 33.27	G	0.86400 ± 0.00003†	105	0.83	291 ± 58	9.85 ± 1.98	0.80 ± 0.09	II	21.16 ± 0.05	-
143	13 38 04.28	+46 46 41.19	Q	1.36900 ± 0.00030†	140	1.21	95 ± 19	9.17 ± 1.87	-	II	21.13 ± 0.06	-
144	13 39 22.70	+50 57 47.40	G	0.316 ± 0.098§	174	0.83	56 ± 11	0.17 ± 0.13	0.66 ± 0.10	II	19.89 ± 0.02	-
145	13 41 03.08	+49 15 59.99	G	0.74672 ± 0.08486★	113	0.85	334 ± 67	7.64 ± 2.62	0.71 ± 0.09	II	21.63 ± 0.10	-
146	13 42 06.98	+47 25 53.04	G	0.17213 ± 0.00004†	369	1.11	366 ± 73	0.30 ± 0.06	0.68 ± 0.09	II	15.92 ± 0.00	-
147	13 43 13.31	+56 00 08.35	G	0.48474 ± 0.00007†	245	1.51	174 ± 35	1.62 ± 0.33	0.97 ± 0.10	II	20.00 ± 0.03	-
148	13 44 15.65	+48 45 48.96	G	0.725 ± 0.160§	202	1.51	495 ± 99	11.50 ± 6.59	0.87 ± 0.09	II	21.66 ± 0.14	-
149	13 44 41.82	+50 22 57.29	G	0.76317 ± 0.00025†	123	0.93	61 ± 12	1.58 ± 0.32	0.86 ± 0.10	II	21.82 ± 0.16	-
150	13 44 52.71	+48 57 49.96	G	0.34021 ± 0.00011†	167	0.84	36 ± 7	0.14 ± 0.03	0.92 ± 0.13	II	19.18 ± 0.02	-
151	13 45 57.55	+54 03 16.62	G	0.16250 ± 0.00003†	334	0.96	2582 ± 516	1.95 ± 0.39	0.89 ± 0.09	II	17.15 ± 0.01	2
152	13 46 00.30	+53 18 41.21	G	0.536 ± 0.096§	156	1.01	10 ± 2	0.12 ± 0.06	<1.09	II	20.61 ± 0.07	-
153	13 46 13.49	+50 35 07.24	G	0.69605 ± 0.00034†	141	1.04	12 ± 3	0.22 ± 0.05	<0.59	II	21.49 ± 0.12	-
154	13 46 45.96	+47 27 19.03	G	0.420 ± 0.049§	184	1.05	148 ± 30	0.91 ± 0.31	-	II	19.83 ± 0.03	-
155	13 47 30.56	+47 05 09.28	G	0.371 ± 0.047§	211	1.11	77 ± 15	0.38 ± 0.14	1.00 ± 0.12	II	19.53 ± 0.02	-
156	13 48 16.94	+49 50 24.80	G	0.64318 ± 0.00017†	120	0.85	8 ± 2	0.13 ± 0.03	<0.68	II	20.24 ± 0.06	-
157	13 48 37.68	+47 08 00.01	Q	0.50724 ± 0.00009†	119	0.75	127 ± 25	1.15 ± 0.23	0.65 ± 0.09	II	19.84 ± 0.05	-
158	13 48 53.20	+46 45 50.63	Q	1.66716 ± 0.00065†	102	0.89	58 ± 12	11.40 ± 2.34	1.01 ± 0.11	II	20.37 ± 0.03	-
159	13 49 27.92	+46 20 15.11	G	0.42110 ± 0.00010†	131	0.75	120 ± 24	0.74 ± 0.15	0.76 ± 0.09	II	19.05 ± 0.02	-
160	13 52 53.13	+46 25 20.66	G	0.471 ± 0.071§	220	1.34	397 ± 79	3.13 ± 1.29	0.72 ± 0.09	II	20.63 ± 0.04	-
161	13 54 14.72	+49 13 15.2	G	0.43885 ± 0.13902★	123	0.72	633 ± 127	4.55 ± 3.53	0.91 ± 0.09	II	22.08 ± 0.18	-
162	13 56 28.50	+52 42 19.23	G	0.42709 ± 0.00011†	297	1.71	64 ± 13	0.37 ± 0.07	0.50 ± 0.09	II	18.62 ± 0.02	-
163	13 56 35.89	+56 09 44.77	G	0.66300 ± 0.00021†	111	0.80	18 ± 4	0.32 ± 0.06	0.76 ± 0.13	II	20.83 ± 0.07	-
164	13 59 51.16	+47 03 21.03	G	0.46224 ± 0.00010†	140	0.85	23 ± 5	0.17 ± 0.03	0.55 ± 0.14	II	19.48 ± 0.03	-
165	14 02 55.41	+51 27 28.60	G	0.51796 ± 0.16062★	135	0.87	304 ± 61	3.07 ± 2.36	0.79 ± 0.09	II	20.93 ± 0.06	-
166	14 03 15.11	+51 44 44.77	G	0.48517 ± 0.16607★	228	1.41	1596 ± 319	14.30 ± 12.00	0.87 ± 0.09	II	21.07 ± 0.06	-
167	14 04 08.61	+46 42 39.42	G	0.537 ± 0.060§	453	2.96	224 ± 45	2.43 ± 0.81	-	I	20.34 ± 0.06	-
168	14 05 40.97	+54 10 55.42	G	0.76118 ± 0.13989★	116	0.88	588 ± 118	14.10 ± 6.96	0.72 ± 0.09	II	20.70 ± 0.04	-
169	14 06 05.42	+55 47 49.87	G	0.78025 ± 0.06341★	114	0.87	598 ± 120	16.50 ± 4.67	0.86 ± 0.09	II	23.09 ± 0.40	-
170	14 06 12.30	+53 38 34.64	G	0.46455 ± 0.00010†	117	0.71	5 ± 2	0.04 ± 0.02	<0.55	II	19.90 ± 0.03	-
171	14 07 18.48	+51 32 04.63	G	0.34048 ± 0.00003†	177	0.89	4246 ± 849	16.50 ± 3.31	0.83 ± 0.09	II	18.52 ± 0.02	-
172	14 07 19.96	+55 06 01.29	G	0.33224 ± 0.00010†	180	0.88	776 ± 155	2.79 ± 0.56	-	II	17.09 ± 0.02	-

Table 3.2: continued.

Sr.No	RA	Dec	Class	z	Size	Size	S_{144MHz}	P_{144MHz}	α_{144}^{1400}	FR	r	Ref
	(HMS)	(DMS)			($''$)	(Mpc)	(mJy)	(10^{26}W Hz^{-1})		Type	Mag	
(1)	(2)	(3)	(4)	(5)	(6)	(7)	(8)	(9)	(10)	(11)	(12)	(13)
173	14 08 32.49	+47 38 37.42	Q	1.43633 ± 0.00052†	85	0.74	282 ± 56	32.50 ± 6.60	0.83 ± 0.09	II	18.90 ± 0.01	-
174	14 09 36.64	+53 40 27.64	G	0.52484 ± 0.00015†	240	1.54	819 ± 164	9.06 ± 1.82	0.93 ± 0.09	II	19.98 ± 0.05	-
175	14 11 17.03	+47 10 29.47	G	0.39350 ± 0.00013†	300	1.64	62 ± 12	0.30 ± 0.06	0.53 ± 0.10	I	18.78 ± 0.02	-
176	14 11 51.97	+55 09 48.74	Q	1.89670 ± 0.00019†	99	0.86	559 ± 112	126.00 ± 25.80	0.85 ± 0.09	II	18.83 ± 0.01	-
177	14 14 08.45	+48 41 56.11	G	1.361 ± 0.130§	107	0.92	1055 ± 211	93.40 ± 29.00	0.67 ± 0.09	II	17.90 ± 0.01	-
178	14 15 04.70	+46 34 28.97	G	0.220 ± 0.029§	332	1.22	129 ± 26	0.18 ± 0.07	0.65 ± 0.09	II	18.13 ± 0.01	-
179	14 15 54.37	+49 09 21.15	Q	1.37310 ± 0.00037†	111	0.96	141 ± 28	14.40 ± 2.93	0.82 ± 0.09	II	19.03 ± 0.01	2
180	14 16 06.64	+47 09 27.72	G	0.534 ± 0.131§	117	0.76	3 ± 1	0.03 ± 0.02	<0.51	II	20.30 ± 0.07	-
181	14 16 25.89	+54 25 45.85	G	0.24474 ± 0.00005†	336	1.33	797 ± 159	1.59 ± 0.32	1.20 ± 0.09	II	18.02 ± 0.01	-
182	14 18 03.59	+48 36 04.61	G	0.51396 ± 0.00019†	134	0.86	2 ± 1	0.03 ± 0.01	<1.46	II	20.35 ± 0.04	-
183	14 18 05.89	+45 49 06.66	G	0.85825 ± 0.00024†	142	1.13	129 ± 26	4.50 ± 0.91	0.88 ± 0.10	II	22.02 ± 0.17	-
184	14 19 35.98	+48 37 43.22	Q	0.49599 ± 0.00006†	127	0.79	552 ± 110	4.77 ± 0.96	0.65 ± 0.09	II	19.11 ± 0.03	-
185	14 20 56.84	+53 13 07.45	G	0.74211 ± 0.00010†	101	0.76	153 ± 31	4.19 ± 0.84	1.06 ± 0.09	II	19.82 ± 0.02	-
186	14 21 22.63	+48 55 22.82	G	0.47680 ± 0.00008†	124	0.76	661 ± 132	5.82 ± 1.17	0.93 ± 0.09	II	19.79 ± 0.03	-
187	14 23 14.59	+47 51 26.99	G	0.666 ± 0.110§	197	1.42	122 ± 24	2.18 ± 0.98	-	II	20.74 ± 0.06	-
188	14 25 36.30	+53 12 48.03	Q	0.91084 ± 0.00020†	139	1.12	97 ± 20	3.61 ± 0.73	-	II	19.35 ± 0.01	-
189	14 26 03.30	+51 29 37.38	G	0.41955 ± 0.15104*	138	0.78	471 ± 94	3.01 ± 2.63	0.88 ± 0.09	II	22.88 ± 0.30	-
190	14 27 42.22	+47 18 47.17	G	0.81534 ± 0.00045†	115	0.90	16 ± 3	0.36 ± 0.07	0.41 ± 0.11	II	21.72 ± 0.16	-
191	14 28 57.40	+54 23 52.99	G	0.40573 ± 0.00011†	127	0.71	66 ± 13	0.40 ± 0.08	0.97 ± 0.11	II	18.54 ± 0.02	-
192	14 28 57.66	+54 36 27.81	G	0.38148 ± 0.00012†	200	1.08	251 ± 50	1.46 ± 0.29	1.27 ± 0.11	II	19.16 ± 0.02	-
193	14 29 14.03	+46 56 11.32	G	0.77764 ± 0.00027†	130	0.99	20 ± 4	0.43 ± 0.09	0.45 ± 0.10	III	21.93 ± 0.12	-
194	14 29 33.45	+54 43 35.29	G	0.12328 ± 0.00002†	452	1.03	797 ± 159	0.32 ± 0.06	0.70 ± 0.09	II	15.89 ± 0.00	-
195	14 29 46.05	+51 09 58.42	G	0.687 ± 0.161§	280	2.04	530 ± 106	12.50 ± 7.58	1.14 ± 0.09	II	21.90 ± 0.14	-
196	14 30 45.29	+45 46 33.57	G	0.393 ± 0.042§	140	0.77	133 ± 27	0.72 ± 0.23	0.83 ± 0.09	II	19.76 ± 0.02	-
197	14 30 45.65	+50 27 10.84	G	0.544 ± 0.058§	110	0.72	109 ± 22	1.22 ± 0.40	0.75 ± 0.09	II	20.06 ± 0.05	-
198	14 31 36.99	+52 27 24.90	G	0.29198 ± 0.00007†	186	0.84	371 ± 74	0.97 ± 0.19	0.62 ± 0.09	II	17.57 ± 0.01	-
199	14 31 41.21	+47 44 35.15	Q	1.17148 ± 0.00052†	91	0.77	205 ± 41	13.70 ± 2.78	-	II	20.77 ± 0.04	-
200	14 33 44.95	+48 08 19.45	G	0.69759 ± 0.00023†	108	0.79	350 ± 70	7.21 ± 1.45	0.82 ± 0.09	II	21.63 ± 0.13	-
201	14 34 41.85	+48 03 40.54	Q	1.61238 ± 0.00041†	124	1.08	147 ± 29	20.60 ± 4.21	-	II	20.96 ± 0.04	-
202	14 35 10.3	+49 48 19.49	Q	0.16606 ± 0.00005†	348	1.02	71 ± 14	0.05 ± 0.01	0.44 ± 0.09	II	17.14 ± 0.00	10
203	14 37 16.47	+46 30 28.39	G	0.683 ± 0.081§	222	1.62	44 ± 9	0.83 ± 0.29	0.73 ± 0.11	III	21.16 ± 0.09	-
204	14 37 30.77	+53 35 42.42	G	0.50279 ± 0.00015†	123	0.78	236 ± 47	2.39 ± 0.48	0.96 ± 0.09	II	20.18 ± 0.04	-
205	14 37 37.66	+51 44 46.45	G	0.49518 ± 0.21509*	207	1.30	244 ± 49	2.35 ± 2.48	0.93 ± 0.09	II	21.42 ± 0.07	-
206	14 38 04.03	+46 50 51.20	G	0.74546 ± 0.00023†	115	0.87	8 ± 2	0.17 ± 0.04	0.57 ± 0.16	II	21.17 ± 0.10	-
207	14 40 07.85	+55 27 06.08	G	0.58442 ± 0.06106*	238	1.62	93 ± 19	1.19 ± 0.38	0.69 ± 0.10	II	20.93 ± 0.06	-
208	14 40 13.98	+50 26 01.87	Q	1.57000 ± 0.00108†	143	1.24	136 ± 27	22.00 ± 4.49	0.96 ± 0.10	II	20.65 ± 0.05	-
209	14 40 17.49	+53 26 20.29	G	0.52672 ± 0.00013†	195	1.26	348 ± 70	3.60 ± 0.72	-	II	20.13 ± 0.04	-
210	14 42 15.00	+47 06 46.09	G	0.44503 ± 0.00011†	121	0.71	197 ± 39	1.33 ± 0.27	0.65 ± 0.09	II	19.85 ± 0.03	-

Table 3.2: continued.

Sr.No	RA (HMS)	Dec (DMS)	Class	z	Size ($''$)	Size (Mpc)	S_{144MHz} (mJy)	P_{144MHz} (10^{26}W Hz^{-1})	α_{144}^{1400}	FR Type	r Mag	Ref
(1)	(2)	(3)	(4)	(5)	(6)	(7)	(8)	(9)	(10)	(11)	(12)	(13)
211	14 42 58.59	+52 09 02.07	G	0.272 ± 0.057§	289	1.24	824 ± 165	1.94 ± 1.02	0.88 ± 0.09	II	17.88 ± 0.01	-
212	14 43 08.22	+51 18 10.01	G	0.46603 ± 0.00011†	152	0.92	7 ± 1	0.06 ± 0.01	<1.10	II	19.63 ± 0.03	-
213	14 43 32.79	+45 46 54.56	G	0.60401 ± 0.00023†	117	0.81	44 ± 9	0.59 ± 0.12	0.61 ± 0.10	II	20.44 ± 0.07	-
214	14 44 07.52	+49 07 30.78	Q	0.91579 ± 0.00009†	193	1.55	175 ± 35	7.59 ± 1.53	0.97 ± 0.09	II	22.01 ± 0.15	-
215	14 44 10.50	+55 47 45.64	G	0.33475 ± 0.00005†	144	0.71	542 ± 108	1.97 ± 0.39	0.72 ± 0.09	II	18.15 ± 0.01	-
216	14 44 58.09	+53 09 29.6	G	0.38228 ± 0.13684★	167	0.90	184 ± 37	0.82 ± 0.71	0.44 ± 0.09	III	19.47 ± 0.03	-
217	14 45 20.87	+54 03 29.62	G	0.43345 ± 0.00013†	162	0.94	127 ± 26	0.81 ± 0.16	0.66 ± 0.09	II	18.72 ± 0.02	-
218	14 46 07.20	+48 41 37.79	G	0.37676 ± 0.00006†	146	0.78	174 ± 35	0.87 ± 0.17	0.89 ± 0.09	II	19.10 ± 0.02	-
219	14 46 48.98	+47 36 31.43	G	0.584 ± 0.052§	274	1.86	59 ± 12	0.74 ± 0.22	0.66 ± 0.11	II	20.48 ± 0.05	-
220	14 47 25.82	+56 37 50.13	G	0.71650 ± 0.00025†	105	0.78	12 ± 3	0.23 ± 0.05	<0.50	III	21.32 ± 0.09	-
221	14 50 02.36	+54 05 28.27	G	0.549 ± 0.076§	126	0.83	507 ± 101	5.78 ± 2.26	-	II	20.51 ± 0.05	-
222	14 50 57.28	+53 00 07.76	Q	0.91800 ± 0.00008†	184	1.48	1407 ± 281	56.50 ± 11.40	0.84 ± 0.09	II	20.59 ± 0.04	-
223	14 51 06.41	+53 33 53.84	Q	0.43220 ± 0.00007†	246	1.43	267 ± 53	1.78 ± 0.36	0.80 ± 0.09	II	18.64 ± 0.01	2
224	14 51 16.59	+51 13 33.28	G	0.509 ± 0.050§	194	1.23	99 ± 20	0.95 ± 0.29	-	II	19.92 ± 0.05	-
225	14 51 21.28	+56 08 35.45	G	0.525 ± 0.073§	208	1.34	57 ± 12	0.57 ± 0.22	0.68 ± 0.10	II	20.73 ± 0.06	-
226	14 52 50.73	+51 37 01.90	G	0.652 ± 0.126§	108	0.77	51 ± 10	0.97 ± 0.50	1.00 ± 0.14	II	21.64 ± 0.11	-
227	14 57 02.81	+48 06 46.64	G	0.26738 ± 0.00007†	168	0.71	5 ± 1	0.01 ± 0.00	<1.11	II	18.00 ± 0.01	-
228	14 57 49.59	+50 45 59.62	G	0.628 ± 0.146§	199	1.40	55 ± 11	0.90 ± 0.54	0.88 ± 0.11	II	21.58 ± 0.11	-
229	15 00 00.56	+50 43 55.62	G	0.415 ± 0.087§	142	0.80	12 ± 2	0.07 ± 0.04	<0.83	II	19.70 ± 0.03	-
230	15 01 32.11	+50 34 55.14	G	0.32062 ± 0.00007†	164	0.79	32 ± 6	0.10 ± 0.02	0.73 ± 0.11	II	17.66 ± 0.01	-
231	15 01 48.47	+52 10 47.16	G	0.492 ± 0.058§	145	0.91	10 ± 2	0.09 ± 0.03	0.67 ± 0.16	II	19.68 ± 0.04	-
232	15 03 33.65	+48 11 17.67	G	0.672 ± 0.095§	111	0.80	80 ± 16	1.81 ± 0.72	1.16 ± 0.13	II	21.52 ± 0.11	-
233	15 04 45.61	+50 30 08.57	G	0.65227 ± 0.05463★	201	1.44	1295 ± 259	23.90 ± 6.83	0.91 ± 0.09	II	21.89 ± 0.17	-
234	15 06 12.81	+51 37 07.11	G	0.61121 ± 0.00010†	262	1.82	574 ± 115	8.38 ± 1.69	-	II	20.25 ± 0.05	-
235	15 06 24.10	+53 55 02.61	G	0.30437 ± 0.00005†	184	0.85	118 ± 24	0.33 ± 0.07	0.57 ± 0.09	II	17.95 ± 0.01	-
236	15 18 30.19	+51 58 17.03	G	0.708 ± 0.168§	105	0.78	51 ± 10	1.17 ± 0.72	0.95 ± 0.11	II	21.84 ± 0.13	-
237	15 18 35.37	+51 04 10.70	G	0.619 ± 0.138§	119	0.83	371 ± 74	5.63 ± 3.25	0.77 ± 0.09	II	21.14 ± 0.08	-
238	15 18 45.36	+52 37 08.56	G	0.52105 ± 0.00011†	110	0.71	312 ± 62	3.66 ± 0.73	1.11 ± 0.09	II	20.24 ± 0.05	-
239	15 23 11.09	+52 03 03.52	Q	0.51667 ± 0.00010†	132	0.84	382 ± 77	4.35 ± 0.87	1.09 ± 0.09	II	20.74 ± 0.06	-

(1) Amirkhanyan et al. (2015); (2) Amirkhanyan (2016); (3) Cotter et al. (1996); (4) Koziel-Wierzbowska & Stasinska (2012); (5) Machalski (1998); (6) Machalski et al. (2001); (7) Nilsson (1998) ; (8) Rentería Macario & Andernach (2017) ; (9) Thwala et al. (2019) ; (10) Kuźmicz et al. (2018)

Table 3.3: LoTSS GRGs in galaxy clusters: Parameters r_{200} and R_{L*} (cluster richness parameter) have been taken from the WHL galaxy cluster catalogue and M_{200} has been computed from Eq.2 of Wen et al. (2012). GRGs marked with † in the redshift column have photometric redshift estimate and the rest have spectroscopic redshifts. r_{200} is the radius within which the mean density of a cluster is 200 times of the critical density of the Universe, and M_{200}, is the mass of the cluster within r_{200}. N_{200} is the number of galaxies within r_{200}. Clusters 6, 7 and 20 are identified from GMBCG cluster catalogue (Hao et al. 2010).

No	Cluster Name	GRG RA	GRG Dec	z	r_{200}	R_{L*}	M_{200}	N_{200}
					(Mpc)		(10^{14} $M_{\odot}$)	
1	WHLJ112126.4+534457	11 21 26.44	+53 44 56.71	0.10378 ± 0.00002	1.7	69.4	4.6	46
2	WHLJ113250.7+505705	11 32 50.67	+50 57 04.68	0.35857 ± 0.00010	0.9	16.9	0.9	14
3	WHLJ113503.2+482612	11 35 03.20	+48 26 12.12	0.22597 ± 0.00006	1.1	21.7	1.2	17
4	WHLJ121900.8+505255	12 19 00.76	+50 52 54.41	0.38509 ± 0.00008	0.9	17.3	0.9	14
5	GMBCG J188.75636+53.29864	12 35 01.52	+53 17 55.09	0.34480 ± 0.00030	-	-	-	-
6	GMBCG J191.35486+47.11948	12 45 25.16	+47 07 10.11	0.51179 ± 0.00015	-	-	-	-
7	WHLJ124913.2+500044	12 49 13.20	+50 00 43.68	0.34956 ± 0.00010	1.1	25.3	1.4	30
8	WHL J125142.1+503425	12 51 42.04	+50 34 24.65	0.54904 ± 0.00007	1.1	24.3	1.4	11
9	WHL J131404.6+543938	13 14 04.60	+54 39 37.88	0.34645 ± 0.00008	1.2	26.1	1.5	23
10	WHLJ132229.1+504845	13 22 29.07	+50 48 44.53	0.18439 ± 0.00004	0.9	15.9	0.8	11
11	WHLJ133258.3+535356	13 32 58.28	+53 53 55.60	0.32261 ± 0.00009	0.9	16.6	0.9	13
12	WHLJ133512.0+494427	13 35 12.01	+49 44 27.20	0.436 ± 0.041†	0.9	14.7	0.7	9
13	WHLJ133618.8+533952	13 36 18.75	+53 39 52.12	0.30138 ± 0.00006	0.9	13.4	0.7	11
14	WHLJ134207.0+472553	13 42 06.98	+47 25 53.04	0.17213 ± 0.00004	0.9	13.2	0.7	13
15	WHLJ142857.4+542353	14 28 57.40	+54 23 52.99	0.40573 ± 0.00011	1.2	30.7	1.8	22
16	WHLJ142933.4+544336	14 29 33.45	+54 43 35.29	0.12328 ± 0.00002	1.3	34.7	2.0	29
17	WHLJ144410.5+554746	14 44 10.50	+55 47 45.64	0.33475 ± 0.00005	1.2	30.1	1.7	26
18	WHLJ144520.9+540330	14 45 20.87	+54 03 29.62	0.43345 ± 0.00013	1.0	25.1	1.4	18
19	GMBCG J222.81919+51.22588	14 51 16.59	+51 13 33.28	0.509 ± 0.050†	-	-	-	-
20	WHLJ150624.1+535503	15 06 24.10	+53 55 02.61	0.30437 ± 0.00005	1.0	19.1	1.0	11

3.6 Supplementary material

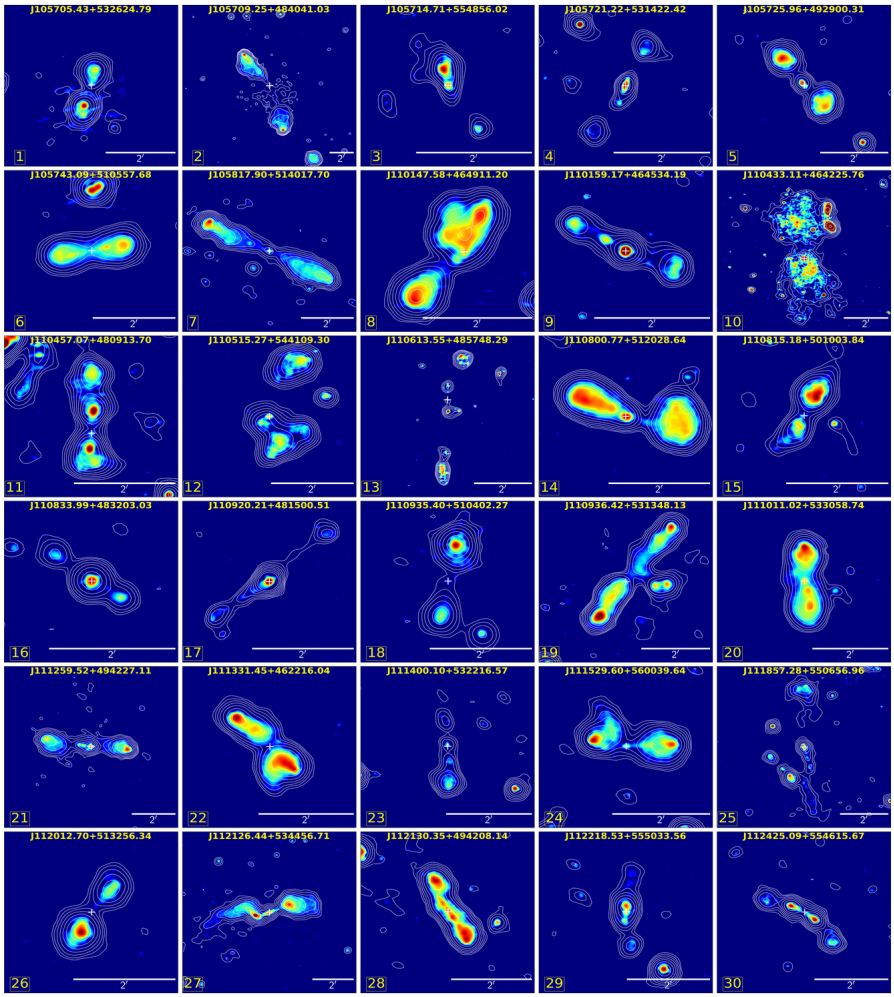

Figure 3.15: LoTSS high resolution (∼6 ″) images 1-30 with LoTSS low resolution (∼20 ″) contours overlaid. The cross '+' marker indicates the location of the host galaxy.The radio contours are drawn with 8 levels which are chosen by equally (log scale) dividing the data value range above $\sim 3\sigma$, where σ is the local RMS of the map.

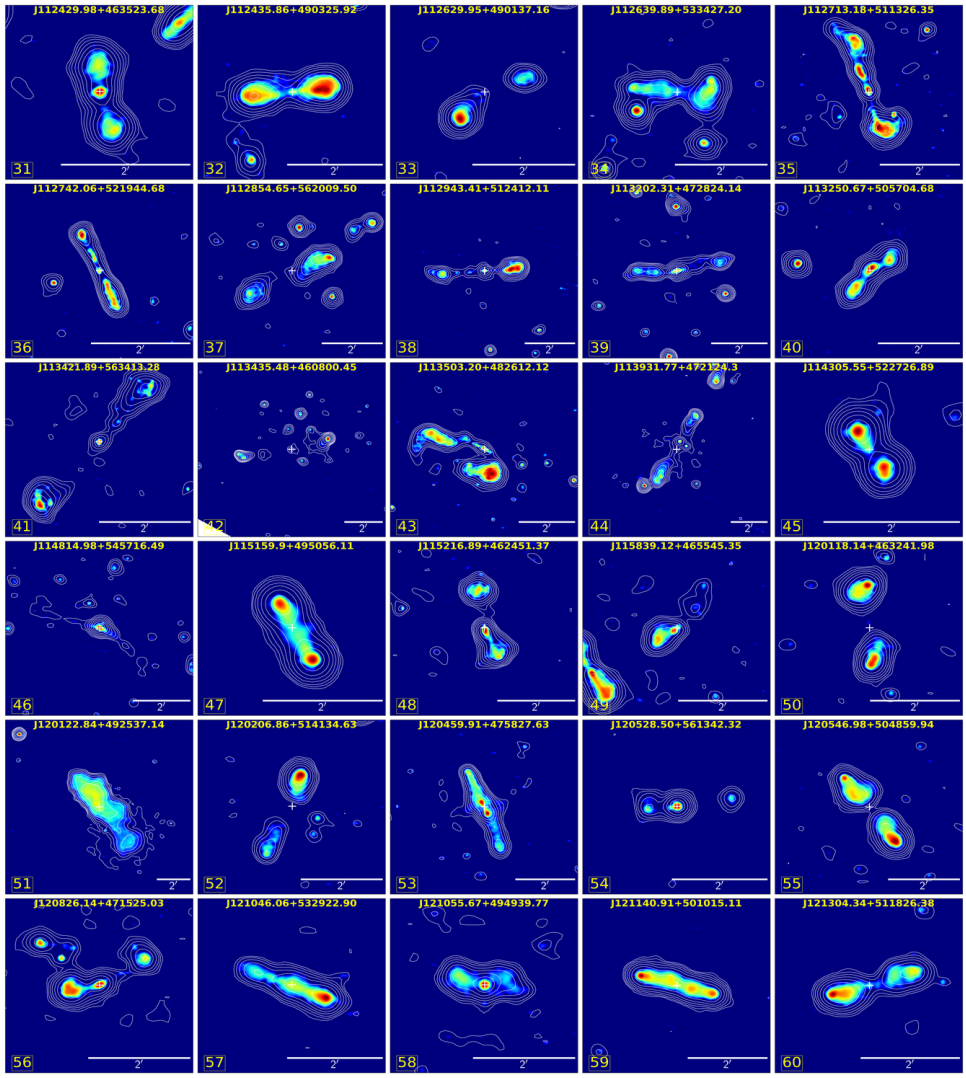

Figure 3.16: LoTSS high resolution (~ 6 ″) images 31-60 with LoTSS low resolution (~ 20 ″) contours overlaid.The cross '+' marker indicates the location of the host galaxy. The radio contours are drawn with 8 levels which are chosen by equally (log scale) dividing the data value range above $\sim 3\sigma$, where σ is the local RMS of the map.

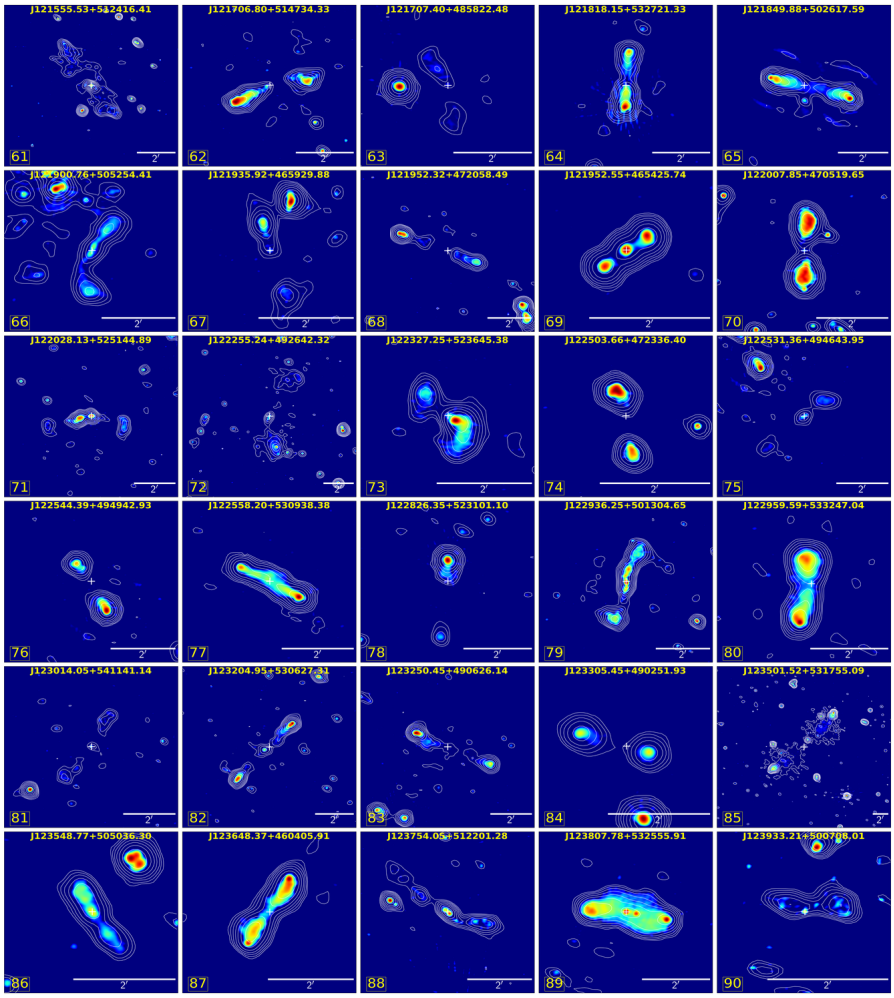

Figure 3.17: LoTSS high resolution (∼ 6 ″) images 61-90 with LoTSS low resolution (∼ 20 ″) contours overlaid. The cross '+' marker indicates the location of the host galaxy. The radio contours are drawn with 8 levels which are chosen by equally (log scale) dividing the data value range above $\sim 3\sigma$, where σ is the local RMS of the map.

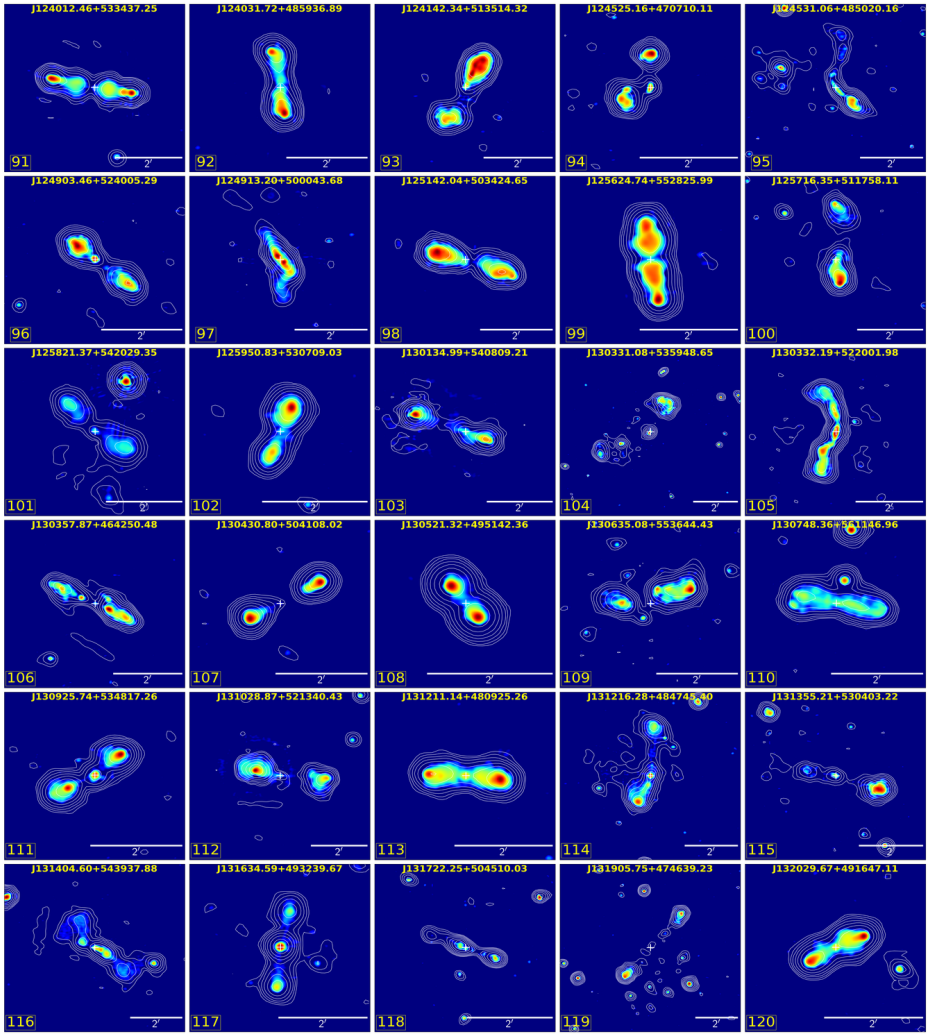

Figure 3.18: LoTSS high resolution (~ 6 ″) images 91-120 with LoTSS low resolution (~ 20 ″) contours overlaid. The cross '+' marker indicates the location of the host galaxy. The radio contours are drawn with 8 levels which are chosen by equally (log scale) dividing the data value range above $\sim 3\sigma$, where σ is the local RMS of the map.

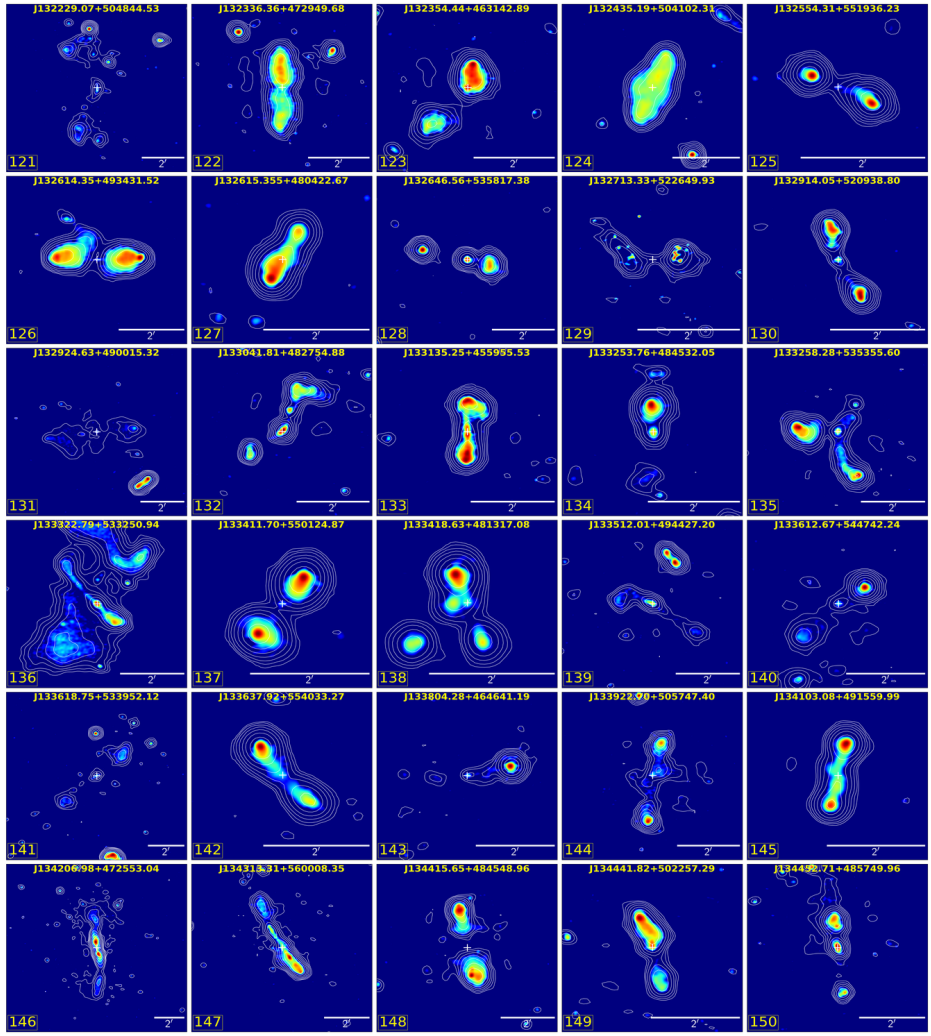

Figure 3.19: LoTSS high resolution (~ 6 ″) images 121-150 with LoTSS low resolution (~ 20 ″) contours overlaid. The cross '+' marker indicates the location of the host galaxy. The radio contours are drawn with 8 levels which are chosen by equally (log scale) dividing the data value range above $\sim 3\sigma$, where σ is the local RMS of the map.

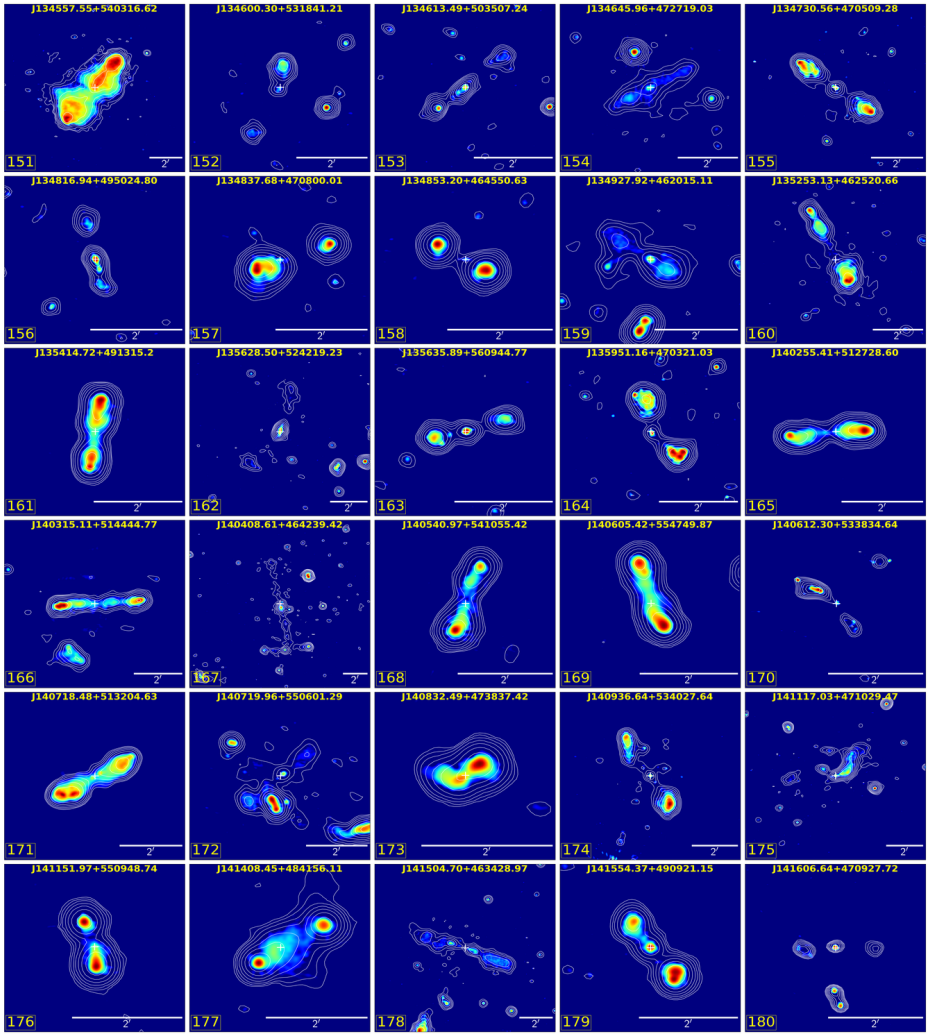

Figure 3.20: LoTSS high resolution (~ 6 ″) images 151-180 with LoTSS low resolution (~ 20 ″) contours overlaid. The cross '+' marker indicates the location of the host galaxy. The radio contours are drawn with 8 levels which are chosen by equally (log scale) dividing the data value range above $\sim 3\sigma$, where σ is the local RMS of the map.

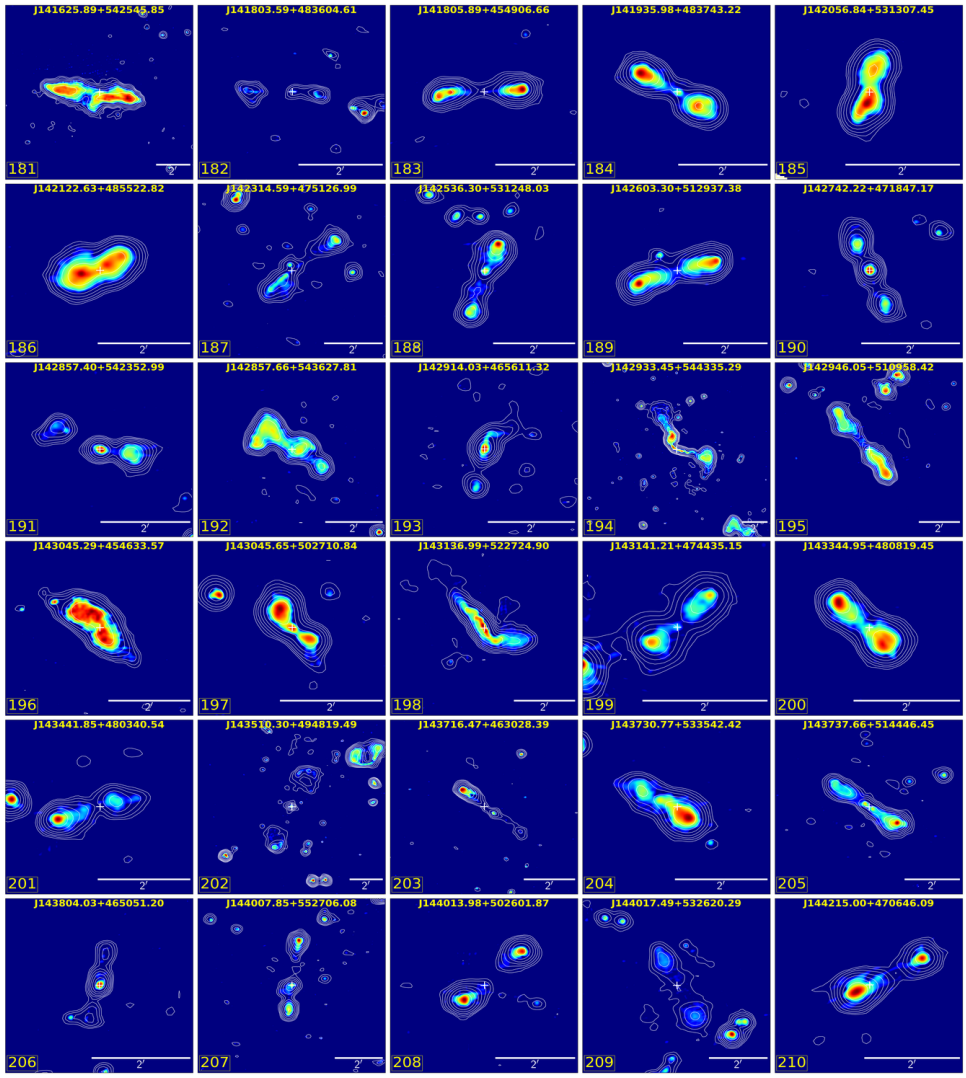

Figure 3.21: LoTSS high resolution (~ 6 ″) images 181-210 with LoTSS low resolution (~ 20 ″) contours overlaid. The cross '+' marker indicates the location of the host galaxy. The radio contours are drawn with 8 levels which are chosen by equally (log scale) dividing the data value range above $\sim 3\sigma$, where σ is the local RMS of the map.

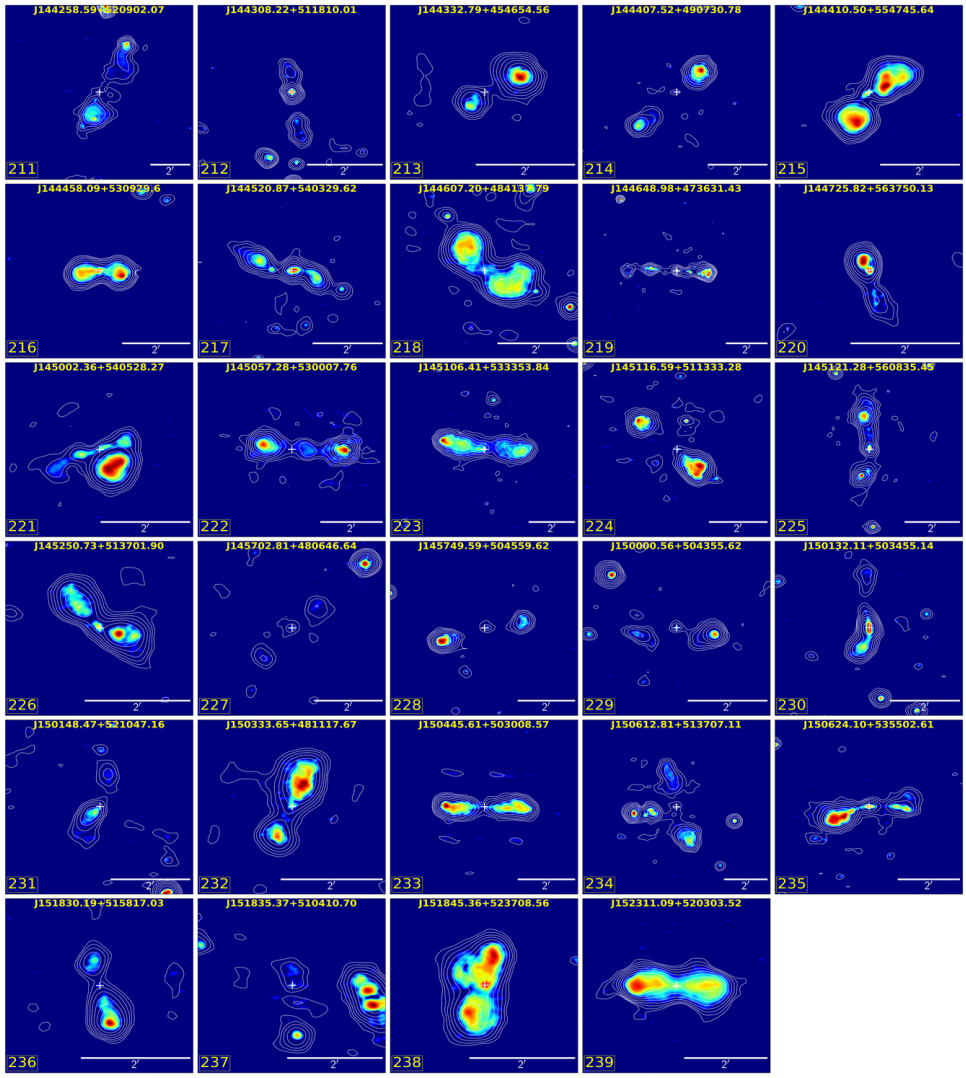

Figure 3.22: LoTSS high resolution (~ 6 ″) images 211-239 with LoTSS low resolution (~ 20 ″) contours overlaid. The cross '+' marker indicates the location of the host galaxy. The radio contours are drawn with 8 levels which are chosen by equally (log scale) dividing the data value range above $\sim 3\sigma$, where σ is the local RMS of the map.

4 | Chapter 4 : SAGAN. I. New sample and multi-wavelength studies

We present the first results of a project called SAGAN, which is dedicated solely to the studies of relatively rare megaparsec-scale radio galaxies in the Universe, called giant radio galaxies (GRGs). We have identified 162 new GRGs primarily from the NRAO VLA Sky Survey (NVSS) with sizes ranging from ∼0.71 Mpc to ∼2.82 Mpc in the redshift range of ∼0.03 - 0.95, of which 23 are hosted by quasars (giant radio quasars, GRQs). As part of the project SAGAN, we have created a database of all known GRGs, the GRG catalogue, from the literature (including our new sample); it includes 820 sources. For the first time, we present the multi-wavelength properties of the largest sample of GRGs. This provides new insights into their nature. Our results establish that the distributions of the radio spectral index and the black hole mass of GRGs do not differ from the corresponding distributions of normal-sized radio galaxies (RGs). However, GRGs have a lower Eddington ratio than RGs. Using the mid-infrared data, we classified GRGs in terms of their accretion mode: either a high-power radiatively efficient high-excitation state, or a radiatively inefficient low-excitation state. This enabled us to compare key physical properties of their active galactic nuclei, such as the black hole mass, spin, Eddington ratio, jet kinetic power, total radio power, magnetic field, and size. We find that GRGs in high-excitation state statistically have larger sizes, stronger radio power, jet kinetic power, and higher Eddington ratio than those in low-excitation state. Our analysis reveals a strong correlation between the black hole Eddington ratio and the scaled jet kinetic power, which suggests a disc-jet coupling. Our environmental study reveals that ∼10% of all GRGs may reside at the centres of galaxy clusters, in a denser galactic environment, while the majority appears to reside in a sparse environment. The probability of finding the brightest cluster galaxy (BCG) as a GRG is quite low and even lower for high-mass clusters. We present new results for GRGs that range from black hole mass to large-scale environment properties. We discuss their formation and growth scenarios, highlighting the key physical factors that cause them to reach their gigantic size.

P. Dabhade, M. Mahato, J. Bagchi, D. J. Saikia, F. Combes, S. Sankhyayan H. J. A. Röttgering, L. C. Ho, M. Gaikwad, S. Raychaudhury, B. Vaidya, and B. Guiderdoni, 2020, A&A, 642, A153
DOI: 10.1051/0004-6361/202038344

4.1 Introduction

In the 1950s, it was revealed that some galaxies dominantly emit at radio wavelengths (Jennison & Das Gupta 1953; Baade & Minkowski 1954) through synchrotron radiation (Shklovskii 1955; Burbidge 1956). These galaxies later came to be known as radio galaxies (RGs), whose radio emission often extends well beyond the physical extent of the galaxies as seen at optical wavelengths. Thereafter, it was realised by theoretical efforts (Salpeter 1964; Lynden-Bell 1969; Bardeen 1970) that a supermassive black hole (10^6 - 10^{10} $M_\odot$) residing at the centre of host galaxy must be responsible for powering (Rees 1971) the radio galaxy through twin collimated and relativistic jets (Blandford & Rees 1974; Scheuer 1974). The creation of the relativistic radio jets is not completely understood and is currently under investigation. Astrophysical models (Blandford & Znajek 1977; hereafter B-Z, Blandford & Payne 1982; Meier et al. 2001) show that they are created by mass-accreting black holes with a certain geometry of the magnetic field that threads the accretion disc.

The B-Z model describes the process that is thought to be responsible for powering jets in galactic microquasars and gamma-ray bursts in addition to radio galaxies and quasars. It has been established in many studies over the years that supermassive black holes (SMBHs) reside at the centres of almost all massive galaxies (Soltan 1982; Rees 1984; Begelman et al. 1984; Magorrian et al. 1998; Kormendy & Ho 2013), and their active phase is triggered only under certain circumstances. These active forms of SMBHs are known as the active galactic nuclei (AGNs), whose signatures can be observed at almost all wavelengths, ranging from radio to gamma-rays.

Those AGNs that predominantly emit at radio wavelengths are called radio-loud AGNs (RLAGNs). A smaller fraction and more powerful class of AGNs are quasars, which are among the most energetic and brightest objects known in the Universe. When quasar AGNs emit radiation at radio wavelengths, they are called radio-loud quasars (RQs). In high-luminosity RGs or RQs, the jets tend to terminate in high-brightness regions, called hotspots, at the outer edges of the radio lobes, which are filled with relativistic non-thermal plasma. This class of RGs is the Fanaroff-Riley II (FR-II) class (Fanaroff & Riley 1974). FR-IIs are edge-brightened RGs, and the Fanaroff-Riley I (FR-I) class RGs are less powerful than FR-II. The FR-I structure is mainly edge-darkened and lobe brightness peaks within the inner half of their extent; they have no hotspot. The largest angular size is usually measured between the peaks in the hotspots for FR-II sources

and the outermost contours at the 3σ level for FR-I sources. The projected linear size of RGs or RQs extends from less than a few kilo parsecs (pc) to several megaparsecs (Mpc).

In the past six decades, thousands of RGs have been found and catalogued, but only a few hundred RGs have been discovered so far to exhibit Mpc-scale sizes. Since their discovery in the 1970s by Willis et al. (1974), this relatively rare sub-class of RGs has been referred to by several names, such as 'giant radio sources' (GRSs), 'large radio galaxies' (LRGs), and 'giant radio galaxies' (GRGs). In order to avoid confusion and to maintain uniformity, we refer to this giant sub-class of RGs as 'giant radio galaxies' (GRGs), as previously adopted in several works (Schoenmakers et al. 2001; Dabhade et al. 2017; Ursini et al. 2018; Dabhade et al. 2020b).

Since the discovery of GRGs in the 1970s to early-2000s, the Hubble constant (H_0) that is used to derive the physical properties of the GRGs had a range of values between 50 to 100 km s^{-1} Mpc^{-1} based on available measurements at that time. This led to over- or under-estimating the sizes of these sources and eventually to inaccurate statistics of their population. With the advent of precision cosmology derived from the cosmic microwave background radiation observed with the Wilkinson Microwave Anisotropy Probe (WMAP; Hinshaw et al. 2013) and Planck mission (Planck Collaboration et al. 2016), the value of H_0 was set to ~ 68 km s^{-1} Mpc^{-1}. The first GRGs discovered by Willis et al. (1974) were 3C236 and DA240, both of which are more than 2 Mpc in size, and hence they did not set a lower size limit for RGs to be classified as GRGs. Later studies (Ishwara-Chandra & Saikia 2000; Schoenmakers et al. 2001) adopted a lower limit of 1 Mpc, assuming H_0 to 50 km s^{-1} Mpc^{-1}. Recent studies (Dabhade et al. 2017; Kuźmicz et al. 2018; Ursini et al. 2018; Dabhade et al. 2020b) have adopted 700 kpc as the lower size limit of GRGs with the updated H_0 value obtained from observations.

In the past six decades, owing to radio surveys such as the third Cambridge radio survey (3CR; Bennett 1962; Laing et al. 1983), the Bologna Survey (B2; Colla et al. 1970), the Faint Images of the Radio Sky at Twenty-Centimeters survey (FIRST; Becker et al. 1995), the NRAO VLA Sky Survey (NVSS; Condon et al. 1998), the Westerbork Northern Sky Survey (WENSS; Rengelink et al. 1997), the Sydney University Molonglo Sky Survey (SUMSS; Bock et al. 1999), the TIFR GMRT Sky Survey (TGSS; Intema et al. 2017), and the LOFAR Two-metre Sky Survey (LoTSS; Shimwell et al. 2019), millions of RGs have been found, and a considerable fraction has been studied in detail. However, only a few hundred of these RGs have

been identified as giants or GRGs. The relatively small number of GRGs might partly be due to difficulties in identifying them. Possible factors include the detection of low surface brightness components, ensuring that two radio components are indeed related, and finding confirmed optical counterparts. However, when we take a complete radio sample such as the 3CRR sample (Laing et al. 1983), the median size* of the RGs or RQs is ∼350 kpc, and only ∼7% of the sample are GRGs.

Over a course of about 45 years, about 40 research papers (Willis et al. 1974; Bridle et al. 1976; Waggett et al. 1977; Laing et al. 1983; Kronberg et al. 1986; de Bruyn 1989; Jones 1989; Ekers et al. 1989; Lacy et al. 1993; Law-Green et al. 1995; Cotter et al. 1996; McCarthy et al. 1996; Subrahmanyan et al. 1996; Ishwara-Chandra & Saikia 1999; Lara et al. 2001a; Machalski et al. 2001; Schoenmakers et al. 2001; Sadler et al. 2002; Letawe et al. 2004; Saripalli et al. 2005; Saikia et al. 2006; Machalski et al. 2007c; Huynh et al. 2007; Machalski et al. 2008; Koziel-Wierzbowska & Stasinska 2012; Hota et al. 2011; Solovyov & Verkhodanov 2014; Molina et al. 2014; Bagchi et al. 2014; Amirkhanyan et al. 2015; Tamhane et al. 2015; Amirkhanyan 2016; Dabhade et al. 2017; Clarke et al. 2017; Kapińska et al. 2017; Prescott et al. 2018; Sebastian et al. 2018; Kuźmicz et al. 2018; Kozieł-Wierzbowska et al. 2020; Dabhade et al. 2020b) have reported about 662 GRGs spread throughout the sky. This estimate is based on a database of GRGs that is compiled by us, for which we adopted 700 kpc as the lower limit of GRG size. We used concordant cosmological parameters from Planck ($H_0 = 67.8$ km s^{-1} Mpc^{-1}, $\Omega_m = 0.308$, $\Omega_\Lambda = 0.692$; Planck Collaboration et al. 2016).

Some of the open questions related to GRGs are the processes through which they grow to Mpc-scale sizes, how rare they are with respected normal radio galaxies, do they host most powerful SMBHs, nature of their accretion states, and how fast their SMBHs are spinning. Owing to their enormous sizes, it essential to investigate whether they grow only in sparser environments, and their contribution to large-scale processes.

Giant radio galaxies are the largest single objects in the Universe. They pose interesting questions related to the formation and evolution of such large structures through relativistic jets that originate in SMBHs. These large RGs must be supplied with energy either continuously or quasi-continuously over timescales of at least 10^7 - 10^8 years when we consider that the hotspots (terminal shocks of the jet) move with sub-relativistic speeds (Best et al. 1995; Scheuer 1995; Arshakian & Longair 2000) of ∼

*https://3crr.extragalactic.info/

0.1c, although highly asymmetric sources such as the apparently one-sided GRGs may require higher velocities (Saikia et al. 1990). It has been suggested that their evolution to such large sizes is due to their occurrence in low-density environments (Mack et al. 1998; Pirya et al. 2012; Malarecki et al. 2015; Saripalli & Malarecki 2015). Pirya et al. (2012) found that GRGs are usually located in low galaxy density environments by counting galaxies in the vicinity of GRGs. However, the structural asymmetries in their sample of giants, in which the nearer component is often brighter, suggest asymmetries in the intergalactic medium that are not apparent from examining the galaxy distribution. Only in the case of 3C326 did they find the closer brighter arm to be possibly interacting with a group of galaxies that is part of a larger filamentary structure. Machalski et al. (2008) reported the discovery of the largest GRG J1420-0545 and suggested that the source is located in a very low-density environment and has a high expansion speed along the jet axis. However, a few studies, such as Komberg & Pashchenko (2009) and Dabhade et al. (2017, 2020b), have shown dozens of GRGs residing in dense cluster environments. A few other studies (Subrahmanyan et al. 1996; Saripalli et al. 2005; Bruni et al. 2019, 2020) have also suggested that GRGs may attain their gigantic size due to the restarted AGN activity. Different explanations may be applicable to different subsets of GRGs, which detailed studies of large samples and comparisons with theoretical models and simulations will help clarify (e.g. Hardcastle (2018b) and references therein).

It has also been suggested that GRGs contain exceptionally powerful central engines that are powered by massive black holes, which are responsible for their gigantic sizes (Gopal-Krishna et al. 1989). Based on the current understanding, the environment alone therefore cannot be the only determining factor for the giant size of GRGs, but a combination of AGN power (including jet power and accretion states), environmental factors, and the longevity of AGN activity (duty cycle) might be playing an equally important role.

Moreover, multi-wavelength studies of only a small fraction of GRGs have been carried out so far to specifically address the important questions related to their unusual nature. This has restricted a comprehensive statistical analysis of the properties of GRGs to understand their true nature.

In order to address these questions in a systematic study of a large number of GRGs, we have initiated a project that is completely dedicated to the study of GRGs, We describe this in the following parts of this paper along with our first results. For the first time, we have been able to obtain

a good understanding of the GRG astrophysics here, spanning an enormous range ($\sim 10^{11}$) of physical scales from $\sim 10^{-5}$ pc in the jet launch zone that lies in the vicinity of the black hole to $\sim$1 Mpc, where the jet termination point is located.

The paper is organised as follows: In Sec. 4.2 we present an overview and the goals of project SAGAN. In Sec. 4.2.1 we describe the search criteria and method for identifying the new GRG sample from the NVSS survey, followed by a discussion of the newly created GRG database in Sec. 4.2.2. In Sec. 4.3 we describe the analysis methods we employed on multi-wavelength data of GRGs to estimate their various properties. Next, we present the results of the analysis along with a discussion and their implications in Sec. 4.4, which is further sub-divided into several subsections, each dedicated to a property of GRGs. We conclude our study of GRGs in project SAGAN and outline its future prospects in Sec. 4.7. Lastly, in Appendix 4.8 we present three main tables consisting of the properties of our new GRG sample, and in Appendix 4.10 we show the multi-frequency radio maps of the GRGs in our new sample.

Throughout this paper, the flat ΛCDM cosmological model is adopted based on the Planck results ($H_0 = 67.8$ km s^{-1} Mpc^{-1}, $\Omega_m = 0.308$, and $\Omega_\Lambda = 0.692$ Planck Collaboration et al. 2016). All the images are presented in a J2000 coordinate system. We use the convention $S_\nu \propto \nu^{-\alpha}$, where S_ν is the flux density at frequency ν, and α is the spectral index.

4.2 Project SAGAN

To understand the physics of these extreme cosmic radio sources much better, and specifically, to address the key questions that remain, we have initiated a project called SAGAN* (Search and analysis of GRGs with associated nuclei), whose pilot study results were presented in the previous paper (Dabhade et al. 2017). Some of the main goals for this project are listed below.

1. We aim to create a complete and uniform database of GRGs from the literature, which spans five decades starting from 1970s, using a single cosmological model with $H_0 = 67.8$ km s^{-1} Mpc^{-1}, $\Omega_m = 0.308$, and $\Omega_\Lambda = 0.692$ (flat ΛCDM).

2. We search for more GRGs from existing radio and optical or infrared survey data.

*https://sites.google.com/site/anantasakyatta/sagan

3. Using the newly created large database of GRGs, we carry out multi-wavelength studies of the host AGNs of the GRGs. We intend to focus on some key physical properties such as the accretion rate (m) of the black hole, excitation type, black hole mass (M_{BH}), Eddington ratio, spin, host galaxy star formation rate (SFR), and high-energy gamma-ray emission from jets.

4. We explore effects of the environment on the morphology and growth of the GRGs.

5. We use magneto-hydrodynamical (MHD) simulations to investigate the jet physics and the conditions required for the collimation and stability of relativistic jets, propagating to megaparsec or larger physical distances from the host AGN.

Broadly, the goal is to understand birth, growth, and evolution of GRGs and their possible contribution to other processes in the Universe.

In this first paper, we present the results of our search for GRGs from the NVSS along with GRGs from other published works and investigate their multi-wavelength properties (in radio, optical, and mid-infrared bands). We not only report a larger sample of 162 hitherto unidentified GRGs, but also shed light for the first time on their AGN and host galaxy physical properties.

4.2.1 New sample of GRGs from NVSS

The NVSS provides radio maps ($\delta > -40^\circ$, 82% of the sky) at 1400 MHz with a modest resolution of 45″ and has root mean square (rms) brightness fluctuations of ~ 0.45 mJy beam^{-1}. The NVSS was released more than 20 years ago, and still it continues to be a source of many interesting discoveries (e.g. for GRGs; Solovyov & Verkhodanov 2011; Amirkhanyan 2016; Proctor 2016; Dabhade et al. 2017).

Proctor (2016) produced a catalogue of 1616 possible giant radio sources (GRSs) from automated pattern-recognition techniques using NVSS data. This catalogue of 1616 sources represents the radio objects that are candidates for GRGs with projected angular size $\geqslant 4'$. Therefore this catalogue serves as a useful database for finding new GRGs.

Following-up on our pilot study, Dabhade et al. (2017), we further carried out our independent manual visual search for GRGs from the NVSS, and the results of the search were combined with the fraction of GRGs we confirmed from the Proctor (2016) sample. In order to confirm potential

GRGs from Proctor's sample, we used the following radio surveys, which complement each other, to understand the radio morphology of the sources:

- NVSS: It has a high sensitivity for large-scale diffuse emission and is one of the best all-sky radio surveys to date.
- FIRST: This survey is at 1400 MHz with a resolution of $\sim 5''$ and 0.15 mJy beam^{-1} rms. Its high-resolution maps provide vital information about the radio cores and hotspots of the sources.
- TGSS: This is a low-frequency radio survey at 150 MHz with a resolution of $\sim 25''$ and an rms of ~ 3.5 mJy beam^{-1}, covering the entire NVSS footprint. It is sensitive to diffuse low radio frequency emission and particularly good at detecting sources with very steep spectra.
- VLASS*: The Very Large Array Sky Survey (Lacy et al. 2019). This is the most recent all-sky radio survey at 3000 MHz with a resolution of $\sim 2.5''$ and rms of ~ 100 μJy and covers the same footprint as the NVSS. This survey is deeper, has a better resolution, and covers a greater sky area than the FIRST. It is very useful for identifying compact structures such as the radio cores of the sources.

After the overall morphology of the sources was determined using the available radio surveys, optical and mid-IR data from the Sloan Digital Sky Survey (SDSS; York et al. 2000; Abolfathi et al. 2018), the Panoramic Survey Telescope and Rapid Response System (Pan-STARRS; Kaiser et al. 2002, 2010; Chambers et al. 2016), and the Wide-field Infrared Survey Explorer (WISE; Wright et al. 2010), respectively, were used to identify the host galaxies of the candidate GRGs.

The following steps and criteria were used to create the final sample of confirmed GRGs from the Proctor (2016) GRS catalogue:

1. Optical/mid-IR and radio maps were overlaid to identify the host galaxy/AGN that coincides with the radio core. Sources that did not have a radio core-host galaxy association were rejected.
2. We selected only those sources via thorough manual inspection whose various components (core, jets, or lobes) were sufficiently well resolved, with no ambiguity in their radio morphology.

*https://archive-new.nrao.edu/vlass/HiPS/VLASS_Epoch1/Quicklook/

Table 4.1: Short summary of the classification of sources from Proctor (2016)

Classification	No. of objects
Ambiguous morphology	156
Independent sources	266
New GRGs	151
Known GRGs	165
Narrow-angle tailed RGs	24
No core	143
No host	20
No redshift	311
RGs	311
Supernova remnant	6
Spiral/disc galaxies	32
Wide-angle tailed RGs	31
Total	1616

3. All the sources selected by the above steps were checked for redshift (z) information of the host galaxy (photometric or spectroscopic) from publicly available optical surveys and databases.

4. The angular sizes of the sources were computed using NVSS radio maps for uniformity, and to ensure that there is no flux or structure loss, which the other higher resolution radio surveys (FIRST, TGSS, and VLASS) are prone to. We measured the largest angular separation of the two components (lobes, hotspots, tails, and jets) of the sources after considering only the parts of the sources that are seen above 3σ. In this way, the angular sizes of all the sources were revised, and the angular extent of some sources was $< 4'$, which is the lower limit of the Proctor (2016) sample.

5. Lastly, we made use of redshift and angular size information to compute the projected linear size of the sources, and only those greater than 700 kpc were considered for our GRG sample (SAGAN GRG sample, or SGS henceforth).

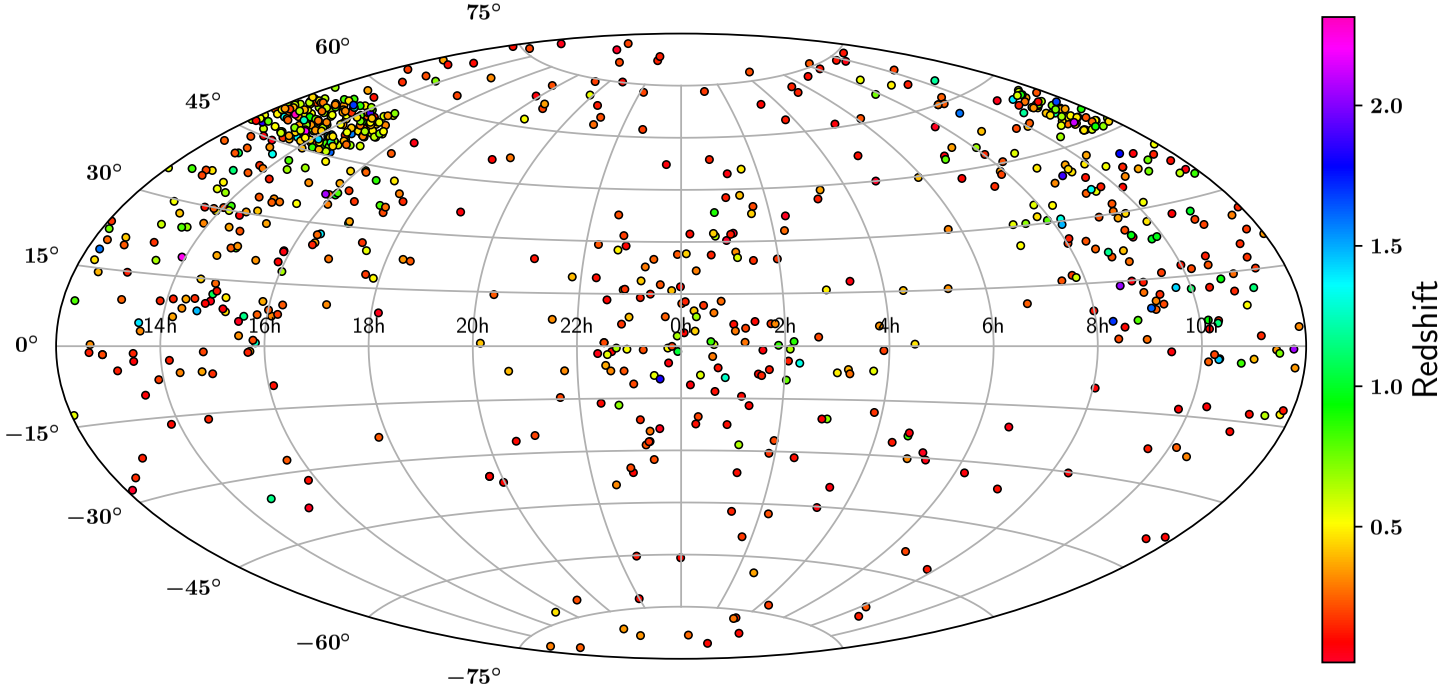

Figure 4.1: Sky distribution of all the known GRGs from 1974 to 2020 together with our SAGAN GRG sample in an Aitoff projection. The total number of GRGs plotted here is 820 (LoTSS: 225 and SAGAN: 162, and all others from literature: 433). The large clustering of GRGs in the northern region of the plot (right ascension 10h45m to 15h30m and declination 45°00′ to 57°00′) is the result of finding the large sample of GRGs (225) in the LoTSS by us (Dabhade et al. 2020b). The colour of the points on the plot corresponds to their redshift, which is indicated in the vertical colour bar at the right side of the plot. We do not use all the 820 GRGs for our analysis in this paper, but only those (762 GRGs) with a redshift lower than 1.

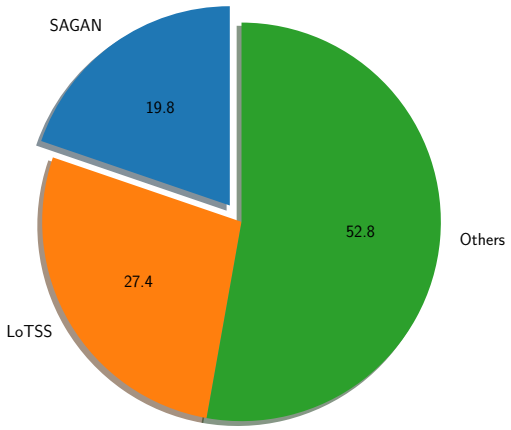

Figure 4.2: Pie diagram representing the contribution of SGS (blue: ∼20%) and LoTSS-GRGs (orange: ∼27%) to the total GRG population. The GRGs reported in the literature until March 2020 are plotted in green. We show all the known (820) sources without any filters.

These steps resulted in identifying 151 new GRGs from the Proctor (2016) sample. We also classified the remaining sources into different categories, which can be useful to the scientific community for future work. The classification was made based on the availability of radio and optical data, which are given in Table 4.1. Many sources from our independent manual search were in common with Proctor (2016) sample, and a total of 11 GRGs were found to be unique (not in the Proctor 2016 sample). After combining the two, we therefore report our final sample (SGS) of 162 GRGs as seen in Table 4.4. The sample is discussed in more detail in Sec. 4.4.

The basic information of the SGS, that is, right ascension (RA) and declination (Dec) of host galaxies in optical, AGN type (galaxy or quasar), redshift, angular size (arcminute), physical size or projected linear size (Mpc), flux density (mJy), and radio powers (W Hz^{-1}) at 1400 MHz and 150 MHz, and spectral index with error estimates are presented in the Table 4.4. About 37.7% of the SGS have photometric redshifts, and the remainder has spectroscopic redshift information. When we consider the lower end of the uncertainties of the photometric redshifts obtained from the SDSS, only three sources in our SGS, SAGANJ010052.6+061641.01, SAGANJ075931.84+082534.59, and SAGANJ125204.82-222645.70, are below the cutoff of 0.7 Mpc. The lower limits of their projected linear sizes are 0.68, 0.67, and 0.69 Mpc, respectively.

4.2.2 The GRG catalogue

In order to explore and study the trends of GRG properties using a statistically significant sample, we combined our SGS with all other known GRGs from the literature (as of April 2020) given in Sec. 4.1, and we refer it as the GRG catalogue throughout this paper. The total number of GRGs in the GRG catalogue, that is, the total number of GRGs known to date, is 820, and it is a unique complete compendium of known GRGs to date. Fig. 4.1 shows the distribution of all the known GRGs (including the GRG sample of this paper) on the sky. The high concentration of GRGs in the northern region of the plot (right ascension 10h45m to 15h30m and declination 45°00′ to 57°00′) is primarily due to the recent discovery of a large sample of new GRGs (225) from the LoTSS by us (Dabhade et al. 2020b), which has contributed about 30% to the known GRG population as shown in Fig. 4.2. Our reporting sample from this paper, called the SGS, has contributed an additional ∼ 20% to the overall known population of GRGs. This means that we contributed about 50% of all known GRGs to date.

We point out our analysis here is restricted to 762 out of 820 GRGs (∼ 93% of the GRG catalogue), and 58 GRGs with $z > 1$ were not considered to avoid any kind of bias. Beyond a redshift of 1, we are limited because no optical data are available and because the radio source properties (luminosity and size) evolve fast in the early cosmic epoch of $z > 1$. SGS, which is now part of the GRG catalogue, has all sources with $z < 1$.

4.3 Analysis

4.3.1 Size

The projected linear size of the sources is taken as the end-to-end distance between the two hotspots (peak fluxes) in case of FR-II sources, and for FR-Is, it is the distance between the maximum extents defined by the outer lobes. For the measurement of angular sizes, only the NVSS maps are considered for uniformity. The projected linear sizes of sources are estimated using the following formula, and they are tabulated in Table 4.4 (Col. 8):

$$\mathrm{D} = \frac{\theta \times \mathrm{D_c}}{(1+\mathrm{z})} \times \frac{\pi}{10800}, \tag{4.1}$$

where θ is the angular extent of the GRG in the sky in units of arcminutes, D_c is the comoving distance in Mpc, z is the redshift of the GRG host galaxy, and D is the projected linear size of the GRG in Mpc.

4.3.2 Flux density and radio power

The integrated flux density of GRGs was estimated using Common Astronomy Software Applications (CASA) (McMullin et al. 2007) with the task CASA-VIEWER by manually selecting the regions of emission associated with each GRG in NVSS* and TGSS† maps. The TGSS maps were convolved to the resolution of NVSS. We used the scheme of Klein et al. (2003) for measuring flux density errors for each source, where we adopted 3% and 20% flux calibration errors, as mentioned in the literature for the NVSS and the TGSS, respectively.

The radio powers of GRGs were calculated using Eq. 2 and are given in Table. 4.4 (Cols. 10 and 12):

$$P_\nu = 4\pi D_L^2 S_\nu (1+z)^{\alpha-1}, \tag{4.2}$$

where D_L is the luminosity distance, S_ν is the measured radio flux density at frequency ν, $(1+z)^{\alpha-1}$ is the standard k-correction term, and α is the radio spectral index (as described in Sec. 4.3.4).

4.3.3 Jet kinetic power

AGN jets, made of relativistic charged particles and magnetic fields, emanate from the central engine and pierce the interstellar medium. Low frequency radio observations enable us to estimate the jet kinetic power, which helps us to study other characteristics of the radio-loud SMBH system as discussed in later sections. High radio frequencies (~ 1 GHz) are ideal for observing nuclear jet components owing to their flatter spectral nature. Because these components have high velocities, relativistic effects such as the Doppler enhancement effects are prominent. Therefore, lower radio frequencies are more suitable for probing the jet kinetic power because the contribution from Doppler enhancement is negligible. We used the following relation from the simulation-based analytical model of Hardcastle (2018b) to estimate the jet kinetic power:

$$L_{150} = 3 \times 10^{27} \frac{Q_{Jet}}{10^{38}\ W} W\ Hz^{-1}, \tag{4.3}$$

where L_{150} is the radio luminosity at 150 MHz, at which Doppler boosting is negligible, and Q_{Jet} is the jet kinetic power. There is a scatter of 0.4

*https://www.cv.nrao.edu/nvss/postage.shtml
†https://vo.astron.nl/tgssadr/q_fits/cutout/form

dex (rms) about the relation for the sources with $z < 0.5$. However, significant scatter is observed in the relationship at higher redshifts, with a major contributor being the increased inverse-Compton scattering. Other contributors include the environment and evolutionary state of the sources (Hardcastle 2018b). In the tracks of the P-D diagram for sources of different jet powers in the models presented by Hardcastle (2018b), the luminosity of the source appears to decrease with size during the giant phase for the different jet powers. Their modelling shows that it is possible to obtain more accurate results by taking environment and age into account. The relation is consistent with the regression line of Ineson et al. (2017) and earlier work by Willott et al. (1999).

Sources in the GRG catalogue taken from the Dabhade et al. (2020b) GRG sample have flux density measurements at 144 MHz from the LoTSS, which is used to derive the 150 MHz radio luminosity. The TGSS was used for the remaining sources in the GRG catalogue to obtain the 150 MHz radio luminosity. This was mainly done for our newly found SGS, and only sources with full structure detection in TGSS were considered for the same. The results are presented in Col. 8 of Table 4.5.

4.3.4 Spectral index

For a radio source, its spectral index (α) represents the energy distribution of the relativistic electrons (Scheuer & Williams 1968), and its measurement should therefore ideally involve covering wide frequency range. Studies have shown that α correlates with radio power and redshift. For synchrotron radiation, unless it is affected by radiative losses and optical depth effects, it is well known that the radio flux density varies with frequency as $S_\nu \propto \nu^{-\alpha}$, resulting in a two-point spectral index measurement, given as follows:

$$\alpha = \frac{\ln S_{\nu_1} - \ln S_{\nu_2}}{\ln \nu_2 - \ln \nu_1} \tag{4.4}$$

The integrated spectral index between 150 and 1400 MHz (α_{150}^{1400}) for the GRGs was computed using the TGSS and the NVSS radio maps (Table. 4.4, Col. 13). We did not include GRGs with incomplete structure detection in the TGSS for the α_{150}^{1400} studies. For these sources, the α_{150}^{1400} is assumed to be 0.75 to determine the radio power at 1400 MHz (P_{1400}). See Sec. 4.4.1 and Sec. 4.5.1 for a more detailed discussion.

For sources SAGANJ090111.78+294338.00 and SAGANJ091942.21+260923.97, TGSS data are lacking because they fall in

a sky area that is not covered in TGSS-ADR-1. Therefore, no spectral index measurements were possible for them.

4.3.5 Absolute r-band magnitude

Using the SDSS, we obtained the apparent r-band magnitudes (m_r) of host galaxies of GRGs in the SGS as well as for all the other objects in the GRG catalogue. The absolute r-band magnitudes (M_r) of galaxies were computed after applying the k-correction on extinction-corrected r-band apparent magnitudes (m_r) of SDSS. The k-correction was computed using the K-CORRECT v4.3 software (Blanton & Roweis 2007) for a rest frame at $z = 0$. Column 5 of Table 4.4 shows m_r of the sources from the SGS.

4.3.6 Black hole mass

We estimated the black hole masses associated with the AGNs in the host galaxies of GRGs using the M_{BH}-σ relation. The M_{BH}-σ relation is based on a strong correlation between the central galactic black hole mass (M_{BH}) and the effective stellar velocity dispersion (σ) in the galactic bulge (Ferrarese & Merritt 2000; Gebhardt et al. 2000) given by

$$\log\left(\frac{M_{BH}}{M_\odot}\right) = \alpha + \beta \log\left(\frac{\sigma}{200 \text{ km s}^{-1}}\right), \tag{4.5}$$

where $\alpha = -0.510 \pm 0.049$ and $\beta = 4.377 \pm 0.290$ (Kormendy & Ho 2013). Estimates for σ (Col. 4 of Table 4.5) were available for only 46 host galaxies of GRGs from the SGS in the SDSS, and hence the M_{BH} of GRGs (Table. 4.5, Col. 5) could be computed with this method.

4.3.7 Eddington ratio

The dimensionless Eddington ratio (λ_{Edd}) is the ratio of the AGN bolometric luminosity to the maximum Eddington luminosity, which in turn is the estimate of the accretion rate of the SMBH in terms of the Eddington accretion rate. The Eddington ratio is expressed by the following relation:

$$\lambda \equiv \frac{L_{bol}}{L_{Edd}}, \tag{4.6}$$

where L_{bol} represents the bolometric luminosity, and the Eddington luminosity is L_{Edd}. The L_{bol} is calculated from the luminosity of the [OIII] emission line using the relation $L_{bol} = 3500 \times L_{[OIII]}$ (Heckman et al. 2004).

The values of λ_{Edd} are tabulated in Col. 7 of Table. 4.5. The Eddington luminosity (also known as the Eddington limit) is derived from the black hole mass, and it is the maximum luminosity that an object could have when the force of radiation acting outwards and the gravitational force acting inwards are balanced. The equation of the Eddington luminosity for pure ionised hydrogen plasma is $L_{Edd} = 1.3 \times 10^{38} \times (\frac{M_{BH}}{M_\odot})$ erg s^{-1}.

4.3.8 Black hole spin

Spin and angular momentum (a and J) are fundamental properties of black holes, together with the mass. This can help us reconstruct the history of mergers and accretion activity (Hughes & Blandford 2003; Volonteri et al. 2007; King et al. 2008; Daly 2011) that have occurred in the central engine in the past billion years and thus paves the way to understanding the energetic astrophysical jets. In the B-Z model, the relativistic jet is the outcome of the combined effect of rotation (frame dragging) and the accumulated magnetic field near the black hole (Blandford & Znajek 1977), which is fed matter by the rotating accretion disc that surrounds it. In the alternative model of Blandford & Payne (1982), the jet power can come from the rotation of the accretion disc with the help of magnetic threading, without invoking a spinning black hole. However, in both the processes, the intensity and geometry of the poloidal component of the magnetic field near the black hole horizon strongly affect the Poynting flux of the emergent jet (Beckwith et al. 2008).

According to the B-Z model (Blandford & Znajek 1977; Blandford 1990), the relationship between the jet power (Q_{Jet}), the black hole mass (M_{BH}), the black hole dimensionless spin ($a = Jc/(GM^2)$), and the poloidal magnetic field (B) threading the accretion disc and ergosphere takes the following form:

$$Q_{Jet} \propto B^2 M_{BH}^2 a^2, \tag{4.7}$$

where Q_{Jet} is in units of 10^{44} erg s^{-1}, B is in units of 10^4 G, M_{BH} is in units of 10^8 $M_\odot$, and a is the dimensionless spin parameter (a=0 refers to a non-rotating black hole, and a=1 is a maximally spinning black hole). The spin (a) can be quantified using the above relation when the other contributing parameters are known or fixed. The constant of proportionality is taken to be $\sim\sqrt{0.5}$, as in the B-Z model. Owing to the challenges of estimating the magnetic field in the vicinity of the black hole to compute the spin, we considered the Eddington magnetic field strength (B_{Edd}) (Beskin 2010;

Daly 2011), which is

$$B \sim B_{Edd} \approx 6 \times 10^4 \left(\frac{M_{BH}}{10^8 M_\odot} \right)^{-1/2} \text{Gauss.} \quad (4.8)$$

This is the upper limit of the magnetic field strength close to the central engine, and it is based on the assumption that the magnetic field energy density balances the total energy density of the accreting plasma that has a radiation field of Eddington luminosity. These estimates are presented in Table 4.6.

The X-ray reflection is the most robust and effective technique employed to date to estimate the spin of black holes (Reynolds 2019). However, owing to the weakness of the signal and because the data for the objects need to be rich, it has been convincingly performed for only ∼20 sources so far. For radio galaxies, which are jetted sources and mostly show weak X-ray reflection signatures, it is possible to estimate the spin assuming the B-Z mechanism (Daly 2011; Mikhailov & Gnedin 2018). In this radio-driven method, the spin (a) of the black hole can be estimated when we have estimates of M_{BH} and Q_{Jet} and adopt B_{Edd} as B. This method provides an indirect estimate of the spin of the black hole.

4.3.9 WISE mid-IR properties

We used the WISE survey to study the hosts of GRGs at mid-IR wavelengths. WISE, which is a space-based telescope, carried out an all-sky survey in four mid-IR bands [W1 (3.4μm), W2 (4.6μm), W3 (12μm), and W4 (22μm)] with an angular resolution of 6.1″, 6.4″, 6.5″ , and 12″ , respectively.

Using the mid-IR colours, we obtained the properties of possible dust-obscured AGN, and estimated its radiative efficiency. The mid-IR information of host galaxies of GRGs is very useful in gauging the radiative efficiency because the optical-UV radiation from the accretion disc of the AGN is absorbed by the surrounding dusty torus (if present) and is re-radiated at mid-IR wavelengths. Moreover, it has been shown in the literature that WISE mid-IR colours can effectively distinguish AGNs from star-forming and passive galaxies, and within the AGN subset itself, high-excitation radio galaxies (HERGs) and low-excitation radio galaxies (LERGs) stand out in the mid-IR colour-colour and mid-IR-radio plots (Stern et al. 2012; Gürkan et al. 2014). In the absence of any dedicated multi-wavelength survey of host galaxies of GRGs, WISE data are therefore ideal for exploring GRG properties.

The WISE All-Sky Source Catalogue was used to obtain magnitudes of host galaxies of GRGs in the four mid-IR bands. After applying photometric quality cuts of 3σ, we obtained reliable mid-IR magnitudes for sources in the GRG catalogue. Upper limits of the magnitudes in the relevant bands were estimated for sources that did not have a 3σ detection as derived with the method prescribed in the WISE documentation.

Gürkan et al. (2014) have demonstrated that data from WISE can be used to distinguish accretion modes in RLAGNs. To achieve this, Gürkan et al. (2014) used four complete radio samples with emission line-based classification of RGs into low-excitation radio galaxies (LERGs), high- excitation radio galaxies (HERGs), quasars, star-forming galaxies (SFGs), narrow line radio galaxies (NLRGs), and ultra-luminous infrared radio galaxies (ULIRGs). These were further placed in the WISE colour-colour plots, where these sub-classes occupied different regions and thereby enabled distinction. Furthermore, other works (O'Sullivan et al. 2015b; Mingo et al. 2016; Whittam et al. 2018) have also confirmed this finding with other radio samples. Therefore we employed the scheme from Mingo et al. (2016), which is based on the earlier work of Wright et al. (2010), Lake et al. (2012), and Gürkan et al. (2014), to classify the host AGN and host galaxies of GRGs into LERGs, HERGs, quasars, SFGs, and ULIRGs.

Fig. 4.3 is a colour-colour plot using four mid-IR bands [W1 (3.4μm), W2 (4.6μm), W3 (12μm), and W4 (22μm)] and shows not only the distinction between LERGs and HERGs, but also effectively distinguishes AGNs from star-forming and passive galaxies. Fig. 4.3 includes 733 sources from the GRG catalogue based on the availability of data and detection in WISE database. It has been separated into four regions, which signify the following:

1. Region I: HERGs and quasars (W1 − W2 $\geqslant$ 0.5 , W2 − W3 < 5.1). This region consists of 250 GRGs, 103 of which are hosted by quasars.

2. Region II: LERGs (W1 − W2 < 0.5 , 0 < W2 − W3 < 1.6). This region hosts 153 sources.

3. Region III: LERGs and star-forming galaxies (W1 − W2 < 0.5 , 1.6 $\leqslant$ W2 − W3 < 3.4)- 297 giants lie in this region.

4. Region IV: ULIRGs (W1 − W2 < 0.5 , W2 − W3 $\geqslant$ 3.4). Only 33 sources lie in this region.

Fig. 4.3 shows that host galaxies of GRGs reveal a variety of AGN excitation types similar to the RG types. This also indicates that the GRG

host galaxy or AGN do not preferentially show any specific AGN excitation type. The quasars in this plot are not identified with this method, but were previously classified from the SDSS and other available literature data. Similar results were presented in Dabhade et al. (2017), but with a much smaller sample. We here placed almost the entire GRG catalogue on the WISE colour-colour plot for AGN diagnostic and classified the known GRG population into their excitation types. We focused on the low- and high-excitation part of the classification, and efforts were made to ensure a clean classification. For a sub-sample (based on the availability of data), we also compared our LERG and HERG classification of GRGs from WISE with the standard classification method based on emission line ratios and found them to be consistent with each other.

We refer to the GRGs with low- and high-excitation types as LEGRG and HEGRG, respectively. Because regions III and IV in Fig. 4.3 both have a mixed population of LERGs as well as star-forming galaxies and ULIRGs, respectively (thereby confusing the classification), we did not consider objects in these regions for our analysis, and considered only sources in region II to be LEGRGs to make a clean sample. Similarly, we excluded from region I known quasars and created a HEGRG sample for our analysis. These two criteria reduce the number of objects available for our further analysis.

4.4 SAGAN GRG sample: Results

The classification of the sources in the SGS is shown in Table 4.2 below. Out of 162 GRGs, 23 sources are found to be hosted by galaxies with quasars as their AGN (we refer to them as GRQs). The quasar nature of these 23 GRQs is identified using the spectroscopic data from the SDSS, Pâris et al. (2018), and other available literature data. All the GRGs have been detected in the redshift range of $\sim$ 0.03 - 0.95, with projected linear sizes varying from $\sim$0.71 - 2.82 Mpc. Three GRGs in our sample have projected linear sizes $\geqslant$ 2 Mpc.

4.4.1 Spectral index distribution of the SGS

We were able to estimate α_{150}^{1400} for a total of 123 from the SGS, 18 of which are GRQs (see Col. 13 of Table 4.4). For the remaining 39 sources in the SGS, TGSS had only partial or no detection, and we therefore assumed the spectral index to be 0.75 to calculate P_{1400}. Therefore the α_{150}^{1400} data for the remaining 39 sources are not included for further studies in this paper. The

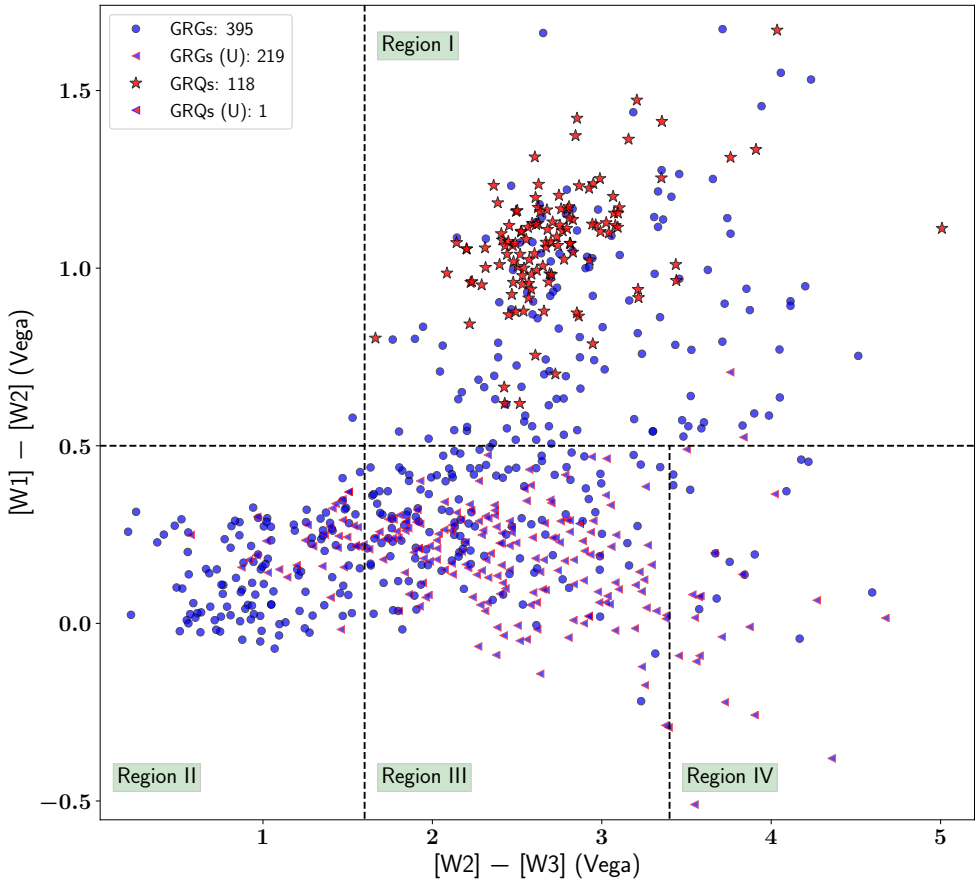

Figure 4.3: Position of GRGs and GRQs (733 sources from GRG catalogue) in the mid-IR colour-colour plot using WISE mid-IR magnitudes (W1, W2, W3, and W4 have 3.4, 4.6, 12, and 22 μm Vega magnitudes, respectively). Objects from the GRG catalogue are included. Region I: [W1]−[W2] $\geqslant$ 0.5 and [W2]−[W3] $<$ 5.1 is mostly occupied by HERGs and quasars. Region II: Objects that have [W1]−[W2] $<$ 0.5 and 0 $<$ [W2]−[W3] $<$ 1.6 are basically LERGs. Region III: Star-forming galaxies and LERGs lie mostly in this region ([W1]−[W2] $<$ 0.5 and 1.6 $\leqslant$ [W2]−[W3] $<$ 3.4). Region IV: ULIRGs lie in the region of [W1]−[W2] $<$ 0.5 and [W2]−[W3] $\geqslant$ 3.4. All the sources have z $<$ 1. The triangle in the plot and the U in the legend indicate the upper limits of the W3 magnitudes.

Table 4.2: Summary of classified sources.

Types	No.
GRQ	23
BCG	18
FR I	8
FR II	149
HyMoRS	4
DDRG	1

median value of α_{150}^{1400} for the GRGs in our sample (0.69 ± 0.02) is similar to that of GRQs (0.69 ± 0.04). Dabhade et al. (2020b) also reported that α_{150}^{1400} of GRGs and GRQs was similar, with almost similar sample size. However, because their sample was chosen from a low-frequency survey such as the LoTSS, they found it to be slighter steeper than our SGS.

4.4.2 PD$z\alpha$ parameters of GRGs

We investigated the correlation between various properties of sources in our sample, such as radio power (P), projected linear size (D), redshift (z), and spectral index (α) (Fig. 4.4). The inferences are presented below.

1. Radio power (P) versus redshift (z): Fig. 4.4 (a) represents the distribution of GRGs in the P-z plane, with the radio power spanning over three orders of magnitude up to a redshift range of ~ 0.95. Most of the sources are within the redshift range of 0.1 to 0.5, and the number of radio sources decreases with increasing redshift beyond $z = 0.5$.

   The non-availability of sources in the lower right quadrant is most likely due to the non-detection of low powered sources at high redshift because of the sensitivity limit of the survey, known as the Malmquist bias. The GRQs occupy the high radio luminosity and high-redshift regime because more optical data are available than for GRGs. The weakest source in our sample is SAGANJ090640.80+142522.97, with a flux density of ~ 24 mJy at 1400 MHz. The dashed line represents the minimum luminosity at different redshifts, corresponding to a minimum flux density of ~ 24mJy assuming a spectral index of 0.75. This is the NVSS limit for detecting objects with low surface brightness, and hence the absence of any source below this line. Recently, Dabhade et al. (2020b) discovered a large sample of new GRGs, and

significant fractions of them were of low luminosity. When we place them on Fig. 4.4 (a), they tend to lie below the sensitivity line of NVSS, implying higher sensitivity of LoTSS.

2. Radio power (P) versus projected linear size (D): The projected linear sizes of the radio sources are plotted against their radio power, measured at 1400 MHz, as shown in Fig. 4.4 (b). This plot is the radio astronomer's equivalent of the traditional Hertzsprung-Russell diagram and is commonly known as the P-D diagram. We can draw the following conclusions from this diagram:

   - Despite the systematic search for giants, very few sources are found to be of extremely large size and very low radio power ($\leqslant 10^{24}$ W Hz^{-1} at 1400 MHz).
   - The upper right region of PD diagram, that is, the region of sources with high radio power and large projected linear size, is devoid of any source. This is indicative of an increase in radiative losses as the sources grow, which decreases the surface brightness and renders them inaccessible to the surveying telescope because of its sensitivity limit.
   - There is a sudden drop in the number of giants with a projected linear size beyond 2 Mpc. The projected linear sizes of only three sources, SAGANJ064408.04+104341.40, SAGANJ225934.13+082040.78, and SAGANJ231622.32+224650.28 in our sample, exceed 2 Mpc. All of them have low redshifts; the highest is 0.405 for source SAGANJ225934.13+082040.78. The projected linear size of only 66 of ∼762 known GRGs from the GRG catalogue ($z < 1$) is greater than 2 Mpc. Among them, four sources have extraordinary large projected linear sizes between 3 to 4 Mpc, while another four sources have projected linear sizes $\geqslant$ 4 Mpc, and the largest GRG known to date spans up to 5.2 Mpc at a redshift of 0.3067 (Machalski et al. 2008). About 50% of the sources are at low redshifts ($z \leqslant 0.4$), and the high-redshift objects are mostly dominated by quasars. This might be attributed to the sensitivity limit of radio surveys. Another possibility might be the limited lifetime of radio sources (Schoenmakers et al. 2001). A large fraction of sources may have switched off before they reach 2 Mpc and beyond.

3. Projected linear size (D) versus redshift (z): Fig. 4.4 (c) shows the

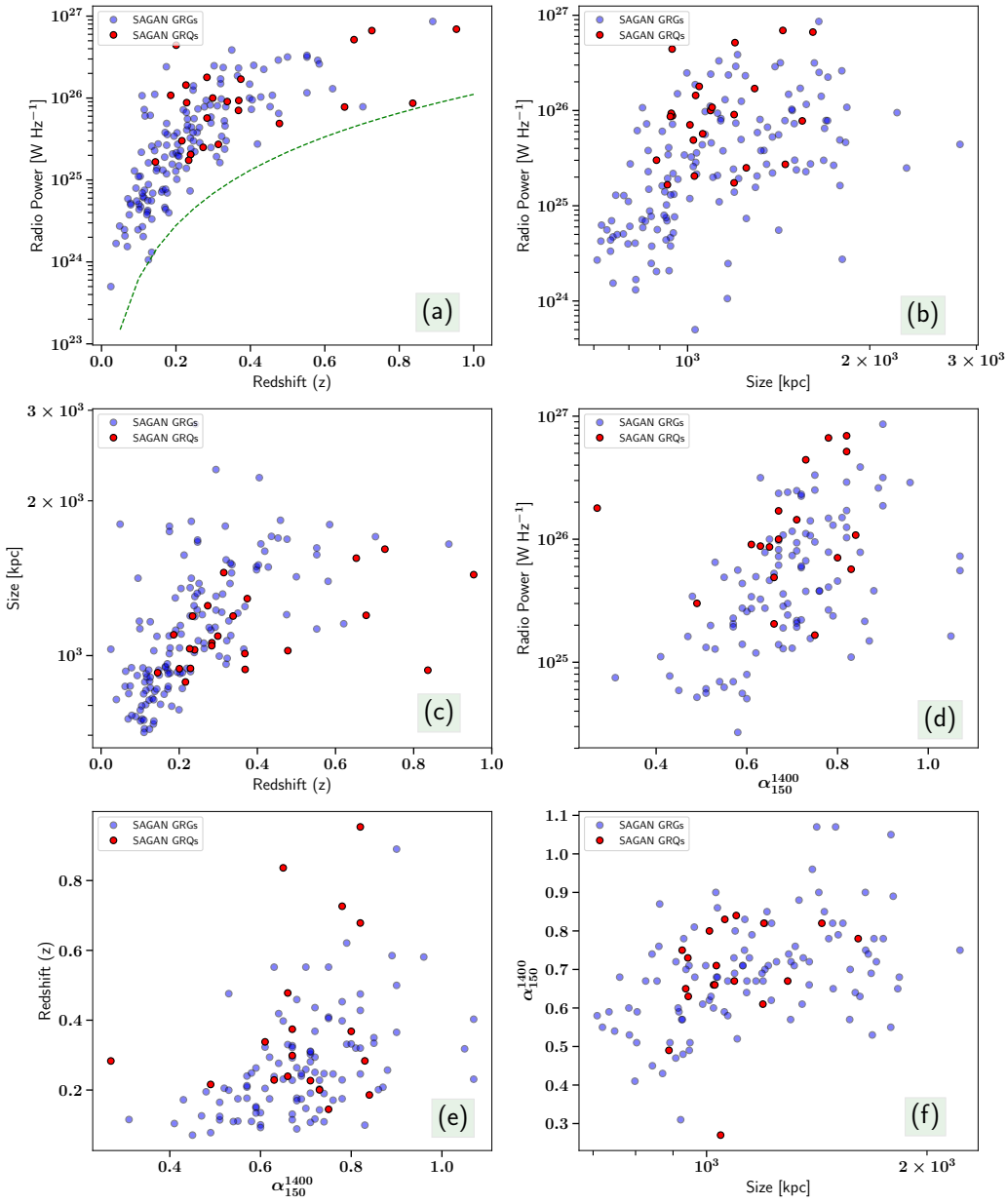

Figure 4.4: Correlations of radio power [W Hz^{-1}] at 1400 MHz , size [kpc], redshift, and spectral index for GRGs and GRQs. Red circles indicate GRQs, and blue circles indicate GRGs. The dashed green line in panel (a) represents the minimum radio luminosity corresponding to a flux density ∼24mJy of source SAGANJ090640.80+142522.97 at different redshifts, assuming a spectral index of 0.75.

positive correlation between projected linear sizes of our sources with redshift (z< 1), which is expected because luminosity strongly correlates with these two parameters. This may be an outcome of the selection bias of the sources considered in this plot. A negative correlation between projected linear size and redshift is expected from the systematic increase in density of the environment at earlier epochs.

4. Radio power (P) versus spectral index (α):

   Fig. 4.4 (d) shows that the spectral index increases with radio power. The correlation is significant for our sources, which are selected at high frequency (1400 MHz), similar to the results of Laing & Peacock (1980) for extended sources. It is also consistent with results of Blundell et al. (1999), who reported that the spectra of hotspots in powerful radio sources are steeper than those in weaker radio sources. Sources with high Q_{Jet} form powerful hotspots with enhanced magnetic fields (Blundell et al. 1999), which in turn leads to the rapid synchrotron cooling of relativistic electrons (cooling time $\tau \propto 1/B^2$). This eventually results in an increase in synchrotron losses, and thus electrons with a steeper energy distribution are injected into the lobes.

5. Redshift (z) versus spectral index (α): Fig. 4.4 (e) shows that at higher z, we obtain relatively steeper α, although there is a large scatter and sources with steep spectra are also seen at low redshifts.

   In a flux-density limited sample where luminosity and redshift are strongly correlated, it is difficult to determine whether the primary dependence is on luminosity or redshift (e.g. Blundell et al. 1999). In addition to the effects discussed above, other suggested explanations for the z-α correlation are as follows:

   - At higher redshifts, the circum-galactic medium is denser, which slows the hotspots down. The hotspots along with the lobes therefore remain in the high-pressure medium for a prolonged duration. A reduction in the velocity will result in the production of electrons with steeper energy distribution (Kirk & Schneider 1987; Mangalam & Gopal-Krishna 1995; Athreya & Kapahi 1998; Klamer et al. 2006; Gopal-Krishna et al. 2012).
   - In addition to higher synchrotron radiative losses due to a higher magnetic field in the more luminous sources, an important factor at high redshifts is inverse-Compton losses. As the redshift increases, there is a rapid increment in the energy density of the

cosmic microwave background radiation (CMBR energy density $\propto (1+z)^4$). When the high-energy electrons of plasma interact with the CMBR photons, energy loss due to inverse Compton radiation increases, and thus the spectra steepen (Krolik & Chen 1991; Athreya & Kapahi 1998; Morabito & Harwood 2018).

6. Spectral index (α) versus projected linear size (D): The sampling of the sources in the D - α plane in Fig. 4.4 (f) shows a weak correlation between the two parameters. The larger the sources, the steeper their spectral index. As the sources grow, they are subjected to radiative losses and thereby steepen the energy distribution. However, it is also reflected in the plot that sources with large projected linear size need not have steep spectra. This result is consistent with the findings of Blundell et al. (1999).

4.4.3 Morphology of GRGs

Using combined information from the VLASS, FIRST, NVSS, and TGSS, we classified the GRGs in our sample into the following types: FR-I, FR-II, HyMoRS, and DDRG. HyMoRS are RGs with a hybrid morphology (Gopal-Krishna & Wiita 2000, 2002) that exhibit an FR-I morphology on one side and an FR-II morphology on the other side of the radio core. The earliest example of this class of objects was presented in Saikia et al. (1996). This classification is listed in Col. 15 in Table 4.4, where HM refers to GRGs that are candidates for HyMoRS. Higher resolution radio maps are needed to confirm the morphology of the four HyMoRS candidate GRGs. For HyMoRS candidates, the radio power range is $P_{1400} \sim 2.74 \times 10^{24}$ W Hz^{-1} - 7.78×10^{25} W Hz^{-1}. The most significant result is that about 92% of the GRGs in the SGS show an FR-II type (edge-brightened hotspots within radio lobes) radio morphology, whereas only 8 out of 162 the GRGs show an FR-I type radio morphology. The radio power (P_{1400}) for FR-I type GRG ranges from $\sim 1.31 \times 10^{24}$ W Hz^{-1} to 11.1×10^{25} W Hz^{-1}, and for FR-II type GRGs. the range extends from $\sim 0.5 \times 10^{24}$ to 8.6×10^{26}. Recently, Dabhade et al. (2020b) used the LoTSS and also found a similar result: most of the GRGs had an FR-II type morphology. Moreover, Mingo et al. (2019) used the LoTSS and reported a significant overlap in radio power of FR-I and FR-II type RGs, along with a new sample of low-luminosity FR-II type RGs.

4.4.4 Environmental analysis of the SGS

We cross-matched the SGS with one of the largest catalogues of galaxy clusters, the WHL catalogue (Wen et al. 2012). We found 18 GRGs from the SGS that were listed as brightest cluster galaxies (BCGs); they are listed in Table 4.7. The mass (M_{200}) and virial radius (r_{200}) of the clusters were obtained from Wen et al. (2012) and are listed in Table 4.7 for these 18 GRGs. The size is expressed as r_{200}, which is the radius within which the galaxy cluster mean density is about 200 times the critical density of the Universe, and the mass of the cluster within r_{200} is denoted by M_{200}. We considered the sizes of these 18 GRGs along with 111 non-BCG-GRGs from our sample in the same redshift range (0.063 - 0.369) with median redshifts of 0.174 and 0.205, respectively. We find that the median values for sizes of BCG-GRGs and non-BCG-GRGs are 0.92 Mpc and 1.03 Mpc, respectively. Even though the median values do not vary largely, this indicates that BCG-GRGs have smaller sizes than non-BCGs, or in other words, the immediate environment plays an active role in curtailing their growth.

4.5 GRG catalogue: Properties and correlations

We describe the derived properties of GRGs, consisting of 762 sources with $z < 1$ using the multi-wavelength data. Our multi-wavelength analysis is divided into the following three parts to understand the nature of GRGs, and we investigate the key astrophysical factors governing their growth to megaparsec scales.

We first studied the differences in AGN types of GRGs: Quasars powering giant radio structures (jets and/or lobes) are called GRQs, which constitute less than 20% of the total known GRG population. The aim is to understand the key differences between giants hosted by quasars and non-quasar AGN. Their properties, such as size, P_{1400}, Q_{Jet}, and α_{150}^{1400} , are compared and discussed in Sec. 4.5.1.

Next, we studied the accretion states (LEGRG or HEGRG) of the central nuclei of GRGs: These two sub-classes are investigated and discussed in Sec. 4.5.2 in the context of their properties, such as size, P_{1400}, Q_{Jet}, M_r, M_{BH} , and λ_{Edd}. Finally, we studied the similarities and dissimilarities between RGs and GRGs: We compared their α_{150}^{1400}, M_{BH} , and λ_{Edd} properties, and the findings are discussed in Sec. 4.5.3.

To test whether two samples that we compared come from the same distribution, we used the two-sample Kolmogorov-Smirnov (K-S) test (Kol-

mogorov 1933; Smirnov 1948; Peacock 1983) and the Wilcoxon-Mann-Whitney (WMW) test (Wilcoxon 1945; Mann & Whitney 1947). In these we tested the null hypothesis H_0 : the two samples are drawn from the same distribution, against the alternative hypothesis H_1: the two samples are not drawn from the same distribution. A lower p-value provides stronger evidence that the null hypothesis is rejected, or in other words, that the two samples are not drawn from the same distribution.

In addition to these comparative studies, we explored the SMBH properties to understand how several aspects such as mass (M_{BH}), spin (a), Eddington ratio (λ_{Edd}), and jet kinetic power (Q_{Jet}) are related in Sec. 4.5.4. Lastly, we discuss in Sec. 4.5.5 the environmental properties of GRGs that are found in clusters of galaxies (BCGs), and explore their relationship with M_{200} and other BCG-RGs.

4.5.1 Comparison of the properties of GRGs and GRQs

As mentioned earlier, we here only considered GRGs with $z < 1$ for analysis. The redshift distribution (Fig. 4.5 top panel) of GRGs and GRQs is not similar (the WMW test p-value is 3.4×10^{-13} and the K-S test p-value is 2.9×10^{-7}), however, because GRQs extend to higher redshifts than GRGs. The mean and median redshifts of GRGs are 0.331 and 0.284, respectively, for the range of 0.016 to 0.910, and for GRQs, the values are 0.515 and 0.475, respectively, for the range of 0.085 to 0.999. In order to ensure that our results are not affected by redshift evolution, we considered a redshift-matched ($0.2< z <0.8$) (Fig. 4.5 lower panel) sub-sample of GRGs (mean z: 0.42 and median z: 0.40) and GRQs (mean z: 0.44 and median z: 0.43) to compare their properties (Fig. 4.7). Here, the redshift distributions of both samples are similar (WMW test p-value is 0.14 and K-S test p-value is 0.54), and our comparison analysis of all properties of GRGs and GRQs gives similar results for the not redshift-matched (Fig. 4.6) and the redshift-matched samples (Fig. 4.7). We therefore present our analysis for the samples of GRGs and GRQs below. The detailed statistics of all properties are presented in Table 4.3.

Distribution of the projected linear size

The distributions of the projected linear size are shown in Fig. 4.6 (a) and Fig. 4.7 (a), and the median values are presented in Table 4.3. Although the median value for quasars appears to be marginally higher when all objects with $z < 1$ in the GRG sample are considered, the difference is reduced and

is within 1σ when the samples are matched in redshift. However, because the GRG sample has been compiled from multiple heterogeneous sources, we also considered the homogeneous samples of the LoTSS and SGS with matched redshifts of GRGs and GRQs. For these two samples, the median values of sizes for GRGs are 0.89 and 1.20 Mpc, and for GRQs, they are 1.00 and 1.06 Mpc, respectively. The WMW test (p-value for the SGS: 0.06, and for the LoTSS: 0.18) shows that the distributions of the projected linear size of GRQs are not significantly different from those of GRGs.

Distribution of the radio power (P_{1400})

Based on the availability of data from the NVSS, we were able to estimate P_{1400} for 604 GRGs and 118 GRQs from the GRG catalogue. The distributions of P_{1400} of GRGs and GRQs are shown in Fig. 4.6 (b) and Fig. 4.7 (b) for not matched and matched samples, respectively, where we observe that GRQs have a higher radio power than GRGs at 1400 MHz. This is well supported by the K-S test (the p-value for the matched sample is 1.20×10^{-7}) and the WMW test (the p-value for the matched sample is 7.88×10^{-11}) of the matched redshift samples, as shown in Table 4.3, which strongly indicates that the two distributions are significantly different. Clearly, prevailing conditions in the central engines of GRQs are able to produce more powerful jets, which results in more radio-luminous sources than for GRGs. GRQs are found to have a higher jet kinetic power than GRGs (as shown below), and they might host more massive black holes that accrete at a higher Eddington rate. Because our sample is restricted to sources with redshift lower than 1, we do not observe even more powerful GRQs, which lie mostly at higher redshifts.

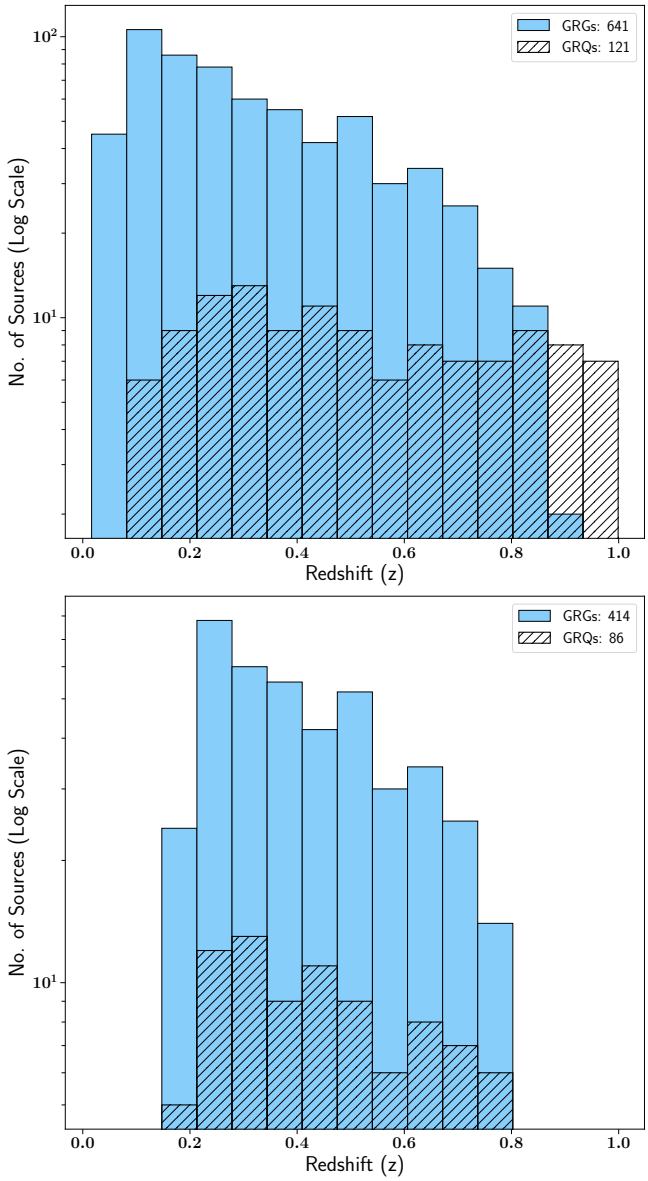

Figure 4.5: The figure shows the redshift (z) distributions of GRGs and GRQs for z <1, represented in unhatched and hatched bins, respectively for redshift matched (lower plot) and unmatched (upper plot) samples.

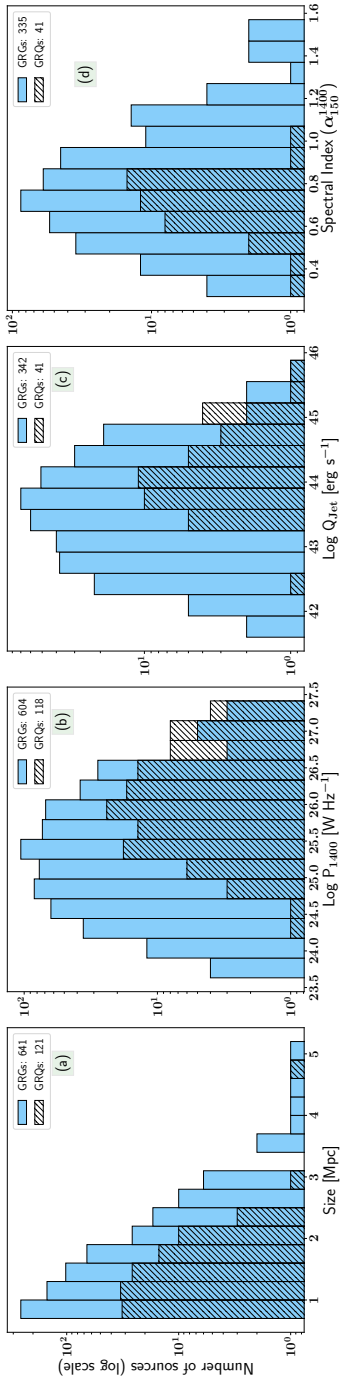

Figure 4.6: Distributions of the unmatched sample of GRGs and GRQs with their different properties, represented in not-hatched and hatched bins, respectively, in the redshift range of $0.01 < z < 1.0$. The mean and median values of the distributions are given in Table 4.3. Panel a: Size distribution. Panel b: Distribution of the radio power at 1400 MHz (P_{1400}). Panel c: Distribution of the jet kinetic power (Q_{Jet}). Panel d: Spectral index (α_{150}^{1400}) distribution.

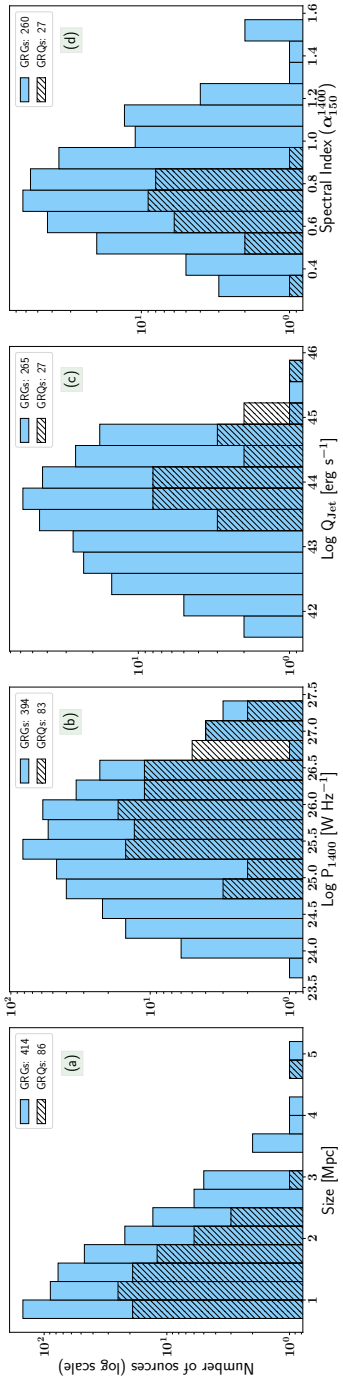

Figure 4.7: Redshift-matched sample of GRG and GRQs in the redshift range of $0.2 < z < 0.8$. The description is same as for Fig. 4.6.

Distribution of the jet kinetic power (Q_{Jet})

The Q_{Jet} of the GRGs and GRQs was estimated using TGSS and the LoTSS, as explained in Sec. 4.3.3. Fig. 4.6 (c) and Fig. 4.7 (c) show the histograms of Q_{Jet} of GRGs and GRQs. It it is evident that the GRQs have higher values of Q_{Jet}, which is also supported by the statistics presented in Table 4.3. From the inverse correlation between jet power and dynamical age, that is, $Q_{Jet} \propto 1/t_{age}^{-2}$ (Ito et al. 2008), it can be inferred that if their sizes are similar, more powerful radio jets of the GRQs would take less time in scaling Mpc distance than the GRGs (if they are placed in an environment of similar ambient density, which is not clear at this stage). Using a sample of 14 GRGs, Ursini et al. (2018) also reported that Q_{Jet} of GRGs lies in the range of $\sim 10^{42}$ erg s^{-1} to 10^{44} erg s^{-1}. It has been observed (Mingo et al. 2014) that some RGs have far higher Q_{Jet} than GRGs, which could be attributed to the severity of the radiative losses suffered by the GRGs over a period of their growth.

Ursini et al. (2018), based on their figure 3, hypothesised that GRGs like RGs at the start of their life have high nuclear luminosities as well as high Q_{Jet}, which eventually fades over a period of time. Because their sample of GRGs was hard X-ray selected, it also shows high nuclear luminosities, and other GRG samples (such as our GRG-catalogue sample), which are radio selected, will occupy the lower luminosity part of Fig. 3 in Ursini et al. (2018). Our findings based on the GRG catalogue support their hypothesis, as we mostly have radio-selected GRGs with L_{bol} in the range of $\sim 10^{42}$ erg s^{-1} to 10^{46} erg s^{-1}, which extends below the L_{bol} range of the Ursini et al. (2018) hard X-ray selected sample of 14 GRGs.

Distribution of the spectral index (α_{150}^{1400})

Fig. 4.6 (d) and Fig. 4.7 (d) shows the histograms of the spectral indices of GRGs and GRQs. A similar criterion (as mentioned in Sec. 4.3.4 and Sec. 4.4.1) of considering only those sources that are fully detected in TGSS (or LoTSS) and NVSS was followed for the sources in the GRG catalogue. The mean value, median value, and the p-values of the K-S and WMW tests (Table 4.3) confirm that the GRGs and GRQs have the same distribution of the spectral index. This result is also consistent with the recent findings of Dabhade et al. (2020b).

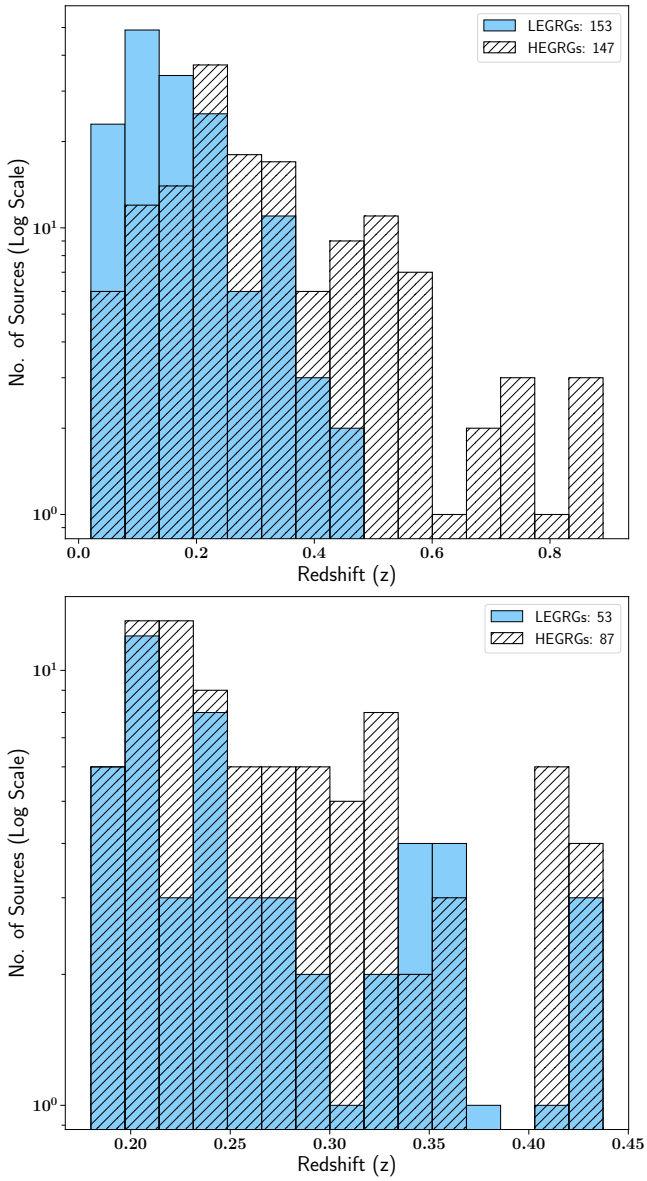

Figure 4.8: The figure shows the redshift (z) distributions of LEGRGs and HEGRGs for $0.02 < z < 0.89$ (unmatched redshift), represented in not-hatched and hatched bins, respectively in the upper plot. Similarly, in lower plot distributions are shown for matched redshift high-z: $0.18 < z < 0.43$ sample of LEGRGs and HEGRGs.

4.5.2 Comparison of the properties of HEGRGs and LEGRGs

Based on the criteria mentioned in Sec. 4.3.9, we classified the GRGs into high- and low-excitation, or HEGRGs and LEGRGs, types. When we consider their respective RG counterparts, called LERGs and HERGs, the LERGs are the dominant population as compared to HERGs. About 12% of the sample of Koziel-Wierzbowska & Stasinska (2012) are HERGs, and is similar for Best & Heckman (2012a). As mentioned previously in Sec. 4.3.9, in order to have a clean sample, we did not consider LERGs or LEGRGs from region III as they are contaminated with possible star formation. Therefore, our LEGRG sample is drastically reduced to 153 because we only considered sources from region II to be LEGRGs. Region I includes 147 HERGs and therefore makes our comparison samples almost equal with each other. In the following subsections, we individually describe the distribution of HEGRGs and LEGRGs in terms of various properties.

The redshift distributions of the HEGRGs and LEGRGs are shown in Fig. 4.8 (upper panel). Their redshifts lie in the range $0.02 < z < 0.89$. We note that the redshift distributions are not the same, and we therefore considered two sub-samples matched in redshifts, whose details are described below.
Low-z: The first sub-sample consists of 27 HEGRGs and 93 LEGRGs in the matched lower redshift range of ~ 0.04 to 0.18. The HEGRGs and LEGRGs have similar mean (LEGRGs: 0.12, and HEGRGs: 0.11) and median (LEGRGs: 0.11, and HEGRGs: 0.10) redshift values as well as the same distribution (K-S test p-value: 0.52 and WMW test p-value: 0.19).
High-z: As shown in Fig. 4.8 (lower), the second sub-sample consists of 87 HEGRGs and 53 LEGRGs in the matched higher redshift range ~ 0.18 to 0.43. They have similar mean (LEGRGs: 0.26, and HEGRGs: 0.27) and median (LEGRGs: 0.24, and HEGRGs: 0.25) redshift values as well as the same distribution (K-S test p-value: 0.47 and WMW test p-value: 0.23).

All three samples of HEGRGs and LEGRGs, that is, the total sample, high-z, and low-z , give similar results in the comparison of their different properties. Therefore, below, we present the results of the total sample and of the high-z sample of HEGRGs and LEGRGs. Fig. 4.9 and Fig. 4.10 show that for each property, the number of sources vary because it is dependent on the availability of data from public archives such as the SDSS, NED, and Vizier.

Distribution of the projected linear size

The projected linear size distributions of LEGRGs and HEGRGs from the GRG catalogue for unmatched and matched redshift samples are shown in Fig. 4.9 (a) and in Fig. 4.10 (a), respectively. Both classes seem to follow different distributions, as indicated by the p-values of the K-S and WMW tests, as shown in Table. 4.3. Our data suggest that HEGRGs tend to grow to larger sizes than the LEGRGs, as seen from their mean and median sizes presented in Table 4.3 for both samples. In other words, the radiatively efficient nature of HEGRGs helps GRGs to grow to larger sizes.

Similarly, when we take a sample of RGs (~ 400 RGs; Koziel-Wierzbowska & Stasinska 2012) for which we have size estimates along with a high- and low-excitation classification (from WISE), we find a similar result: the sizes of high-excitation sources (HERGs) are larger than those of low-excitation sources (LERGs). This particular property is clearly similar for RGs and GRGs and is independent of the overall size of the source.

Distribution of the radio power (P_{1400})

Fig. 4.9 (b) and Fig. 4.10 (b) show P_{1400} distributions of LEGRGs and HEGRGs for unmatched and matched redshift samples, respectively. Based on these, we infer that the HEGRGs spread over a larger range of P_{1400} than LEGRGs. The distributions are different, as is strongly indicated by the p-values of the K-S and WMW tests. Their distributions also overlap significantly, with HEGRGs having higher P_{1400} than LEGRGs, as shown in Table. 4.3. This result complements the fact that HEGRGs are in a high-accretion state, resulting in the high radio power of GRGs. Koziel-Wierzbowska & Stasinska (2012) also found that HERGs, like HEGRGs, which are radiatively efficient, have a higher radio power at 1400 MHz.

Distribution of the jet kinetic power (Q_{Jet})

The Q_{Jet} of both the populations varies over a wide range, with HEGRGs occupying the higher end of the distributions, as shown in Fig. 4.9 (c) and Fig. 4.10 (c). The difference in Q_{Jet} is statistically significant; the median $Q_{Jet} \sim 10^{44} \mathrm{ergs}^{-1}$ of HEGRGs is about ten times higher than that of LEGRGs. The high mean and median values of HEGRGs (as shown in Table. 4.3) compared to LEGRGs strongly indicate that the AGNs of GRGs with high-excitation type are responsible for launching higher powered jets, resulting in more radio-luminous sources (higher P_{1400} as above).

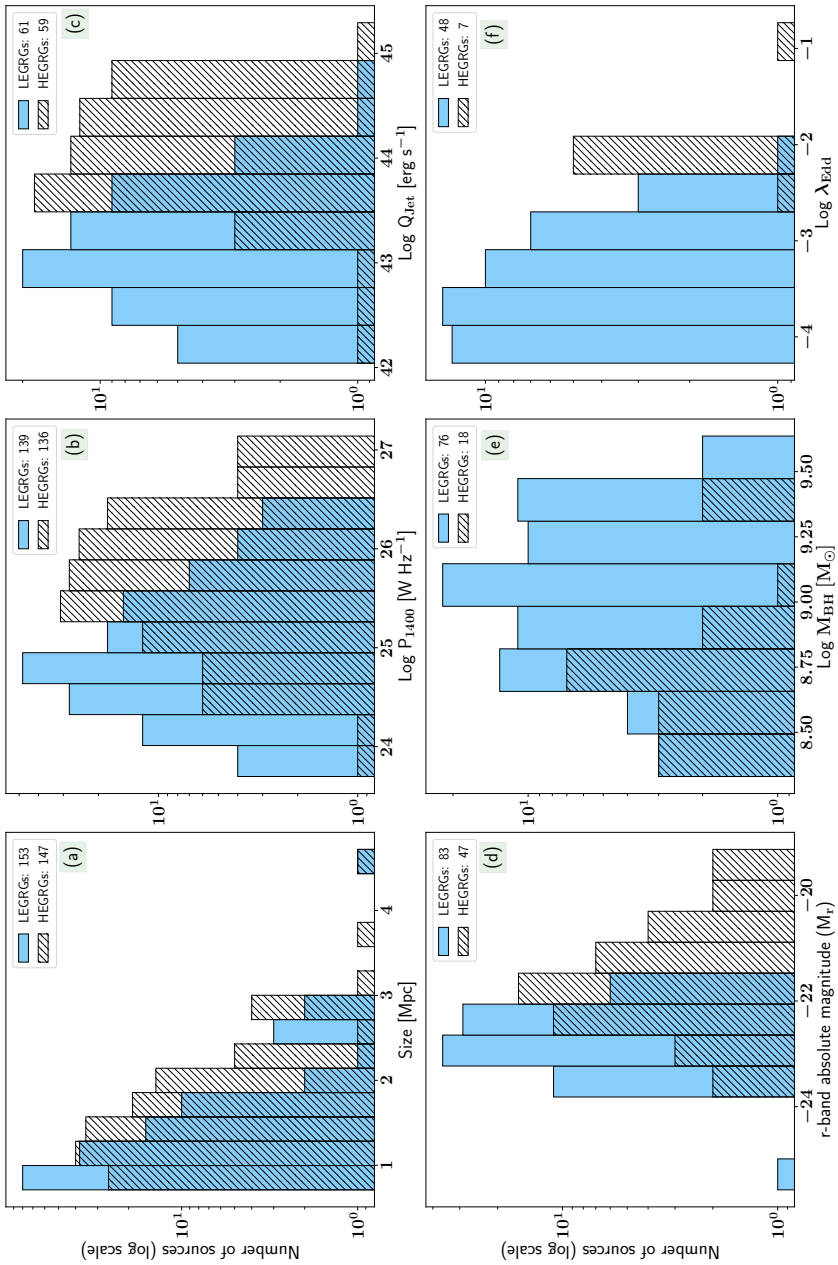

Figure 4.9: Distributions of LEGRGs and HEGRGs according to their various physical properties. They are represented in not-hatched and hatched bins, respectively, in the redshift range of $0.01 < z < 1.0$. The mean and median values of the distributions are given in Table 4.3. Panel a: Distribution of the physical size (Mpc). Panel b: Distribution of the radio power at 1400 MHz (P_{1400}). Panel c: Distribution of the jet kinetic power (Q_{Jet}). Panel d: Distribution of the absolute r-band magnitude (M_r). Panel e: Distribution of the black hole mass (M_{BH}). Panel f: Distribution of the Eddington ratio (λ_{Edd}).

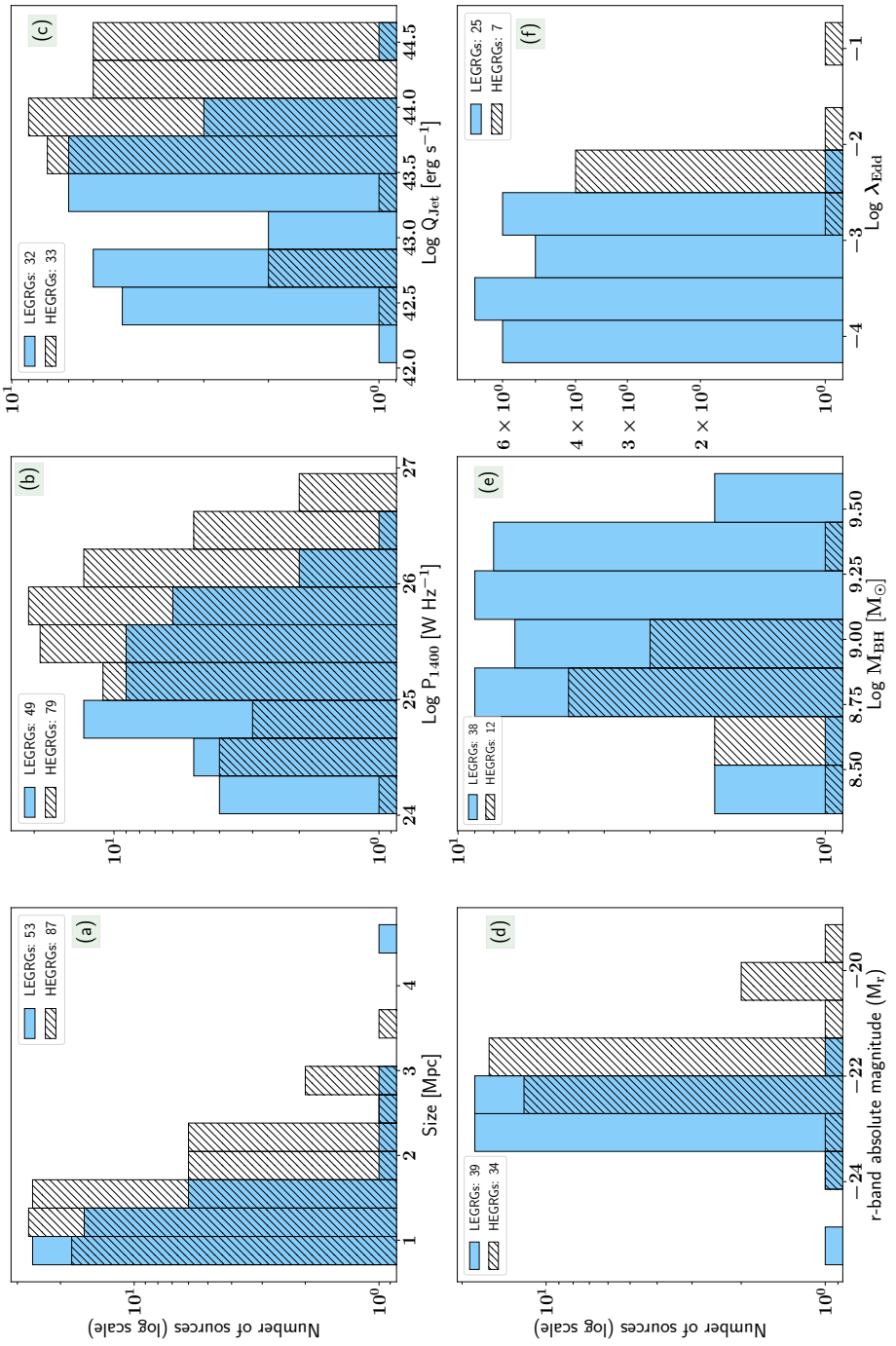

Figure 4.10: Redshift-matched samples of LEGRGs and HEGRGs in the range $0.18 < z < 0.43$. The description is same as for Fig. 4.9.

Distribution of the absolute r-band magnitude (M_r)

The distributions of M_r in unmatched and matched redshift bins of LEGRGs and HEGRGs are presented in Fig. 4.9 (d) and Fig. 4.10 (d). These figures show two distinct populations, and this is also supported by the low p-value of the K-S and WMW tests (Table 4.3). The LEGRGs are found to be optically brighter by ~ 1 magnitude than HEGRGs, indicating that LEGRGs are mostly hosted by bright giant elliptical galaxies comprising an old stellar population, which is quite prominently visible from their absolute r-band magnitudes. This is consistent with the findings of Hardcastle et al. (2007), who have shown this for LERGs.

Overall, Fig. 4.9 (d) and Fig. 4.10 (d) show the M_r distribution of GRGs, which ranges from ~ -19 to -25 in brightness. A similar distribution has been observed for host galaxies of normal-sized RGs (Govoni et al. 2000; Sadler et al. 2007; Capetti et al. 2017).

Distribution of the black hole mass (M_{BH})

A study of the M_{BH} distribution in LEGRGs and HEGRGs is very crucial for understanding one of the key factors driving the two different accretion modes. For this study, our sample was restricted to 94 sources (unmatched redshift sample) based on the availability of the spectroscopic data from the SDSS. Fig. 4.9 (e) (unmatched redshift sample) and Fig. 4.10 (e) (matched-redshift sample) show the distributions of M_{BH} in these two classes, in which the mean and median (see Table. 4.3) of LEGRGs are found to be greater than HEGRGs. The higher values of mean and median of the M_{BH} of LEGRGS compared to HEGRGs as well as the low p-value of the K-S and WMW tests implies that HEGRGs have lower M_{BH} than LEGRGs.

Distribution of the Eddington ratio (λ_{Edd})

In this study, the sample was restricted to just 55 (unmatched redshift sample) because of the availability of reliable [OIII] line flux data from the SDSS, which is essential for estimating the L_{bol}. Out of this, a total of 48 GRGs are classified as LEGRG, and 7 are classified as HEGRG in the GRG catalogue based on their mid-IR properties. Nearly 87% of the sample are LEGRGs, which is consistent with earlier studies (Hardcastle 2018a), which showed that LERGs are the dominant population of radio galaxies. LERGs or LEGRGs are dominated by the radiatively inefficient accretion flow, or RIAF (Yuan & Narayan 2014). In Fig. 4.9 (f) and Fig. 4.10 (f) we observe the distribution of the λ_{Edd} , which ranges from $\sim 10^{-4}$ to 10^{-2} for

LEGRGs and from 10^{-2} to 10^{-1} for HEGRGs, with a little overlap. The lower λ_{Edd} values of (Table 4.3) of LEGRGs implies a radiatively inefficient state governed by a low accretion rate. HEGRGs, in contrast to LEGRGs, are rarer and have a comparatively higher λ_{Edd} (Table 4.3), indicating their radiatively efficient mode and higher accretion rate. Our results for GRGs are similar to previous findings for RGs by Koziel-Wierzbowska & Stasinska (2012), Smolčić (2009), and Best & Heckman (2012a), who have shown that λ_{Edd} is higher for HERGs than for LERGs. The λ_{Edd} of LEGRGs peaks around 10^{-4}, which is consistent with the findings presented in Ho (2008).

HEGRG-LEGRG comparison overview

In the six subsections above we compared HEGRGs to LEGRGs by comparing several properties of LEGRGs and HEGRGs in the total sample as well as redshift-matched ones. The results are similar: (a) The HEGRGs tend to be larger, more luminous, and have a higher jet power than LEGRGs, (b) LEGRGs are optically brighter by ~ 1 magnitude than HEGRGs, (c) LEGRGs have lower Eddington ratios, harbour higher mass black holes, and launch lower power jets (by a factor of 10) than HEGRGs. This implies that higher mass black holes grow in the nucleus of optically brighter and more massive galaxies, whose central engines are presently found in low-excitation, radiatively inefficient, low mass accretion state but are capable of producing sufficiently powerful FR-II jets that result in Mpc-scale GRGs, which clearly constitute the vast majority ($> 80\%$) of all GRGs selected in our study. Although it is beyond the scope of this work, it will be useful in future when the detailed properties of LERGs are compared with LEGRGs and HERGs with HEGRGs in order to gain much deeper insight into the inner workings of the GRG central engine.

4.5.3 How similar are GRGs and RGs ?

The following studies were carried out to understand the factors that cause a very small population of RGs to transform into GRGs. We carried out this investigation by studying three of their properties: α, M_{BH} , and λ_{Edd}, in this section. Possible differences in black hole spin and their implications are discussed in Sec. 4.5.4.

Table 4.3: Mean and median values of the properties of the sources in the GRG catalogue for comparison between their sub-types like GRG-GRQ, HEGRG-LEGRG, and GRG-RG. The p-values correspond to K-S and WMW tests for the respective distributions. The GRG-GRQ comparison of properties is shown in Fig. 4.6 for unmatched redshift sample and Fig. 4.7 for the matched-redshift sample. Fig. 4.9 shows the distribution of HEGRGs and LEGRGs for unmatched redshift sample and Fig. 4.10 shows the distribution for matched redshift sample.

Property	No of sources	Mean	Median	No of sources	Mean	Median	K-S test p-value	WMW test p-value
$[0.01 < z < 1$ (unmatched)]		GRG			GRQ			
Size [Mpc]	641	1.26	1.09	121	1.35	1.23	7.01×10^{-3}	2.31×10^{-3}
P_{1400} [W Hz^{-1}]	604	8.53×10^{25}	2.09×10^{25}	118	26.22×10^{25}	9.09×10^{25}	1.23×10^{-16}	8.23×10^{-22}
Q_{Jet} [erg s^{-1}]	342	13.23×10^{43}	4.03×10^{43}	41	37.85×10^{43}	12.30×10^{43}	2.98×10^{-5}	7.46×10^{-7}
α_{150}^{1400}	335	0.75	0.73	41	0.72	0.75	0.14	0.43
$[0.2 < z < 0.8$ (matched)]		GRG			GRQ			
Size [Mpc]	414	1.32	1.20	86	1.40	1.29	2.28×10^{-2}	2.14×10^{-2}
P_{1400} [W Hz^{-1}]	394	11.19×10^{25}	3.04×10^{25}	83	21.98×10^{25}	8.72×10^{25}	1.20×10^{-7}	7.88×10^{-11}
Q_{Jet} [erg s^{-1}]	265	14.38×10^{43}	4.60×10^{43}	27	36.52×10^{43}	12.20×10^{43}	5.18×10^{-4}	1.02×10^{-4}
α_{150}^{1400}	260	0.77	0.75	27	0.70	0.73	0.14	0.06
$[0.02 < z < 0.89$ (unmatched)]		HEGRG			LEGRG			
Size [Mpc]	147	1.45	1.34	153	1.12	0.97	5.46×10^{-11}	1.11×10^{-11}
P_{1400} [W Hz^{-1}]	136	11.29×10^{25}	4.94×10^{25}	139	1.68×10^{25}	0.65×10^{25}	2.56×10^{-24}	1.50×10^{-24}
Q_{Jet} [erg s^{-1}]	59	20.66×10^{43}	10.20×10^{43}	61	2.70×10^{43}	0.95×10^{43}	3.71×10^{-15}	4.01×10^{-14}
M_r	47	-21.67	-21.84	83	-22.75	-22.76	1.20×10^{-11}	4.74×10^{-13}
M_{BH} [$M_\odot$]	18	0.72×10^{9}	0.52×10^{9}	76	1.26×10^{9}	1.11×10^{9}	2.24×10^{-4}	1.20×10^{-4}
λ_{Edd}	7	3.25×10^{-2}	8.15×10^{-3}	48	6.75×10^{-4}	2.86×10^{-4}	5.72×10^{-6}	1.82×10^{-5}
$[0.18 < z < 0.43$ (matched)]		HEGRG			LEGRG			
Size [Mpc]	87	1.42	1.35	53	1.21	1.05	3.12×10^{-3}	2.34×10^{-4}
P_{1400} [W Hz^{-1}]	79	8.26×10^{25}	4.51×10^{25}	49	2.79×10^{25}	1.22×10^{25}	6.83×10^{-6}	6.31×10^{-7}
Q_{Jet} [erg s^{-1}]	33	12.37×10^{43}	8.80×10^{43}	32	3.67×10^{43}	2.15×10^{43}	1.71×10^{-6}	1.19×10^{-6}
M_r	34	-21.84	-21.91	39	-22.71	-22.73	2.91×10^{-7}	1.52×10^{-7}
M_{BH} [$M_\odot$]	12	0.74×10^{9}	0.54×10^{9}	38	1.41×10^{9}	1.20×10^{9}	8.98×10^{-3}	1.57×10^{-3}
λ_{Edd}	7	3.25×10^{-2}	8.15×10^{-3}	25	9.85×10^{-4}	3.11×10^{-4}	4.85×10^{-5}	7.73×10^{-5}
(Matched)		GRG			RG			
M_{BH} [$M_\odot$]	164	1.04×10^{9}	0.84×10^{9}	14543	1.10×10^{9}	0.84×10^{9}	0.86	0.46
λ_{Edd}	99	40.5×10^{-4}	5.41×10^{-4}	12998	60.9×10^{-4}	25.9×10^{-4}	2.78×10^{-14}	1.38×10^{-14}

Spectral index (α)

Several radio spectral index studies of RGs (Kellermann et al. 1969; Oort et al. 1988; Gruppioni et al. 1997; Kapahi et al. 1998; Sirothia et al. 2009; Ishwara-Chandra et al. 2010; Mahony et al. 2016) have established the mean spectral index value to be ~ 0.75. Until recently, it was believed that GRGs have steeper spectral index values. However, Dabhade et al. (2020b), using their large sample of GRGs, found that the spectral index of RGs and GRGs is very similar. Now, with our GRG catalogue (which comprises of LoTSS and SGS), we establish this result strongly with a larger (> 250) sample size, as shown in Table 4.3: the mean α for GRGs and GRQs is ~ 0.75 and ~ 0.72, respectively, for the unmatched redshift sample. For the matched-redshift sample, the mean α for GRGs and GRQs is 0.77 and 0.70, respectively. These values are similar to those of the RGs and RQs.

Black hole mass (M_{BH})

Here, in the first point we describe how we derived the redshift matched RG sample for comparison along with its properties. In the second point we describe our sub-sample of GRGs derived from the GRG catalogue. Lastly, in the third point we present the result of our comparative study.

1. RG sample. In order to compare the M_{BH} of GRGs and RGs, we used the RG sample from Best & Heckman (2012a). This RG sample was created using the SDSS DR7 (Abazajian et al. 2009) optical spectroscopic data along with the FIRST and NVSS radio data. This sample has been filtered from star-forming galaxies (SFGs) and only consists of radio-loud AGNs (RLAGNs) or RGs. Furthermore, we used their stellar velocity dispersion (σ) information to compute M_{BH} from the SDSS DR14 database (Abolfathi et al. 2018) through CasJobs*, and retained only galaxies with reliable spectra, that is, a redshift warning flag, ZWarning = 0, from the SDSS DR14 database. Next, only sources with σ in the range of $80 < \sigma < 420$ km s^{-1} were selected based on the criterion provided by Bolton et al. (2012). Lastly, in order to have a more clean and robust sample, we also imposed an additional filter to the sources in the sample to have a σ error smaller than 30%. The redshift range of the RG sample was restricted to the range of 0.034 to 0.534 to match the redshift range of the GRG sample (from the GRG catalogue) used for this study (see below), and

*http://skyserver.sdss.org/CasJobs/

radio-loud quasars were not considered for this study. This reduced the original RG sample of Best & Heckman (2012a) to 14543. We call this sample as BH12 in the remainder of the paper.

2. The GRG sample. In our SGS, only 46 GRGs have spectroscopic data from the SDSS, and only these therefore have M_{BH} estimates derived from the M_{BH}-σ relation. In order to carry out a comparative study of M_{BH} that is statistically significant, we make use of the GRG catalogue. Out of 820 GRGs in the GRG catalogue (including the SGS), 164 have clean, reliable σ information from the SDSS. For the purpose of the M_{BH} RG-GRG comparison study, our sample of GRGs was therefore restricted to 164.

3. Distribution of the black hole mass. Fig. 4.11 (a) shows that the distributions of RGs and GRGs are largely similar. The spread of RGs is wider at the lower end of the plot than for GRGs, but both distributions peak at a similar value and have similar mean and median values (GRG: mean = 1.04×10^9 $M_\odot$, and median = 0.84×10^9 $M_\odot$; RG: mean = 1.10×10^9 $M_\odot$, and median = 0.84×10^9 $M_\odot$). This establishes that both RGs and GRGs have the same M_{BH} distribution, and it is also supported by the K-S and WMW tests, where the p-values are 0.86 and 0.46, respectively.

Eddington ratio (λ_{Edd})

Based on the availability of the [OIII] line flux information from the SDSS, we have the estimates of λ_{Edd} for 99 GRGs from the GRG catalogue and 12998 RGs from BH12, whose distribution is shown in Fig. 4.11 (b). Based on our analysis of the available data, it appears that the RGs and GRGs have different mean and median values (Table. 4.3). The plot shows that the distributions are different, which is statistically evident from the p-value of 2.78×10^{-14} from K-S test and from the p-value of 1.38×10^{-14} from the WMW test. Thus, our data indicate that λ_{Edd} of RGs is higher than that of GRGs. We can further extrapolate and conjecture that GRGs mostly have RIAF as compared to RGs, as almost all the GRGs have $\lambda_{Edd} < 0.01$ (which is the RIAF regime).

4.5.4 Astrophysical processes near accreting black holes in GRGs

In this section we discuss the black hole properties of GRGs based on our estimates of spin, Eddington ratio and jet kinetic power. We also present

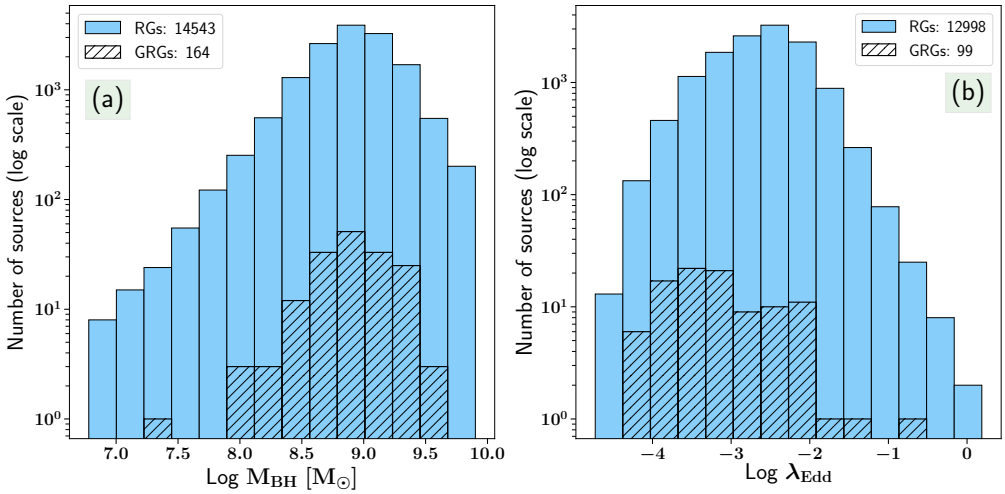

Figure 4.11: Distribution of black hole mass (M_{BH}) in panel (a) and Eddington ratio (λ_{Edd}) in panel (b) of RGs (not-hatched bins) and GRGs (hatched bins). The RG sample has been derived from Best & Heckman (2012a) and the GRG sample is from the GRG catalogue created by us.

the possible astrophysical scenarios leading to the observed properties of GRGs.

Black hole spin (a)

The spin of the accreting black hole has been identified as one of the key ingredients for powering the relativistic jets in AGN for a timescale of millions of years or more. Spin is coupled with the strength and geometry of the magnetic field, and by rearranging equation 4.7, we obtain

$$a \propto \frac{\sqrt{Q_{Jet}}}{B \times M_{BH}}. \tag{4.9}$$

The spin (a) of the black hole of GRGs was estimated using our M_{BH} and Q_{jet} estimates, as explained in Sec. 4.3.8 and given in Table. 4.6. We emphasise here that these are crude estimates based on certain assumptions. We rejected sources with an error of 60% and higher in their M_{BH} estimates, and our sample (GRG catalogue) was therefore restricted to 95 sources for this particular study, as listed in Table 4.6. Fig. 4.12 shows the distribution of black hole spin with respect to M_{BH} varying over two orders of magnitude, that is, 10^7 to 10^9 $M_\odot$. The spin range spans from 0.007 to 0.518, resulting

in mean and median values of 0.079 and 0.055, respectively, for GRGs in our sample. We also plot iso-tracks with their respective colours, which indicate the constant jet kinetic powers obtained for various ranges of spin, M_{BH} , and magnetic field strength.

Fig. 4.12 shows distribution of spin as a function of black hole mass in various bins of Q_{Jet} from 10^{41} erg s^{-1} to 10^{45} erg s^{-1}, which we simulated using equations 4.7 and 4.8. With the plausible values of black hole mass, magnetic field, and spin, clearly no GRG is observed to acquire a $Q_{Jet} \geqslant 10^{45}$ erg s^{-1}. For the objects with a low value of Q_{Jet} ($\sim 10^{41}$ erg s^{-1}), even a drastic change in the magnetic field or M_{BH} would lead to only a minute change in spin, whereas for the objects with higher Q_{Jet} ($\sim 10^{44}$ erg s^{-1}) values, a small change in the magnetic field or M_{BH} would result in a significant change in spin values. Based on our sample, we observe that the spin values of 99% of GRGs are constrained within 0.3. For the source with the highest spin value of 0.518, a correct combination of lower mass and high jet power as compared to the rest of the sources served as a favourable condition. AGNs of both types, that is, with and without powerful jets, have SMBHs that spin rapidly, which in turn implies that spin alone is not the driving factor for the production of powerful relativistic jets. Our spin estimates are based on assuming the maximum possible magnetic field, that is, B_{Edd}, which indicates that these are the lowest possible values. Below we discuss the implications of this result, which is a possible scenario for GRGs.

King & Pringle (2006) reported that if a black hole has a series of accretion episodes whose principal angular momentum vectors are randomly orientated (a chaotic random-walk process), in which the black hole angular momentum dominates, then it leads to lower black hole spin values. However, the successive accretion flows accumulate the poloidal magnetic flux in the vicinity of the black hole, and this strong magnetic flux threading the black hole accretion disc might lead to the state of a magnetically arrested disc (MAD), which affects the dynamical accretion process onto the black hole itself (Narayan et al. 2003; Tchekhovskoy et al. 2011). This state disrupts the accretion flow by breaking the flow into small streams. The velocity of the stream decreases with respect to free-fall velocity as the material in the stream has to find its way to the black hole through magnetic interchange and reconnection, which results in lower spin values of the black hole. Similarly, the low spin value of GRGs can be explained when we invoke the state of MAD, or equivalently, a dynamically important magnetic field B_{dyn}, which indicates that their accretion history was

chaotic rather than a smooth, progressive process. The dynamically important magnetic field field near the black hole has been observationally shown to exist (Eatough et al. 2013).

Another possible scenario might be self-gravity, which fragments the material in the disc into small clouds with randomly oriented angular momentum (Fanidakis et al. 2011). This leads to randomly oriented numerous accretion episodes that collectively lower the spin of the black hole. The lower spin correlating with higher mass black holes (Fig. 4.9) suggests that SMBHs powering the GRGs were perhaps formed in episodes of quasi-isotropic chaotic accretion events.

Alternatively, when we assume a maximally spinning (Thorne limit: $a = 0.998$) black hole (Thorne 1974) for our GRGs, then using our M_{BH} and Q_{Jet} estimates of a sample 95 GRGs, we can set a lower limit on their magnetic field strength (B or B_{dyn}). Thus we obtain the values of B_{dyn} in the range of $1.1 \times 10^2 < B_{dyn} < 1.8 \times 10^4$ G for our GRGs with the mean value of 2.2×10^3 G. These limits on B match the limits given using very long baseline interferometry (VLBI) observations of RLAGN, which can probe the parsec to sub-parsec scale region around the black hole (Zamaninasab & ., et al. 2014; Martí-Vidal et al. 2015; Baczko et al. 2016; Hodgson et al. 2017; Boccardi et al. 2017).

Disc-jet coupling: Interplay between Eddington ratio (λ_{Edd}), spin (a), and jet kinetic power (Q_{Jet})

The role of the black hole spin and accretion rate in launching the observed radio jets is still highly contentious and an unsolved issue (Reynolds 2019). Most often, the jet radio luminosity is taken as a good indicator of the jet kinetic power, but in reality, it is only a small fraction of the latter. The question then is what the source of the radio jet power is that we observe in black hole systems that fuels the extremely large GRGs. How its luminosity scales with the black hole spin and accretion rate is another open question.

The growth and evolution of an AGN is coupled with the accretion phenomenon and the spin of the central black hole. In order to understand the possible co-dependence of various parameters of the black holes for the purpose of jet launching and propagation, we studied how λ_{Edd} affects the Q_{Jet}. We created a sub-sample of 57 GRGs (based on their data availability) from the GRG catalogue and find a linear correlation between the Eddington ratio (λ_{Edd}) and Q_{Jet}/L_{Edd} (dimensionless jet kinetic power), which is strongly supported by the Spearman correlation coefficient of 0.8, as shown in Fig. 4.13 (a). The relation between the two parameters takes the following form:

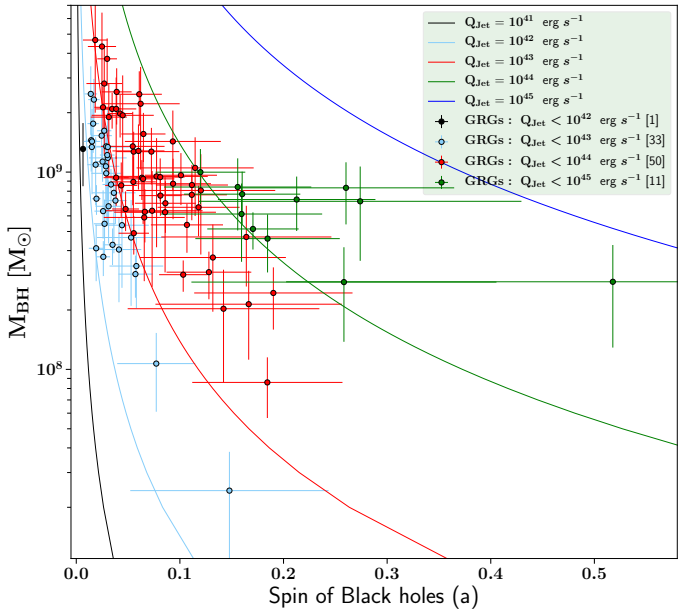

Figure 4.12: Simulation of black hole spin (using Eq. 4.9) as a function black hole mass over various ranges of jet kinetic power. Coloured points represent estimated values from GRG observations. The solid curved lines with their respective colours indicate the different values of spin attainable by a black hole for a mass range of 10^7 $M_\odot$ to 10^9 $M_\odot$ at that particular jet kinetic power. The solid circles with different colours indicate the GRGs in our sample with their estimated spin values lying in the range of jet kinetic power specified. The total number of GRGs is 95. Figures mentioned in the square brackets in the legend of the plot indicate number of GRGs in respective kinetic jet power bins. The magnetic field used to compute the black hole spin (a) was assumed to be B_{Edd}, which is derived from the M_{BH}.

log λ_{Edd} = 0.81 × log(Q_{Jet}/L_{Edd}) − 0.005 based on our data. This implies that L_{bol} has a significant effect on the collimated kinetic jet output (Q_{Jet}) of the AGN because $\lambda_{Edd} = \frac{L_{bol}}{L_{Edd}}$, and the corresponding equation takes the form log L_{bol} = 0.66 × log(Q_{Jet}) + 15.38, as evident from Fig. 4.13 (b). The Spearman correlation coefficient for this correlation is 0.7.

The formation and propagation of highly relativistic magnetised jets is dependent (disc-jet coupling) on the magnetic field strength coupled to magnetic field geometry of the accretion disc (McKinney & Narayan 2007). Zamaninasab & ., et al. (2014) have shown that a strong correlation exists between the jet magnetic field ϕ_{Jet} and the accretion disc luminosity (L_{acc} or L_{bol}). Furthermore, they also concluded that the launching regions of jets

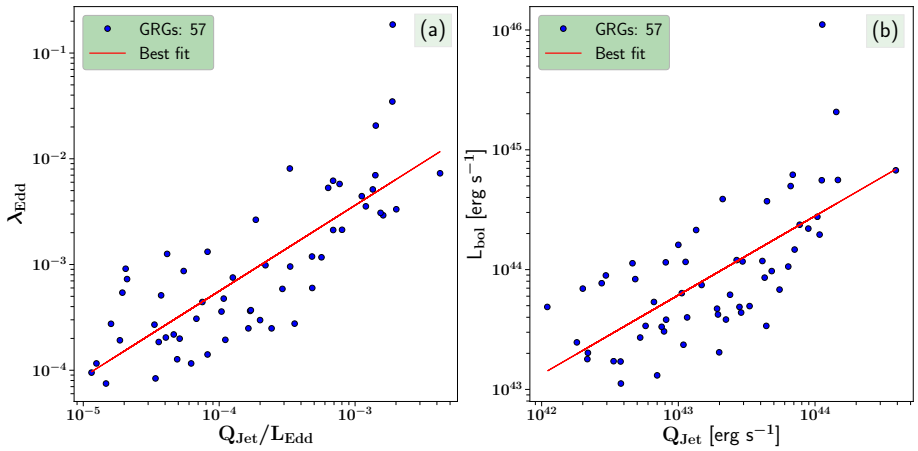

Figure 4.13: As discussed in Sec. 4.5.4, in figure (a) we present a linear correlation for 57 objects between the Eddington ratio (λ_{Edd}) and the ratio of the jet kinetic power (Q_{Jet}) to the Eddington luminosity (L_{Edd}), which can be represented as log λ_{Edd} = 0.81 × log(Q_{Jet}/L_{Edd}) − 0.005. In figure (b), we show the bolometric luminosity (L_{bol}) as a function of jet kinetic power (Q_{Jet}), which takes the equation form log L_{bol} = 0.66 × log(Q_{Jet}) + 15.38. The Spearman correlation coefficient is 0.8 and 0.7 for panels (a) and (b), respectively. The red line indicates the best linear fit of the correlations in the log-log plots.

are threaded by dynamically important magnetic fields with the possible effect of the black hole spin. They strongly favoured the MAD model of the accretion disc. Similarly, Sikora & Begelman (2013) also argued in favour of magnetic flux threading of black hole over spin and Eddington ratio as the governing factor for the launch of collimated powerful radio jets. Zamaninasab & ., et al. (2014) reported that the magnetic flux of the black hole $\phi_{BH} \propto \sqrt{L_{bol}}\ M_{BH}$, and in absence of direct measurements of ϕ_{BH}, we can therefore use L_{bol} as a proxy. Therefore, our L_{bol} - Q_{Jet} correlation (discussed above) is also indicative of a strong effect of ϕ_{BH} on Q_{Jet}. This strongly indicates a disc-jet coupling phenomenon where the magnetic field in the magnetically arrested disc surrounding the black hole controls the dynamics of accretion flow responsible for the jet launching. A lower magnetic field might therefore also be responsible for the lower Q_{Jet} , as evident from Fig. 4.13 (b), where L_{bol} acts as a proxy for the magnetic field (ϕ_{BH}).

In an advection-dominated accretion flow (ADAF, Narayan & Yi 1994),

Q_{Jet} is related to L_{Edd} (Fanidakis et al. 2011) by

$$Q_{Jet} \sim 0.01 a^2 L_{Edd}, \tag{4.10}$$

where Q_{Jet} and L_{Edd} are in erg s^{-1}. This shows that 1% of L_{Edd} at most can be converted into Q_{Jet} when we consider a maximum spin value of 0.998. Based on our analysis, we infer that $\sim$0.06% of L_{Edd} on an average is converted into Q_{Jet} for GRGs. Therefore it is evident from this result and the discussion that for GRGs the fraction of L_{Edd} that is converted into Q_{Jet} is quite low. It is therefore expected that the spin values are lower as well. This matches the estimated spin values we presented in Sec. 4.5.4, where the mean spin value is $\sim$0.079. The spin values for our GRGs were estimated using independently computed Q_{Jet} and M_{BH} values. Here, Q_{Jet} is the lower limit as the Q_{Jet} relation (Eq. 4.3) from Hardcastle (2018b) is expected to underestimate the Q_{Jet} for GRGs, and the spin values are therefore also expected to be the lower limits. From the correlations shown in Fig. 4.13 (a), we expect a significant correlation between the spin and λ_{Edd} as well, represented in the relation $\log \lambda_{Edd} = 1.62 \times \log(a) - 1.02$ based on the same data. The Spearman correlation coefficient for the above is 0.8.

Based on our results, we observe strong evidence of a tight correlation between the spin and λ_{Edd} at least for the lower regime of spin and λ_{Edd} values. Fig. 4.12 clearly shows that the spin value decreases with increasing black hole mass, which is quite consistent with the findings of Daly (2011) and Griffin et al. (2019), but the magnitude of the spin for GRGs is lower than in their sample studies.

Observations (Reynolds 2019) from the X-ray reflection of nearly two dozen SMBHs (prone to bias) have shown that the higher mass black holes ($\geqslant 10^8$ $M_\odot$) tend to have low spin ($a \leqslant 0.7$) values, which is quite similar to our results for the GRGs, although our average spins are much lower. It is not ideal to compare properties of an X-ray selected AGN sample (as mentioned in Reynolds 2019) and radio-selected AGN (like our GRGs).

The two correlations as shown in Fig. 4.13 (a) and Fig. 4.13 (b) together may explain the effect of magnetic field and spin on the kinetic output of relativistic jets. An increment in spin leads to an increment in λ_{Edd}, and this eventually enhances the conversion of L_{Edd} into Q_{Jet}. In other words, the higher the Eddington ratio, the higher the accumulation of magnetic flux near the black hole. leading to saturation of the magnetic field (MAD). It drives the magneto-rotational instabilities, which carry away the angular momentum of the in-falling material, and thus control the accretion

flow. The magnetic flux in the jetted output scales with the magnetic flux threading the black hole. Furthermore, the spin twists the magnetic field lines around the black hole to transfer energy in the form of Poynting flux through jets. The magneto-hydrodynamics and spin of black holes thus play a crucial role in the formation of the powerful jets which could extend to large distances.

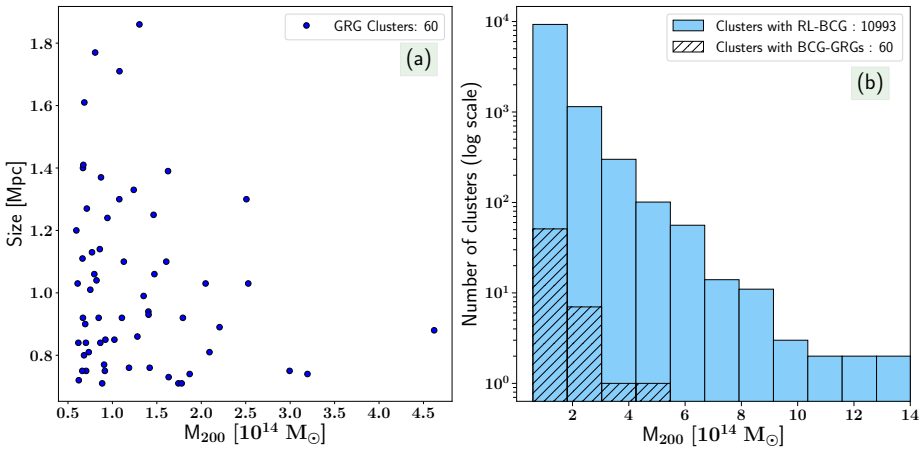

Figure 4.14: Panel (a): Mass of the galaxy cluster hosting the BCG-GRG (x-axis) and size of the GRG (y-axis). Panel (b): Distribution of M_{200} of clusters with radio-loud BCGs and clusters with GRG as BCGs from the GRG catalogue.

4.5.5 Environment analysis

We used the GRG catalogue to determine how many GRGs might be hosted by BCGs in galaxy clusters. To do this, we used the WHL galaxy cluster catalogue, as done for SGS in Sec. 4.4.4. We find that a total of 60 GRGs from the GRG catalogue are BCGs, residing in a dense cluster environment. These 60 BCG-GRGs clearly provide strong evidence that sparse environment alone is not responsible for the large size of all GRGs, and powerful AGNs like these can pierce the dense cluster environment to grow to Mpc scales.

In Fig. 4.14 (a), we explore the relation between the sizes of the GRGs and the M_{200} of the respective galaxy clusters. We observe that GRGs with sizes $\geqslant$ 1 Mpc are not found in clusters with M_{200} greater than 2.5 $\times 10^{14} M_{\odot}$. Fig. 4.14 (b) shows the distribution of M_{200} of clusters with radio-loud BCGs and BCG-GRGs, where we observe that radio-loud BCGs occur

in clusters with a wide range of M_{200}. About 95% of the BCG-GRGs in our sample are located in clusters with M_{200} lower than $2 \times 10^{14} M_{\odot}$. Below we test whether this result is statistically significant. Interestingly, no GRG found to be residing in the cluster environment is observed to grow beyond the virial radius (R_{200}) of the host cluster. Also, we do not find a correlation between the total P_{1400} of the GRGs and the mass of the cluster.

The K-S test on the distributions of M_{200} of BCG-GRGs and radio-loud BCGs gives a p-value of 0.83, which indicates that the two distributions are identical. When we take the ratio of the number of BCG-GRGs to the radio-loud BCGs in the first four mass (M_{200}) bins, we obtain 0.0055, 0.0061, 0.0033, and 0.0099, respectively, with an average value of 0.0062. If we assume this ratio to be true for all mass bins, then this indicates that we should expect that only 0.62 % of the radio-loud BCGs in clusters are GRGs. The cosmological halo mass function of evolving structures shows that the abundance of low-mass clusters is much higher than the abundance of high-mass clusters in the local Universe (Sheth et al. 2001). Moreover, as the number of high-mass clusters is interestingly very low, we obtain an even lower number of radio-loud BCGs hosting GRGs in the cluster environment. For example, when we take the mass bin around $7 \times 10^{14} M_{\odot}$ (6^{th} bin), then there are 14 radio-loud BCGs in this bin. The average value of the ratio, 0.0062, suggests that we needed about 160 clusters of such high masses with a radio-loud BCG to detect at least one GRG. Therefore the probability of finding a radio-loud BCG as a GRG in clusters is indeed very low, and it is very difficult to find them in massive clusters.

We also observe that the radio morphology of BCG-GRGs is not linear and symmetric, but is rather deformed to a certain degree. This clearly illustrates the effect of the environment on the GRGs, which, despite the resistance of the intra-cluster medium and cluster weather, are able to grow to megaparsec scales.

In order to study the environment of the GRGs more thoroughly, we need to determine precisely the fraction of the GRG population that resides in clusters (BCG or a cluster member), which can only be achieved with a controlled and complete sample. We will be focusing on this aspect in our future work within project SAGAN.

4.6 Discussion

Based on our study, we further discuss the overall results in the context of GRGs in this section. Nearly 20-year-old surveys such as the NVSS, when

combined with other radio and optical surveys, still have a high discovery potential. This is evident from the large sample (SGS) of 162 GRGs discovered by us, which increases the overall known GRG population by nearly 25%.

Our GRG compilation work within project SAGAN, which led to the construction of the GRG catalogue, has revealed that GRGs are not as rare as thought before. Nevertheless, the GRG catalogue consists of only 820 sources, which still is quite small compared to the overall RG population. This large compilation of GRGs has enabled us to reveal new properties of these rare sources, leading to a better understanding.

The central engine powering the GRGs is hosted both by galaxies (GRGs) and quasars (GRQs). We studied the key similarities and dissimilarities in their properties to understand the effect of the central powering engine on their respective properties. Our analysis (Sec. 4.5.1) showed that the projected linear size of the GRQs and GRGs is nearly similar (from the homogeneous sample of LoTSS and SAGAN). The GRQs are also more powerful in terms of their central engine, P_{1400} , and Q_{Jet}. This implies that the GRQs might scale megaparsec distances in a shorter time than the GRGs. However, the study of their spectral indices reveals that they have similar distributions and a similar value of the spectral index. It has been shown (Dennett-Thorpe et al. 1999; Ishwara-Chandra & Saikia 2000) previously that the hotspots of RQs are steeper than those of RGs, and the same argument can be applicable to GRQs as well. Thus, the flatter core and steeper hotspots of GRQs counterbalance each other, resulting in a similar spectral index to that of GRGs.

AGNs are broadly classified into two categories: the radiatively efficient (RE) mode, and the radiatively inefficient (RI) mode. In the context of radio galaxies, these modes are referred to as HERGs (RE) and LERGs (RI), and similarly for GRGs, as HEGRGs-LEGRGs. In the literature, these modes are also referred to as the radiative mode (RE) and the jet mode (RI). The quasars lie in the RE mode; and in this discussion we primarily focus on non-quasar AGNs below, which does not include the GRQs.

The GRG-AGN activity (HEGRG and LEGRG) can regulate different characteristics of AGN in terms of radiative efficiency and the formation and powering of relativistic jets. Best & Heckman (2012a) concluded that HERGs are associated with lower mass black holes with higher accretion rates than LERGs. A similar picture is reflected in the properties of HEGRGs and LEGRGs using the GRG catalogue, where our results (Sec.

4.5.2) also show that the λ_{Edd} is higher for HEGRGs than LEGRGs. There is a significant overlap in the distribution of λ_{Edd} of HEGRGs and LEGRGs without a sharp boundary that separates the two populations. This is similar to RGs (Best & Heckman 2012a; Mingo et al. 2014), but the observed overlap might also partly be due to the uncertainties in estimating L_{Bol} and M_{BH}. The high λ_{Edd} implies a high accretion rate in HEGRGs, which might be responsible for producing powerful relativistic jets, which in turn might account for the larger sizes of HEGRGs compared to LEGRGs.

One of the most fundamental properties of the black hole is its mass (M_{BH}). SMBHs residing in AGNs have masses in the range of $\sim 10^7$ to 10^{10} $M_\odot$. The aim of carrying out a comparative study (Sec. 4.5.3) of the AGN properties of RGs and GRGs is to find factors that allow a tiny subset of RGs to grow to GRGs. Although their M_{BH} distribution is very similar, the λ_{Edd} distribution varies: GRGs have predominantly lower values than RGs. Our study clearly rules out the possibility that M_{BH} alone is the crucial factor for driving RGs to GRG scales. AGNs with low values ($\lambda_{Edd} < 0.01$) of the Eddington ratio follow the RIAF model, and our study therefore shows that almost all the GRGs (except for GRQs and a few HEGRGs) seem to be fuelled by radiatively inefficient flows at low accretion rates. Objects with RIAFs have a very low Eddington ratio, and quite often, this cause the absence of the so-called big blue bump. This causes the accretion disc to be under-luminous, and accordingly weak in the X-ray regime (Ho 2008; Hardcastle 2018a). The formation of powerful jets is quite favourable in RIAFs because of the thick-disc structure, which boosts the large-scale poloidal component of the magnetic field, resulting in the launch of collimated jets (Rees et al. 1982; Meier 1999). Interestingly, Bagchi et al. (2014) reached the same conclusion for an extremely unusual GRG hosted by the spiral galaxy 2MASX J23453268-0449256 in an under-dense environment: the launch of powerful FR-II jets in it is facilitated by an advection-dominated, magnetised accretion flow at low Eddington rate onto a supermassive and moderately spinning $a \sim 0.7$ central black hole. Our previous and present results therefore provide fundamental insight into the accretion disc-relativistic jet coupling process in GRGs.

The RGs, as evident from their distribution of λ_{Edd}, have a higher mass accretion rate as well as a high accretion efficiency, which leads to the formation of powerful relativistic jets that reach hundreds of kiloparsecs. We can further conjecture that GRGs at the start of their lives are RGs with higher λ_{Edd}, which diminishes over the period of their growth to GRGs. The SMBHs that grow over a period of time through mergers and coherent

disc accretion are most likely responsible for fast-spinning black holes (such as quasars, Seyferts, and HERGs). On the other hand, the slowly spinning black holes (such as GRGs) with high-mass black holes may have been formed by more isotropic chaotic accretion (Volonteri et al. 2005, 2013; Reynolds 2019).

One of the most striking results obtained from the large sample of GRGs available to us is about their radio morphologies, where we find that FR-II population is dominant. The LoTSS and SGS have $> 90\%$ FR-II type GRGs. The FR-I type GRGs prefer low-excitation type AGN and FR-IIs high-excitation type AGN.

After evaluating all the properties derived by us and their distributions, along with the comparisons with RG samples, it is clear that no one sole factor or parameter, but the correct combination of multiple parameters leads to the growth of GRGs. A possibility to be explored in future studies is estimating and assessing the fueling process of the SMBHs in GRGs in conjunction with their environments.

4.7 Summary

We presented a sample of 162 new GRGs (also called the SAGAN GRG sample, or SGS for short) with a projected linear size above ~ 0.7 Mpc, based on our searches in the NVSS. This investigation used the Proctor (2016) catalogue of probable GRG candidates and employed a visual search for extended sources. The ancillary data from radio surveys such as the FIRST, TGSS, WENSS, and VLASS were very crucial in confirming the morphology of these sources. The identification and classification of the hosts were made using spectroscopic data from the SDSS, Pan-STARRS, and mid-IR data from the WISE survey. As a result, 23 out of 162 radio giants are confirmed to be GRQs, and the remainder are GRGs. The mean and median values of several properties of the GRGs are presented in Table 4.3. A brief summary of our results is given below.

1. GRGs are known to be relatively rare. Considering that only ~ 658 have been known so far, the addition of another 162 new sources increases the known population by $\sim 25\%$. This helps to better study these objects statistically in multiple wavelengths to decipher the reasons for their gigantic nature and rarity.

2. SGS: The projected linear sizes of all sources in SGS lie in the range of ~ 0.71 Mpc to ~ 2.82 Mpc, with P_{1400} as low as 10^{23} W Hz^{-1} at

1400 MHz.

3. SGS: About 92% of the GRGs in SGS have an FR-II morphology. The remaining sample consists of eight FR-I, four HyMoRS, and one DDRG. It is clear that giants are dominated by the FR-II population.

4. The study of GRGs of two AGN types (galaxy or quasar) revealed that the radio power and jet kinetic power are higher in GRQs than in GRGs. This clearly shows that GRQs have more powerful central engines than GRGs. However, the projected linear size and spectral index of the two populations are similar.

5. The study of high- and low-excitation GRGs revealed that those with lower black hole mass, higher accretion efficiency, radio power, and jet kinetic power, that is, the HEGRGs, grow to the maximum extent.

6. We established using our large database of GRGs, the GRG catalogue, that the radio spectral index (between 150 MHz and 1400 MHz) of RGs and GRGs is similar.

7. Assuming a maximum magnetic field, we showed that the black holes hosted by GRGs might be spinning slowly, with a maximum spin up to ~ 0.3, which indicates a chaotic accretion history of the GRG host galaxies.

8. There is a strong correlation between $\lambda_{\rm Edd}$ and the amount of Eddington luminosity that is converted into jet kinetic power. It significantly implies that efficient accretion is responsible for the formation of powerful jets, and disc-jet coupling is at play.

9. GRGs tend to avoid a rich cluster environment, and it is rare to find a GRG in a very massive galaxy cluster of $M_{200} > 2 \times 10^{14} M_{\odot}$. We find 60 GRGs hosted by BCGs in dense cluster environments. The analysis of their projected linear sizes indicated that the size of BCG-GRGs is limited with respect to other GRGs in the same redshift range by the dense ambient medium. Our study and the previous results from the literature clearly show that the local environment indeed plays a role in the growth of GRGs, but is not the sole factor that affects their size.

4.8 Tables

Table 4.4: In Col. (1), Sr.No with superscript 'i' represents the sources found from an independent manual search. Col. (2) and Col. (3) represent the right ascension (RA) in HMS and declination (Dec) in DMS of the host galaxies of the GRGs. Col. (4) represents the host type, where G stands for galaxy and Q stands for quasar. In Col. (5), m_r represents the apparent r-band magnitude of the host galaxy from the SDSS. In Col. (6), z† symbolises spectroscopic redshifts, while the rest are photometric redshift estimates. Col. (7) and Col. (8) list the total projected linear size of the sources in arcmins and megaparsecs, respectively. Col. (9) and Col. (11) list the integrated flux densities (S_ν), and Col.(10) and Col. (12) list the total power P_ν of the sources at 1400 MHz and 150 MHz, respectively. Col. (13) states the α_{150}^{1400} , which is the two-point spectral index between 1400 MHz (NVSS) and 150 MHz (TGSS). Col. (14) contains redshift references ($z_{\rm ref}$), given at the end of the table. Column (15) lists the morphological type of the sources:- I represents FR-I type, II represents FR-II type, HM represents probable HyMoRS type, and RM represents remnant galaxy.

Sr.No	RA	Dec	Type	m_r	z	Size	Size	S_{1400}	P_{1400}	S_{150}	P_{150}	α_{150}^{1400}	$z_{\rm ref}$	Morphology
	(HMS)	(DMS)				(′)	(Mpc)	(mJy)	(10^{25}W Hz^{-1})	(mJy)	(10^{25}W Hz^{-1})			
(1)	(2)	(3)	(4)	(5)	(6)	(7)	(8)	(9)	(10)	(11)	(12)	(13)	(14)	(15)
1	00 04 50.25	12 48 40.10	G	17.18 ± 0.01	0.14300 ± 0.00020†	7.01	1.09	1983 ± 60	11.10 ± 0.36	10048 ± 2010	56.30 ± 11.30	0.73 ± 0.21	12	II
2	00 06 23.24	26 35 44.66	G	21.29 ± 0.08	0.43600 ± 0.18820	4.88	1.71	339 ± 10	22.40 ± 22.90	1705 ± 343	113.00 ± 117.00	0.72 ± 0.21	1	II
3	00 11 19.35	32 17 13.83	G	16.28 ± 0.00	0.10714 ± 0.00002†	7.80	0.95	722 ± 22	2.18 ± 0.07	3564 ± 714	10.80 ± 2.16	0.71 ± 0.21	1	II
4	00 15 02.43	10 10 56.33	G	20.98 ± 0.11	0.41900 ± 0.14980	4.67	1.60	47 ± 2	2.75 ± 2.32	196 ± 41	11.50 ± 10.00	0.64 ± 0.22	1	II
5	00 17 41.45	08 27 55.72	Q	18.82 ± 0.01	0.67841 ± 0.00007†	2.75	1.20	267 ± 8	51.60 ± 2.90	1662 ± 335	321.00 ± 66.30	0.82 ± 0.21	1	II
6	00 18 15.21	21 41 33.42	G	18.51 ± 0.02	0.30256 ± 0.00005†	3.60	1.00	862 ± 26	24.80 ± 0.95	4188 ± 838	121.00 ± 24.30	0.71 ± 0.21	1	II
7	00 26 13.63	11 43 43.66	G	17.82 ± 0.01	0.17500 ± 0.01620	9.72	1.78	582 ± 18	4.90 ± 1.02	2001 ± 405	16.80 ± 4.85	0.55 ± 0.21	1	II
8	00 36 22.99	−02 58 21.55	G	18.97 ± 0.02	0.29400 ± 0.05690	4.51	1.23	188 ± 6	4.96 ± 2.22	745 ± 155	19.70 ± 9.67	0.62 ± 0.22	1	II
9	00 38 09.89	09 36 01.33	G	18.17 ± 0.02	0.29416 ± 0.00005†	4.80	1.30	216 ± 7	5.87 ± 0.23	1089 ± 219	29.60 ± 5.99	0.72 ± 0.21	1	II
10	00 45 17.11	38 25 03.23	G	21.60 ± 0.13	0.89000 ± 0.09560	3.44	1.65	222 ± 7	86.10 ± 23.40	1673 ± 336	649.00 ± 219.00	0.90 ± 0.21	1	II
11	00 46 53.63	12 55 41.01	G	18.54 ± 0.02	0.26400 ± 0.06240	4.10	1.03	135 ± 4	2.85 ± 1.54	613 ± 124	12.90 ± 7.45	0.68 ± 0.21	1	II
12^i	00 55 48.79	−22 31 16.50	G	-	0.11437 ± 0.00015†	6.25	0.80	179 ± 6	0.61 ± 0.02	555 ± 115	1.89 ± 0.39	0.51 ± 0.22	2	II
13	01 00 52.60	06 16 41.01	G	15.72 ± 0.00	0.11100 ± 0.00700	5.76	0.72	195 ± 6	0.63 ± 0.09	660 ± 135	2.12 ± 0.52	0.55 ± 0.21	1	II
14	01 02 37.34	04 21 00.26	G	18.44 ± 0.01	0.29200 ± 0.01000	4.20	1.14	312 ± 9	8.23 ± 0.72	1404 ± 283	37.00 ± 8.06	0.67 ± 0.21	6	II
15	01 03 40.05	42 39 35.63	G	16.26 ± 0.00	0.13500 ± 0.00720	6.90	1.02	530 ± 16	2.58 ± 0.31	2039 ± 409	9.94 ± 2.30	0.60 ± 0.21	1	II
16	01 03 56.32	32 06 07.83	G	17.05 ± 0.01	0.12600 ± 0.01290	6.20	0.87	205 ± 6	0.88 ± 0.20	-	-	-	1	HM?
17	01 08 03.52	27 00 01.99	G	19.21 ± 0.02	0.32700 ± 0.05530	4.00	1.17	696 ± 21	23.60 ± 9.30	3087 ± 618	105.00 ± 46.20	0.67 ± 0.21	1	II
18	01 09 36.45	25 24 03.76	G	22.07 ± 0.16	0.58100 ± 0.04760	3.43	1.39	202 ± 6	28.90 ± 5.91	1729 ± 347	247.00 ± 70.50	0.96 ± 0.21	1	II
19	01 11 04.70	−14 22 32.60	G	-	0.10406 ± 0.00015†	6.75	0.80	402 ± 12	1.11 ± 0.04	996 ± 201	2.75 ± 0.56	0.41 ± 0.21	2	II
20^i	01 12 22.34	−28 16 26.60	Q	-	0.65312 ± 0.00015†	3.61	1.55	46 ± 2	7.78 ± 0.38	-	-	-	2	HM?
21	01 13 41.11	01 06 08.52	G	18.48 ± 0.01	0.28100 ± 0.00001	4.26	1.12	383 ± 12	9.36 ± 0.35	1858 ± 373	45.40 ± 9.15	0.71 ± 0.21	1	II
22	01 14 30.75	05 08 30.64	G	17.22 ± 0.01	0.20456 ± 0.00003†	6.50	1.35	229 ± 7	2.73 ± 0.10	902 ± 181	10.70 ± 2.17	0.61 ± 0.21	1	II
23^i	01 14 40.34	−36 16 31.80	G	-	0.11207 ± 0.00011†	7.04	0.89	61 ± 3	0.20 ± 0.01	-	-	-	2	I
24	01 23 59.92	43 12 55.78	G	19.84 ± 0.03	0.40900 ± 0.05650	4.90	1.65	436 ± 13	25.10 ± 8.27	2326 ± 471	134.00 ± 51.70	0.75 ± 0.21	1	II
25	01 25 32.16	07 03 37.11	G	15.91 ± 0.00	0.09800 ± 0.01010	10.40	1.17	98 ± 4	0.25 ± 0.06	-	-	-	1	II
26	01 28 48.89	24 31 52.10	G	16.12 ± 0.01	0.16455 ± 0.00002†	5.45	0.95	100 ± 4	0.76 ± 0.03	-	-	-	1	II
27	01 33 27.24	−08 24 16.52	G	15.93 ± 0.00	0.14893 ± 0.00013†	5.70	0.92	234 ± 7	1.40 ± 0.05	878 ± 178	5.27 ± 1.07	0.59 ± 0.21	1	II
28	01 35 36.11	50 40 38.54	G	19.84 ± 0.04	0.47600 ± 0.01810	4.59	1.68	86 ± 3	6.49 ± 0.68	285 ± 61	21.40 ± 5.07	0.53 ± 0.23	1	II
29	01 42 08.56	−06 41 43.4	G	15.13 ± 0.00	0.12447 ± 0.00015†	6.45	0.89	138 ± 5	0.56 ± 0.02	431 ± 89	1.75 ± 0.36	0.51 ± 0.22	2	II

Table 4.4: continued.

Sr.No	RA (HMS)	Dec (DMS)	Type	m_r	z	Size	Size	S_{1400}	P_{1400}	S_{150}	P_{150}	α_{150}^{1400}	z_{ref}	Morphology
						(′)	(Mpc)	(mJy)	(10^{25}W Hz^{-1})	(mJy)	(10^{25}W Hz^{-1})			
(1)	(2)	(3)	(4)	(5)	(6)	(7)	(8)	(9)	(10)	(11)	(12)	(13)	(14)	(15)
30	01 48 49.35	06 22 43.26	G	19.03 ± 0.03	0.32000 ± 0.03650	3.34	0.96	445 ± 13	15.00 ± 3.99	2724 ± 545	91.60 ± 30.40	0.81 ± 0.21	1	II
31	01 52 01.00	−30 33 19.00	G	-	0.16999 ± 0.00021†	5.22	0.94	57 ± 2	0.46 ± 0.02	-	-	-	3	II
32	01 58 26.09	24 51 36.38	G	16.59 ± 0.01	0.17660 ± 0.00002†	5.00	0.92	81 ± 3	0.69 ± 0.03	288 ± 60	2.48 ± 0.52	0.57 ± 0.22	1	II
33	02 25 27.01	−31 37 37.00	G	-	0.11000 ± 0.00021†	5.71	0.71	85 ± 3	0.27 ± 0.01	314 ± 77	0.99 ± 0.24	0.58 ± 0.26	3	II
34	03 21 25.91	18 06 09.84	G	14.12 ± 0.00	0.06155 ± 0.00014	11.85	0.87	260 ± 8	0.25 ± 0.01	-	-	-	4	I
35	03 21 55.75	43 46 40.78	G	18.21 ± 0.02	0.36530 ± 0.01000	3.28	1.03	401 ± 12	18.70 ± 1.43	2985 ± 597	139.00 ± 29.60	0.90 ± 0.21	5	II
36	03 25 33.95	−39 27 26.80	G	-	0.06300 ± 0.00015†	12.41	0.93	209 ± 7	0.21 ± 0.01	-	-	-	18	II
37	03 42 53.70	−06 52 24.40	G	20.72 ± 0.07	0.55200 ± 0.03330	4.08	1.62	289 ± 9	31.60 ± 4.87	1180 ± 238	129.00 ± 32.50	0.63 ± 0.21	6	II
38	03 49 10.95	05 34 26.69	G	18.34 ± 0.02	0.33500 ± 0.04710	5.06	1.50	82 ± 3	3.01 ± 0.99	-	-	-	1	II
39[i]	03 50 45.56	−18 18 29.80	G	-	0.17474 ± 0.00015†	5.50	1.01	141 ± 5	1.19 ± 0.04	555 ± 114	4.71 ± 0.96	0.62 ± 0.21	2	II
40	03 53 39.31	−01 13 19.73	G	16.85 ± 0.01	0.19100 ± 0.00970	5.69	1.12	199 ± 6	2.08 ± 0.25	970 ± 196	10.10 ± 2.35	0.71 ± 0.21	1	II
41	04 22 34.14	−26 16 43.20	G	-	0.13100 ± 0.05000†	5.72	0.83	1333 ± 40	6.15 ± 5.08	5957 ± 1191	27.50 ± 23.40	0.67 ± 0.21	7	II
42	04 39 32.51	−23 31 08.60	G	-	0.07457 ± 0.00015†	9.95	0.87	265 ± 8	0.38 ± 0.01	-	-	-	2	HM?
43	05 15 36.11	15 18 21.31	G	19.38 ± 0.06	0.33100 ± 0.03880	5.14	1.51	66 ± 2	2.38 ± 0.66	382 ± 78	13.70 ± 4.69	0.79 ± 0.21	1	II
44	05 43 59.77	30 47 48.28	G	18.31 ± 0.07	0.30900 ± 0.04670	4.32	1.21	64 ± 2	1.93 ± 0.68	314 ± 65	9.48 ± 3.85	0.71 ± 0.22	1	II
45	06 12 03.50	−32 57 47.00	G	-	0.07791 ± 0.00015†	10.38	0.95	341 ± 11	0.52 ± 0.02	1017 ± 207	1.55 ± 0.32	0.49 ± 0.21	8	II
46	06 44 08.04	10 43 41.40	G	14.56 ± 0.00	0.24177 ± 0.01000	11.95	2.82	250 ± 8	4.41 ± 0.44	-	-	-	5	II
47	07 08 44.11	30 30 12.73	G	21.08 ± 0.07	0.55200 ± 0.05740	3.96	1.57	103 ± 4	11.60 ± 2.98	495 ± 102	55.80 ± 18.30	0.70 ± 0.22	1	II
48	07 25 38.75	40 04 12.52	G	16.16 ± 0.00	0.16148 ± 0.00002†	4.89	0.84	98 ± 3	0.71 ± 0.02	-	-	-	1	II
49	07 28 05.86	50 34 45.80	G	-	0.35000 ± 0.05000	3.96	1.21	927 ± 28	38.60 ± 13.00	6131 ± 1227	255.00 ± 99.50	0.85 ± 0.21	15	II
50	07 32 05.49	15 58 31.06	G	18.56 ± 0.01	0.23100 ± 0.03070	6.20	1.41	326 ± 10	5.56 ± 1.68	3534 ± 708	60.20 ± 21.80	1.07 ± 0.21	1	II
51	07 50 21.33	16 32 59.35	G	-	0.58500 ± 0.06800	4.41	1.80	185 ± 6	26.10 ± 7.45	1355 ± 273	191.00 ± 66.40	0.89 ± 0.21	1	II
52	07 59 31.84	08 25 34.59	G	17.31 ± 0.01	0.12400 ± 0.00890	5.22	0.72	103 ± 4	0.42 ± 0.07	-	-	-	1	RM?
53	08 29 41.34	22 47 58.41	G	18.31 ± 0.01	0.25700 ± 0.02960	5.42	1.34	183 ± 6	3.81 ± 1.01	1307 ± 263	27.20 ± 9.01	0.88 ± 0.21	1	II
54	08 47 18.28	42 23 41.33	G	19.97 ± 0.04	0.47498 ± 0.00003†	3.28	1.20	348 ± 11	29.10 ± 1.35	2181 ± 437	182.00 ± 37.10	0.82 ± 0.21	1	II
55	08 47 46.06	38 31 39.33	Q	16.56 ± 0.00	0.31399 ± 0.00001†	5.10	1.45	86 ± 3	2.72 ± 0.10	-	-	-	1	II
56	08 53 49.78	14 52 26.04	G	14.80 ± 0.00	0.06933 ± 0.00002†	9.18	0.75	127 ± 4	0.15 ± 0.01	-	-	-	1	II
57	08 56 32.99	59 57 46.89	Q	16.72 ± 0.00	0.28347 ± 0.00003†	4.00	1.06	222 ± 7	5.70 ± 0.22	1406 ± 281	36.00 ± 7.26	0.83 ± 0.21	1	II
58	09 01 11.78	29 43 38.00	G	17.31 ± 0.01	0.21979 ± 0.00003†	4.30	0.94	502 ± 15	7.18 ± 0.22	-	-	-	1	II
59	09 01 23.31	19 14 17.12	G	17.87 ± 0.01	0.27649 ± 0.00004†	4.36	1.13	337 ± 10	7.81 ± 0.29	1416 ± 286	32.80 ± 6.67	0.64 ± 0.21	1	II
60	09 06 40.80	14 25 22.97	G	17.01 ± 0.00	0.12600 ± 0.01180	8.33	1.16	25 ± 2	0.11 ± 0.02	-	-	-	1	II
61	09 08 39.13	59 45 12.82	G	17.04 ± 0.01	0.24004 ± 0.00003	5.55	1.30	123 ± 4	2.05 ± 0.08	441 ± 90	7.37 ± 1.51	0.57 ± 0.21	1	II
62	09 22 56.47	24 53 23.68	Q	18.35 ± 0.01	0.95360 ± 0.00024†	2.94	1.44	160 ± 5	69.30 ± 4.89	1000 ± 208	433.00 ± 94.00	0.82 ± 0.22	1	II
63	09 24 38.24	30 28 37.14	Q	18.20 ± 0.01	0.27300 ± 0.00002†	4.85	1.25	108 ± 4	2.50 ± 0.09	-	-	-	1	II
64	09 25 45.01	40 47 39.04	G	19.54 ± 0.03	0.45293 ± 0.00013†	4.74	1.69	106 ± 4	7.85 ± 0.38	610 ± 126	45.00 ± 9.45	0.78 ± 0.22	1	II
65	09 34 21.58	38 23 05.64	G	16.41 ± 0.01	0.12299 ± 0.00004†	5.99	0.82	100 ± 4	0.40 ± 0.02	-	-	-	1	II
66[i]	09 35 46.29	−22 40 17.30	G	-	0.13476 ± 0.00015†	5.55	0.82	26 ± 2	0.13 ± 0.01	-	-	-	2	I
67	09 54 55.43	40 59 14.11	Q	20.21 ± 0.03	0.47798 ± 0.00005†	2.78	1.02	61 ± 2	4.89 ± 0.29	270 ± 67	21.60 ± 5.46	0.66 ± 0.26	1	II
68	10 08 25.61	−03 17 34.82	G	18.04 ± 0.01	0.24600 ± 0.02820	5.53	1.32	206 ± 7	3.79 ± 1.00	1115 ± 235	20.50 ± 6.87	0.76 ± 0.22	1	II
69	10 08 34.30	−21 39 14.00	G	-	0.24600 ± 0.05000†	5.13	1.23	671 ± 20	12.50 ± 5.77	4164 ± 833	77.50 ± 39.00	0.82 ± 0.21	7	II

Table 4.4: continued.

Sr.No	RA	Dec	Type	m_r	z	Size	Size	S_{1400}	P_{1400}	S_{150}	P_{150}	α_{150}^{1400}	z_{ref}	Morphology
	(HMS)	(DMS)				(′)	(Mpc)	(mJy)	(10^{25}W Hz^{-1})	(mJy)	(10^{25}W Hz^{-1})			
(1)	(2)	(3)	(4)	(5)	(6)	(7)	(8)	(9)	(10)	(11)	(12)	(13)	(14)	(15)
70	10 09 43.50	03 37 22.72	G	14.78 ± 0.00	0.10513 ± 0.00002†	6.31	0.75	162 ± 5	0.47 ± 0.01	-	-	-	1	II
71	10 09 45.37	16 25 46.17	G	17.88 ± 0.01	0.20800 ± 0.01490	4.10	0.86	115 ± 4	1.49 ± 0.24	802 ± 164	10.40 ± 2.70	0.87 ± 0.21	1	II
72	10 31 29.21	16 50 24.53	G	18.17 ± 0.01	0.22800 ± 0.01300	5.29	1.19	91 ± 3	1.39 ± 0.19	404 ± 85	6.16 ± 1.52	0.67 ± 0.22	1	II
73[i]	10 46 18.84	−03 26 31.00	Q	18.01 ± 0.01	0.83633 ± 0.00018†	1.99	0.94	30 ± 2	8.65 ± 0.69	129 ± 28	36.80 ± 8.28	0.65 ± 0.23	2	II
74	10 46 32.22	54 35 59.69	Q	17.37 ± 0.01	0.14475 ± 0.00002†	5.90	0.93	288 ± 9	1.66 ± 0.06	1554 ± 312	8.97 ± 1.80	0.75 ± 0.21	1	II
75	10 52 24.06	37 30 04.53	Q	18.70 ± 0.01	0.37417 ± 0.00003†	4.05	1.29	369 ± 11	17.00 ± 0.71	1660 ± 333	76.30 ± 15.50	0.67 ± 0.21	1	II
76	10 53 09.33	26 01 42.13	G	18.86 ± 0.01	0.20300 ± 0.03420	5.54	1.14	315 ± 9	3.77 ± 1.42	1610 ± 322	19.30 ± 8.22	0.73 ± 0.21	1	II
77	10 55 39.78	14 33 52.23	G	18.00 ± 0.01	0.25900 ± 0.03080	4.84	1.20	362 ± 11	7.37 ± 2.01	1722 ± 345	35.00 ± 11.80	0.70 ± 0.21	1	II
78	11 24 22.77	15 09 57.90	G	16.36 ± 0.00	0.17194 ± 0.00003†	5.09	0.92	52 ± 3	0.44 ± 0.02	-	-	-	1	II
79	11 28 00.60	−39 33 16.60	G	-	0.10032 ± 0.00015†	6.84	0.78	194 ± 6	0.51 ± 0.02	737 ± 149	1.92 ± 0.39	0.60 ± 0.21	2	II
80[i]	11 29 46.01	−01 21 40.55	Q	17.53 ± 0.01	0.72638 ± 0.00003†	3.60	1.61	299 ± 9	66.60 ± 3.86	1721 ± 344	383.00 ± 78.90	0.78 ± 0.21	1	II
81	11 35 01.03	34 44 01.65	G	21.79 ± 0.14	0.62100 ± 0.10070	2.75	1.15	84 ± 3	13.00 ± 5.18	491 ± 101	75.70 ± 33.80	0.79 ± 0.22	1	II
82	11 40 53.13	25 25 46.53	Q	17.74 ± 0.01	0.29878 ± 0.00002†	3.97	1.09	360 ± 11	10.00 ± 0.39	1622 ± 326	45.00 ± 9.11	0.67 ± 0.21	1	II
83	11 43 44.42	22 29 06.80	G	16.56 ± 0.00	0.18079 ± 0.00003†	4.23	0.80	43 ± 2	0.40 ± 0.02	-	-	-	1	II
84	11 44 27.19	37 08 31.87	G	16.24 ± 0.00	0.11482 ± 0.00002†	6.64	0.86	2079 ± 62	7.24 ± 0.23	9212 ± 1843	32.10 ± 6.43	0.67 ± 0.21	1	II
85	11 47 38.90	−38 15 42.00	G	-	0.08853 ± 0.00015†	7.43	0.76	639 ± 19	1.29 ± 0.04	2893 ± 580	5.84 ± 1.17	0.68 ± 0.21	2	II
86	11 49 06.70	−12 04 33.00	G	-	0.11700 ± 0.00100†	6.93	0.91	1655 ± 50	6.04 ± 0.22	8270 ± 1654	30.20 ± 6.07	0.72 ± 0.21	11	II
87	12 03 43.71	23 43 04.72	G	16.66 ± 0.01	0.17670 ± 0.00005†	5.59	1.03	409 ± 12	3.59 ± 0.12	1858 ± 374	16.30 ± 3.29	0.68 ± 0.21	1	II
88	12 07 05.20	−27 41 47.00	G	-	0.02507 ± 0.00005†	32.90	1.01	331 ± 11	0.05 ± 0.00	-	-	-	16	I
89	12 08 55.60	46 41 13.79	G	16.12 ± 0.00	0.10096 ± 0.00001†	6.48	0.75	163 ± 5	0.44 ± 0.01	-	-	-	1	I
90	12 16 06.10	20 20 54.80	G	18.39 ± 0.01	0.26300 ± 0.01830	4.21	1.06	213 ± 7	4.37 ± 0.71	792 ± 161	16.20 ± 4.20	0.59 ± 0.21	1	II
91	12 16 15.21	16 24 32.28	G	19.53 ± 0.03	0.45908 ± 0.00003†	5.09	1.83	147 ± 5	10.80 ± 0.51	677 ± 137	49.60 ± 10.20	0.68 ± 0.21	1	II
92	12 24 44.60	−25 44 42.00	G	-	0.16474 ± 0.00015†	5.43	0.95	180 ± 6	1.32 ± 0.05	558 ± 115	4.10 ± 0.85	0.51 ± 0.22	2	II
93	12 39 08.61	00 18 33.00	G	18.90 ± 0.02	0.33005 ± 0.01000	4.70	1.38	153 ± 5	5.27 ± 0.43	663 ± 135	22.90 ± 4.97	0.66 ± 0.21	5	II
94	12 39 44.96	19 54 25.41	Q	17.52 ± 0.01	0.23936 ± 0.00006†	4.38	1.03	121 ± 4	2.05 ± 0.08	524 ± 109	8.87 ± 1.86	0.66 ± 0.22	1	II
95	12 51 54.40	35 19 11.97	G	17.81 ± 0.01	0.20100 ± 0.02060	5.05	1.03	179 ± 6	2.15 ± 0.50	1227 ± 246	14.70 ± 4.49	0.86 ± 0.21	1	II
96	12 52 04.82	−22 26 45.70	G	16.51 ± 0.00	0.13400 ± 0.00860	5.00	0.74	116 ± 4	0.56 ± 0.08	432 ± 100	2.07 ± 0.56	0.59 ± 0.24	1	II
97	12 53 08.78	−01 39 51.73	G	18.65 ± 0.01	0.20507 ± 0.01000	5.29	1.10	169 ± 5	1.99 ± 0.23	541 ± 118	6.37 ± 1.55	0.52 ± 0.23	5	II
98	12 58 09.42	42 11 09.18	G	17.02 ± 0.01	0.24863 ± 0.00004†	4.44	1.07	310 ± 9	5.61 ± 0.21	1133 ± 229	20.50 ± 4.16	0.58 ± 0.21	1	II
99	13 01 52.71	14 48 43.01	G	15.51 ± 0.00	0.13761 ± 0.00002†	5.66	0.85	133 ± 5	0.69 ± 0.02	-	-	-	1	II
100[i]	13 08 40.02	−04 56 45.00	G	-	0.13520 ± 0.00021†	5.03	0.75	67 ± 3	0.33 ± 0.01	-	-	-	3	I
101	13 12 31.35	21 15 43.42	G	17.22 ± 0.01	0.17086 ± 0.00001†	4.78	0.86	460 ± 14	3.80 ± 0.13	2499 ± 501	20.60 ± 4.15	0.76 ± 0.21	1	II
102	13 24 04.20	43 34 07.13	Q	18.27 ± 0.01	0.33789 ± 0.00003†	4.00	1.19	252 ± 8	9.06 ± 0.37	994 ± 200	35.70 ± 7.24	0.61 ± 0.21	1	II
103	13 37 42.35	29 42 23.31	G	15.16 ± 0.00	0.11547 ± 0.00002†	7.12	0.92	221 ± 7	0.75 ± 0.02	443 ± 95	1.50 ± 0.32	0.31 ± 0.22	1	II
104	13 52 28.39	09 35 36.02	G	17.15 ± 0.01	0.14735 ± 0.00001†	5.88	0.94	219 ± 7	1.30 ± 0.04	1054 ± 217	6.28 ± 1.29	0.70 ± 0.21	1	I
105	14 07 00.50	10 09 18.77	G	16.90 ± 0.01	0.14262 ± 0.00002†	5.55	0.86	407 ± 13	2.28 ± 0.07	-	-	-	1	II
106	14 19 47.89	08 14 23.39	G	18.43 ± 0.02	0.32180 ± 0.00005†	3.70	1.07	298 ± 9	9.74 ± 0.39	1318 ± 265	43.10 ± 8.73	0.67 ± 0.21	1	II
107	14 35 48.55	20 13 21.38	Q	18.55 ± 0.01	0.36800 ± 0.00001†	3.20	1.01	153 ± 5	7.07 ± 0.30	925 ± 188	42.70 ± 8.76	0.80 ± 0.21	17	II
108	14 44 08.73	26 01 26.43	G	18.57 ± 0.01	0.22900 ± 0.01890	4.11	0.93	258 ± 8	4.08 ± 0.77	1488 ± 299	23.50 ± 6.44	0.78 ± 0.21	1	II

Table 4.4: continued.

Sr.No	RA (HMS)	Dec (DMS)	Type	m_r	z	Size (′)	Size (Mpc)	S_{1400} (mJy)	P_{1400} (10^{25}W Hz^{-1})	S_{150} (mJy)	P_{150} (10^{25}W Hz^{-1})	α_{150}^{1400}	z_{ref}	Morphology
(1)	(2)	(3)	(4)	(5)	(6)	(7)	(8)	(9)	(10)	(11)	(12)	(13)	(14)	(15)
109[i]	14 49 28.63	−01 16 17.44	G	16.36 ± 0.00	0.20233 ± 0.00003[†]	4.48	0.92	86 ± 3	1.02 ± 0.04	-	-	-	1	II
110	14 53 46.50	22 43 14.96	G	19.16 ± 0.02	0.33200 ± 0.03620	3.71	1.09	125 ± 4	4.57 ± 1.17	756 ± 153	27.60 ± 8.97	0.80 ± 0.21	1	II
111	14 54 43.40	12 25 10.39	G	15.81 ± 0.00	0.12199 ± 0.00002[†]	6.90	0.94	95 ± 3	0.38 ± 0.01	-	-	-	1	II
112	15 01 48.34	43 46 32.50	G	20.29 ± 0.04	0.49979 ± 0.00004[†]	3.78	1.42	326 ± 10	31.70 ± 1.53	2453 ± 498	239.00 ± 49.30	0.90 ± 0.21	1	II
113	15 07 25.32	08 29 44.51	G	14.20 ± 0.00	0.07857 ± 0.00001[†]	8.32	0.77	315 ± 10	0.50 ± 0.02	-	-	-	1	II
114	15 16 11.83	−38 19 21.50	G	-	0.03914 ± 0.00012[†]	17.11	0.82	447 ± 14	0.17 ± 0.01	-	-	-	4	II
115	15 41 31.89	−27 07 36.57	G	-	0.23860 ± 0.01000[†]	4.34	1.01	194 ± 6	3.25 ± 0.33	789 ± 161	13.20 ± 2.97	0.63 ± 0.21	1	II
116	15 46 39.13	01 24 22.04	G	16.27 ± 0.00	0.20836 ± 0.00004[†]	4.40	0.93	158 ± 5	1.94 ± 0.07	564 ± 116	6.94 ± 1.43	0.57 ± 0.21	1	II
117	15 48 17.75	07 25 54.85	G	18.79 ± 0.02	0.24700 ± 0.02740	6.94	1.66	765 ± 23	14.10 ± 3.60	4020 ± 804	74.30 ± 23.90	0.74 ± 0.21	1	II
118	15 51 40.30	10 35 48.66	G	18.00 ± 0.02	0.36824 ± 0.00008[†]	3.95	1.25	517 ± 16	23.20 ± 0.96	2576 ± 515	116.00 ± 23.40	0.72 ± 0.21	1	II
119	16 00 27.78	08 37 43.04	Q	17.64 ± 0.01	0.22687 ± 0.00003[†]	4.58	1.03	946 ± 28	14.40 ± 0.51	4577 ± 916	69.60 ± 14.00	0.71 ± 0.21	1	II
120	16 05 13.74	07 11 52.56	G	18.43 ± 0.01	0.31117 ± 0.00004[†]	4.66	1.32	262 ± 8	8.05 ± 0.32	1287 ± 258	39.50 ± 7.99	0.71 ± 0.21	1	II
121	16 05 30.66	−09 27 28.99	G	-	0.10900 ± 0.00100[†]	6.84	0.84	3399 ± 102	10.70 ± 0.40	17554 ± 3511	55.20 ± 11.10	0.74 ± 0.21	9	II
122	16 11 57.36	07 38 56.19	G	17.80 ± 0.01	0.19000 ± 0.02360	6.60	1.29	150 ± 5	1.56 ± 0.43	790 ± 164	8.20 ± 2.83	0.74 ± 0.22	1	II
123	16 12 42.06	43 13 19.82	G	18.14 ± 0.01	0.25069 ± 0.00003[†]	5.70	1.38	116 ± 4	2.21 ± 0.09	581 ± 119	11.00 ± 2.28	0.72 ± 0.21	1	II
124	16 15 34.52	09 57 09.96	Q	17.18 ± 0.01	0.23423 ± 0.00001[†]	5.18	1.19	106 ± 4	1.74 ± 0.06	-	-	-	1	I
125	17 06 27.63	10 24 53.72	G	19.26 ± 0.02	0.32000 ± 0.04470	5.33	1.54	508 ± 15	17.10 ± 5.58	3173 ± 635	107.00 ± 40.70	0.82 ± 0.21	1	II
126	17 21 07.89	26 24 32.17	G	17.68 ± 0.01	0.16963 ± 0.00002[†]	5.38	0.96	236 ± 7	1.90 ± 0.07	1090 ± 221	8.77 ± 1.78	0.68 ± 0.21	1	II
127[i]	17 21 09.49	35 42 16.09	Q	17.77 ± 0.01	0.28321 ± 0.00002[†]	3.95	1.05	803 ± 24	17.90 ± 0.67	1473 ± 297	32.80 ± 6.67	0.27 ± 0.21	1	II
128	17 31 05.95	24 28 51.85	G	20.59 ± 0.05	0.55200 ± 0.03730	2.84	1.13	288 ± 9	33.20 ± 5.66	1542 ± 310	178.00 ± 46.60	0.75 ± 0.21	1	II
129	17 42 06.97	18 27 20.66	Q	16.49 ± 0.00	0.18588 ± 0.00006[†]	5.70	1.10	1075 ± 32	10.80 ± 0.37	7046 ± 1411	70.90 ± 14.20	0.84 ± 0.21	19	II
130	18 08 23.17	08 41 03.00	G	-	0.04871 ± 0.00012[†]	30.50	1.80	467 ± 15	0.27 ± 0.01	-	-	-	4	HM?
131	18 20 07.41	22 51 20.04	G	18.68 ± 0.02	0.33400 ± 0.01920	4.89	1.45	209 ± 7	7.83 ± 1.09	1401 ± 281	52.50 ± 12.70	0.85 ± 0.21	1	II
132	18 29 38.62	22 30 08.63	G	18.05 ± 0.01	0.24000 ± 0.07050	5.07	1.19	141 ± 5	2.42 ± 1.61	652 ± 136	11.20 ± 7.77	0.69 ± 0.22	1	II
133	19 03 04.60	36 16 50.92	G	-	0.07084 ± 0.00012[†]	10.08	0.84	473 ± 14	0.59 ± 0.02	1280 ± 259	1.60 ± 0.32	0.45 ± 0.21	4	II
134	19 43 49.35	−35 46 46.10	G	-	0.09258 ± 0.00015[†]	8.58	0.91	361 ± 11	0.79 ± 0.03	1373 ± 297	3.02 ± 0.65	0.60 ± 0.22	2	II
135	19 58 30.60	−37 38 26.00	G	-	0.09458 ± 0.00015[†]	13.01	1.41	238 ± 8	0.55 ± 0.02	-	-	-	2	II
136	20 19 38.37	14 17 01.22	G	20.59 ± 0.06	0.23800 ± 0.03980	5.36	1.25	43 ± 2	0.73 ± 0.28	-	-	-	1	II
137	20 40 19.60	−06 59 10.19	G	18.81 ± 0.02	0.39769 ± 0.01000	4.50	1.49	192 ± 6	10.00 ± 0.74	827 ± 167	43.40 ± 9.22	0.65 ± 0.21	5	II
138	20 59 47.18	−25 06 11.03	G	-	0.19953 ± 0.00015[†]	3.85	0.78	116 ± 4	1.28 ± 0.05	381 ± 84	4.23 ± 0.93	0.53 ± 0.23	2	II
139	21 30 39.21	07 35 30.28	G	19.09 ± 0.02	0.32285 ± 0.00002[†]	3.41	0.99	105 ± 4	3.41 ± 0.15	411 ± 89	13.30 ± 2.91	0.61 ± 0.23	1	II
140	21 37 45.20	−14 32 54.90	Q	-	0.20047 ± 0.00001[†]	4.61	0.94	3796 ± 114	44.20 ± 1.52	19593 ± 3919	228.00 ± 45.80	0.73 ± 0.21	14	II
141	21 49 20.70	19 40 43.51	G	18.77 ± 0.02	0.39800 ± 0.07250	4.44	1.47	271 ± 8	14.80 ± 6.40	1548 ± 310	84.80 ± 40.20	0.78 ± 0.21	1	II
142	22 15 36.84	29 02 35.90	Q	15.80 ± 0.00	0.22880 ± 0.00040[†]	4.17	0.94	577 ± 17	8.79 ± 0.31	2351 ± 471	35.80 ± 7.21	0.63 ± 0.21	20	II
143	22 18 15.55	19 31 43.76	G	15.17 ± 0.00	0.10964 ± 0.00002[†]	6.05	0.75	223 ± 7	0.69 ± 0.02	739 ± 149	2.31 ± 0.46	0.54 ± 0.21	1	II
144	22 31 14.32	01 00 41.80	G	17.71 ± 0.01	0.21246 ± 0.00003[†]	7.33	1.57	178 ± 6	2.28 ± 0.09	633 ± 136	8.11 ± 1.75	0.57 ± 0.22	1	II
145	22 32 49.13	−05 29 58.10	Q	17.75 ± 0.01	0.36870 ± 0.00015[†]	2.98	0.94	205 ± 6	9.35 ± 0.32	-	-	-	2	II
146	22 38 36.14	−07 04 57.93	G	18.38 ± 0.01	0.31800 ± 0.01000	6.23	1.79	46 ± 2	1.63 ± 0.14	484 ± 99	17.20 ± 3.76	1.05 ± 0.22	6	II
147[i]	22 46 13.00	−16 54 23.10	G	-	0.70226 ± 0.00018[†]	3.86	1.70	39 ± 2	7.83 ± 0.42	-	-	-	2	II

Table 4.4: continued.

Sr.No	RA	Dec	Type	m_r	z	Size	Size	S_{1400}	P_{1400}	S_{150}	P_{150}	α_{150}^{1400}	z_{ref}	Morphology
	(HMS)	(DMS)				(′)	(Mpc)	(mJy)	(10^{25}W Hz^{-1})	(mJy)	(10^{25}W Hz^{-1})			
(1)	(2)	(3)	(4)	(5)	(6)	(7)	(8)	(9)	(10)	(11)	(12)	(13)	(14)	(15)
148	22 46 21.66	31 42 07.94	G	16.35 ± 0.00	0.19500 ± 0.02080	4.64	0.93	327 ± 10	3.43 ± 0.82	951 ± 192	9.97 ± 3.11	0.48 ± 0.21	1	II
149	22 51 03.39	06 19 25.49	G	17.61 ± 0.01	0.17203 ± 0.00002†	4.81	0.87	97 ± 3	0.77 ± 0.03	256 ± 62	2.04 ± 0.50	0.43 ± 0.25	1	II
150	22 51 25.53	16 07 53.60	G	21.38 ± 0.11	0.42800 ± 0.08770	4.30	1.49	156 ± 6	10.30 ± 5.00	973 ± 202	63.90 ± 33.80	0.82 ± 0.22	1	II
151	22 53 21.28	16 20 16.77	G	19.88 ± 0.03	0.17500 ± 0.08170	9.49	1.74	304 ± 10	2.66 ± 2.74	1748 ± 353	15.30 ± 16.00	0.78 ± 0.21	1	II
152	22 53 56.30	−07 06 38.60	G	18.11 ± 0.01	0.23100 ± 0.11200	8.00	1.82	296 ± 9	4.63 ± 5.06	1266 ± 255	19.80 ± 22.00	0.65 ± 0.21	1	II
153	22 59 34.13	08 20 40.78	G	19.67 ± 0.04	0.40500 ± 0.04420	6.63	2.22	168 ± 5	9.50 ± 2.48	900 ± 183	50.80 ± 16.80	0.75 ± 0.21	1	II
154	23 10 46.70	−21 08 13.90	G	-	0.15216 ± 0.00013†	4.91	0.80	439 ± 13	2.75 ± 0.09	1624 ± 329	10.20 ± 2.07	0.59 ± 0.21	10	II
155	23 16 22.32	22 46 50.28	G	19.10 ± 0.02	0.29400 ± 0.06740	8.47	2.30	91 ± 4	2.49 ± 1.32	-	-	-	1	II
156	23 19 56.30	−27 28 12.40	G	-	0.17420 ± 0.00021†	5.97	1.09	2826 ± 85	24.10 ± 0.81	13186 ± 2637	112.00 ± 22.50	0.69 ± 0.21	3	II
157	23 23 44.52	14 57 59.35	G	15.11 ± 0.00	0.12600 ± 0.01000	6.50	0.91	390 ± 12	1.62 ± 0.28	1107 ± 223	4.59 ± 1.22	0.47 ± 0.21	6	II
158	23 25 11.80	−32 36 34.60	Q	-	0.21600 ± 0.00015†	4.10	0.89	230 ± 7	3.01 ± 0.11	686 ± 138	8.98 ± 1.81	0.49 ± 0.21	13	II
159	23 35 12.35	17 41 50.38	G	18.70 ± 0.01	0.22800 ± 0.06330	6.00	1.36	433 ± 13	6.68 ± 4.18	2190 ± 439	33.80 ± 22.20	0.73 ± 0.21	1	II
160	23 41 37.14	08 28 17.25	G	-	0.24700 ± 0.00004†	7.00	1.68	164 ± 5	3.00 ± 0.11	765 ± 156	14.00 ± 2.87	0.69 ± 0.21	1	II
161	23 48 47.77	16 00 10.32	G	20.25 ± 0.04	0.40274 ± 0.00002†	4.50	1.50	117 ± 4	7.28 ± 0.33	1276 ± 257	79.20 ± 16.10	1.07 ± 0.21	1	II
162	23 59 11.07	17 06 10.97	G	16.34 ± 0.00	0.09940 ± 0.00001†	9.93	1.13	421 ± 13	1.10 ± 0.04	2683 ± 539	7.01 ± 1.41	0.83 ± 0.21	1	II

1- SDSS; Abolfathi et al. 2018, 2 -6dF; Jones et al. 2009, 3 -2dF; Colless et al. 2001, 4 -2MASS; Huchra et al. 2012, 5 - Delli Veneri et al. 2019, 6 - Gao et al. 2018, 7 - McCarthy et al. 1996, 8 - Dressler & Shectman 1988, 9 - Best et al. 1999, 10 - Caretta et al. 2004, 11 - Danziger & Goss 1983, 12 - Drake et al. 2004, 13 - Grupe et al. 1998, 14 - Ho & Kim 2009, 15 - Machalski 1998, 16 - Kaldare et al. 2003, 17 - McGreer et al. 2009, 18 - Ratcliffe et al. 1998, 19 - Véron-Cetty & Véron 2006, 20 - Wei et al. 1998

Table 4.5: The table lists the black hole properties, radio core and jet kinetic power of the SGS. Col.(1) : serial number, Col.(2) : GRG name, Col.(3) : galaxy or quasar type host, Col.(4) σ : velocity dispersion (km s^{-1}) of host galaxies of GRGs, Col. (5) M_{BH} : central black hole mass ($M_{\odot} \times 10^9$) estimated from the M_{BH}-σ relation, Col. (6) $S^c_{1400MHz}$: core flux density at 1400 MHz (FIRST), Col. (7) λ_{Edd} : Eddington ratio, and Col. (8) Q_{Jet} is the jet kinetic power.

Sr.No	Name	Type	σ (km s^{-1})	M_{BH} (10^9 $M_{\odot}$)	$S^c_{1400MHz}$ (mJy)	λ_{Edd} (10^{-4})	Q_{Jet} (10^{43} erg s^{-1})
(1)	(2)	(3)	(4)	(5)	(6)	(7)	(8)
1	SAGANJ000450.25+124840.10	G	-	-	-	-	18.80
2	SAGANJ000623.24+263544.66	G	-	-	-	-	37.60
3	SAGANJ001119.35+321713.83	G	245.65 ± 9.27	0.67 ± 0.14	-	-	3.59
4	SAGANJ001502.43+101056.33	G	-	-	-	-	3.83
5	SAGANJ001741.45+082755.72	Q	-	-	33.4 ± 1.0	-	107.00
6	SAGANJ001815.21+214133.42	G	250.78 ± 18.45	0.75 ± 0.31	-	-	40.20
7	SAGANJ002613.63+114343.66	G	-	-	7.5 ± 0.2	-	5.61
8	SAGANJ003622.99−025821.55	G	-	-	-	-	6.56
9	SAGANJ003809.89+093601.33	G	264.24 ± 24.68	1.01 ± 0.53	0.6 ± 0.2	-	9.86
10	SAGANJ004517.11+382503.23	G	-	-	-	-	216.00
11	SAGANJ004653.63+125541.01	G	-	-	-	-	4.31
12	SAGANJ005548.79−223116.50	G	-	-	-	-	0.63
13	SAGANJ010052.60+061641.01	G	-	-	-	-	0.70
14	SAGANJ010237.34+042100.26	G	-	10.31 ± 0.35	-	-	-
15	SAGANJ010340.05+423935.63	G	-	-	-	-	3.31
17	SAGANJ010803.52+270001.99	G	-	-	-	-	34.90
18	SAGANJ010936.45+252403.76	G	-	-	-	-	82.40
19	SAGANJ011104.70−142232.60	G	-	-	-	-	0.92
21	SAGANJ011341.11+010608.52	G	228.75 ± 32.77	0.45 ± 0.36	1.2 ± 0.2	-	15.10
22	SAGANJ011430.75+050830.64	G	200.27 ± 11.28	0.21 ± 0.07	-	-	3.58
24	SAGANJ012359.92+431255.78	G	-	-	-	-	44.70
25	SAGANJ012532.16+070337.11	G	-	-	1.5 ± 0.2	-	-
26	SAGANJ012848.89+243152.10	G	219.19 ± 12.93	0.35 ± 0.12	-	-	-
27	SAGANJ013327.24−082416.52	G	309.37 ± 8.32	2.45 ± 0.37	22.6 ± 0.7	-	1.76
28	SAGANJ013536.11+504038.54	G	-	-	-	-	7.13
29	SAGANJ014208.56−064143.4	G	-	-	0.5 ± 0.1	-	0.58
30	SAGANJ014849.35+062243.26	G	-	-	-	-	30.50
32	SAGANJ015826.09+245136.38	G	291.95 ± 9.28	1.76 ± 0.32	-	-	0.83
33	SAGANJ022527.01−313737.00	G	-	-	-	-	0.33
35	SAGANJ032155.75+434640.78	G	-	-	-	-	46.50
37	SAGANJ034253.70−065224.40	G	-	-	-	-	43.00
39	SAGANJ035045.56−181829.80	G	-	-	-	-	1.57
40	SAGANJ035339.31−011319.73	G	-	-	-	-	3.38
41	SAGANJ042234.14−261643.20	G	-	-	-	-	9.16
43	SAGANJ051536.11+151821.31	G	-	-	-	-	4.58
44	SAGANJ054359.77+304748.28	G	-	-	-	-	3.16
45	SAGANJ061203.50−325747.00	G	-	-	-	-	0.52
47	SAGANJ070844.11+303012.73	G	-	-	-	-	18.60
48	SAGANJ072538.75+400412.52	G	310.02 ± 8.49	2.48 ± 0.38	39.7 ± 1.2	-	-
49	SAGANJ072805.86+503445.80	G	-	-	-	-	85.10
50	SAGANJ073205.49+155831.06	G	-	-	-	-	20.10
51	SAGANJ075021.33+163259.35	G	-	-	-	-	63.50
53	SAGANJ082941.34+224758.41	G	-	-	2.8 ± 0.2	-	9.08
54	SAGANJ084718.28+422341.33	G	171.43 ± 31.83	0.09 ± 0.09	-	-	60.80
55	SAGANJ084746.06+383139.33	Q	-	-	6.9 ± 0.3	-	-
56	SAGANJ085349.78+145226.04	G	282.38 ± 7.52	1.46 ± 0.22	13.1 ± 0.4	0.64	-
57	SAGANJ085632.99+595746.89	Q	-	-	26.3 ± 0.8	-	12.00
58	SAGANJ090111.78+294338.00	G	250.21 ± 13.82	0.74 ± 0.23	15.7 ± 0.5	29.98	-
59	SAGANJ090123.31+191417.12	G	233.86 ± 21.87	0.51 ± 0.27	-	69.80	10.90
60	SAGANJ090640.80+142522.97	G	-	-	2.6 ± 0.2	-	-
61	SAGANJ090839.13+594512.82	G	305.75 ± 12.38	2.29 ± 0.52	4.3 ± 0.2	-	2.46
62	SAGANJ092256.47+245323.68	Q	-	-	8.9 ± 0.3	-	144.00
63	SAGANJ092438.24+302837.14	Q	-	-	3.9 ± 0.2	-	-
64	SAGANJ092545.01+404739.04	G	215.24 ± 39.17	0.32 ± 0.33	-	-	15.00
65	SAGANJ093421.58+382305.64	G	215.21 ± 17.46	0.32 ± 0.14	2.0 ± 0.2	9.69	-
67	SAGANJ095455.43+405914.11	Q	-	-	3.0 ± 0.2	-	7.19
68	SAGANJ100825.61−031734.82	G	-	-	-	-	6.83
69	SAGANJ100834.30−213914.00	G	-	-	-	-	25.80
70	SAGANJ100943.50+033722.72	G	274.69 ± 7.15	1.25 ± 0.18	13.3 ± 0.4	-	-
71	SAGANJ100945.37+162546.17	G	-	-	-	-	3.47
72	SAGANJ103129.21+165024.53	G	-	-	-	-	2.05
73	SAGANJ104618.84−032631.00	Q	-	-	8.4 ± 0.3	-	12.30

Table 4.5: continued.

Sr.No	Name	Type	σ	M_{BH}	$S^{c}_{1400MHz}$	λ_{Edd}	Q_{Jet}
			(km s^{-1})	(10^9 $M_\odot$)	(mJy)	(10^{-4})	(10^{43} erg s^{-1})
(1)	(2)	(3)	(4)	(5)	(6)	(7)	(8)
74	SAGANJ104632.22+543559.69	Q	-	-	7.8 ± 0.3	-	2.99
75	SAGANJ105224.06+373004.53	Q	-	-	2.0 ± 0.3	-	25.40
76	SAGANJ105309.33+260142.13	G	-	-	1.0 ± 0.2	-	6.43
77	SAGANJ105539.78+143352.23	G	-	-	-	-	11.70
78	SAGANJ112422.77+150957.90	G	269.40 ± 10.48	1.12 ± 0.25	2.3 ± 0.3	3.49	-
79	SAGANJ112800.60−393316.60	G	-	-	-	-	0.64
80	SAGANJ112946.01−012140.55	Q	-	-	7.4 ± 0.2	-	128.00
81	SAGANJ113501.03+344401.65	G	-	-	-	-	25.20
82	SAGANJ114053.13+252546.53	Q	-	-	-	-	15.00
83	SAGANJ114344.42+222906.80	G	323.02 ± 12.69	3.12 ± 0.69	1.5 ± 0.4	0.53	-
84	SAGANJ114427.19+370831.87	G	224.78 ± 9.13	0.40 ± 0.09	4.7 ± 0.4	29.19	10.70
85	SAGANJ114738.90−381542.00	G	-	-	-	-	1.95
86	SAGANJ114906.70−120433.00	G	-	-	-	-	10.10
87	SAGANJ120343.71+234304.72	G	253.57 ± 18.06	0.80 ± 0.32	-	5.99	5.43
89	SAGANJ120855.60+464113.79	G	209.64 ± 6.31	0.27 ± 0.05	63.7 ± 2.0	10.18	-
90	SAGANJ121606.10+202054.80	G	-	-	-	-	5.41
91	SAGANJ121615.21+162432.28	G	216.58 ± 38.15	0.33 ± 0.33	-	-	16.50
92	SAGANJ122444.60−254442.00	G	-	-	-	-	1.37
93	SAGANJ123908.61+001833.00	G	-	-	10.0 ± 0.3	-	7.62
94	SAGANJ123944.96+195425.41	Q	-	-	2.4 ± 0.2	-	2.96
95	SAGANJ125154.40+351911.97	G	-	-	3.0 ± 0.2	-	4.91
96	SAGANJ125204.82−222645.70	G	-	-	-	-	0.69
97	SAGANJ125308.78−013951.73	G	-	-	-	-	2.12
98	SAGANJ125809.42+421109.18	G	259.38 ± 15.52	0.91 ± 0.30	-	11.69	6.83
99	SAGANJ130152.71+144843.01	G	278.55 ± 9.42	1.35 ± 0.26	4.2 ± 0.2	-	-
100	SAGANJ130840.02−045645.00	G	-	-	24.1 ± 0.8	-	-
101	SAGANJ131231.35+211543.42	G	246.19 ± 12.53	0.68 ± 0.19	12.2 ± 0.4	61.96	6.88
102	SAGANJ132404.20+433407.13	Q	-	-	3.6 ± 0.2	-	11.90
103	SAGANJ133742.35+294223.31	G	268.86 ± 9.55	1.11 ± 0.22	3.1 ± 0.2	1.85	0.50
104	SAGANJ135228.39+093536.02	G	149.29 ± 10.56	0.04 ± 0.02	39.8 ± 1.3	347.24	2.09
105	SAGANJ140700.50+100918.77	G	186.41 ± 11.70	0.14 ± 0.05	-	75.74	-
106	SAGANJ141947.89+081423.39	G	251.32 ± 21.57	0.76 ± 0.37	-	51.20	14.40
107	SAGANJ143548.55+201321.38	Q	-	-	7.5 ± 0.3	-	14.20
108	SAGANJ144408.73+260126.43	G	-	-	1.6 ± 0.3	-	7.82
109	SAGANJ144928.63−011617.44	G	325.03 ± 12.69	3.23 ± 0.71	40.2 ± 1.2	1.09	-
110	SAGANJ145346.50+224314.96	G	-	-	2.8 ± 0.2	-	9.19
111	SAGANJ145443.40+122510.39	G	226.73 ± 9.89	0.42 ± 0.10	16.2 ± 0.6	-	-
112	SAGANJ150148.34+434632.50	G	226.67 ± 45.40	0.42 ± 0.48	1.0 ± 0.2	-	79.60
113	SAGANJ150725.32+082944.51	G	322.86 ± 7.17	3.11 ± 0.39	3.2 ± 0.1	0.83	-
115	SAGANJ154131.89−270736.57	G	-	-	- -	-	4.39
116	SAGANJ154639.13+012422.04	G	353.67 ± 14.72	5.20 ± 1.22	2.3 ± 0.2	1.26	2.31
117	SAGANJ154817.75+072554.85	G	-	-	2.3 ± 0.2	-	24.80
118	SAGANJ155140.30+103548.66	G	241.95 ± 26.76	0.61 ± 0.38	4.3 ± 0.2	71.83	38.60
119	SAGANJ160027.78+083743.04	Q	-	-	-	-	23.20
120	SAGANJ160513.74+071152.56	G	194.99 ± 21.78	0.18 ± 0.11	-	-	13.20
121	SAGANJ160530.66−092728.99	G	-	-	-	-	18.40
122	SAGANJ161157.36+073856.19	G	-	-	12.2 ± 0.4	-	2.73
123	SAGANJ161242.06+431319.82	G	240.66 ± 14.56	0.59 ± 0.20	-	-	3.68
124	SAGANJ161534.52+095709.96	Q	-	-	7.1 ± 0.3	-	-
125	SAGANJ170627.63+102453.72	G	-	-	-	-	35.60
126	SAGANJ172107.89+262432.17	G	181.63 ± 23.37	0.12 ± 0.09	2.6 ± 0.2	44.30	2.92
127	SAGANJ172109.49+354216.09	Q	-	-	393.0 ± 11.8	-	10.90
128	SAGANJ173105.95+242851.85	G	-	-	-	-	59.20
129	SAGANJ174206.97+182720.66	Q	-	-	-	-	23.60
131	SAGANJ182007.41+225120.04	G	-	-	-	-	17.50
132	SAGANJ182938.62+223008.63	G	-	-	-	-	3.72
133	SAGANJ190304.60+361650.92	G	-	-	-	-	0.53
134	SAGANJ194349.35−354646.10	G	-	-	-	-	1.01
137	SAGANJ204019.60−065910.19	G	-	-	-	-	14.50
138	SAGANJ205947.18−250611.03	G	-	-	-	-	1.41
139	SAGANJ213039.21+073530.28	G	208.24 ± 21.71	0.26 ± 0.15	-	-	4.45
140	SAGANJ213745.20−143254.90	Q	-	-	-	-	76.10
141	SAGANJ214920.70+194043.51	G	-	-	-	-	28.30
142	SAGANJ221536.84+290235.90	Q	-	-	-	-	11.90
143	SAGANJ221815.55+193143.76	G	273.87 ± 7.91	1.23 ± 0.20	-	-	0.77
144	SAGANJ223114.32+010041.80	G	276.10 ± 13.64	1.29 ± 0.36	6.1 ± 0.2	-	2.70
145	SAGANJ223249.13−052958.10	Q	-	-	21.8 ± 0.7	-	-
146	SAGANJ223836.14−070457.93	G	-	-	-	-	5.72
148	SAGANJ224621.66+314207.94	G	-	-	-	-	3.32
149	SAGANJ225103.39+061925.49	G	199.24 ± 9.68	0.20 ± 0.06	3.2 ± 0.2	-	0.68

Table 4.5: continued.

Sr.No	Name	Type	σ (km s^{-1})	M_{BH} (10^9 $M_\odot$)	$S^c_{1400MHz}$ (mJy)	λ_{Edd} (10^{-4})	Q_{Jet} (10^{43} erg s^{-1})
(1)	(2)	(3)	(4)	(5)	(6)	(7)	(8)
150	SAGANJ225125.53+160753.60	G	-	-	-	-	21.30
151	SAGANJ225321.28+162016.77	G	-	-	-	-	5.09
152	SAGANJ225356.30−070638.60	G	-	-	-	-	6.60
153	SAGANJ225934.13+082040.78	G	-	-	1.5 ± 0.2	-	16.90
154	SAGANJ231046.70−210813.90	G	-	-	-	-	3.40
156	SAGANJ231956.30−272812.40	G	-	-	-	-	37.50
157	SAGANJ232344.52+145759.35	G	-	-	-	-	1.53
158	SAGANJ232511.80−323634.60	Q	-	-	-	-	2.99
159	SAGANJ233512.35+174150.38	G	-	-	-	-	11.30
160	SAGANJ234137.14+082817.25	G	289.43 ± 15.33	1.68 ± 0.50	1.3 ± 0.2	-	4.66
161	SAGANJ234847.77+160010.32	G	243.11 ± 15.53	0.63 ± 0.23	-	-	26.40
162	SAGANJ235911.07+170610.97	G	198.95 ± 6.42	0.20 ± 0.04	-	-	2.34

Table 4.6: The table lists the jet kinetic power and black hole properties of GRGs from GRG catalogue as discussed in Sec. 4.5.4. Col. (1) indicates the sample from which the GRGs originate, where 'Others' refers to GRGs from the GRG catalogue that are not part of LoTSS or SGS. Col. (2) and Col. (3) represent the right ascension (RA) in HMS and declination (Dec) in DMS of the GRG host galaxies. Col. (4) consists of the jet kinetic power (Q_{Jet}). Col. (5) lists M_{BH} : the central black hole mass (10^9 $M_\odot$) estimated from the M_{BH}-σ relation. Col. (6) includes the B_{Edd}: Eddington magnetic field (10^4 G), and Col. (7) lists the estimated GRG spin.

Sample	RA (HMS)	Dec (DMS)	Q_{Jet} (10^{43} erg s^{-1})	M_{BH} (10^9 $M_\odot$)	B_{Edd} (10^4 G)	Spin
(1)	(2)	(3)	(4)	(5)	(6)	(7)
SGS	00 11 19.35	32 17 13.83	3.60 ± 0.72	0.76 ± 0.16	2.18 ± 0.23	0.08 ± 0.02
SGS	00 18 15.21	21 41 33.42	40.60 ± 8.13	0.83 ± 0.29	2.08 ± 0.36	0.26 ± 0.10
SGS	00 38 09.89	09 36 01.33	9.91 ± 1.98	1.05 ± 0.45	1.86 ± 0.40	0.11 ± 0.06
SGS	01 14 30.75	05 08 30.64	3.67 ± 0.73	0.31 ± 0.08	3.40 ± 0.46	0.13 ± 0.04
SGS	01 33 27.24	−08 24 16.52	1.79 ± 0.36	2.09 ± 0.43	1.31 ± 0.14	0.03 ± 0.01
SGS	01 58 26.09	24 51 36.38	0.85 ± 0.17	1.62 ± 0.34	1.49 ± 0.16	0.03 ± 0.01
Others	07 46 33.68	17 08 09.63	0.81 ± 0.17	0.33 ± 0.13	3.28 ± 0.64	0.06 ± 0.03
Others	07 51 08.93	42 31 23.6	2.70 ± 0.54	0.94 ± 0.21	1.96 ± 0.22	0.06 ± 0.02
Others	08 57 01.76	01 31 30.93	2.89 ± 0.58	1.35 ± 0.67	1.63 ± 0.41	0.05 ± 0.03
SGS	09 01 23.31	19 14 17.12	11.20 ± 2.25	0.61 ± 0.26	2.42 ± 0.52	0.16 ± 0.08
Others	09 01 36.70	21 46 33.80	1.12 ± 0.25	4.67 ± 2.67	0.88 ± 0.25	0.02 ± 0.01
SGS	09 08 39.13	59 45 12.82	2.55 ± 0.51	1.98 ± 0.48	1.35 ± 0.16	0.04 ± 0.01
Others	09 11 54.57	08 12 31.13	6.64 ± 1.33	0.66 ± 0.19	2.33 ± 0.33	0.12 ± 0.04
Others	09 32 38.30	16 11 57.22	14.30 ± 2.85	0.77 ± 0.23	2.16 ± 0.32	0.16 ± 0.06
Others	10 21 31.84	05 19 02.90	1.00 ± 0.02	0.94 ± 0.26	1.96 ± 0.28	0.04 ± 0.01
Others	10 32 58.88	56 44 53.27	0.22 ± 0.04	1.34 ± 0.23	1.64 ± 0.14	0.01 ± 0.00
Others	10 34 03.90	18 40 49.00	4.43 ± 0.89	0.54 ± 0.15	2.58 ± 0.36	0.11 ± 0.03
Others	10 36 36.30	38 35 07.50	0.81 ± 0.16	1.35 ± 0.37	1.63 ± 0.22	0.03 ± 0.01
Others	10 48 43.30	11 08 00.30	4.45 ± 0.89	0.94 ± 0.23	1.95 ± 0.24	0.08 ± 0.02
LoTSS	10 57 09.25	48 40 41.03	8.40 ± 1.68	0.81 ± 0.42	2.11 ± 0.56	0.12 ± 0.07
LoTSS	11 04 33.11	46 42 25.76	0.46 ± 0.09	0.11 ± 0.05	5.79 ± 1.24	0.08 ± 0.04
LoTSS	11 05 15.27	54 41 09.30	0.75 ± 0.15	0.79 ± 0.40	2.14 ± 0.54	0.04 ± 0.02
LoTSS	11 18 57.28	55 06 56.96	9.09 ± 1.82	0.47 ± 0.21	2.77 ± 0.61	0.16 ± 0.08
LoTSS	11 21 26.44	53 44 56.71	0.38 ± 0.08	0.43 ± 0.09	2.90 ± 0.30	0.04 ± 0.01
Others	11 21 45.00	17 24 25.30	0.74 ± 0.15	0.72 ± 0.17	2.24 ± 0.27	0.04 ± 0.01
LoTSS	11 24 35.86	49 03 25.92	3.31 ± 0.67	0.63 ± 0.32	2.40 ± 0.60	0.09 ± 0.05
LoTSS	11 27 13.18	51 13 26.35	0.78 ± 0.16	1.18 ± 0.62	1.75 ± 0.46	0.03 ± 0.02
LoTSS	11 32 02.31	47 28 24.14	0.28 ± 0.06	1.09 ± 0.41	1.81 ± 0.34	0.02 ± 0.01
LoTSS	11 32 50.67	50 57 04.68	0.89 ± 0.18	1.34 ± 0.79	1.64 ± 0.48	0.03 ± 0.02
LoTSS	11 35 03.20	48 26 12.12	0.66 ± 0.13	1.53 ± 0.53	1.53 ± 0.27	0.02 ± 0.01
Others	11 35 35.23	39 01 45.77	0.38 ± 0.08	0.02 ± 0.01	12.20 ± 3.48	0.15 ± 0.10
SGS	11 44 27.19	37 08 31.87	10.80 ± 2.16	0.52 ± 0.11	2.64 ± 0.28	0.17 ± 0.04
LoTSS	11 48 14.98	54 57 16.49	0.11 ± 0.02	0.41 ± 0.13	2.96 ± 0.47	0.02 ± 0.01
SGS	12 03 43.71	23 43 04.72	5.49 ± 1.10	0.87 ± 0.30	2.03 ± 0.34	0.09 ± 0.04
LoTSS	12 18 49.88	50 26 17.59	11.30 ± 2.26	0.46 ± 0.15	2.80 ± 0.46	0.18 ± 0.07
LoTSS	12 20 28.13	52 51 44.89	0.75 ± 0.15	0.54 ± 0.28	2.59 ± 0.67	0.04 ± 0.03
LoTSS	12 22 55.24	49 26 42.32	0.34 ± 0.07	1.76 ± 0.51	1.43 ± 0.21	0.02 ± 0.01

Table 4.6: continued.

Sample	RA	Dec	Q_{Jet}	M_{BH}	B_{Edd}	Spin
	(HMS)	(DMS)	(10^{43} erg s^{-1})	(10^9 $M_\odot$)	(10^4 G)	
(1)	(2)	(3)	(4)	(5)	(6)	(7)
LoTSS	12 25 31.36	49 46 43.95	0.24 ± 0.05	1.43 ± 0.66	1.59 ± 0.36	0.02 ± 0.01
LoTSS	12 29 36.25	50 13 04.65	0.94 ± 0.19	0.47 ± 0.26	2.78 ± 0.76	0.05 ± 0.03
LoTSS	12 32 04.95	53 06 27.31	0.49 ± 0.10	0.41 ± 0.19	2.98 ± 0.69	0.04 ± 0.02
LoTSS	12 41 42.34	51 35 14.32	6.17 ± 1.24	2.22 ± 1.19	1.27 ± 0.34	0.06 ± 0.04
Others	12 47 33.31	67 23 16.34	0.20 ± 0.04	0.73 ± 0.13	2.22 ± 0.19	0.02 ± 0.00
Others	12 53 03.20	45 00 44.80	0.70 ± 0.14	0.86 ± 0.17	2.04 ± 0.20	0.03 ± 0.01
Others	12 55 50.13	58 18 41.72	1.48 ± 0.31	2.81 ± 1.58	1.13 ± 0.32	0.03 ± 0.02
SGS	12 58 09.42	42 11 09.18	7.08 ± 1.42	0.96 ± 0.28	1.93 ± 0.28	0.10 ± 0.03
LoTSS	13 03 31.08	53 59 48.65	0.29 ± 0.06	0.55 ± 0.18	2.56 ± 0.42	0.03 ± 0.01
LoTSS	13 03 32.18	52 20 02.02	0.63 ± 0.13	1.07 ± 0.42	1.83 ± 0.36	0.03 ± 0.01
SGS	13 12 31.35	21 15 43.42	6.87 ± 1.37	0.77 ± 0.20	2.17 ± 0.28	0.11 ± 0.03
Others	13 13 57.70	64 25 55.00	1.95 ± 0.40	0.89 ± 0.30	2.01 ± 0.34	0.06 ± 0.02
LoTSS	13 14 04.60	54 39 37.88	8.91 ± 1.79	1.43 ± 0.62	1.59 ± 0.35	0.09 ± 0.05
LoTSS	13 22 29.07	50 48 44.53	0.30 ± 0.06	0.63 ± 0.17	2.38 ± 0.33	0.03 ± 0.01
LoTSS	13 24 35.19	50 41 02.31	4.27 ± 0.86	0.21 ± 0.10	4.10 ± 0.97	0.17 ± 0.09
LoTSS	13 31 35.25	45 59 55.53	1.91 ± 0.38	4.33 ± 2.10	0.91 ± 0.22	0.02 ± 0.01
LoTSS	13 32 58.28	53 53 55.60	2.23 ± 0.45	2.09 ± 0.93	1.31 ± 0.29	0.04 ± 0.02
LoTSS	13 36 18.75	53 39 52.12	0.47 ± 0.09	0.67 ± 0.24	2.32 ± 0.41	0.03 ± 0.01
SGS	13 37 42.35	29 42 23.31	0.53 ± 0.10	1.13 ± 0.24	1.79 ± 0.19	0.03 ± 0.01
LoTSS	13 42 06.98	47 25 53.04	1.02 ± 0.20	2.13 ± 0.58	1.30 ± 0.18	0.03 ± 0.01
Others	13 45 03.60	39 52 31.00	1.99 ± 0.40	0.63 ± 0.19	2.39 ± 0.36	0.07 ± 0.02
LoTSS	13 45 57.55	54 03 16.62	6.36 ± 1.27	0.24 ± 0.08	3.84 ± 0.67	0.19 ± 0.08
LoTSS	13 49 27.92	46 20 15.11	2.46 ± 0.49	0.64 ± 0.38	2.38 ± 0.70	0.07 ± 0.05
Others	13 50 00.70	29 47 21.40	0.22 ± 0.06	1.45 ± 0.44	1.58 ± 0.24	0.01 ± 0.01
SGS	13 52 28.39	09 35 36.02	2.10 ± 0.42	0.09 ± 0.03	6.47 ± 1.10	0.18 ± 0.07
LoTSS	13 56 28.50	52 42 19.23	1.35 ± 0.27	1.90 ± 0.92	1.38 ± 0.34	0.03 ± 0.02
LoTSS	13 59 51.16	47 03 21.03	0.59 ± 0.12	0.99 ± 0.43	1.91 ± 0.42	0.03 ± 0.01
Others	14 00 43.40	30 19 19.00	7.71 ± 1.54	0.86 ± 0.23	2.05 ± 0.27	0.11 ± 0.03
LoTSS	14 07 18.48	51 32 04.63	53.70 ± 10.80	0.28 ± 0.15	3.60 ± 0.97	0.52 ± 0.32
LoTSS	14 16 25.89	54 25 45.85	4.81 ± 0.96	1.27 ± 0.41	1.68 ± 0.27	0.07 ± 0.03
Others	14 18 37.75	37 46 23.00	1.06 ± 0.21	0.65 ± 0.15	2.35 ± 0.27	0.05 ± 0.01
SGS	14 19 47.89	08 14 23.39	14.70 ± 2.94	0.84 ± 0.33	2.07 ± 0.41	0.16 ± 0.07
LoTSS	14 28 57.66	54 36 27.81	4.11 ± 0.83	0.95 ± 0.54	1.95 ± 0.55	0.08 ± 0.05
LoTSS	14 29 33.45	54 43 35.29	1.09 ± 0.22	0.49 ± 0.11	2.71 ± 0.30	0.06 ± 0.01
Others	14 31 03.40	33 45 41.60	0.48 ± 0.11	2.33 ± 0.64	1.24 ± 0.17	0.02 ± 0.01
LoTSS	14 31 36.99	52 27 24.90	3.32 ± 0.67	1.28 ± 0.47	1.68 ± 0.30	0.06 ± 0.03
LoTSS	14 44 10.50	55 47 45.64	6.60 ± 1.32	2.48 ± 0.76	1.20 ± 0.18	0.06 ± 0.02
LoTSS	14 45 20.87	54 03 29.62	2.80 ± 0.56	1.94 ± 1.15	1.36 ± 0.40	0.04 ± 0.03
Others	14 45 27.40	09 32 18.00	0.18 ± 0.04	0.37 ± 0.07	3.11 ± 0.31	0.03 ± 0.01
LoTSS	14 46 07.20	48 41 37.79	2.76 ± 0.56	0.92 ± 0.38	1.97 ± 0.40	0.06 ± 0.03
Others	14 53 02.93	33 08 40.80	10.30 ± 2.07	1.00 ± 0.31	1.90 ± 0.29	0.12 ± 0.04
LoTSS	14 57 02.81	48 06 46.64	0.04 ± 0.01	1.31 ± 0.46	1.66 ± 0.29	0.01 ± 0.00
LoTSS	15 01 32.11	50 34 55.14	0.35 ± 0.07	2.49 ± 0.95	1.20 ± 0.23	0.01 ± 0.01
LoTSS	15 06 24.10	53 55 02.61	1.16 ± 0.23	0.86 ± 0.26	2.05 ± 0.32	0.04 ± 0.02
Others	15 24 44.60	19 59 57.08	1.83 ± 0.40	0.59 ± 0.31	2.47 ± 0.65	0.07 ± 0.04
SGS	15 46 39.13	01 24 22.04	2.39 ± 0.48	3.75 ± 1.01	0.98 ± 0.13	0.03 ± 0.01
SGS	15 51 40.30	10 35 48.66	38.40 ± 7.71	0.71 ± 0.36	2.25 ± 0.56	0.27 ± 0.16
SGS	16 05 13.74	07 11 52.56	13.30 ± 2.66	0.28 ± 0.14	3.61 ± 0.91	0.26 ± 0.15
SGS	16 12 42.06	43 13 19.82	3.70 ± 0.74	0.69 ± 0.20	2.28 ± 0.33	0.09 ± 0.03
SGS	17 21 07.89	26 24 32.17	2.95 ± 0.59	0.20 ± 0.12	4.21 ± 1.21	0.14 ± 0.09
SGS	21 30 39.21	07 35 30.28	4.61 ± 0.92	0.37 ± 0.17	3.12 ± 0.73	0.13 ± 0.07
Others	21 45 04.53	−06 59 07.76	2.79 ± 0.58	2.55 ± 0.81	1.19 ± 0.19	0.04 ± 0.01
SGS	22 18 15.55	19 31 43.76	0.78 ± 0.16	1.22 ± 0.23	1.72 ± 0.17	0.03 ± 0.01
SGS	22 31 14.32	01 00 41.80	2.80 ± 0.56	1.27 ± 0.33	1.69 ± 0.22	0.06 ± 0.02
SGS	22 51 03.39	06 19 25.49	0.71 ± 0.14	0.30 ± 0.07	3.44 ± 0.41	0.06 ± 0.02
SGS	23 41 37.14	08 28 17.25	4.72 ± 0.94	1.56 ± 0.43	1.52 ± 0.21	0.06 ± 0.02
SGS	23 48 47.77	16 00 10.32	23.60 ± 4.74	0.73 ± 0.22	2.23 ± 0.34	0.21 ± 0.08
SGS	23 59 11.07	17 06 10.97	2.32 ± 0.46	0.30 ± 0.05	3.45 ± 0.31	0.10 ± 0.02

Table 4.7: RA and Dec represent the right ascension and declination of the GRG host galaxies in HMS and DMS, respectively. Col. 5 shows the m_r of the BCGs. Parameters such as r_{200} and R_{L*} have been obtained from the WHL galaxy cluster catalogue, and M_{200} has been estimated using equation 2 of Wen et al. (2012). r_{200} is the virial radius (Mpc) of the galaxy cluster, M_{200} is the mass ($10^{14} M_\odot$) of the cluster within r_{200}, and N_{200} is the number of galaxies present within r_{200}. Column 11 shows the comoving number density of galaxies within r_{200}. Col. 12 includes the ratio of half of the linear extent of the source to the virial radius.

No	WHL Cluster	RA (HMS)	Dec (DMS)	m_r	z	r_{200} (Mpc)	R_{L*}	M_{200} ($10^{14} M_\odot$)	N_{200}	Density Mpc^{-3}	Ratio
(1)	(2)	(3)	(4)	(5)	(6)	(7)	(8)	(9)	(10)	(11)	(12)
1	J013327.2−082417	01 33 27.24	−08 24 16.52	15.90	0.14893	0.87	16.26	0.85	15	5.44	0.53
2	J014208.5−064143	01 42 08.56	−06 41 43.40	15.12	0.12447	1.30	36.91	2.21	22	2.39	0.34
3	J072538.8+400413	07 25 38.75	40 04 12.52	16.14	0.16148	0.85	12.42	0.62	9	3.50	0.49
4	J085349.8+145226	08 53 49.78	14 52 26.04	14.79	0.06933	0.81	13.18	0.66	9	4.04	0.46
5	J090123.3+191417	09 01 23.31	19 14 17.12	17.87	0.27649	0.90	15.02	0.77	10	3.27	0.63
6	J090839.1+594513	09 08 39.13	59 45 12.82	17.01	0.24004	1.36	41.19	2.51	37	3.51	0.48
7	J100943.5+033723	10 09 43.50	03 37 22.72	14.77	0.10513	0.95	17.40	0.92	8	2.23	0.39
8	J112422.8+150958	11 24 22.77	15 09 57.90	16.34	0.17194	1.17	30.92	1.79	22	3.28	0.39
9	J114344.4+222907	11 43 44.42	22 29 06.80	16.55	0.18079	0.76	13.51	0.68	14	7.61	0.53
10	J120343.7+234305	12 03 43.71	23 43 04.72	16.64	0.17670	1.36	41.48	2.53	40	3.80	0.38
11	J121606.1+202055	12 16 06.10	20 20 54.80	18.39	0.26300	0.89	15.45	0.80	13	4.40	0.60
12	J125154.4+351912	12 51 54.40	35 19 11.97	17.81	0.20100	0.83	12.28	0.61	11	4.59	0.62
13	J130152.7+144843	13 01 52.71	14 48 43.01	15.51	0.13761	0.98	17.50	0.92	12	3.04	0.43
14	J133742.3+294223	13 37 42.35	29 42 23.31	15.16	0.11547	0.93	13.30	0.67	9	2.67	0.49
15	J144928.6−011617	14 49 28.63	−01 16 17.44	16.32	0.20233	1.04	20.47	1.11	15	3.18	0.44
16	J154639.1+012422	15 46 39.13	01 24 22.04	16.22	0.20836	1.04	25.13	1.41	12	2.55	0.45
17	J155140.3+103549	15 51 40.30	10 35 48.66	17.98	0.36824	1.13	25.99	1.46	23	3.81	0.55
18	J221815.6+193144	22 18 15.55	19 31 43.76	15.14	0.10964	1.35	47.92	2.99	28	2.72	0.28

4.9 Notes on individual sources from SGS

Here we present our findings and important notes related to some interesting GRGs from our sample.

- SAGANJ000450.25+124840.10 and SAGANJ011341.11+010608.52. These two sources show two symmetric winged back-flows that emanate from the two hotspots. They can therefore be referred to as X-shaped radio galaxies. For X-shaped radio galaxies, three models exist: i) the twin AGN model, ii) the rapid-jet reorientation models, and iii) the back-flow diversion model. They have been proposed to explain this phenomenon in RGs. After inspecting high-resolution maps of FIRST and VLASS, we found no evidence of the presence of twin AGN at the core. However, our observations support the model that the pair of wings arises from the diversion of synchrotron plasma from the hotspots due to ambient pressure gradient.

- SAGANJ075931.84+082534.59. The radio core of the source is only detected at 3000 MHz in the high-resolution survey VLASS (2″). It coincides with a galaxy at a redshift of 0.124 with an r-band magnitude of 17.31. The diffuse plasma, spread along the jet axis on either side of the core, is seen properly in the NVSS, but only partially well in the TGSS, as shown in Fig. 4.17. Thus, the overall intricacies of this object make it a good candidate for a remnant radio-loud AGN (Parma et al. 2007; Mahatma et al. 2018) with a projected linear size of ∼0.72 Mpc. This is likely to be a young active source with a fading plasma from the earlier activity of the source. The integrated two-point spectral index of ∼0.68 also supports this argument. This source is important in order to understand the last phase of the duty cycle of AGN activity after the jets have switched off.

- SAGANJ105309.33+260142.13. Contamination is observed near the western side of the core, which is quite clear in the contours of FIRST in the montage in Fig. 4.18. The measured flux density at 1400 MHz (NVSS) is 336.2 mJy, which includes the flux density of the contaminating source (henceforth source A). For source A, using FIRST, where it is sufficiently resolved, we estimate a flux density of 21.6 mJy, and when this value is subtracted from the total measured flux density, we obtain the corrected flux density value of 314.6 mJy. A similar method is followed for the flux density correction at 150 MHz (TGSS). Because source A is not sufficiently well resolved in TGSS

map, the 3σ contours of the source from the FIRST map are overlaid on the TGSS map, and the flux density of the corresponding region (3σ) is considered to be the flux density of source A in TGSS. The respective value (77.9 mJy) is then subtracted from the measured flux density (1688.3 mJy) of the source, and therefore the corrected flux density is 1610.4 mJy, as given in Table 4.4. The two corrected flux densities at the respective frequencies are used for further calculations of radio power.

- SAGANJ112422.77+150957.90. This is the only double-double radio galaxy (DDRG) identified in our sample of 162 GRGs based on the available radio maps. The DDRG clearly displays aligned radio components, consisting of radio core and two inner and two outer lobes. The double-double morphology is prominently seen in the montage Fig. 4.18, where images from the NVSS (45″), TGSS (25″), and FIRST (5″) are overlaid. The outer lobes are well detected in the NVSS (1400 MHz), but the inner structure is unresolved there. In the TGSS (150 MHz), there is a hint of detection of the outer and inner components of the source, but they are not bright enough to confirm the DDRG nature. However, the high-resolution FIRST map confirms the inner structure, showing that the two inner lobes have an edge-brightened FR-II morphology, and VLASS (3000 MHz) with its higher resolution of 2″ clearly reveals the radio core. Because of the relatively low surface brightness sensitivity, the FIRST (1400 MHz) and VLASS (3000 MHz) surveys have resolved out the outer components of the source. The inner doubles are very compact compared to the outer ones. The two outer hotspots are quite prominent in the NVSS map, and a winged flow is observed to be emitted from the northern hotspot. The angular size of the inner double is 0.82′ , projecting a linear size of $\sim$0.15 Mpc, whereas the outer double spans up to $\sim$0.92 Mpc. The radio core of the DDRG coincides with an optical galaxy with an r-band magnitude of 16.36. This source has been classified as a DDRG by Kozieł-Wierzbowska et al. (2020).

- SAGANJ114427.19+370831.87. A winged back-flow is observed to emanate from the northern hotspot, but no such feature is seen near the southern hotspot. However, this source has been classified as an X-shaped radio galaxy by Kozieł-Wierzbowska et al. (2020).

- SAGANJ225321.28+162016.77. The source was mentioned in Solovyov & Verkhodanov (2014) as a candidate GRG.

4.10 Radio maps of all GRGs from the SGS.

Below we present the maps of GRGs from the SGS. Blue represents the radio emission detected in the NVSS, and black and yellow contours are from the TGSS and the FIRST, respectively. Absence of contours from any survey means either that the survey did not cover the part of the sky or that the survey did not detect the source. The red crosses represent the location of the host galaxy, which is also given in the name of the source at the top of each image. The lower right corner of each image shows the angular scale for reference. Numbers in the lower left corner represent the serial numbers from Table 4.4.

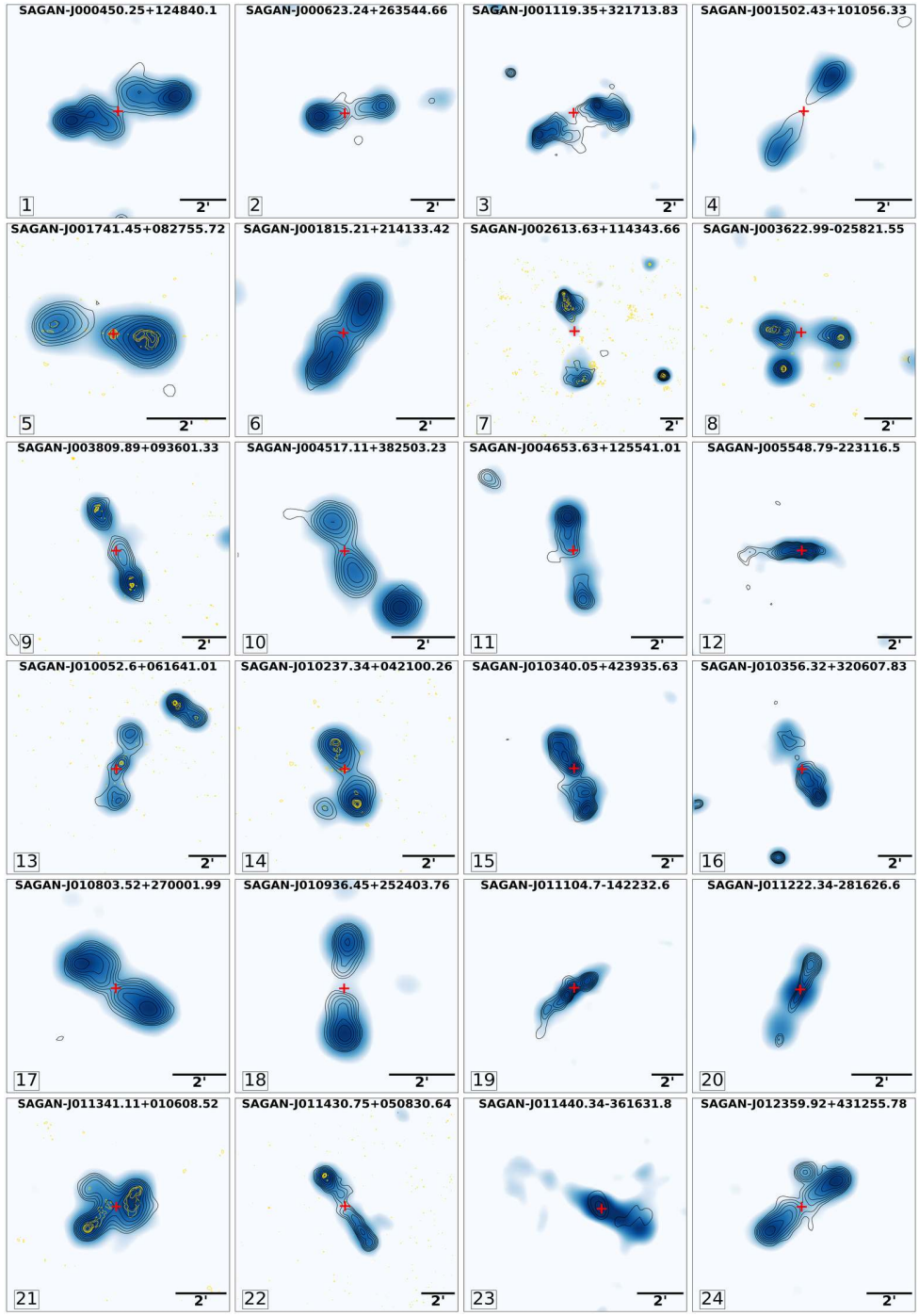

Figure 4.15: Radio maps of 1 to 24 GRGs from the SGS as described in Sec. 4.10.

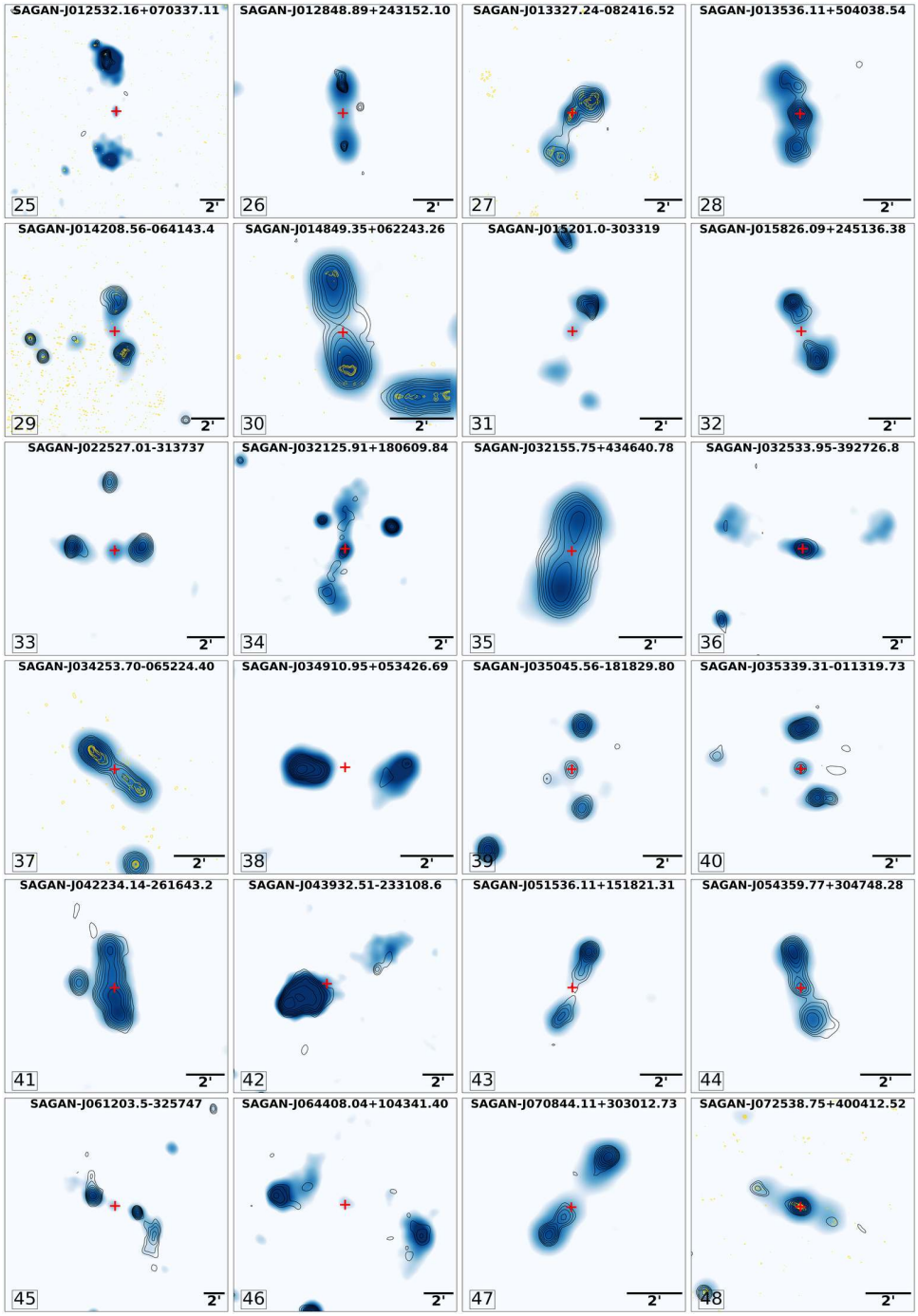

Figure 4.16: Radio maps of 24 to 48 GRGs from the SGS as described in Sec. 4.10.

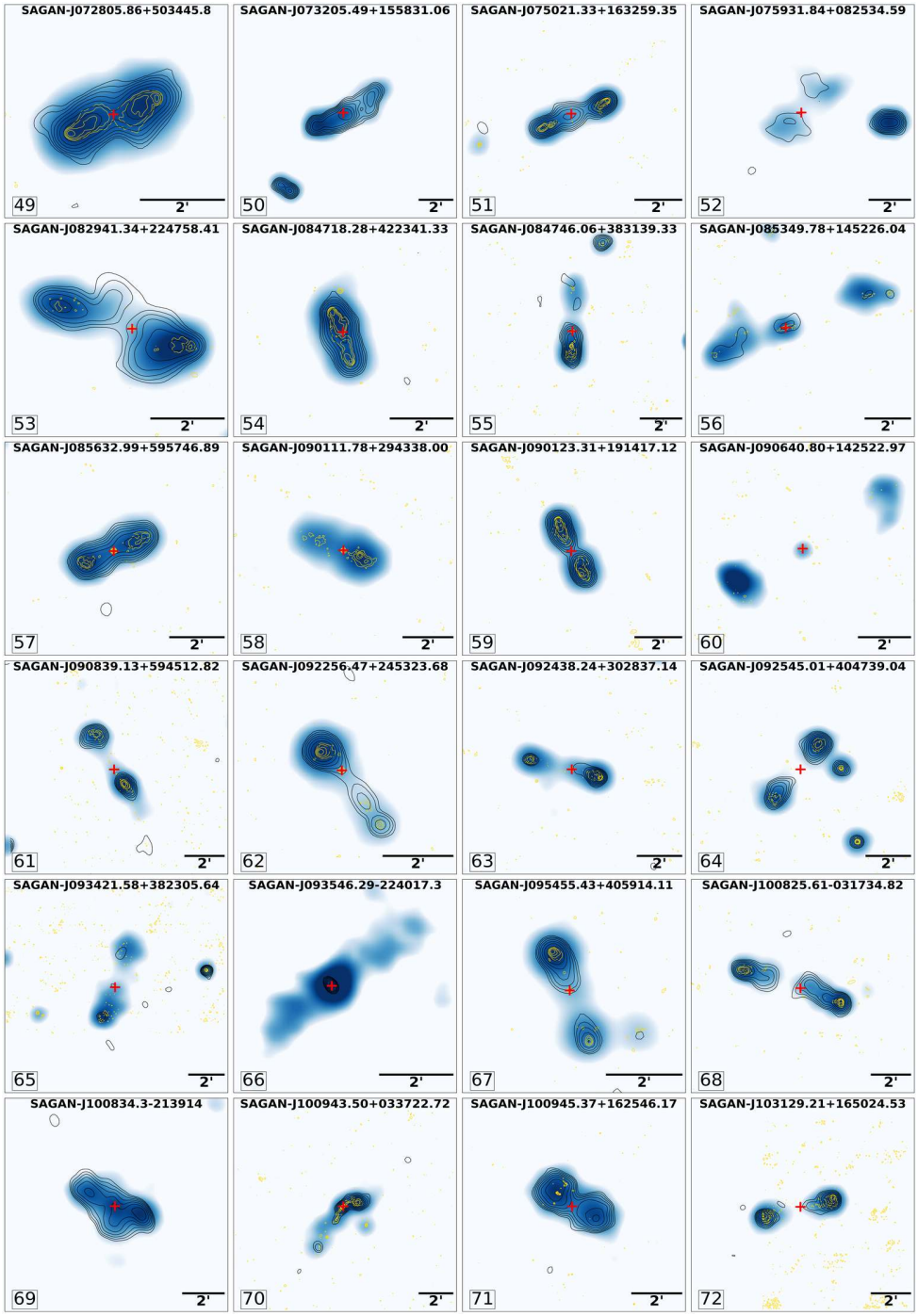

Figure 4.17: Radio maps of 49 to 72 GRGs from the SGS as described in Sec. 4.10.

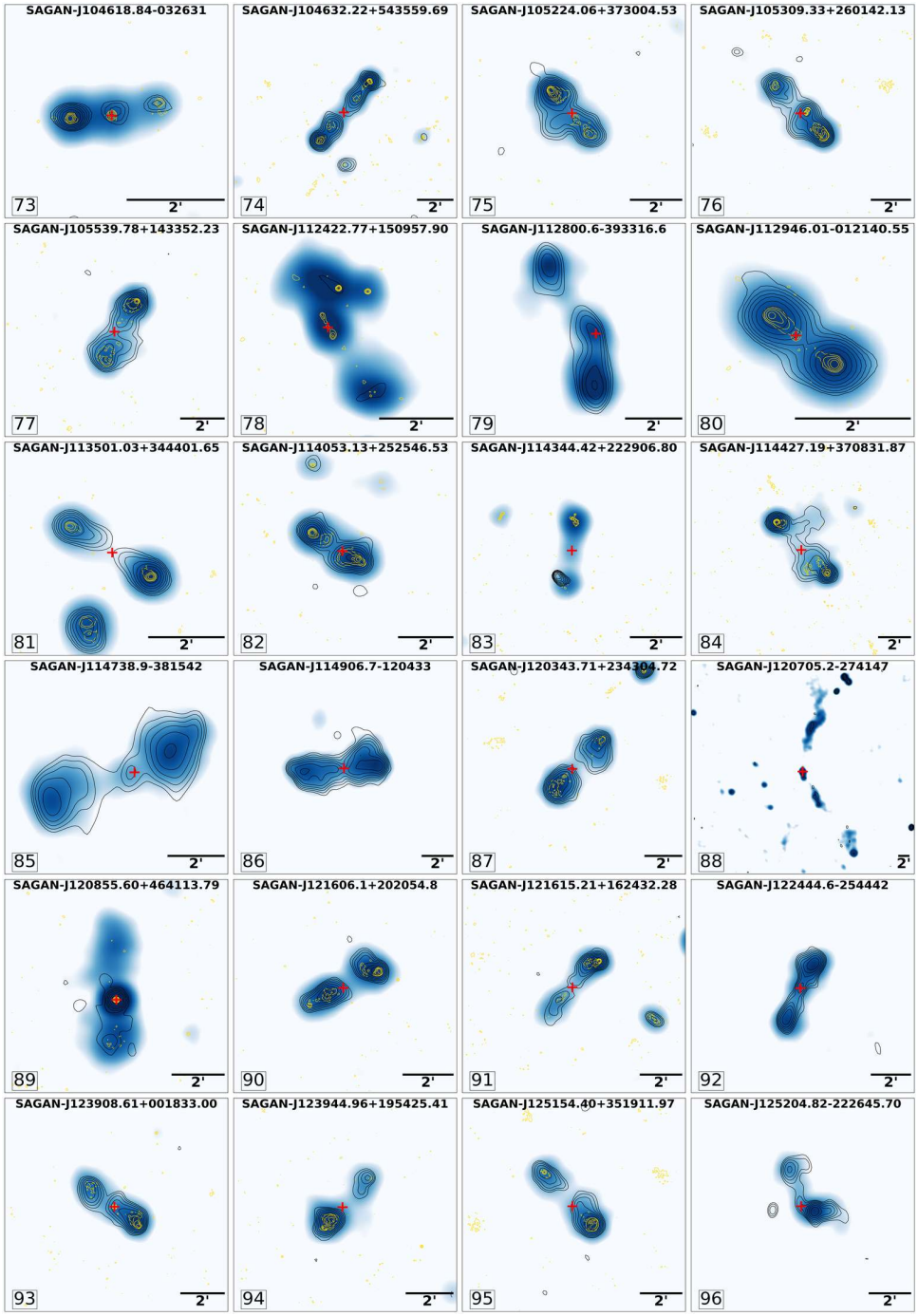

Figure 4.18: Radio maps of 73 to 96 GRGs from the SGS as described in Sec. 4.10.

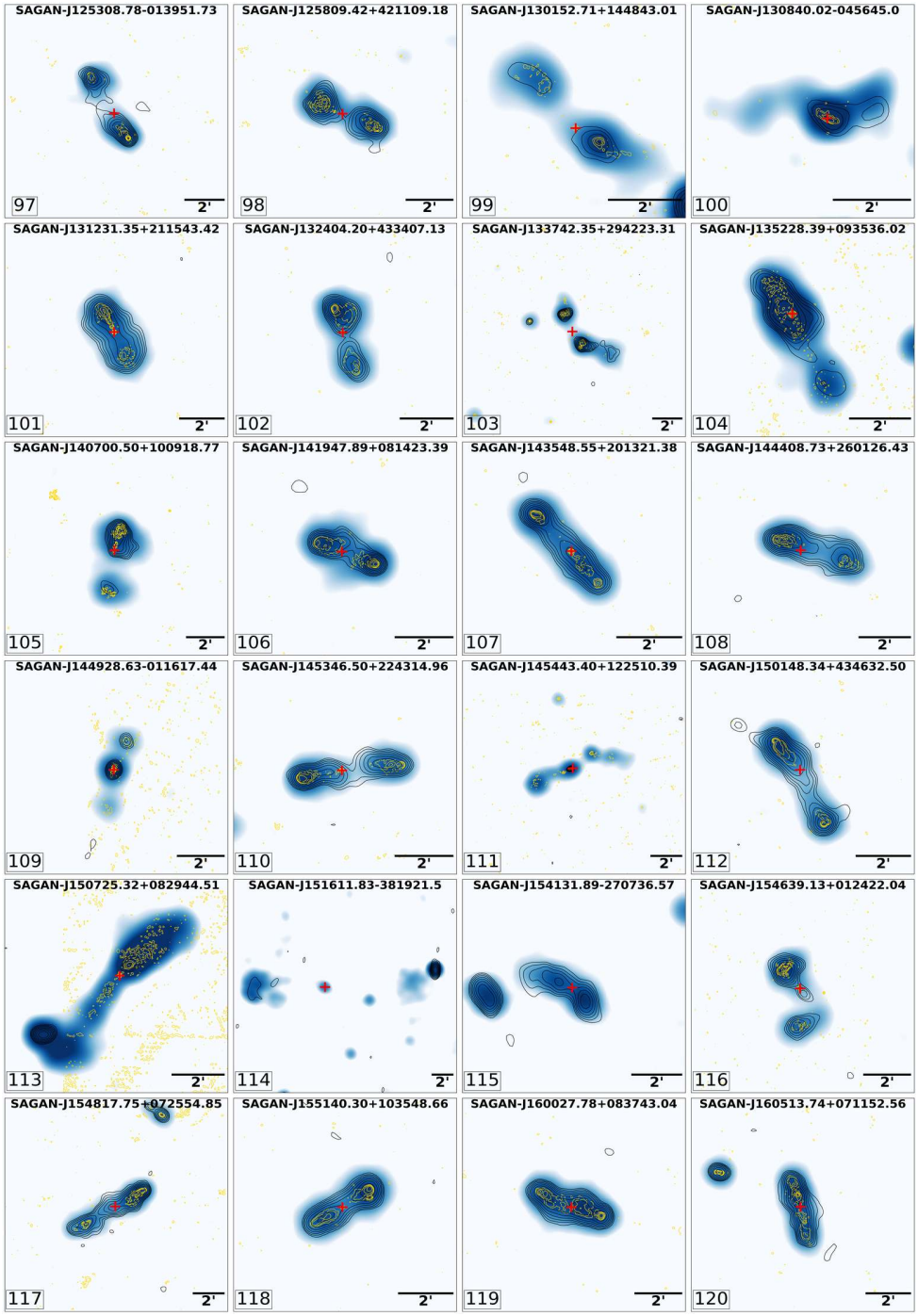

Figure 4.19: Radio maps of 97 to 120 GRGs from the SGS as described in Sec. 4.10.

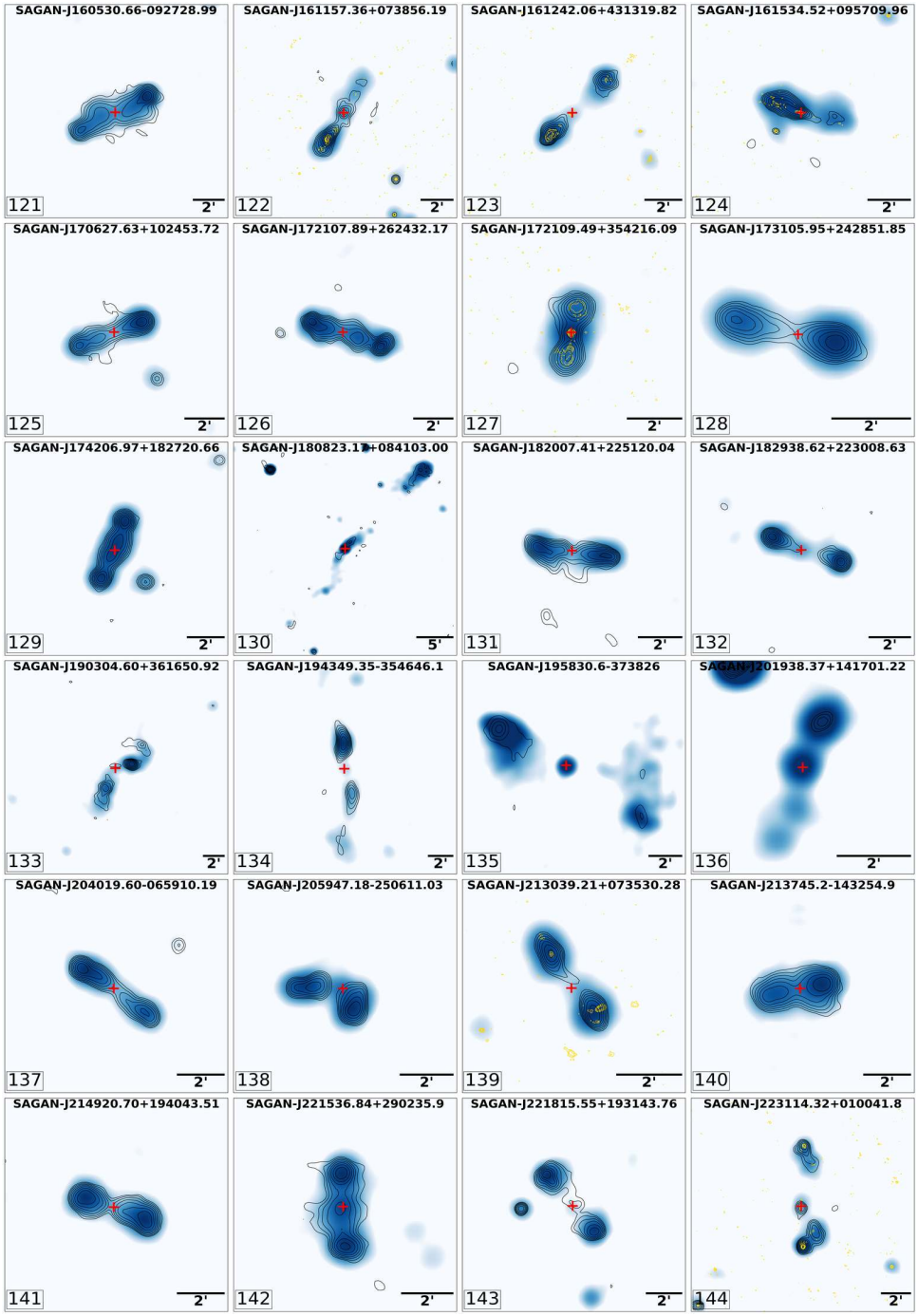

Figure 4.20: Radio maps of 121 to 144 GRGs from the SGS as described in Sec. 4.10.

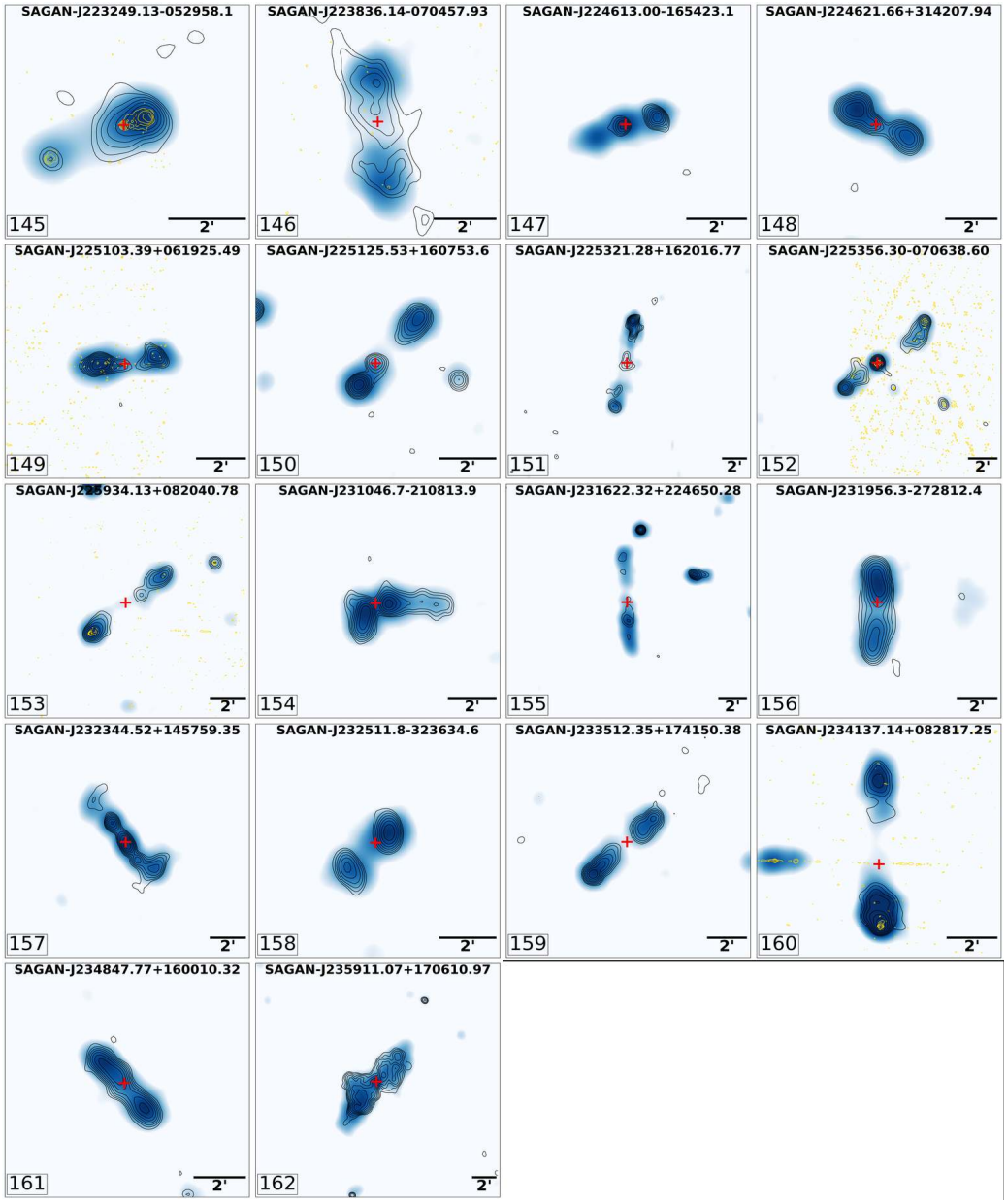

Figure 4.21: Radio maps of 145 to 162 GRGs from the SGS as described in Sec. 4.10.

5 | SAGAN. II : Molecular gas content of giant radio galaxies- Based on observations carried out with IRAM-30m

Radio galaxies with jets of relativistic particles are usually hosted by massive elliptical galaxies with active nuclei powered by accretion of interstellar matter onto a supermassive black hole. In some rare cases (<5%), their jets drive the overall structure to sizes larger than 700 kpc, and they are called giant radio galaxies (GRGs). A very small fraction of the population of such radio galaxies contains molecular and atomic gas in the form of rings or discs that can fuel star formation. The origin of this gas is not well known; it has sometimes been associated with a minor merger with a gas-rich disc galaxy (e.g. Centaurus A) or cooling of material from a hot X-ray atmosphere (e.g. cooling flows). The giant radio jets might be the extreme evolution of these objects, and they can teach us about the radio galaxy evolution.
We selected 12 targets from a catalogue of 820 GRGs that are likely to be in a gas-accretion and star formation phase. The targets were selected from the mid-infrared to contain heated dust. We report here the results of IRAM-30m observations, the molecular gas content, and the star formation efficiency, and we discuss the origin of the gas and disc morphology. Three out of our 12 targets are detected, and for the others, we report significant upper limits. We combine our three detections and upper limits with four additional detected GRGs from the literature to discuss the results. Most of the GRG targets belong to the main sequence, and a large fraction are in the passive domain. Their star formation efficiency is comparable to normal galaxies, except for two galaxies that are deficient in molecular gas with a short ($\sim$ 200 Myr) depletion time, and a quiescent gas-rich giant spiral galaxy. In general, the depletion time is much longer than the lifetime of the giant radio jet.

P. Dabhade, F. Combes, P. Salomé, J. Bagchi and M. Mahato, 2020, A&A, 643, A111
DOI: 10.1051/0004-6361/202038676

5.1 Introduction

It has recently become evident that galaxies and their central supermassive black holes (SMBHs) co-evolve (Heckman & Best 2014), and new research continues to bring forth new facts that improve our understanding. The simultaneous growth of SMBHs and bulges of galaxies might be a consequence of AGN feedback, which plays a fundamental regulating role on star formation (SF), and might result in the observed tight correlation between their masses (e.g. Croton et al. 2006; Magorrian et al. 1998; Marconi & Hunt 2003). Energy transfer from the AGN can produce outflows and temporarily starve galaxies of fresh gas, thus quenching the star formation (e.g. Cicone et al. 2014). It is now understood that the galaxy's SMBH can play a vital role in its growth and evolution, and vice versa. The most spectacular manifestations of massive black holes in AGNs are the powerful bipolar relativistic jets that produce twin-lobed structures on $\sim 10^2$-10^3 kpc scales. Most of the time, evidence for SF quenching is obtained from studying radio-loud AGN, where molecular gas is entrained by the radio jets. These radio galaxies (RGs) are a unique opportunity to study the AGN-fueling process during the radio-mode phase as well as the AGN feedback.

The AGN feedback and outflows can be studied through the cold molecular gas properties of the galaxy, and current studies have been restricted to mostly luminous AGNs. In the past three decades, several studies at lower (Evans et al. 2005a; Ocaña Flaquer et al. 2010; Prandoni et al. 2010; Smolčić & Riechers 2011; Salomé et al. 2015; Lanz et al. 2016; Ruffa et al. 2019) and higher redshifts (Hughes et al. 1997; van Ojik et al. 1997; De Breuck et al. 2003; Emonts et al. 2014; Nesvadba et al. 2017) have been conducted to probe the molecular gas content, SFR, and cold gas as potential fuel supply in RGs. A CO study of a sample of low-luminosity RGs carried out by Prandoni et al. (2010) supported the idea that RGs might be fuelled by cold gas, restricted to kiloparsec-scale nuclear discs or rings around the AGN. Ruffa et al. (2019) have shown a strong possibility that jet-cold gas interacts in a few objects. They also reported inflows inferred from dominant radial motions, indicating that cold gas fuels the RGs.

The members of an extreme sub-class of RGs, which grow to megaparsec scales and are relatively rare, are called the Giant Radio Galaxies (GRGs). The projected linear size of GRGs is greater than 0.7 Mpc and can grow to about 5 Mpc, which is comparable to large galaxy clusters. This makes them one of the largest single astrophysical objects known to date. They have accreting SMBHs of mass 10^8 – 10^{10} $M_\odot$, which under certain conditions launch collimated bipolar relativistic jets orthogonal to their accretion disc (Lynden-Bell 1969; Begelman et al. 1979). Like normal radio galaxies, GRGs are almost always hosted by bright elliptical galaxies. GRGs were discovered (Willis et al. 1974) almost 20 years after the discovery of RGs (Jennison & Das Gupta 1953), and since then, only about 820 (Dabhade et al. 2020c) of them have been found, compared to thousands of RGs.

Some CO observations of GRGs have been attempted before (3C236: Labiano et al. 2013, 3C 326: Nesvadba et al. 2010) but were mostly single-object studies.

Saripalli & Mack (2007), as part of their work on restarted RGs, observed five GRGs with the 15m Swedish-ESO Millimetre Telescope (SEST) in the CO(1-0) and CO(2-1) line transitions and obtained only upper limits for all their GRGs.

To understand these extreme cosmic radio sources better, and specifically, to address the key questions about their size and power, we have initiated a project called Search and Analysis of GRGs with Associated Nuclei (SAGAN*), whose pilot study was presented in Dabhade et al. (2017). In this project, we have built an uniform database of all known GRGs, which was lacking before (Dabhade et al. 2020c). With this GRG database, we aim to carry out multi-wavelength studies of their host galaxies, focusing on physical properties such as their black hole accretion rate; the excitation type, which is either high-power radiatively efficient giant radio galaxies ('high-excitation', HEGRGs) or low-power radiatively inefficient giant radio galaxies ('low-excitation', LEGRGs); the black hole mass (M_{BH}); their galaxy star formation rate (SFR); and their molecular gas content. The key to understanding the giant nature of GRGs may lie in the accretion properties of these peculiar AGNs, and we can probe this by tracing molecular gas to determine whether these objects are fueled by cold gas in the disc. The presence or absence of cold molecular gas in the host galaxies of GRGs can provide information about their star formation rate, accretion state, and stellar mass properties.

This paper is organised in the following way: In Section. 5.2 we describe our sample, observations are presented in Section. 5.3, and the results are reported in Section. 5.4. The interpretation of these results is presented and their effect on the evolution scenarios is discussed in Section. 5.5. The conclusions of our work are presented in Section. 5.6. To compute distances, we have adopted a flat ΛCDM cosmology, with Ω_m=0.29, Ω_Λ=0.71, and the Hubble constant of $H_0 = 70$ km s^{-1}Mpc^{-1}.

5.2 The sample

With the project SAGAN (Dabhade et al. 2020c), we have created the largest database of GRGs to date, and we applied the following criteria to form a subsample to be studied at millimetre waves using IRAM-30m (Baars et al. 1987) to probe the cold molecular gas content: (i) the GRG is not hosted by a quasar, (ii) the GRG is well detected in the Wide-field Infrared Survey Explorer (WISE) at 22μm (fourth band) (Wright et al. 2010), (iii) the redshift of the host galaxy of the GRG is accurately known from spectroscopic measurements, and (iv) the GRG is observable in the sky of IRAM-30m telescope. GRGs, like RGs, are mainly early-type galaxies, and only a minority of them (~ 17%, Kozieł-Wierzbowska et al. 2020) are late types and may still have some gas; the WISE selection is there to find this minority. After applying all the above filters to our GRG-catalogue, we selected a sample of 12 GRGs that is representative of this minority; the GRGs are listed in Table. 5.1. In Cols. 3 and 4 of Table. 5.1 we list the accurate position

*https://sites.google.com/site/anantasakyatta/sagan

(RA and Dec) of the host galaxies, and their accurate spectroscopic redshifts are listed in column 5. Column 6 includes the luminosity distances of the sources. The information obtained from the WISE fourth band and its derived properties are presented in columns 7 and 8, where in column 8, $L_{22\mu m}$ is the luminosity of the host galaxies at 22μm. Column 9 contains the GRG references of the sources and/or the optical identification. Figure. 5.1 displays the SDSS images for the sources when they are available. For the others, the PanSTARRS i band images of the hosts of the GRGs in our sample are given in Figure. 5.2.

For all the 12 galaxies of the sample, the star formation rate (SFR) was first estimated from the 22μm luminosity (Calzetti et al. 2007). When a more accurate estimate existed in the literature from the SED or multi-wavelength tracers, we used it from Chang et al. (2015) for R1-2, R1-3, R2-0, R2-3, R2-6 to R2-9, and from Salim et al. (2018) for R2-0, R2-3, R2-7 and R2-8. Because several estimates are available, we took an average value. SFR tracers in general suffer from uncertainties, but the SFR estimated from 22μm was found to be compatible within the uncertainties with the value derived from the FIR when available. Moreover, recent studies of Cluver et al. (2014), Gürkan et al. (2015), and Catalán-Torrecilla et al. (2015) have used 22μm from WISE to determine the SFR effectively. Although the 22μm flux could also come from the AGN, it is statistically well correlated to the more specific far-infrared SFR indicator, even for AGN (Gürkan et al. 2015). Stellar masses were estimated from observed optical and near-infrared (NIR) magnitudes, using standard relations as a function of colours, derived from stellar population models (Bell et al. 2003). Because the targets have a low redshift, K-corrections were applied using the analytical approximations from Chilingarian et al. (2010). All adopted values are listed in Table. 5.2, together with the CO results we obtained using IRAM-30m data. Table. 5.2 also lists the angular sizes (column 2) of the galaxies, acquired by us from the i-band stellar profiles of the galaxies: ten were from the SDSS, and four from PanSTARRS, see Figures. 5.1 and 5.2.

Table 5.1: General properties of our sample of 12 GRGs. Here R1 and R2 refer to observation runs 1 and 2 with IRAM-30m. RA and Dec are expressed in the J2000 coordinate system. Object R1-0 is a radio-loud quasar, and object R2-0 is a radio galaxy. These two objects were recently classified as non-GRGs based on new available data. All the redshifts listed in column (5) are from spectroscopic measurements, where redshifts marked with a dagger are taken from the SDSS. In the absence of SDSS spectroscopic redshift measurement, the redshift was taken from the reporting paper (Column (9)). Columns (7) and (8) represent the WISE band 4 magnitude and luminosity, respectively.

Sr.No	Name	RA (HMS)	Dec (DMS)	z	D_L (Mpc)	W4 ($22\mu m$) mag (snr)	Log $L_{22\mu m}$ (erg s^{-1})	Ref
(1)	(2)	(3)	(4)	(5)	(6)	(7)	(8)	(9)
R1-1	2MASX J23453268−0449256	23 45 32.70	−04 49 25.4	0.07557	342	7.135 (8.5)	43.35	(1)
R1-2	CGCG 245−031	13 12 17.00	+44 50 21.3	0.03557†	156	8.133 (5.7)	42.27	(2)
R1-3	B2 1029+28	10 32 14.02	+27 56 01.7	0.08519†	389	6.821 (11)	43.58	(2)
R2-1	WNB0313+683	03 18 18.98	+68 29 31.4	0.09010	412	6.187 (23.9)	43.18	(3)
R2-2	LCRS B132559.3−025215	13 28 34.37	−03 07 44.8	0.08526†	389	7.067 (13.5)	42.77	(4)
R2-3	2MASX J14504940+1006497	14 50 49.40	+10 06 49.1	0.05453†	243	8.112 (4.9)	41.95	(5)
R2-4	NGC 6251	16 32 31.97	+82 32 16.4	0.02471	108	5.561 (33)	42.24	(6)
R2-5	LEDA 2785926	21 45 30.90	+81 54 53.7	0.14570	692	6.320 (28.3)	43.57	(7)
R2-6	B2 0951+27	09 54 19.19	+27 15 59.9	0.47120†	2649	7.469 (7.0)	44.26	(8,9)
R2-7	LEDA 1406818	10 21 24.21	+12 17 05.4	0.12940†	606	8.248 (3.5)	42.66	(10)
R2-8	Speca	14 09 48.85	−03 02 32.5	0.13749†	651	8.332 (2.2)	42.69	(11)
R2-9	J121615.21+162432.1	12 16 15.21	+16 24 32.2	0.45908†	2569	7.556 (6.3)	44.19	(12)
R1-0	PKS 0211−031	02 13 47.00	−02 56 37.5	0.35679	1906	7.412 (8.8)	44.73	(13)
R2-0	B2 0915+32B (NE)	09 18 59.41	+31 51 40.7	0.06212	278	8.582 (3.3)	41.85	(14)

– References (1) Bagchi et al. (2014) – (2) Schoenmakers et al. (2001) – (3) Schoenmakers et al. (1998) – (4) Machalski et al. (2001) – (5) Clarke et al. (2017) – (6) Waggett et al. (1977) – (7) Schoenmakers et al. (2000a) – (8) Proctor (2016) – (9) Amirkhanyan (2016) – (10) Koziel-Wierzbowska & Stasinska (2012) – (11) Hota et al. (2011) – (12) Dabhade et al. (2020c) – (13) Owen et al. (1995) – (14) Kuźmicz et al. (2018).

5.2.1 R1-1: 2MASX J23453268−0449256

The galaxy 2MASX J23453268−0449256 (R1-1) is one of the largest (projected linear size ∼1.6 Mpc at radio wavelengths) radio galaxy known to date, hosted by a massive, late-type spiral galaxy that lacks a classical bulge at the redshift of 0.0755 (Bagchi et al. 2014). It shows FR-II and double-double (two sets of lobes, indicating episodic activity) radio morphology; the jet axis is nearly orthogonal to the disc of the host galaxy. This is very unusual because such large-scale radio jets are in general hosted by ellipticals (Taylor et al. 1996; McLure et al. 2004). It shows several other unusual properties that challenge the standard paradigms for black hole growth in galaxies lacking classical bulges. Its general properties as presented by Bagchi et al. (2014) and Bagchi et al. (2020 - in preparation) are similar to those of passive red spirals (Masters et al. 2010), although the WISE mid-infrared (mid-IR) colours suggest that star formation is still occurring within its disc. With $M_r \sim -23.0$ mag, it lies at the very top of the luminosity function of red spirals. The galaxy rotation curve derived from the Hα line peaks at about 429 ± 30 km s^{-1} at a large radius, which is quite high for spirals, after correcting for i = 65° inclination angle (cf. HyperLeda*). This implies an estimated dynamical mass of $\sim 10^{13}$ $M_\odot$ within the virial radius of 450 kpc, assuming a flat rotation curve. The central bulge velocity dispersion is $\sigma = 351 \pm 25$ km s^{-1}, which is close to the highest velocity dispersion found among nearby E and S0 galaxies (van den Bosch et al. 2012). Walker et al. (2015) used Chandra to detect the hot X-ray halo of the galaxy, which extends to r > 80 kpc; it is one of just a few high-mass spirals for which hot gaseous haloes have directly been detected through X-ray imaging to date (Bregman et al. 2018). Intriguingly, the X-ray emitting hot halo is highly elongated parallel to the host galaxy disc, suggesting that feedback by the radio jet has disrupted or expelled hot gas from a region extending roughly 80 kpc above and below the disc plane. Radio-mode feedback like this is rarely seen in spiral galaxies (Mukherjee et al. 2016, 2018).

5.2.2 R1-2: CGCG 245−031

CGCG 245−031 (R1-2) is a flat-spectrum radio source (Healey et al. 2007). It has a low value for its integrated spectral index and is a young radio source. It is a good candidate for a restarting class.

5.2.3 R1-3: B2 1029+28

B2 1029+28 is hosted by a Seyfert type-1 galaxy (Véron-Cetty & Véron 2006) called 2MASX J10321402+2756015. In this galaxy, the stellar populations are not old, but have intermediate ages (Kuźmicz et al. 2019).

*http://leda.univ-lyon1.fr/

5.2.4 R2-1: WNB0313+683

The GRG R2-1 or WNB0313+683 has a projected linear size of 1.52 Mpc with a GHz-peaked spectrum (GPS) core, FR-II type morphology, and recurrent activity (Schoenmakers et al. 1998; Bruni et al. 2019). It is hosted by a Seyfert type-1 galaxy (LEDA 3095635) at $z \sim 0.09$ that is detected in hard X-rays (Winter et al. 2008). Schoenmakers et al. (1998) estimated its spectral age to be ∼ 144 Myr, but recently, Machalski (2011) estimated the age of the lobes to be ∼ 250 Myr.

5.2.5 R2-2: LCRS B132559.3−025215

Machalski & Condon (1999) identified LCRS B132559.3−025215 as a GRG. It is hosted by the Seyfert 2-type (Véron-Cetty & Véron 2006) galaxy called 2MASX J13283434−0307442.

5.2.6 R2-3: 2MASX J14504940+1006497

Source R2-3 is hosted by a central dominant galaxy (the core of a triplet, which is also known as UGC 09555 NED03) of a low-density galaxy group (MSPM 02158), as shown in Figure. 5.1. Based on their SED analysis, Clarke et al. (2017) concluded that the host galaxy is an S0-type galaxy with an SFR of 1.2 ± 0.3 M$\odot$ yr^{-1}. Clarke et al. (2017) also presented its LOFAR 142 MHz radio map, which reveals a large diffuse structure that is not seen in any other radio survey. The bright radio core and high diffuse emission along the jet axis strongly indicate a restarted source. Based on its radio core spectrum, it has been classified as a flat-spectrum galaxy (Healey et al. 2007) with frequencies between ∼ 1 to 10 GHz, and it has an inverted core spectrum with frequencies between 22 to 43 GHz (Park et al. 2013). This further supports the hypothesis that this is a restarted AGN.

5.2.7 R2-4: NGC 6251

NGC 6251 is our nearest target, and it has been the object of many observations since its identification (Waggett et al. 1977; Laing et al. 1983). Chen et al. (2011) studied the neighbouring 17 galaxies, which may form a loose group, but with very low background X-ray gas, explaining the large 1.6 Mpc radio jets. The main jet and lobes are centre-brightened like FR-I, but there are also hot spots near the end of the north and south lobes that suggest a FR-II type of morphology. The radio power is in between the two FR types. Recent LOFAR observations at 150 MHz have revealed low surface brightness extensions and backflows of the lobes (Cantwell et al. 2020), with ages older than 200 Myr. A dust lane has been discovered by Nieto et al. (1983), roughly parallel to the radio jet, with a size of about 5 kpc. The inner orientation of the jets is still unclear; it appears at least that the inner jet and outer lobes are misaligned (Jones & Wehrle 2002).

5.2.8 R2-8: Speca

Only about ten RGs (Ledlow et al. 2001; Hota et al. 2011; Bagchi et al. 2014; Singh et al. 2015; Mao et al. 2015; Mulcahy et al. 2016) have been found to be hosted by spiral galaxies up to now, and only two (2MASX J23453268−0449256 and Speca) of them belong to the GRG subclass. Along with its unusual property of being hosted by a spiral (Hota et al. 2011), Speca is classified as the central galaxy, called MaxBCG J212.45357-03.04237 cluster or group. Another peculiar property of this object is its three pairs of lobes, also called a triple-double, with clear evidence of restarting activity. The outer lobes look like relics revived by shocks coming from the interaction between the cluster and cosmic filaments. The galaxy shows very recent star formation that might be fueled by a cooling flow from merging activity ∼500 Myr ago (Hota et al. 2011).

5.2.9 Other GRGs

R2-5 (Seyfert 2) and R2-7 are also dominant galaxies of their groups, with indications of star formation in the recent past (Kuźmicz et al. 2019). R2-9 is one of the most recently identified GRG, at relatively high redshift (Dabhade et al. 2020c). It appears to be actively forming stars. R2-9 is the most luminous GRGs at 22 microns (WISE band 4) in our sample, and appears to be harbouring a dust-obscured powerful AGN based on its red colour.

5.2.10 Non-GRGs

At the beginning of our study, two objects were thought to be GRG and were observed at IRAM. We report the results, which may serve other studies, although the objects are not GRGs, but normal RGs or RQs. B2 0915+32B is a galaxy pair, and the two companions lie at a distance of 43 kpc. The early-type northern galaxy is the host of the giant radio jet, and its southern companion is a late-type blue spiral galaxy, which could be the reservoir of gas to fuel the northern AGN. PKS 0211-031 is radio-loud quasar with FR-II type morphology.

5.3 Observations

Observations of the CO(1-0), CO(2-1) (and for one target CO(3-2)) emission lines have been carried out with the IRAM-30m telescope at Pico Veleta, Granada, Spain, during June and September 2016 for the first run (called R1), and then in March 2020 for the second run (called R2). The beam full width at half-maximum (FWHM) is 23″and 12″at the frequencies of 115 GHz and 230 GHz, respectively. The redshifts of our targets (except for two objects) range from 0 to 0.1, and the corresponding beams are up to 10% larger, accordingly. The SIS receivers (EMIR) were used for observations in the wobbler-switching mode, and the reference positions were offset by ±120 arcsec in azimuth. The main-beam

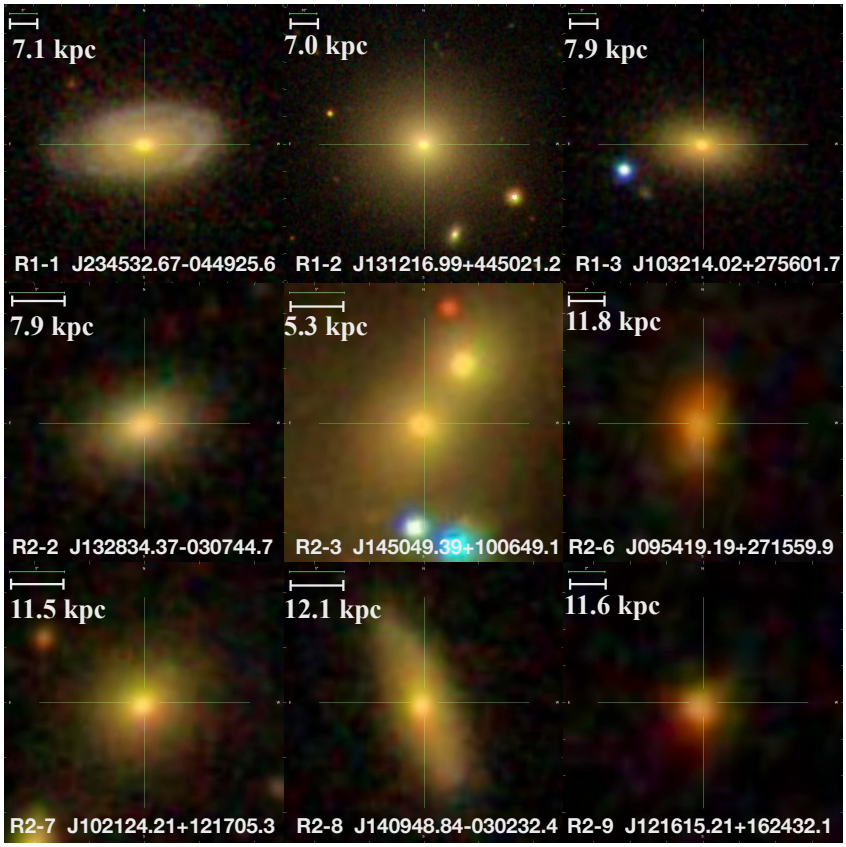

Figure 5.1: Host galaxies of nine GRGs from SDSS. The bar at the top left represents the angular scale in kpc for reference.

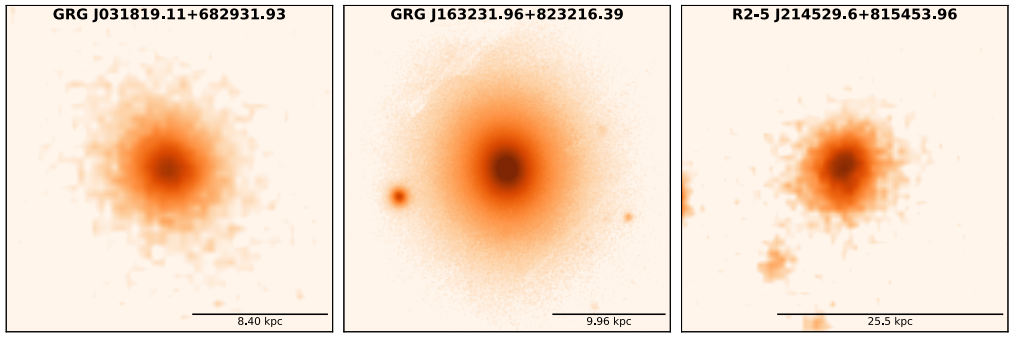

Figure 5.2: PanSTARRS i-band image of the hosts of GRGs that are absent in the SDSS footprint. The bar at the bottom indicates the angular scale of 5″, 20″, and 10″ in kiloparsec (kpc) for R2-1, R2-4, and R2-5, respectively.

efficiency of IRAM is $\eta_{mb} = T_A^*/T_{mb} = 0.79$ and 0.63 at 105 GHz and 210 GHz, respectively. The system temperatures ranged between 150 K and 400 K at 2.6 mm, and between 200 K and 600 K at 1.3 mm. The pointing was regularly checked every two hours on a nearby planet or a bright continuum source, and the focus was reviewed after each sunrise or when a suitable planet was available, as well as at the beginning of each day. The time on source typically ranged from four to five hours, depending on the weather. Two backends were used simultaneously, the Wideband Line Multiple Autocorrelator (WILMA) and the the Fourier transform spectrometer (FTS). The T_{mb} rms noise level in four hours of integration was σ_{mb} ~0.7mK with a spectrometer resolution of 50 km s^{-1} for 105 GHz and σ_{mb} ~0.9mK for 210 GHz. These can be lower in very good weather. The upper limits reported in the next section for the integrated CO fluxes are computed by $S(CO)dV = 3 \times rms_{300}$ JypK $\times$ 300 km s^{-1} , where JypK is the conversion from K to Jy (=5 Jy K^{-1} for the IRAM-30m), and rm_{300} is the rms estimated in 300 km s^{-1} wide bins. A typical FWHM of 300 km s^{-1} is usually taken for early-type galaxies, which RGs and GRGs are, as reported in the catalogue by Young et al. (2011).

Two of our sample sources have previously been observed with the IRAM-30m by Ocaña Flaquer et al. (2010). For NGC 6251, we combined our spectra in CO(1-0) to improve the upper limit and provide a CO(2-1) search, which was lacking. As for B2 0951+32B, which is a pair of galaxies with a projected separation of 36″, the previous pointing was directed towards the NED middle position in between the two galaxies, and did not cover either. We observed towards the north-eastern elliptical galaxy, which is the host of the RG (Fanti et al. 1987).

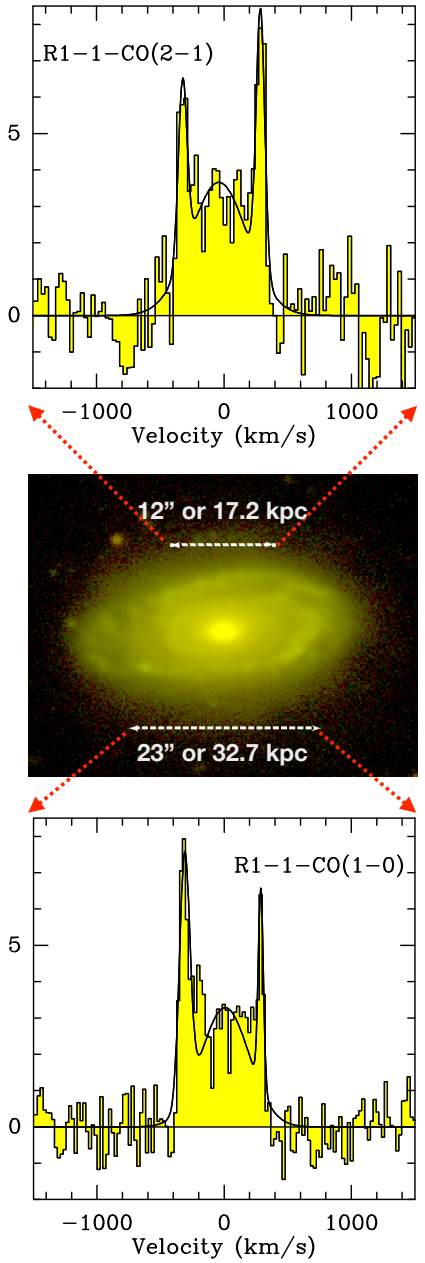

Figure 5.3: Two spectra obtained towards R1-1 or GRG-J2345−0449 in CO(1-0) (bottom) and CO(2-1) (top). The vertical scale is T_{mb} in mK. The middle optical image of the host spiral galaxy of J2345−0449 is obtained by combining G- and R-band data of MegaCam on the CFHT. The G and R-band data belong to the first-generation filters on the MegaCam. The scale on the image represents the beam of the IRAM observations at the respective frequencies.

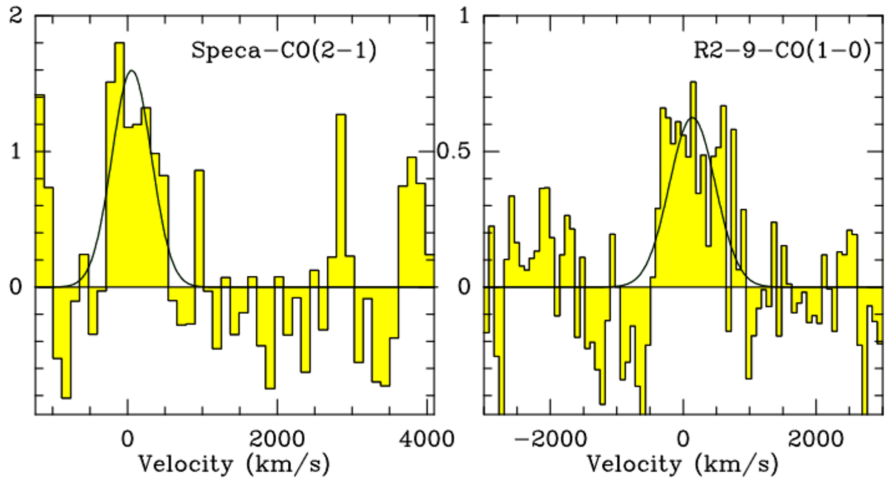

Figure 5.4: Tentative spectra obtained towards Speca in CO(2-1) (left) and R2-9 in CO(1-0) (right). The vertical scale is T_{mb} in mK. The CO(2-1)/CO(1-0) line ratios for the two objects are within reasonable expectations, as shown in Table 5.2.

5.4 Results

As shown in Table. 5.2, only the spiral galaxy R1-1 (J2345−0449) has been clearly detected, and upper limits are reported for the 11 other GRGs, with tentative detections for 2 of them. The two-horn spectra of R1-1 (Figure. 5.3) were fitted by three Gaussians each, and the fits are reported in Table. 5.3. These fits are only empirical, which is better for computing the total intensity, but do not imply any underlying physical components. The upper limit for the R1-0 RG (PKS0211−031) is relatively high because it is a source with one of the highest redshifts. However, the molecular mass is expected to increase with redshift (Tacconi et al. 2018), and based on the measured SFR, a much higher molecular mass was expected. Therefore the upper limit is significant. The tentative signals are displayed in Figure 5.4 for CO(2-1) in the spiral galaxy Speca, and for CO(1-0) for J121615.21+162432.1. Only linear baselines were subtracted from the spectra, but uncertainties are still present because of the presence wavy baselines, although the signal appears at 5σ and 6σ , respectively.

In the following subsections, we present the results we derived from our detections and upper limits of the molecular gas content of the hosts of GRGs, and also compare it with the SFR derived from the mid-IR fluxes. All our upper limits are significant, as we discuss in Sec. 5.5 and show in particular in Fig. 5.8 and Fig. 5.9. In these scaling relations, the upper limits are within or below the expectations. Using our observed quantities, we were also able to estimate the gas depletion time $t_{dep} = M(H_2)/SFR$ and compare it with the radiative lifetime of

the GRGs. From the shape of the detected profile (two-horn shape, and contrast), we derived the gas concentration in the host and discuss the origin of the cool gas. The two-horn profile indicates an extended disc or ring, which is relaxed in the potential, suggesting a quite old galaxy accretion or merger origin for the gas. When the gas comes from cooling filaments alone, it generally has no time to relax in the galaxy potential, and no such profile is expected.

Table 5.2: Derived properties of the GRG sample, where R_e is the half-light radius, SFR is the star formation rate, CO refers to CO flux in the respective bands, log $M(H_2)$ represents the molecular mass (log scale), t_{dep} is the depletion time, and logM_* refers to the stellar mass (log scale) of the galaxy.

Sr.No	R_e	R_e	SFR	CO(1-0)	CO(2-1)	log $M(H_2)$	t_{dep}	logM_*
	(arcsec)	(kpc)	($M_\odot$ yr^{-1})	(Jy km s^{-1})	(Jy km s^{-1})	($M_\odot$)	Gyr	($M_\odot$)
(1)	(2)	(3)	(4)	(5)	(6)	(7)	(8)	(9)
R1-1	5.4	7.76	2.95	14.0	16.3	10.21	5.49	11.37
R1-2	6.1	4.32	0.19	<1.7	<2.7	<8.63	<2.24	10.51
R1-3	3.6	5.77	2.45	<1.5	<7.5	<9.35	<0.91	10.84
R2-1	0.96	1.62	2.07	<1.3	<2.2	<9.34	<1.05	10.63
R2-2	2.2	3.53	0.91	<0.9	<1.3	<9.13	<1.48	10.52
R2-3	0.78	0.83	0.09	<0.9	<1.9	<8.73	<5.96	11.25
R2-4(2)	15.6	7.78	0.31	<1.2	<4	<8.16	<0.47	11.40
R2-5	0.7	1.79	4.64	<1.1	<1.9	<9.69	<1.06	11.03
R2-6(1)	0.95	5.63	170	<1.3	<2.7	<10.82	<0.39	11.70
R2-7	2.4	5.59	1.44	<1.1	<1.9	<9.59	<2.70	11.41
R2-8	3.3	8.04	1.48	<0.9	1.1	9.04	0.74	11.50
R2-9(1)	0.6	3.55	8.33	0.54	<1.1	10.42	3.15	10.89
R1-0(1)	0.87	4.37	48.9	<0.45	<1.6	<10.11	<0.26	10.87
R2-0	5.6	6.70	0.47	<1.1	<2.7	<8.93	<1.81	11.46

(1) For these sources, we observed CO(3-2) instead of CO(2-1). (2) This source was also observed by Ocaña Flaquer et al. (2010). All upper limits are computed at 3σ and assuming an FWHM = 300 km s^{-1}.

Table 5.3: Fit results for R1-1 (GRG-J2345−0449) CO spectra.

Line	Area[(1)] mK km s^{-1}	V km s^{-1}	FWHM km s^{-1}	T_{mb} peak mK
CO(1-0)	1232±167	-316±4	207±11	5.6±0.8
CO(1-0)	800±121	10±18	235±50	3.2±0.8
CO(1-0)	779±150	291±15	179±30	4.1±0.8
CO(2-1)	930±115	-324±8	141±20	6.2±0.9
CO(2-1)	1368±265	-35±33	357±70	3.6±0.9
CO(2-1)	972±110	286±5	113±13	8.1±0.9

(1) Integrated signal in the main-beam temperature scale.

5.4.1 Molecular masses

To quantify the amount of molecular gas found in each target, we relied on the empirically established proportionality between the CO(1-0) luminosity and H_2 mass for a large number of Milky Way-like galaxies (e.g. Bolatto et al. 2013). We converted the integrated intensities in each beam (in T_{mb}) into integrated fluxes S(CO)dV, with a conversion of 5 Jy per Kelvin, as appropriate for the IRAM-30m telescope. From the integrated CO(1-0) flux S(CO)dV (Jy km s^{-1}) found within each region, the molecular mass was obtained through the formula (e.g. Solomon & Vanden Bout 2005)

$$L'_{CO}(K\,km\,s^{-1}pc^{-2}) = 3.25\times10^{7}\frac{S(CO)dV}{(1+z)}\left(\frac{D_L}{\nu_{rest}}\right)^2, \tag{5.1}$$

where ν_{rest} =115.271 GHz, and D_L is the luminosity distance in megaparsec. The molecular mass, including helium, was then derived from $M(H_2) = 4.36\ L'_{CO}$ assuming the standard CO-to-H_2 conversion factor of $X_{CO} = 2\times10^{20}$ cm^{-2}(K km s^{-1})$^{-1}$, as applicable to Milky Way-like galaxies. The region encompassed by the CO(1-0) beams in each galaxy is sufficiently large to cover the entire CO emission (even in the nearest galaxy, NGC 6251 (R2-4), it is 11 kpc). It is, therefore, possible to compare the total molecular masses with other published samples without any aperture correction.

5.4.2 Deconvolving the two-horn spectra

In Figure. 5.3 the CO(1-0) and CO(2-1) spectra show a two-horn shape, with a different depth between the two peaks; the CO(1-0) spectrum is deeper. This means that the molecular component is not too highly concentrated towards the centre and that we are beginning to resolve it in the CO(2-1) line. Because the rotational velocity is zero at the nucleus, the central part of the profile is boosted

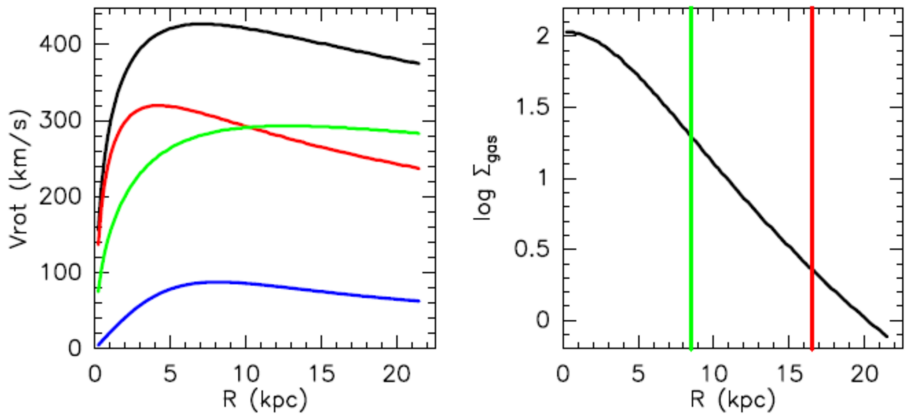

Figure 5.5: Mass model for R1-1 or GRG-J2345−0449 (left), with the contributions to the rotational velocity of the stellar mass (red), the dark matter (green), and the gas (blue). The right panel shows the adopted gas surface density. The two vertical lines indicate the FWHM beam of the CO(1-0) (red) and CO(2-1) (green).

by a high gas concentration. With a large beam, that is, for CO(1-0), the outer parts of the disc are preponderant, and the two-horn profile is more contrasted. The smaller CO(2-1) beam begins to resolve the disc, and the central part is more weighted than the outer parts in this line profile. To interpret the kinematics of our CO data more quantitatively, we used a simple analytical model that computes the velocity spectrum from the rotation velocity profile of the galaxy (Wiklind et al. 1997). The rotation velocity profile is determined from the stellar mass distribution, assuming it follows the simple potential-density pair proposed by Hernquist (1990). We adjusted the size and mass of the stellar component to fit the half-light radius and M_* as shown in Table. 5.2. We completed this mass at high radii by dark matter, in order to flatten the rotation curve. The dark matter mass inside 24.5 kpc was taken to be 1.5 M_*, and its characteristic radius was three times that of the stars. The gas disc was also taken into account in the potential, as shown in Figure. 5.5, with the mass shown in Table. 5.2. Its characteristic scale can be determined by modelling the two-horn spectra. Based on the ellipticity obtained from the optical image (Figure. 5.1), we derive an inclination of 65°, which is also close to the value given by Hyperleda (65.7°).

The gas distribution is assumed to be axisymmetric with a surface density $\Sigma(r)$ in a disc with negligible thickness. For each velocity dv, the code calculates the density contained in the isovelocity (equation 5.2). The velocity spectrum corresponds to the velocity histogram. We then convolved the computed spectrum with a Gaussian with a standard $\sigma = 10\,\mathrm{km\ s^{-1}}$ to account for the gas velocity

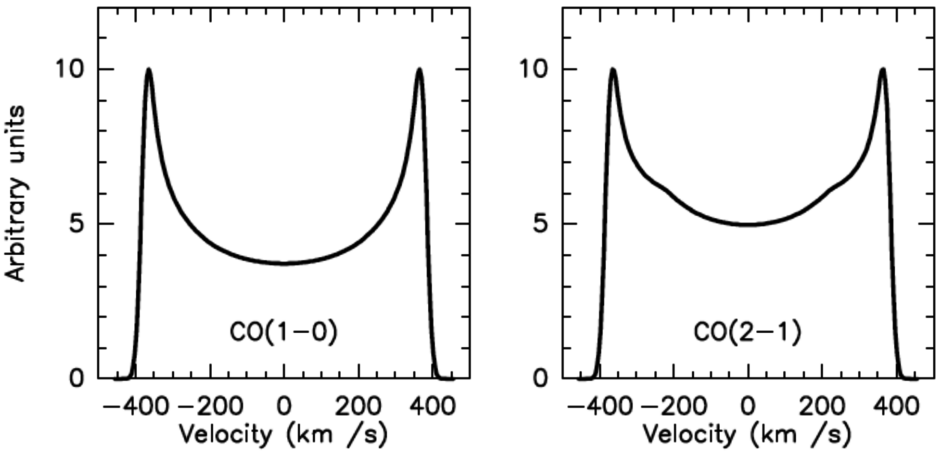

Figure 5.6: Spectra obtained from the model for the CO(1-0) line with a beam of 23″= 33 kpc (left) and for the CO(2-1) line with a beam of 12″=17 kpc (right). The assumed inclination of the disc is 65°.

dispersion,

$$\frac{dN}{dv}(v) = \int \frac{\Sigma(r)\, r dr}{v_{rot}(r) \sin i \left(1 - [\frac{v}{v_{rot}(r) \sin i}]^2\right)^{1/2}}. \quad (5.2)$$

To determine the concentration of gas in the galaxy, we adopted an analytical profile, with a potential-density pair, which facilitates computing the rotation velocity. We selected the formulation of a Toomre disc of order 2: $\Sigma(r) = \Sigma_0 \left(1 + \frac{r^2}{d^2}\right)^{-5/2}$ (Toomre 1964). Figure. 5.5 shows that the profile is close to an exponential, which is realistic. We also tried models with rings, using the difference between two Toomre discs with different scales, but a single gas disc was an even better fit. The exponential scale of the best-fit disc is 4.34 kpc, leading to a half-light radius of 7.3 kpc, which is very close to that of the stellar component. This corresponds to what is generally found for the molecular distributions (Lisenfeld et al. 2011).

5.5 Discussion

GRGs are rarer than the RG population, and very few studies have been conducted to detect molecular gas in their host galaxies. We list the detections reported in the literature in Table. 5.4. In the following section, we consider the four GRGs listed in Table. 5.4 that are hosted by early-type galaxies. NGC 315 is the brightest elliptical (cD) galaxy of a group (O'Sullivan et al. 2015a), and has also been detected in HI-21cm absorption and emission (Morganti et al. 2009). 3C 31,

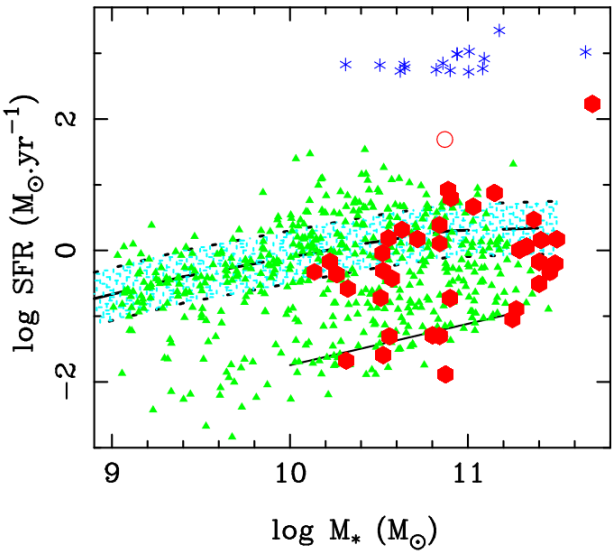

Figure 5.7: Location of our targets (red hexagons) in the SFR-M_{star} diagram. They are compared with the xCOLD GASS sample of 532 galaxies with local redshift 0.01 < z < 0.05 from Saintonge et al. (2017) (green triangles), and with the starburst galaxies (blue stars) in the comparable range 0.2 < z < 0.6 (Combes et al. 2011). The SDSS main sequence is shown with the cyan-shaded region, and delimited by dashed lines (at ±0.4 dex), and the red sequence by a full line. Open red circles belong to non-GRGs observed by us.

hosted by NGC 383, is a lenticular galaxy which is well detected in CO (Evans et al. 2005a; Ocaña Flaquer et al. 2010), but neither in emission nor in absorption (Emonts et al. 2010) of HI-21cm. The host of 3C 236 is a massive elliptical galaxy with a distorted morphology, and a prominent dust lane. Its CO spectrum is blue-shifted by ∼300 km s^{-1} with respect to the optical velocity (Labiano et al. 2013), and it corresponds to the peak of the HI-21cm absorption (Morganti et al. 2005). The oldest and youngest spectral ages of different parts of GRG 3C 236 are 159 Myr and 51 Myr (Shulevski et al. 2019). The radio core of 3C 326 comprises two early-type galaxies, and the most massive galaxy in the north (3C 326N : 15:52:09.10 +20:05:48.32)) is the host galaxy (Rawlings et al. 1990). Its molecular gas in the cold (Nesvadba et al. 2010) and warm phase (Ogle et al. 2007) traces shocks, possibly due to the radio-jet feedback.

5.5.1 Star formation and gas mass

The host galaxies of GRGs have not previously been studied with respect to their SFR as a function of stellar mass and have not been compared with the main-sequence galaxies, starbursts, or quiescent objects. We show our comparisons

Table 5.4: Properties of GRGs taken from literature: Column (2) lists the half-light radius (R_e), column (3) the star formation rate (SFR), column (4) the molecular mass ($\log M(H_2)$), column (5) the stellar mass ($\log M_*$), column (6) the 22μm luminosity derived from WISE ($\log L_{22\mu m}$), and column (7) the CO(1-0) line width (FWHM) obtained from the respective references listed in column (8). Column (8) Ref: (1) Ocaña Flaquer et al. (2010); (2) Labiano et al. (2013); (3) Nesvadba et al. (2010)

Name	R_e	SFR	$\log M(H_2)$	$\log M_*$	$\log L_{22\mu m}$	FWHM	Ref
	(kpc)	($M_\odot yr^{-1}$)	($M_\odot$)	($M_\odot$)	(erg s^{-1})	(km s^{-1})	
(1)	(2)	(3)	(4)	(5)	(6)	(7)	(8)
NGC315	6.3	0.63	7.87	11.49	42.18	150	(1)
3C31	4.6	1.02	9.22	11.29	41.51	550	(1)
3C236	7.4	7.51	9.32	11.15	43.07	-	(2)
3C326N	6.9	0.67	9.18	11.40	42.09	351	(3)

in Figure. 5.7 , where the xCOLD GASS sample of Saintonge et al. (2017) is a reference for tracing the main sequence at low redshift and as part of the red sequence. Starburst galaxies at comparable redshifts are plotted from Combes et al. (2011). It is important to have samples at the same z because the location of the main sequence strongly depends on redshift (Whitaker et al. 2012). Eight of our targets are on the main sequence (MS), including the detected R1-1, four are in a starburst phase, and seven are in the red passive sequence. The position close to the MS is associated with disc morphology (Wuyts et al. 2011), and the slope and scatter of the MS depend on morphology (Whitaker et al. 2015).

The star formation rate is expected to be related to the interstellar gas content, and the precise relationship has been discussed either from the atomic or molecular gas or both (Kennicutt 1998; Bigiel et al. 2008). The relation is much tighter and linear with the molecular gas. The relation can be expressed with the global quantities (SFR versus M_{mol}), or with the surface densities, when normalised with the effective area. The latter are computed from the effective radius, containing half of the light (displayed in Table. 5.2). This is a global quantity for the galaxy because we do not resolve the inner parts of the galaxies with our observations with IRAM-30m. However, the relation between the two average surface densities yields another very useful point of view, as discussed by Kennicutt (1998). Figure. 5.8 displays both relations. In the global quantity diagram, most of our upper limits fall in the region of normal MS galaxies, traced by the straight line corresponding to a depletion time $t_{dep} = M(H_2)/SFR = 1$ Gyr. The R1-1 detected spiral galaxy has a long t_{dep} of 5.5 Gyr, and the tentative detection R2-9 has t_{dep} of 3.15 Gyr, and the two detected GRG (NGC 315 and 3C 236) have an exceptionally short t_{dep} of 120 and 280 Myr, as well as two upper limits that are more typical of starbursts. When normalised to the galaxy surface, the R1-1 spiral galaxy and other outliers fall much closer to the main sequence in the KS diagram, except for NGC 315 and NGC 6251, which are still exceptionally deficient in molecular gas. R1-1, which is

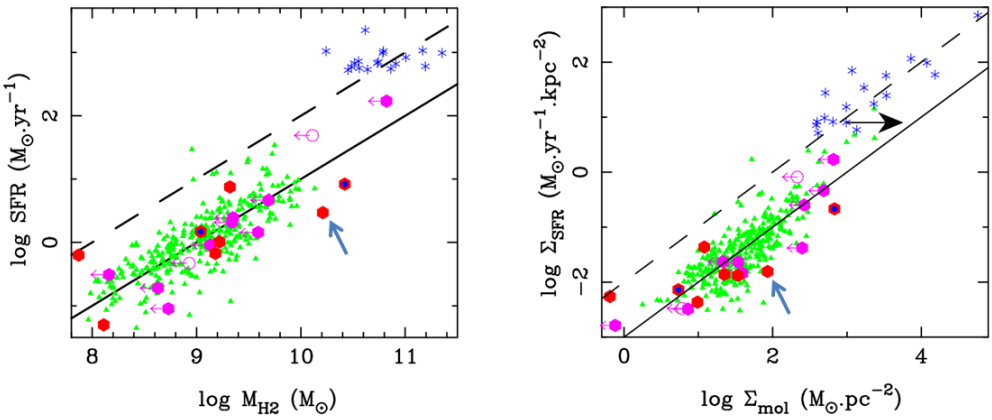

Figure 5.8: Star formation rate as a function of the molecular content for our targets compared to normal galaxies and starbursts at comparable redshifts. The global SFR-M_{mol} diagram is shown at the left, and the surface densities of the same quantities, representing the unresolved Kennicutt-Schmidt relation (Kennicutt 1998), are shown at the right. The straight lines are power laws of slope 1. The full line corresponds to a depletion time of 1 Gyr, and the dashed line to 100 Myr. Symbols are the same as in Figure. 5.7; upper limits of our targets are shown in pink, and tentative detections as a blue hexagon inside the red one. The blue arrow points to the location of R1-1 (GRG-J2345−0449) in the respective plots.

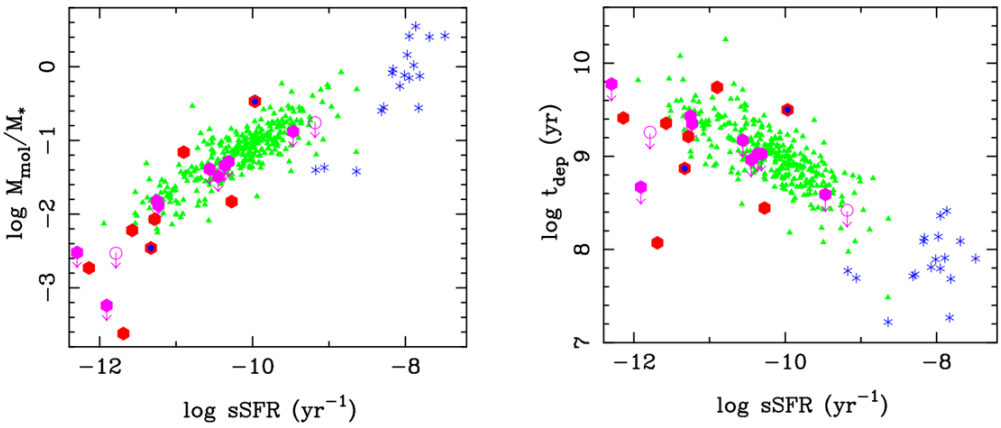

Figure 5.9: Trends of specific star formation with other properties: The left plot shows the ratio of molecular gas to stellar mass as a function of sSFR. On the right we show the depletion time as a function of sSFR. Further details can be found in Sec. 5.5.1. The symbols in this plot are same as in Figure. 5.8.

a giant spiral galaxy, does not have a high SFR, as seen in Figure. 5.8, although its reservoir of M_{H2} is large, which may be connected with the restarted nature of the GRG. In these relations, the molecular masses of the starburst sample were obtained with a different CO-to-H_2 conversion factor, as is justified for starbursts (Solomon & Vanden Bout 2005). With a larger factor, the difference to the MS would be much smaller, as is indicated by the arrow in the right panel of Figure. 5.8.

The fraction of gas in the baryonic content of a galaxy, measured by the ratio of gas to stellar mass, is a key factor in understanding the various observed star formation rates. This relative gas content is plotted versus the specific SFR (sSFR=SFR/M_*) in the left plot in Figure. 5.9. The GRG targets follow the main-sequence galaxies of the xCOLD GASS sample, two of which are gas-poor, NGC 315 and NGC 6251. Together with the gas fraction, SFR depends on the efficiency of star formation with respect to the amount of fuel, that is, SFR/M_{mol}, which is the inverse of the depletion time t_{dep}. The latter is plotted versus sSFR in the right panel of Figure. 5.9. Here again, most of our targets follow the MS scaling relations, except for two, NGC 315 and NGC 6251, which appear to be too efficient to form stars because they lack molecular gas. Their t_{dep} (the inverse of star formation efficiency) is shorter than expected from the scaling relation.

5.5.2 Radio power and fueling

The nuclear activity in galaxies is thought to be triggered when the central supermassive black hole accretes a significant mass of gas from its interstellar reservoir.

Table 5.5: Other properties of GRGs. We computed $P_{1.4}$, D, and Q_{Jet} from the data available in the literature, whose details can be found in Sec. 5.5.2. Column 6 indicates whether the GRG shows signs of restarted AGN activity, and column (7) shows their membership in a group (Gr) or cluster (Cl). Sources below the horizontal line are from the literature. The minus indicates non-availability of data or classification.

Name	FR	log $P_{1.4}$ (W Hz^{-1})	D (Mpc)	HE/LE	Re	Gr/Cl	Q_{Jet} (10^{43} erg s^{-1})
(1)	(2)	(3)	(4)	(5)	(6)	(7)	(8)
R1-1	II	24.31	1.64	LE	Yes	No	-
R1-2	I	23.95	0.96	LE	-	Gr	-
R1-3	II	24.71	1.05	HE	-	Gr	0.53
R2-1	II	25.20	1.52	HE	Yes	-	2.45
R2-2	II	24.57	1.47	HE	-	Gr	-
R2-3	I/II	-	2.48	LE	-	Gr	0.36
R2-4	I/II	24.41	1.96	SF	No	-	1.21
R2-5	II	25.36	2.80	HE	-	Gr	1.77
R2-6	II	25.94	1.79	HE	No	-	17.94
R2-7	II	24.71	2.24	LE		Gr	-
R2-8	II	24.83	1.39	LE	Yes	GR	-
R2-9	II	26.02	1.78	HE	No	-	16.53
NGC 315	I	24.15	1.15	SF	-	Gr	0.16
3C 31	I	24.48	0.93	LE	-	Gr	0.54
3C 236	II	26.05	4.45	HE	Yes	-	14.76
3C 326N	II	25.66	2.02	LE	Yes	-	10.42

Typical accretion phases in AGN may last ∼40 million years, with a duty cycle of a few percent (Shankar et al. 2009; Hopkins & Quataert 2010). The GRGs are thought to be at the end of an active and powerful phase of radio galaxy evolution. Several hypotheses have been proposed to account for their extreme sizes, but the role of each factor is still unclear. The possibilities include the power of the radio jet, implying a higher velocity (Schoenmakers et al. 2000a), the effect of the environment (jets are able to extend further in voids, but see Dabhade et al. 2020c), or a restarted activity (Bruni et al. 2019, 2020). In the latter case, the sources are identified with two jets at different orientations, called double-double, or X-shaped (Saripalli et al. 2013), and/or a young central source (Machalski et al. 2007c), with a flat spectral index (Schoenmakers et al. 1998), which has recently been refuelled.

The determination of their gas reservoir can confirm and quantify these fueling mechanisms, and help to understand the complex processes involved in their radio-

jet launching and evolution. The important clues for the giant nature of GRGs may lie in the accretion rates, which translate into high excitation (HE) or low excitation (LE). The HE objects are defined to have an accretion rate above one-hundredth of the Eddington rate, while the LE objects accrete below this limit. The latter belong to a regime of radiatively inefficient accretion, which foster the formation of radio jets. Table. 5.5 shows our classification of GRGs in our sample with respect to their AGN excitation type, high and low, or HEGRG and LEGRG. We do not find that HEGRGs have higher molecular gas mass than LEGRGs, as was found by Smolčić & Riechers (2011) for RGs. Dabhade et al. (2020c) showed that LEGRGs and HEGRGs have distinct properties, such as their respective small size counterparts LERGs and HERGs. We do not have enough statistics here to see a difference with molecular gas fraction.

Recent gas accretion could be violent, through major mergers, or more secular through minor mergers of cold gas accretion from cosmic filaments. The observation of the molecular component may bring important clues, showing a perturbed component in case of galaxy interaction, or a regular disc for secular evolution. It has been observed that the detection rate of molecular gas is high in the edge-darkened Fanaroff-Riley (FR) type 1 radio galaxy (Fanaroff & Riley 1974) and low in edge brightened FR-II type (Evans et al. 2005a). More than 90% of the GRGs have a morphology of FR-II type (Dabhade et al. 2020b,c), and it is very interesting to determine whether GRGs with FR-II type morphology also have fewer molecular gas detections.

Table. 5.5 summarises the FR type, total radio power ($P_{1.4}$), projected linear size (D), excitation state, and jet kinetic power (Q_{Jet}) of all GRGs in our sample along with other GRGs taken from the literature. The 1.4 GHz power was estimated using the NRAO VLA Sky Survey (Condon et al. 1998) flux of the GRG at 1.4 GHz. We used the method described by Hardcastle (2018b) to estimate Q_{Jet} using the 150 MHz flux from TIFR GMRT Sky Survey (Intema et al. 2017) and other observations from the literature. A similar scheme was used in Dabhade et al. (2020c) to compute the above parameters for a large sample of GRGs. The excitation state (accretion mode) of GRGs is determined from the mid-infrared fluxes, as in Dabhade et al. (2020c). It helps separate star-forming objects from objects whose emission is dominated by the AGN, as well as HE from LE radio galaxies with the mid-infrared ratios obtained in the WISE bands. WISE colours have been demonstrated to be very useful diagnostics of the accretion mode of radio galaxies (Gürkan et al. 2014).

Evans et al. (2005a) conducted a survey to investigate the molecular content in RGs, where they found detections in FR-I and compact sources, but rarely in FR-II objects. It could be expected that restarted RGs, requiring molecular gas to fuel their activity, would be detected, but only a few have been found to be rich in molecular gas, for example, the post-merger 3C293 (Evans et al. 2005a; Labiano et al. 2014). Evans et al. (2005a) also searched for a possible correlation between the CO luminosity and the 1.4 GHz core luminosity and found none. We studied the possible effect of the radio jets on the host galaxy properties by ex-

ploring the connections between Q_{Jet} and parameters derived from our IRAM-30m observations. Based on the current data, we find no correlation between these parameters. These results may not uncover the whole aspect because our observations with IRAM-30m presents the global cumulative molecular gas properties, and correlations may exist for nuclear region components alone.

GRGs have more intermediate-age stellar populations than the smaller FR-II radio sources (Kuźmicz et al. 2019). This is also true for their neighbours within 1.5 Mpc, which show in general younger populations, suggesting triggered star formation due to their environment. This triggering, either through mergers or cold streams, might also be responsible for their giant sizes. A large fraction of GRGs in our sample belong to groups, like R1-2, R1-3, R2-2, R2-3, R2-5, and R2-7 (cf Table. 5.5). R2-3, in particular, resides at the centre of a quite disturbed tight galaxy group. It is one of the galaxies of the UGC9555 triplet, hosting a compact flat-spectrum radio source (Clarke et al. 2017). There is evidence that the AGN has been fueled by recent interactions and minor mergers from its group galaxies. None of the other galaxies in the sample shows any signs of recent mergers that might be responsible for their fueling.

Finally, four out of seven of the CO-detected GRGs belong to the restarted class, implying that the molecular gas has recently (within ~ 100 Myr) refuelled the AGN and radio jets. However, there seems to be a struggle between star formation and nuclear activity for the fueling. Some of these galaxies are actively forming stars, and their depletion time is quite short (740 Myr and 280 Myr for Speca and 3C236, respectively), while others are rather quiescent and favour the AGN, like R1-1 and 3C326 (with t_{dep} of 5.5 Gyr and 2.26 Gyr). Using observations of the Hubble Space Telescope, Tremblay et al. (2010) have shown bursts of repeated star formation in the host galaxy of 3C 236, which has a dusty disc around the AGN. Because 3C 236 is known to be a restarted AGN, this might be connected with the young starburst property of the host galaxy. Based on the studies of GRGs conducted so far and our results, we understand that we observe each GRG in its different evolutionary phase. Therefore we are unlikely to find a similar fueling trend (e.g. cold gas fueling) for all GRGs because the trend closely depends on the AGN accretion state.

In the future, it will be fruitful to observe the GRGs with ALMA to probe the sphere of influence of the black holes that reside in the AGN. This might be a test for the presence of a molecular torus, as was recently found in some low-luminosity AGNs by Combes et al. (2019).

5.6 Summary

We have presented our first IRAM results for a sample of 12 GRGs, selected from the GRG catalogue (Dabhade et al. 2020c). We detected the two first rotational lines of CO in one GRG, which is the giant spiral GRG-J2345−0449, and report tentative signals for two others (R2-8 and R2-9). The two-horn shape of the spectra of R1-1 (GRG-J2345-0449) allowed us to determine the concentration of the

molecular gas in the giant spiral galaxy. The best-fit model is a roughly exponential disc for the molecular component, and its half-light radius is comparable to that of the stellar component.

We added four GRGs from the literature with CO line detections to our sample. Comparing this sample of 16 GRGs with the MS star-forming galaxies at comparable redshift from Saintonge et al. (2017) and a sample of starburst galaxies at similar z (Combes et al. 2011), we find that most (8) of our targets are on the MS, 7 are on the red sequence, and 4 are starbursts. The molecular content of CO-detected GRGs is quite compatible with what is expected from their SFR, although our detected giant spiral appears to be deficient in star formation, with a depletion time of 5.5 Gyr that is about three times longer than the average of the MS.

Most of the GRGs detected in molecular gas to date are restarted radio galaxies or are in groups, suggesting that the environment plays an important role to refuel the central AGN. The accreted gas also fuels star formation, and the depletion time is sometimes quite short, a few 100 Myr. This is comparable to timescales similar to the spectral ages of the GRGs. Up to now, the number of GRGs with CO detections is low, and more detections are required to draw firmer conclusions.

6 | Chapter 6 : Barbell shaped giant radio galaxy with ~100 kpc kink in jet

We present here the study of a peculiar giant radio galaxy (GRG) - GRG-J2233+1315 using deep multi-frequency radio observations from GMRT and LOFAR along with optical spectroscopic observations with WHT 4.2m optical telescope. Our observations have firmly established its redshift of 0.09956 and unveiled its exceptional jet structure extending more than ~ 200 kpc culminating into a peculiar 'kink' structure of ~ 100 kpc. We measure the overall size of this GRG to be ~ 1.9 Mpc, which exhibits lobes without any prominent hotspots and closely resembles to a 'Barbell'. The magnetic field strength $\sim 5\,\mu$G and spectral ages of > 110 Myr for the radio lobes were estimated using high resolution radio data from LOFAR 144 MHz observations and GMRT 323 and 612 MHz observations. The deep low frequency radio maps also reveals many diffuse emission regions associated with the GRG. Despite its enormous size, the Barbell GRG is found to be residing in dense environment of either a small galaxy cluster or galaxy group. We discuss the possible causes for the 'kink' feature using various models of jet plasma instabilities.

P. Dabhade et al. 2021- A&A To be submitted

6.1 Introduction

Galaxies hosting active galactic nuclei (AGNs) which are strongly radiating at radio wavelengths are referred to as radio galaxies (RGs), which exhibit relativistic radio jets. Extended RGs with lobes (or edge-brightened) are categorised as Fanaroff-Riley type-II or FR-II (Fanaroff & Riley 1974) and the ones with centre-brightened features with bright jets and no lobe-hotspots are called the Fanaroff-Riley type-I or FR-I. This launching and propagation of jets is explained by the standard 'beam model' (Longair et al. 1973; Scheuer 1974; Blandford & Rees 1974), where collimated jets resulting from outflows originating from black holes, propel the extended structure. The dichotomy between the two classes of FR-I and FR-II type RGs is thought to be rooted in the AGN accretion mode and its connection with the jet power (Best & Heckman 2012a; Mingo et al. 2014; Hardcastle 2018a).

RGs extending to megaparsec (Mpc) scales are defined as giant radio galaxies (GRGs), which are quite rarer than RG population as shown in recent studies (Dabhade et al. 2020b,c). They are thought to be growing in the underdense environments and/or supplied with continuous jet power for a long duration ($\sim 10^8$ Myr), thereby allowing them to scale larger distances. Efforts to constrain models explaining the giant nature of GRGs are currently on-going (Gopal-Krishna et al. 1989; Subrahmanyan et al. 1996; Saripalli et al. 2005; Hardcastle et al. 2019; Dabhade et al. 2020c,a; Bruni et al. 2020). More discussion on the above can be found in Dabhade et al. (2020c).

The last few years has seen a resurgence in studies of GRGs owing to the new sensitive surveys at radio wavelengths like the LOFAR Two Metre Sky Survey (LoTSS; Shimwell et al. 2019), which is largely complemented by optical spectroscopic surveys like the Sloan Digital Sky Survey (SDSS; York et al. 2000; Abolfathi et al. 2018).

In the course of identifying giant radio galaxies and carrying out detailed multi-wavelength studies of GRGs under our project SAGAN* (Dabhade et al. 2017, 2020c), we have discovered a peculiar giant radio galaxy J223301+131502 (GRG-J2233+1315 for short form) from the NRAO VLA SKY SURVEY (NVSS; Condon et al. 1998) as reported in Dabhade et al. 2017. In this paper, we present our results on GRG-J2233+1315 based on optical and radio observations taken by us.

GRG-J2233+1315 is hosted by SDSS J223301.30+131502.5 galaxy, which exhibits a big diffuse stellar halo with apparent SDSS r-band magnitude (m_r) of 15.21 (Fig. 6.1). It has an elliptical morphology (Lintott et al. 2011) and has been classified to be of S0-a type galaxy (Paturel et al. 2003) with the isophotal diameter of (logd25) of 0.77±0.06. The stellar mass of the galaxy is $\sim 1.62 \times 10^{11}\,M_\odot$ (Lin et al. 2018).

It also has been identified as the brightest cluster galaxy (BCG) by MaxBCG Catalog of 13,823 Galaxy Clusters from the Sloan Digital Sky Survey (Koester et al. 2007) as MaxBCG338.25543+13.25070, GMBCG Galaxy Cluster Catalog of 55,424 Rich Clusters from SDSS DR7 (Hao et al. 2010) as J338.25544+13.25070,

*https://sites.google.com/site/anantasakyatta/sagan

and WHL cluster catalogue (Wen et al. 2012) of 132,684 clusters from SDSS-III data as WHLJ223301.3+131503. This is in contrast to the prevailing belief of GRGs residing in sparse environment (Mack et al. 1998; Subrahmanyan et al. 2008; Malarecki et al. 2015). Recently, large GRG samples from the LoTSS and NVSS have revealed more than 60 such examples of GRGs residing at the centres of galaxy clusters and groups (Dabhade et al. 2020b,c).

Earlier, Dabhade et al. 2017 used the photometric redshift (z) of ~ 0.093 from SDSS to estimate the total projected linear size of the GRG-J2233+1315 to be ~ 1.71 Mpc. Based on the only available radio data of NVSS at 1.4 GHz, Dabhade et al. 2017 observed a bright region possibly part of the GRG on the western side of the host galaxy and it was thought to be a 'knot' in the jet which is unresolved.

The important issue is to understand the growth and evolution of GRGs, which despite the dense environment manage to grow to megaparsec lengths. The combination of radio and X-ray data of such sources will enable us to study the inter-galactic medium (IGM) as well as the intra cluster medium (ICM). The interaction of the radio plasma with the hot ICM can possibly lead to the formation of 'cavities', which show up as depressions in the X-ray surface brightness maps (Bîrzan et al. 2004; McNamara et al. 2005). Research still continues on how these cavities influence the ICM as they could be supplying a dynamically important amount of heat and/or magnetic field to the ICM (Kronberg et al. 2001b; Quilis et al. 2001; Brüggen & Kaiser 2002; Fabian et al. 2002; Heinz et al. 2002; McNamara & Nulsen 2007). Hence, a GRG with nearly 2 Mpc size, residing in an over dense environment with peculiar radio morphology consisting of bright unresolved features and diffuse lobes warrants a detailed study using multi-frequency radio data.

6.2 Observations and data analysis

In this section we provide the details of the optical and radio observations and their corresponding data analysis for GRG-J2233+1315.

6.2.1 Optical

An accurate redshift of the GRG is needed to estimate its properties and hence, efforts were made to update the SDSS photometric redshift of 0.093 with spectroscopic observations. The optical spectrum of the host galaxy (SDSS J223301.30+131502.5) was obtained using the long-slit at 4.2m William Herschel Telescope (WHT), which is located at La Palma, Canary Islands. The observations were carried out on 27$^{\text{th}}$ June 2017 under the program id : W17AN014 using the Intermediate dispersion Spectrograph and Imaging System (ISIS*) instrument with a 3′ slit length and a slit width of 1.5″. Further details of the observations and data reduction are presented in section 2.2.1 of Saxena et al. (2019).

*http://www.ing.iac.es/astronomy/instruments/isis/index.html

We use the standard procedure of comparing the wavelengths of red-shifted lines (observed wavelengths) with the rest-frame emission and absorption lines as observed in Fig. 6.2 to estimate the redshift. We have used the standard IAU conversion from air to vacuum wavelengths (Morton 1991). The center, full width half maxima (FWHM) and error in FWHM for emission lines of the object, and the lamp spectra were measured using the Gaussian fitting routines. The instrumental broadening of grism 7 is 6.78Å. We have calculated the intrinsic FWHM using the instrumental broadening. We have calculated redshift from the observed wavelength and the error in redshift has been calculated using corrected FWHM. Using the corrected FWHM, we have also estimated stellar velocity dispersion (σ).

Table 6.1: Details of radio observations of GRG-J2233+1315 are provided in this table, where observations at 1280, 610, and 325 MHz are with GMRT and 144 MHz is with LOFAR. Primary calibrator refers to flux calibrator and secondary is the phase calibrator. Observation date format is dd/mm/yy. Project codes marked with * symbol are projects with co-observing scheme with the LoTSS.

Frequency (MHz)	Project Code	Observation Date	Obsid	Time on Source (mins)	Bandwidth MHz	Channels	Integration Time (secs)	Correlations	Primary Calibrator	Secondary Calibrator
(1)	(2)	(3)	(4)	(5)	(6)	(7)	(8)	(9)	(10)	(11)
1280	31_084	23/10/2016	8940	193	32	512	8	RR & LL	3C48	2148+069
612	28_020	17/05/2015	7785	225	32	512	8	RR & LL	3C48	2130+050
323	31_084	03/11/2016	8962	349	32	512	8	RR & LL	3C48	2212+018
144	LC6_024	05/09/2016	544937	480	49	231	1	RR & LL	3C196	3C196
144	LC11_009*	23/02/2019	695799	480	49	231	1	RR & LL	3C295	3C295
144	LC11_009*	11/05/2019	708070	480	49	231	1	RR & LL	3C295	3C295
144	LT10_010*	17/01/2020	765089	480	49	231	1	RR & LL	3C295	3C295
144	LT10_010*	26/03/2020	773699	480	49	231	1	RR & LL	3C295	3C295

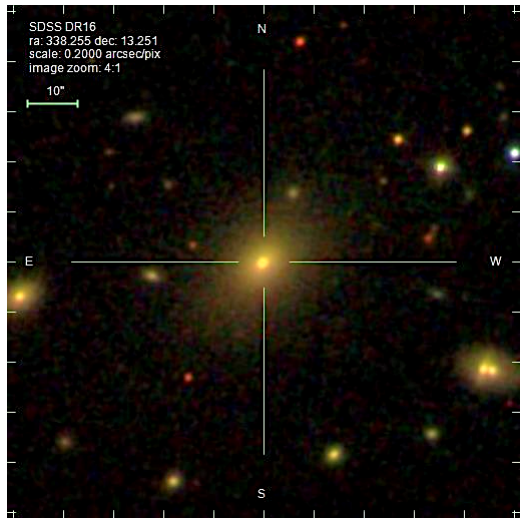

Figure 6.1: Multi-band colour composite optical image of SDSS J223301.30+131502.5 galaxy. The scales are given in the top left corner of the image.

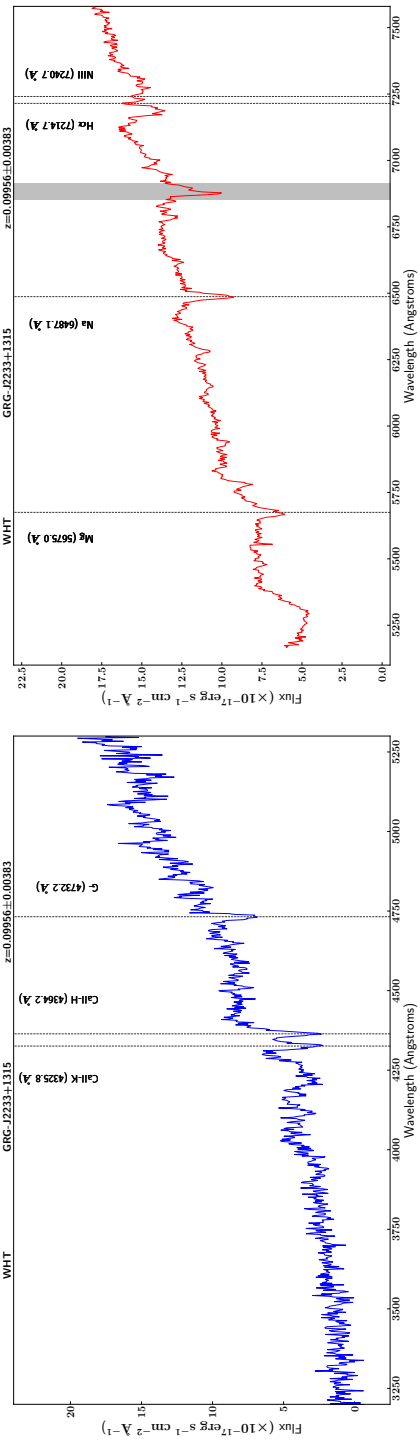

Figure 6.2: The plot shows 4.2m-WHT ISIS blue and red arm spectrum of the GRG-J2233+1315 in the shown wavelength ranges. The identified emission and absorption lines in the spectrum are marked with black dashed vertical lines. Spectrum from blue and red detectors are colour coded with their respective colours. The grey band represents telluric lines. More details can be seen in Sec. 6.2.1.

6.2.2 Radio Observations and data analysis

The GRG-J2233+1315 was observed (Tab. 6.1) at three frequencies with the Giant Metre-wave Radio Telescope (Swarup 1991; Swarup et al. 1991) covering the frequency range from ~300 to 1400 MHz. We obtained the coverage below 300 MHz with the LOw Frequency ARray's high band antennae (HBA) (van Haarlem et al. 2013). Below we describe the observations and data analysis.

GMRT observation and analysis

GRG-J2233+1315 was observed with GMRT in 2015-2016 at three frequencies as given in detail in Tab. 6.1 under the projects 28_20 and 31_84 (PI: Pratik Dabhade). The raw visibility GMRT data of all three frequencies was analysed using the Source Peeling and Atmospheric Modelling (SPAM; Intema et al. 2017) package. SPAM is based on the Astronomical Image Processing System (AIPS; Greisen 2003) and python programming language. To access tasks in AIPS, python based parseltongue interface (Kettenis et al. 2006) is used in SPAM. The analysis steps in SPAM starts with the flux and bandpass calibrations, which were derived from the respective calibrators after three cyclic iterations of flagging (Radio Frequency Interference-RFI) and calibrations based on models (e.g. Scaife & Heald 2012). In addition to the above, instrumental phase calibrations are also determined using methods of Intema et al. 2009. For ionospheric calibration, direction dependent gains are derived from the strong sources present in the field of view (FOV), which are then used to fit a time variable phase screen over the whole array. This phase screen is used later during imaging for correcting the entire FOV for effects caused by ionospheric phases. The derived calibrations were transferred to the target (GRG-J2233+1315) data. This was followed with imaging which consisted of several cyclic iterations of self-calibration with phase only gain calibration initially using local sky model derived from surveys like NVSS and others. The iterations also involved flagging of remaining weaker RFI. Finally, wide-field facet based imaging is carried out, with visibility weighting scheme of ROBUST -1 (AIPS) as it present a finer point spread function. Another three more iterations of self-calibrations were carried out with addition of amplitude calibration in the final round. In each round the process of peeling (Noordam 2004) was performed (see Intema et al. 2017 for details).

LOFAR observation and analysis

The GRG-J2233+1315 was observed three times between 2016-09 and 2020-03, once in a dedicated 8 hours LOFAR observation (project LC6_024, observation ID 544933, PI: Pratik Dabhade) and also as part of LoTSS where if we account for the target being offset from the pointing centre the effective integration time at the location of the target was also approximately 8 hrs (project LT10_010, co-observing project LC11_009 and observation IDs 695799, 708070, 765089, 773699). These observations were all conducted in HBA Dual Inner Mode and for this project we

made use of 231 0.195 MHz sub-bands between 120 and 169 MHz. Two 10 min calibrator observations were observed before and after each target observation. The basic details of these observations are summarised in Tab. 6.1.

The data were processed using the PreFactor pipeline* as described in van Weeren et al. (2016), Williams et al. (2016) and de Gasperin et al. (2019) which corrects the data for direction independent effects such as the bandpass, ionospheric Faraday rotation, clock offsets between different stations and an offset between XX and YY phases. The data were then processed with the latest version of the LoTSS direction dependent calibration pipeline, DDF-pipeline† which is summarised in Sec. 5.1 of Shimwell et al. (2019) and described in more detail in Tasse et al. 2020. This pipeline uses the calibration package kMS (Tasse 2014 and Smirnov & Tasse 2015) and imaging package DDFacet (Tasse et al. 2018) to perform a direction dependent self-calibration loop where calibration solutions are derived and gradually refined for 45 different directions spanning an $8° \times 8°$ field of view and applied during the imaging. After each individual pointing is imaged we used the procedure described in van Weeren et al. 2020 to refine the solutions in the direction of our target and allow for each re-imaging. For each pointing this involved subtracting sources away from the target region before phase shifting all datasets to be centred on the target and then performing a direction independent self calibration that makes use of WSClean (Offringa et al. 2014) and DPPP (van Diepen et al. 2018).

*https://github.com/lofar-astron/prefactor
†https://github.com/mhardcastle/ddf-pipeline

Table 6.2: Basic information about GRG. RA and Dec are Right Ascension and Declination of the host galaxy. S_ν is integrated flux density of the source and the P_ν is the radio power computed at frequency ν. $S_{1400MHz}$ is measured from NVSS. α_{int} is the integrated spectral index of the GRG from 144 MHz to 1400 MHz. Angular size refers to the largest angular size (LAS) of the GRG as measured from the radio maps. The flux density and corresponding power at 1300 MHz are from GMRT L-band observations. Here, $S_\nu \propto \nu^{-\alpha}$ convention is followed.

Properties	Values
RA	22 33 01.30
Dec	+13 15 02.52
r_{band} (mag)	15.04
Angular Size ($'$)	16.1
Redshift (z)	0.09956 ± 0.00383
Projected Size (Mpc)	1.83
$S^{Core}_{1300MHz}$ (mJy)	3.72 ± 0.84
$S_{1400MHz}$ (mJy)	231 ± 7.8
S_{612MHz} (mJy)	479 ± 24.3
S_{323MHz} (mJy)	835 ± 83.5
S_{144MHz} (mJy)	1487 ± 297.4
$P^{Core}_{1300MHz}$ ($\times 10^{22}$ W Hz^{-1})	9.30 ± 2.20
$P_{1400MHz}$ ($\times 10^{25}$ W Hz^{-1})	0.60 ± 0.05
P_{612MHz} ($\times 10^{25}$ W Hz^{-1})	1.3 ± 0.12
P_{323MHz} ($\times 10^{25}$ W Hz^{-1})	2.2 ± 0.30
P_{144MHz} ($\times 10^{25}$ W Hz^{-1})	3.9 ± 0.82
α^{1400}_{144}	0.82 ±0.18
Q_{Jet} (erg s^{-1})	1.3×10^{43}

Table 6.3: Radio properties of GRG-J2233+1315 as measured from our observations from GMRT and LOFAR along with archival NVSS data. EL and WL refer to the eastern and western lobes, respectively.

Region	$S_{1400MHz}$ (mJy)	$P_{1400MHz}$ $10^{24}WHz^{-1}$	S_{612MHz} (mJy)	P_{612MHz} $10^{25}WHz^{-1}$	S_{323MHz} (mJy)	P_{323MHz} $10^{25}WHz^{-1}$	S_{144MHz} (mJy)	P_{144MHz} $10^{25}WHz^{-1}$	α_{144}^{1400}
(1)	(2)	(3)	(4)	(5)	(6)	(7)	(8)	(9)	(10)
WL	30 ± 2.3	0.8 ± 0.08	90 ± 5	0.24 ± 0.02	177 ± 18	0.61 ± 0.03	344.3 ± 68.9	0.92 ± 0.20	1.07
EL	56.7 ± 3.1	1.5 ± 0.14	145.5 ± 7.8	0.39 ± 0.04	301.5 ± 30.3	0.80 ± 0.10	559.6 ± 112.1	1.49 ± 0.32	1.02

6.3 Results & Discussion

6.3.1 Redshift

The redshift (z) of GRG-J2233+1315 was found to be 0.09956 ± 0.00383 (Sec. 6.2.1). The observed spectrum (Fig. 6.2) lacks prominent emission lines and has detected absorption lines like Calcium H and K lines along with Magnesium and Sodium lines. Hence the galaxy appears to be a low-excitation GRG or LEGRG having old stellar populations. As discussed in Dabhade et al. 2020c the LEGRGs are the dominant population in comparison with the high excitation GRGs (HEGRGs).

6.3.2 Size, radio power and jet kinetic power

Using our radio observations with GMRT and LOFAR as described in Sec. 6.2.2, we obtained deep and high resolutions images at 1300, 612, 323, and 144 MHz as seen in Fig. 6.3. GMRT 323 MHz and LOFAR 144 MHz images are the deepest images showing the maximum extent of the source (largest angular size; LAS) of 16.1′, yielding a projected linear size of 1.83 Mpc. This has been computed with the formula given in Dabhade et al. 2020c and by using the cosmological parameters from Planck (H_0 = 67.8 km s^{-1} Mpc^{-1}, Ω_m = 0.308, Ω_Λ = 0.692; Planck Collaboration et al. 2016; scale at z=0.09956 is 1.896 kpc/″). We use the same parameters throughout the paper to estimate other properties.

In Tab. 6.2 we provide the measured and estimated properties of GRG-J2233+1315, where the total or integrated radio flux density and power are estimated in similar way as given in Dabhade et al. 2020c at various frequencies. At 1.4 GHz the total radio power of the GRG is $\sim 5\times 10^{24}$ W Hz^{-1}, which is somewhat on the lower side of GRGs as compared to typical radio powers of FR-II radio galaxies. Recent study of Mingo et al. 2019 has shown a population of low luminosity FR-II radio galaxies using LoTSS, which have radio powers below 10^{24} W Hz^{-1}.

The jet kinetic power has been estimated as per the scheme given by Hardcastle 2018b to be 1.4×10^{43} erg s^{-1}, which is not very high compared to very powerful FR-II radio galaxies and quasars which are usually above $\sim 10^{45}$ erg s^{-1} (Godfrey & Shabala 2013). As per figure 3 of Godfrey & Shabala 2013, GRG-J2233+1315 lies very close to the division between FR-I and FR-II type radio galaxies.

6.3.3 Radio morphology

Using the NVSS radio map of GRG-J2233+1315, Dabhade et al. 2017 reported a bright unresolved feature on the western side of the host galaxy, which was thought to be a knot in the jet. Now, with our deep and high resolution observations with GMRT and LOFAR, we have resolved the overall structure of the GRG-J2233+1315 in detail. Our multi-frequency radio maps from GMRT and LOFAR 144 MHz in Fig. 6.3, reveal a thin collimated jet emanating from the radio core

Table 6.4: Information of images shown in Fig. 6.3. The * symbol indicates high resolution image from LOFAR.

Image	Frequency (MHz)	RMS (mJy)	Resolution (″)
a	1300	0.013	2.5″ × 2.1″, 62.3°
b	612	0.039	7.1″ × 6.8″, 22.3°
Kink	612	0.031	5.1″ × 4.5″, 31.5°
c	323	0.081	12.1″ × 8.8″, 51.9°
d	144	0.242	20.0″ × 20.0″, 90.0°
d*	144	0.145	9.9″ × 5.5″, 80.9°

(detected only at 1300 MHz GMRT map) transforming into a ∼100 kpc 'omega' (**Ω**) shaped structure called the 'kink' on the western side. It is most likely that the 'kink' feature is also present on the eastern side in some form of symmetry. While the 'kink' on the western side of the jet is prominently seen, the 'kink' on the eastern side of the jet fails to show the same morphology. We suspect the 'kink' to be in different planes where only one of them is clearly observed due to projection effects. The radio images of all frequencies in our study show this highly complex and rare feature in the structure of the GRG. Beyond the **Ω** shaped 'kink' feature, the jet appears to re-collimate again having wider width than before and feed the mushroom shaped lobe. The two point sources embedded in the western lobe (Fig. 6.3 c) are unrelated sources and their flux densities were subtracted from the total flux density of the lobe.

Our highest resolution (2.5″ × 2.1″) radio map at 1300 MHz from GMRT reveals the radio core, which coincides with the galaxy called SDSS J223301.30+131502.5 and confirms its host nature. On the eastern side too we observe a twisted jet feature which eventually feeds the lobe. The jet terminating into the eastern lobe is fainter, possibly due to Doppler dimming, compared to the western side. The full jet connection to the lobe can be seen only in the GMRT 323 MHz and LOFAR 144 MHz maps. Interestingly, both the lobes are diffuse without any prominent hotspots, giving an impression of two buoyant bubbles being pushed out by the jets. Overall, the radio morphology of GRG-J2233+1315 resembles that of weight lifting equipment for exercises called the 'Barbell' (henceforth Barbell GRG).

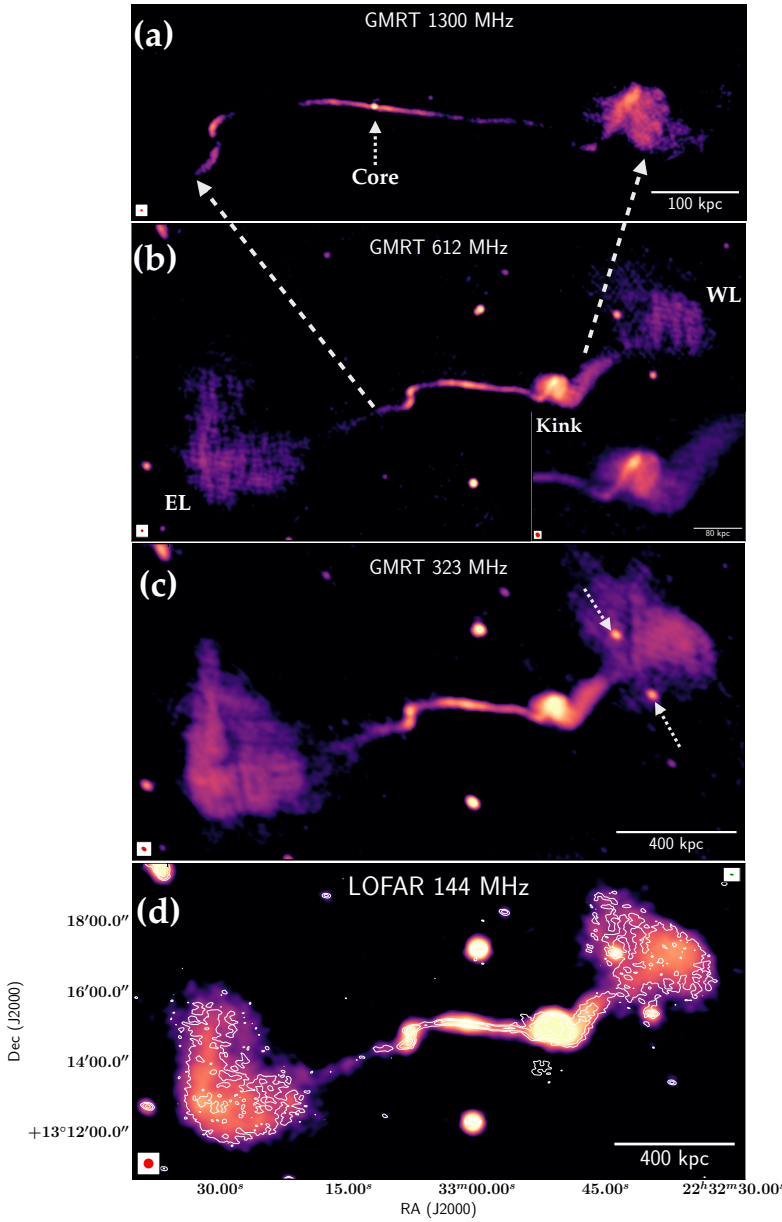

Figure 6.3: Radio images of GRG-J2233+1315 at 1300 (a), 612 (b), 323 (c) and 144 MHz (d) from top to bottom. The RMS and resolution information of respective images is provided in Tab. 6.4. The white box at bottom left represents the beam. In sub-image (b), additional zoom in image of the kink feature of the GRG is shown at the right bottom corner. The two arrows in sub-image (c) show two independent sources. In sub-image (d) LOFAR 144 MHz image is presented in two resolutions where the higher resolution is represented by contours, whose beam is shown on the top right corner of the sub-image.

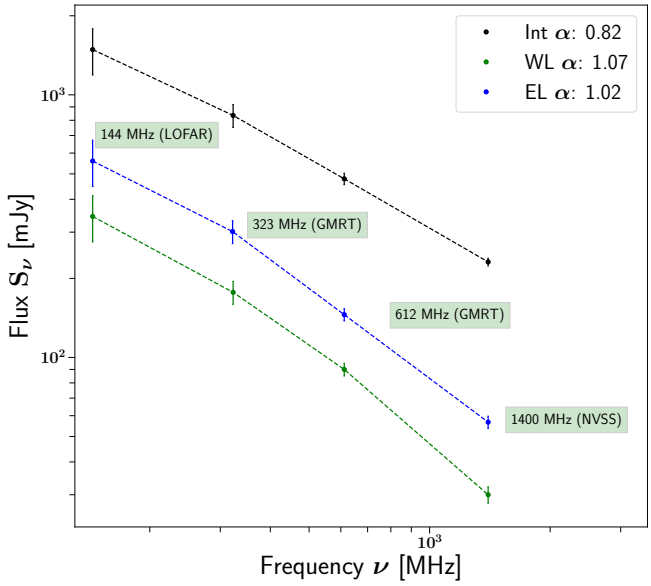

Figure 6.4: Spectral index plot of western (WL) and eastern (WL) lobes along with the full source (Int), where the 1400 MHz flux density was obtained from archival NVSS data. The possible break frequency is seen around ~ 323 MHz.

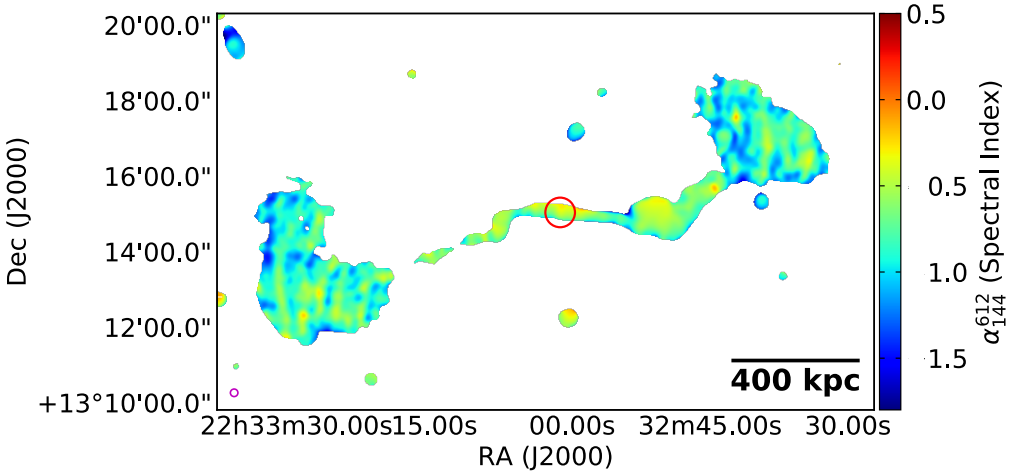

Figure 6.5: The figure shows the spectral index map made using LOFAR 144 MHz, GMRT 323 MHz and GMRT 612 MHz maps as described in Sec. 6.3.4. The red colour circular marker indicates the location of the radio core/host galaxy. The magenta colour circle at the bottom left represents the beam of 13″× 13″.

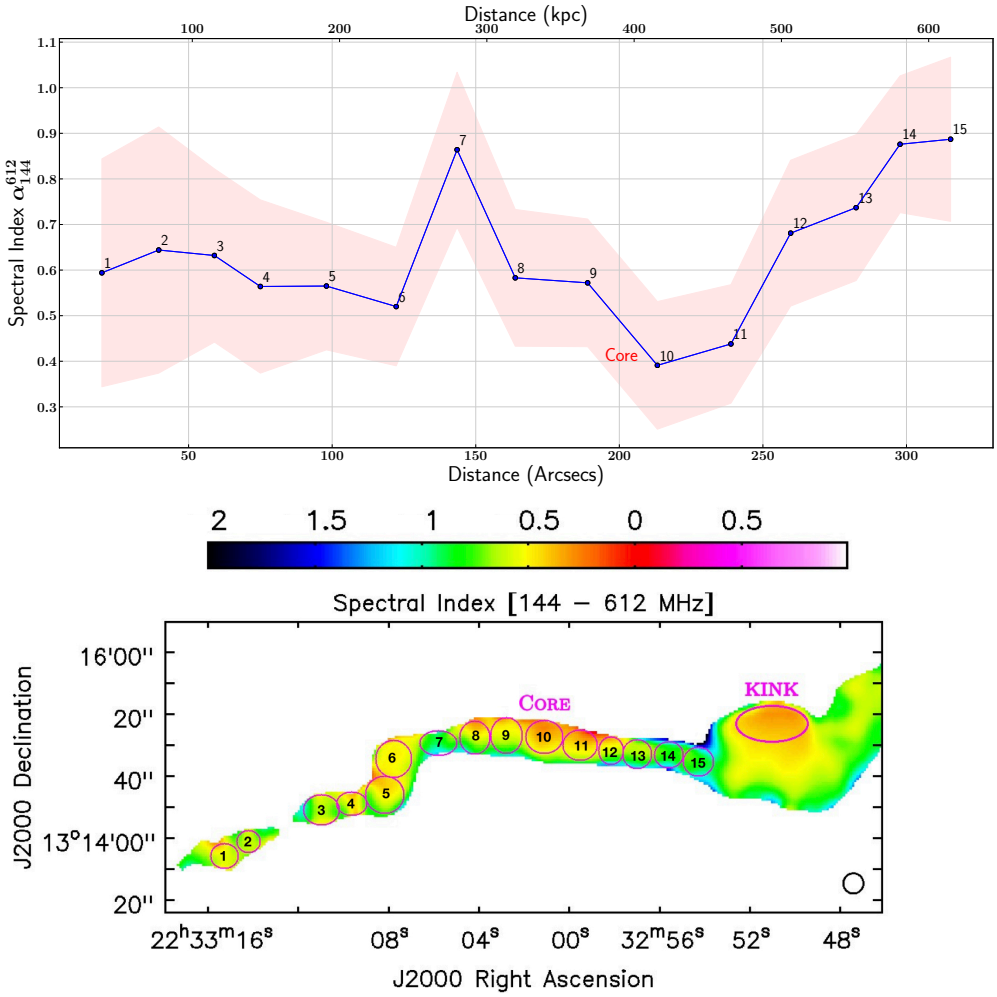

Figure 6.6: Upper figure shows the jet spectral index gradient with respect to distance as per the marked region seen in the lower plot. The shaded region indicates the uncertainties with the measurements. Lower figure zoomed in portion of Fig. 6.5 highlights the core, jet and the kink with numbered regions drawn on them.

6.3.4 Spectral index (α)

In Fig. 6.5 we see the three point spectral index map of the Barbell GRG made using LOFAR 144 MHz, GMRT 323 MHz and GMRT 612 MHz data at a resolution of 13″. Here, the frequency coverage on the higher side was restricted to 612 MHz due to lack of similar resolution maps at ∼1400 MHz which recover the entire source. The NVSS map with its coarser resolution of 45″ does not resolve the jets and 'kink' feature well, even though it does show the entire source emission. The other high frequency map available to us is from the GMRT 1300 MHz observation where the fine resolution and lack of short spacing do not recover the whole source. Therefore, in order to obtain high resolution spectral index information of the whole source, the NVSS and GMRT 1300 MHz data were not used.

The steps followed for making the three-frequency spectral index maps are based on the procedure given in Hoang et al. 2017. Firstly, the individual data sets (maps presented in Fig. 6.3) were further re-imaged with similar UV range ($0.2k\lambda$ to $50k\lambda$) and weighting schemes with uv-tapering to obtain maps at common resolution of 13″. From each map, only pixels with $\geqslant 3\times$ noise/RMS were used for the purpose of making spectral index calculation and map. The GMRT images were aligned with respect to the LOFAR image along with regridding all images to a common pixelisation. For the process of image aligning, we fitted compact point sources with 2D Gaussian function to find their accurate locations and average displacement thus was determined between the three images. Likewise, the GMRT images were appropriately shifted along the RA and Dec axes. The spectral index map as seen in Fig. 6.5 clearly shows flatness (∼0.5) of the radio core and the 'kink'. Both the lobes show steep (∼1) spectral index indicating older plasma.

6.3.5 Spectral ageing and magnetic field

One of the ways of estimating the life span of radio galaxies is through interpreting the radio spectrum ($S_\nu \propto \nu^{-\alpha}$) of their electron population, often known as the spectral age of the source. The shape of the spectra is highly influenced by two factors- the injection of energetic electrons and the electron population undergoing synchrotron and inverse-Compton losses. Energy losses for high energy electrons are indicated by a frequency break in the spectrum. It becomes steeper when the electrons are not rejuvenated due to the pause/end of AGN activity. The low-frequency (MHz) radio observations play an important role in determining the break (break frequency ; $\nu_{\rm br}$) in the power-law which occurs due to synchrotron losses. As more time elapses, the $\nu_{\rm br}$ moves to lower radio frequencies (Kardashev 1962; Pacholczyk 1970; Jaffe & Perola 1973). With the knowledge of break frequency and the magnetic field of the source, the spectral age can be calculated using the following formula :

$$\tau_{\rm sp} = 50.3 \left[\frac{\rm B^{0.5}}{(\rm B^2 + B_{IC}^2)} \frac{1}{[(1+z)\nu_{\rm br}]^{0.5}} \right] \tag{6.1}$$

where $B_{IC} = 3.25(1+z)^2$ is the magnetic field strength equivalent to the cosmic microwave background radiation and B is the magnetic field strength in various regions, which is expressed in μG . The term z is the redshift of the source and ν_{br} is the spectral break frequency in GHz above which the radio spectrum steepens from initial power-law spectrum. In the simple spectral ageing model, the magnetic field is assumed to be constant in a given region throughout the energy loss process. Also, it is assumed that there is no energy loss due to expansion process and the particles have a constant power law energy spectrum. To determine the spectral ages of eastern lobe (EL) and western lobe (WL) of the Barbell GRG, a cylindrical geometry is assumed, and the sizes (d) of the specified regions are computed from the lowest frequency map of LOFAR 144 MHz. The magnetic fields in the corresponding regions are calculated using both classical (Miley 1980) and revised (Beck & Krause 2005) formalism by assuming minimum energy conditions. The following formulae have been used for calculations :

$$u_{\min}\left[\frac{\text{erg}}{\text{cm}^3}\right] = \xi(\alpha,\nu_1,\nu_2)(1+k)^{4/7}(\nu_0\,[\text{MHz}])^{-4\alpha/7} \times (1+z)^{(12-4\alpha)/7}\left(I_0\,[\frac{\text{mJy}}{\text{arcsec}^2}]\right)^{4/7}(d\,[\text{kpc}])^{-4/7} \tag{6.2}$$

$$B_{\text{eq}}[\text{G}] = \left(\frac{24\pi}{7}\,u_{\min}\right)^{1/2}, \tag{6.3}$$

$$\text{B}'_{\text{eq[G]}} \sim 1.1\gamma_{\min}^{\frac{1-2\alpha}{3+\alpha}} \times \text{B}_{\text{eq}}^{\frac{7}{2(3+\alpha)}}. \tag{6.4}$$

Assuming a uniform magnetic field and an isotropic particle distribution, the minimum energy density ($u_{\min}$) is computed, where the parameter ξ is a function of spectral index α. Different values of ξ are taken from Table 1 in Govoni & Feretti 2004. In classical formalism, the spectrum is integrated from ν_1 to ν_2, usually from 10 MHz to 100 GHz, which corresponds to a minimum Lorentz factor (γ_{min}) of $\approx$ 10 and a maximum Lorentz factor (γ_{max}) of $\approx 10^4 - 10^5$ respectively. k represents ratio of energies in relativistic protons to electrons (1 or 100), I_0 is the surface brightness at the measuring frequency and d is the mean of major and minor axis (source depth). Also we assume the filling factor to be 1. The terms B_{eq} and B'_{eq} represent the classical and revised equipartition magnetic fields, respectively, which are related to $u_{\min}$ as seen in equation 6.3.

Based on our analysis, the equivalent magnetic field of the lobes is around 5μG (Tab. 6.5) which is similar to that of other GRGs (Ishwara-Chandra & Saikia 1999; Konar et al. 2004; Kronberg et al. 2004; Harwood et al. 2016). Also, when compared with RGs of similar radio power and located in galaxy cluster centres from Bîrzan et al. 2008 sample, the magnetic filed strengths are comparable. It has been suggested that powerful radio galaxies, especially GRGs covering Mpc scale volumes are strong candidates for magnetising the intergalactic medium (Rees 1987; Ruzmaikin et al. 1989; Jafelice & Opher 1992; Kronberg 1994; Kronberg et al. 2001b). This largely depends on how powerful the RG/GRG is along with its environment and hence, its direct effect may vary as per the source. A study

by Jafelice & Opher 1992 of modelling powerful radio galaxies (e.g. M84, 3C 465, and NGC 6251) based on observations have estimated the inter-galactic medium magnetic fields to be in the range of $10^{-6} - 10^{-10}$ G.

Considering synchrotron radiation mechanism in which the electrons are losing energy, the spectral ages are defined to be the time progressed since the acceleration of the particles. In addition to the above mentioned radiative cooling losses, the depletion in particle and field energy in the radio lobe can also be caused due to adiabatic expansion (Scheuer & Williams 1968). This can lead to reduction in magnetic field and break frequency, causing the measured spectral age to surpass the actual age of the radio source. Our results for the spectral ages of the Barbell GRG are presented in Tab. 6.5, where adopting the commonly used k-value of 1, spectral ages of >110 Myr have been obtained for the radio lobes. To match the spectral age with the dynamical age, the jet head speed would need to be as low as ~ 0.03c (considering distance between the radio core and western lobe). The spectral age estimation suffers from some uncertainties like inhomogeneity in magnetic field and lack of accurate injection index values. It is often found (Machalski et al. 2009) that the spectral age differs from the dynamical age of the source which mainly depends on the geometry and brightness of the radio source.

The spectral ages of the both the lobes for the Barbell GRG are quite on the higher side as compared to RGs, however past studies of GRGs on spectral ageing have yielded wide range of values between ~ 10 Myr to 250 Myr (Mack et al. 1998; Schoenmakers et al. 2000b; Konar et al. 2004, 2008; Jamrozy et al. 2008; Shulevski et al. 2019; Cantwell et al. 2020). It is worth noting that the method for estimating spectral ages was not uniform across all the above mentioned spectral ageing work on GRGs.

Table 6.5: Values of Equipartition Magnetic Field and Spectral Age estimated for the entire source as described in Sec. 6.3.5. The assumed break Frequency (ν_b) is 323 MHz. Terms with (cl) are from classical formalism and the ones with (rev) are using revised formalism of Beck & Krause 2005.

Region	K-value	α	d	u_{min}	B_{eq}(cl)	B'_{eq}(rev)	(ν_b)	τ_{sp}(cl)	τ_{sp}(rev)
			kpc	$\times 10^{-12}$ (erg cm^{-3})	(μG)	(μG)	(MHz)	(Myr)	(Myr)
WL	1	1.07	520	1.30	3.8	6.7	323	175	115
	100	1.07	520	0.13	11.7	17.4	323	60	35
EL	1	1.02	610	1.05	3.4	5.7	323	185	133
	100	1.02	610	9.80	10.3	15.2	323	70	42

6.3.6 Jet and the kink

The Barbell GRG shows a remarkable long collimated jet of $\sim 113''$ in length corresponding to ~ 210 kpc (projected). A very few radio galaxies have shown long collimated jets extending to hundreds (> 200 kpc) of kpc, e.g. NGC 315 and HB13 (Jaegers 1987), CGCG 049-033 (Bagchi et al. 2007), and 4C 34.47 (Hocuk & Barthel 2010). However, unlike these sources, the Barbell GRG exhibits a counter jet on the eastern side, which is rare in GRGs with FR-II type morphology. In subfigure (c) and (d) of Fig. 6.3, we clearly see the counter jet feeding the eastern lobe. The projected length from eastern lobe to the prominent 'kink' on the western side exceeds ~ 400 kpc in length. Since the Barbell GRG is not residing in an underdense environment, it must be possessing a very energetic jet powered by a SMBH of the host BCG.

There are many similarities between the Barbell GRG and NGC 6251, which is also a ~ 2 Mpc GRG residing in a relatively denser environment with a ~ 200 kpc one sided (north-western) jet (Waggett et al. 1977). This jet dubbed as the 'blow-torch jet' has been a subject of several studies (e.g. Perley et al. 1984; Mack et al. 1997; Evans et al. 2005b) ranging from radio to X-rays wavelengths. A counter-jet of ~ 50 kpc was detected by Perley et al. 1984 using VLA and recently, better maps showing extended jet emission by Cantwell et al. 2020 using LOFAR and VLA were presented. The spectral ages (~ 200 Myr) too are similar for both NGC 6251 (Cantwell et al. 2020) and Barbell GRG, which are on the older side compared to some other GRGs.

In Fig. 6.6, we show the spectral index (α) gradient along the jet and the counter-jet which ranges from ~ 0.6 to 0.9, which is quite similar to that of the jet in NCG 6251 as presented by Perley et al. 1984. The radio jets produced near to the central super-massive black holes are collimated by magnetic field and their collimation require external confinement (Tomimatsu 1994; Beskin et al. 1998). For the external confinement, the gas pressure profile plays a vital role and hence, influences the jet acceleration and collimation along with the magnetic field configuration. For the jet in GRG NGC 6251, Perley et al. 1984 have discussed a model for jet confinement at large scales due to thermal pressure of the environment and how its non-uniformity can affect the overall source morphology. Hence, in Barbell GRG it is interesting to see ~ 280 kpc collimated jet propagating in low mass galaxy cluster environment with weak X-ray emission (no detection in ROentgen SATellite or ROSAT sky survey). In absence of the gas pressure profile of this dense environment it is not possible to model the parameters of the jet.

Gower et al. 1982 presented a simple yet effective kinematical model of precessing twin jets with relativistic bulk velocity which explained peculiar radio jets with twists and turns of several radio galaxies and quasars. Parts of the Barbell GRG resemble that of the radio galaxy 3C 449, whose peculiar jet morphology with mirror symmetry has been explained by Gower & Hutchings 1982 with a simple precessing beam model having relativistic bulk motion. The precessing jets model is required to be explored further in detail to explain aspects of the complex jet and 'kink' morphology in the Barbell GRG.

The Magnetohydrodynamic (MHD) processes govern the launch, acceleration and collimation of astrophysical jets. Several works (Hummel et al. 1992; Baum et al. 1997; Feretti et al. 1999; Lobanov & Zensus 2001; Marshall et al. 2001; Mertens et al. 2016) in the past three decades have shown the presence of peculiar features in the jets on sub-parsec to kpc scales, which appear to be wiggles or 'kinks'. However, almost all of them are on smaller scales (~ 10 kpc), and not scales of ~100 kpc as in the case of 'kink' in the Barbell GRG. The ~ 100 kpc omega shaped 'kink' structure seen on the western side of the radio core is the only one known, and an unique example of plasma instability on such large scale. As discussed previously in Sec. 6.3.3, there is a possibility that eastern side also harbours a 'kink' but is not visible due to possible projection effects. However, we do see flat spectral index (though as not as flat as on the western side) near the twisted part of the jet on the eastern side, which is marked with six numbered circles in Fig. 6.6. Below, we will discuss the 'kink' feature of the Barbell GRG based on the clearly observed one on the western side and its possible causes.

The radio jets are susceptible to Kelvin-Helmholtz (KH) instabilities when they encounter ambient medium with contrasting densities and flows (Birkinshaw 1991; Hardee 2007; Perucho et al. 2007). The environment in which the Barbell GRG is residing, most certainly provides ideal conditions for development of KH instabilities and the observed 'kink' feature could possibly be its manifestation in some form.

Another possibility is that the observed 'kink' feature in the Barbell GRG could also be the site for possible magnetic reconnection (Romanova & Lovelace 1992), where the brightening in the jet is observed. This bright or excess emission in the jet can be explained by magnetic reconnection rather than shocks (Sironi et al. 2015) as it has been shown via simulations that shocks while efficiently dissipating energy, do not accelerate particles much above the thermal energy. Recent observation based studies (Shukla & Mannheim 2020; Meyer et al. 2020) also have shown compelling evidence of magnetic reconnection in jets of AGNs using high energy instruments, however these are on much smaller scale as well as closer to the AGN.

The current-driven (CD) 'kink' or shear-flow instability can also cause the jets to be unstable and often lead to brightening in regions of the jets Chiuderi et al. 1989; Nakamura & Meier 2004. Using three-dimensional MHD simulations, Nakamura & Meier 2004; Nakamura et al. 2007 have proposed that the main reason for the observed wiggles or 'kink' features in jets is due to CD instability. In this type of instability, a helical structure is developed with a relatively low growth rate. Simulation studies by Mizuno et al. 2009, 2012, 2014 have shown that CD instability can stimulate large-scale helical motions in the jets leading to deformation and but need not disrupt the jet completely. Here, the distorted magnetic field structure can possibly prompt the creation of magnetic reconnection. Their simulations also revealed that the CD instability mainly depends strongly on the magnetic pitch profile and moderately on the density profile. Also, the velocity shear radius relative to the characteristic radius of the magnetic field determined

the static and non-static feature of the 'kink'. In case of Barbell GRG we observe the jet on the western side to develop 'kink' like feature and again recollimating to feed the western lobe.

High resolution studies of radio AGN using Very Long Baseline Arrays are extremely important for studying jets as they allow us to peer close to the region of jet launching. Using multi-epoch VLBA observations at 15 GHz for BL Lacertae (BL Lac), Cohen et al. 2015 have shown a strong possibility of detecting Alfvén waves propagating in the radio jet emanating from the black hole. Their observations have shown the existence of a strong transverse component of the magnetic field belonging to the BL Lac's jet. Assuming the magnetic field to be helical based on previous observational studies (Gabuzda et al. 2004), they suggest that the observed features in the BL Lac are due to transverse S (shear) Alfvén waves propagating along with longitudinal component of the magnetic field. These Alfvén waves appear to be stimulated by changes in the position angle of the recollimation shock, which is analogous to a 'whip'* in action. Currently, it is unclear whether such disturbances along with jets can propagate to larger scales but the above study does certainly draw some similarities to that of the observed peculiar 'kink' feature in the Barbell GRG.

An interesting mechanism is proposed by Nakamura et al. 2001 using helical kink instability to explain the observed 'wiggles' or 'kink' features in radio jets of AGNs. It is based on the 'Sweeping Magnetic-Twist' model, which conjectures that the AGN core provides the necessary large amount of energy required for producing systematic magnetic configuration. Their simulations conclude that the most optimum mode of carrying this energy is via the Poynting flux of torsional Alfvén wave train (TAWT), which is produced by interaction of rotating accretion disk of the AGN and the large scale magnetic field. The observed 'wiggles' or 'kink' then can arise from MHD processes under the influence of TAWT which when encounters low Alfvén velocity, creates a pinched region and other deformations in the jet. Unlike the previously discussed models above, this model explains distortions in jets on larger scale, as the magnetic twist cannot be created at large distances locally, the TWAT can come along the jet from the radio core of the AGN.

The brightest part of the Barbell GRG is the 'kink' feature, which is possibly the working surface of supersonic jets in which the bulk kinetic energy is abruptly dissipated within decelerating shock waves. At the location of the shock fronts formed in the jets, the relativistic electrons are efficiently accelerated due to the impact with the ambient surrounding medium. This is evident from the flat spectral index (0.38) of the top of the 'kink' feature' as seen in the lower figure of Fig. 6.6. The 'kink' feature could also be due to the flow of plasma along a bent magnetic field.

Assuming the region highlighted in ellipse in the lower figure of Fig. 6.6 to represent a shock front, we attempt to estimate its mach number using diffusive shock acceleration (DSA) mechanism (Blandford & Eichler 1987), where

*link

$$\alpha_{\rm inj} = -\frac{1}{2}\left(\frac{1+3/\mathcal{M}^2}{1-1/\mathcal{M}^2}\right). \tag{6.5}$$

The radiative losses of electrons will lead to steepening of the radio spectrum and upon integrating over larger frequency range, the spectral index of the integrated power law will take the form-

$$\alpha_{\rm int} = \alpha_{\rm inj} - 0.5 = -\left(\frac{1+1/\mathcal{M}^2}{1-1/\mathcal{M}^2}\right). \tag{6.6}$$

The integrated spectral index $\alpha_{\rm int}$ at the top of the 'kink' feature as marked with an ellipse in Fig. 6.6 (top) is $\sim$0.38. Using the $\alpha_{\rm int}$ value and the Eq. 6.6, the mach number ($\mathcal{M}$) of the possible shock front is $\sim$1.5, which is not very high. However, jets with relativistic plasma which are magnetically dominated are not efficient sites for shock acceleration (Sironi et al. 2013, 2015). Hence, the magnetic reconnection explanation for the observed brightening in the 'kink' seems plausible.

6.3.7 Environment Studies

It is essential to study the environment of GRGs as one of the most favoured explanation for their gigantic sizes is attributed to their under-dense environment (Mack et al. 1998). Another important reason to study their environment is to understand its effect on their morphologies. Some GRG studies (Schoenmakers et al. 2000b; Lara et al. 2001a; Subrahmanyan et al. 2008; Pirya et al. 2012) have indicated that the observed asymmetries in the morphologies of the GRGs trace the asymmetries in their environment. Hence, GRGs with their large sizes become a natural probe of environment asymmetries over megaparsec scales (Subrahmanyan et al. 2008; Safouris et al. 2009). In the case of Barbell GRG which resides in a relatively denser environment, we do observe asymmetries in its jets which possibly could be due to their immediate environments.

GRGs hosted by BCGs in cluster environment are quite rare, and as shown by Dabhade et al. 2020c, less than 10% of the known GRG population are BCGs. Using information from Wen et al. 2012, we have estimated the following information about the galaxy cluster in which GRG-J2233+1315 resides (Fig. 6.7)-
$\mathbf{R_{200}}$ =1.02 Mpc (virial radius of the galaxy cluster)
$\mathbf{R_*}$ = 20.04 (richness of the galaxy cluster)
$\mathbf{N_{200}}$ =13 (No. of galaxies observed within $\mathbf{R_{200}}$)
$\mathbf{M_{200}} = 1.1 \times 10^{14}\ \mathbf{M_\odot}$ (Mass within $\mathbf{R_{200}}$)
Volume = 4.4 $\mathbf{Mpc^3}$ (Volume of cluster within $\mathbf{R_{200}}$)
Density = $2.4 \times 10^{13}\ \mathbf{M_\odot}$ / $\mathbf{Mpc^3}$
$\mathbf{L_x} = 3 \times 10^{43}$ erg s^{-1} (Cluster X-ray luminosity)
$\mathbf{T_x}$ = 2.3 KeV [X-ray band - 0.1 to 2.4 KeV]

The mass ($\mathbf{M_{200}}$) of the galaxy cluster reflects that it is either a low mass galaxy cluster or a massive galaxy group. Also, based on the available information, it was

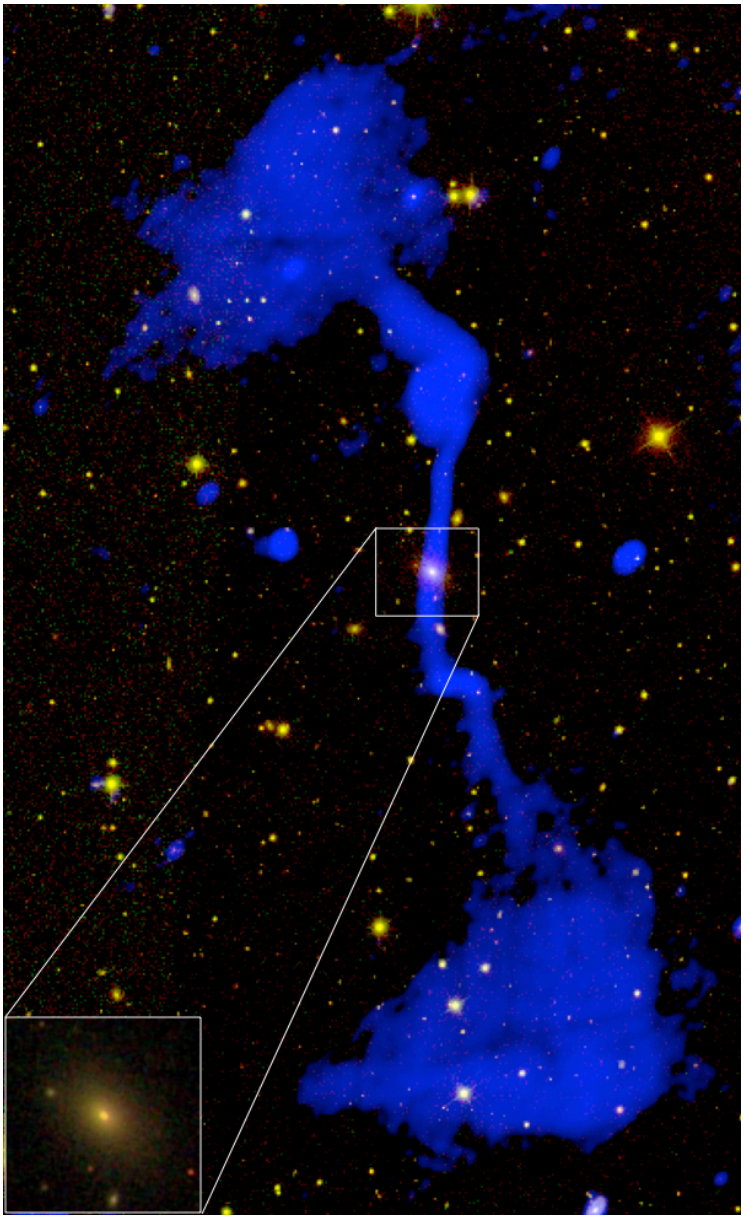

Figure 6.7: Optical and radio colour composite image where the background yellow colour image represents SDSS and the blue represents radio emission as seen in GMRT 325 MHz map. At the top left a zoom in view of the host galaxy i.e., the BCG is shown.

shown that GRGs do not reside in centres of very massive clusters Dabhade et al. 2020c. If R_{200} is indeed ~1.02 Mpc, then the GRG-J2233+1315 lies within the virial radius of the galaxy cluster. If R_{200} is lower than 1.02 Mpc then the lobes can possibly be located at the edge of R_{200} or beyond, where thermal pressure from external medium for confining the radio lobes will be less and thereby allowing free adiabatic expansion. Hence their expansion dynamics will be governed by inter-galactic medium and will possibly move in the direction of low pressure gradient due to buoyancy.

As seen above, the Barbell GRG resides in relatively low mass cluster and the lack of detection in the ROSAT sky survey supports the finding. Hence, it can be said that with the right combination of kinetic jet power and the ambient medium, the collimated jet has been able to travel to large distance unhindered until developing the 'kink'. Based on the observed peculiar morphology of the GRG, it is apparent that environment certainly has influenced its growth. Further deep optical spectroscopic data of surrounding galaxies and X-ray data of the galaxy group/cluster will be needed to explore its exact dynamics.

6.4 Summary

We have presented our study on a ~ 1.9 Mpc large GRG called the Barbell GRG, which is hosted in a dense cluster/group environment. Our optical spectroscopic data from WHT has established the redshift of the GRG and hence, its projected linear size. Our deep and high resolution radio images from GMRT and LOFAR reveal a ~ 210 kpc jet emanating from the radio core and leading to ~ 100 kpc 'kink' structure possibly caused due to some form of instability. Our multi-frequency radio data has enabled us to estimate the magnetic field and spectral ages of the diffuse lobes. The classical equivalent magnetic field of the lobes is $\sim 5\,\mu$G and the spectral ages of ~ 180 Myr. The discovery of the ~ 100 kpc 'kink' structure from our study provides an unique possibility for testing various MHD models on large scales. We have discussed few possibilities which could have lead to the creation of such peculiar structure in a dense environment. Further observations in X-rays and optical along with simulations are needed to understand this complex system better.

Bibliography

Abazajian, K. N., Adelman-McCarthy, J. K., Agüeros, M. A., et al. 2009, ApJS, 182, 543

Abolfathi, B., Aguado, D. S., Aguilar, G., et al. 2018, The Astrophysical Journal Supplement Series, 235, 42

Alam, S., Albareti, F. D., Allende Prieto, C., et al. 2015, ApJS, 219, 12

Amendola, L., Appleby, S., Bacon, D., et al. 2013, Living Reviews in Relativity, 16, 6

Amirkhanyan, V. R. 2016, Astrophysical Bulletin, 71, 384

Amirkhanyan, V. R., Afanasiev, V. L., & Moiseev, A. V. 2015, Astrophysical Bulletin, 70, 45

Antonucci, R. 1993, ARA&A, 31, 473

Arshakian, T. G., & Longair, M. S. 2000, MNRAS, 311, 846

Artyukh, V. S., & Ogannisyan, M. A. 1988, Soviet Astronomy Letters, 14, 301

Assef, R. J., Kochanek, C. S., Brodwin, M., et al. 2010, ApJ, 713, 970

Athreya, R. M., & Kapahi, V. K. 1998, Journal of Astrophysics and Astronomy, 19, 63

Baade, W. 1956, ApJ, 123, 550

Baade, W., & Minkowski, R. 1954, ApJ, 119, 206

Baars, J. W. M., & Hooghoudt, B. G. 1974, A&A, 31, 323

Baars, J. W. M., Hooghoudt, B. G., Mezger, P. G., & de Jonge, M. J. 1987, A&A, 175, 319

Baczko, A. K., Schulz, R., Kadler, M., et al. 2016, A&A, 593, A47

Bagchi, J., Durret, F., Neto, G. B. L., & Paul, S. 2006, Science, 314, 791

Bagchi, J., Gopal-Krishna, Krause, M., & Joshi, S. 2007, ApJ, 670, L85

Bagchi, J., & Kapahi, V. K. 1994, Journal of Astrophysics and Astronomy, 15, 275

Bagchi, J., Vivek, M., Vikram, V., et al. 2014, ApJ, 788, 174

Baldwin, J. E. 1982, in IAU Symposium, Vol. 97, Extragalactic Radio Sources, ed. D. S. Heeschen & C. M. Wade, 21–24

Bankowicz, M., Koziel-Wierzbowska, D., & Machalski, J. 2015, SALT Science Conference 2015 (SSC2015), 34

Barai, P., & Wiita, P. J. 2006, MNRAS, 372, 381

Bardeen, J. M. 1970, Nature, 226, 64
Barkana, R., & Loeb, A. 2001, Phys. Rep., 349, 125
Barthel, P. D. 1987, in Superluminal Radio Sources, ed. J. A. Zensus & T. J. Pearson, 148–154
Barthel, P. D. 1989, ApJ, 336, 606
Barthel, P. D. 1994, in Astronomical Society of the Pacific Conference Series, Vol. 54, The Physics of Active Galaxies, ed. G. V. Bicknell, M. A. Dopita, & P. J. Quinn, 175
Basu-Zych, A. R., Hornschemeier, A. E., Haberl, F., et al. 2020, MNRAS, 498, 1651
Bauleo, P. M., & Rodríguez Martino, J. 2009, Nature, 458, 847
Baum, S. A., O'Dea, C. P., Giovannini, G., et al. 1997, ApJ, 483, 178
Baumann, D. 2009, arXiv e-prints, arXiv:0907.5424
Beck, R., & Krause, M. 2005, Astronomische Nachrichten, 326, 414
Becker, R. H., White, R. L., & Helfand, D. J. 1995, ApJ, 450, 559
Beckwith, K., Hawley, J. F., & Krolik, J. H. 2008, The Astrophysical Journal, 678, 1180–1199
Begelman, M. C., Blandford, R. D., & Rees, M. J. 1984, Reviews of Modern Physics, 56, 255
Begelman, M. C., Rees, M. J., & Blandford, R. D. 1979, Nature, 279, 770
Bell, E. F., McIntosh, D. H., Katz, N., & Weinberg, M. D. 2003, ApJS, 149, 289
Bennett, A. S. 1962, MmRAS, 68, 163
Beskin, V. S. 2010, Physics Uspekhi, 53, 1199
Beskin, V. S., Kuznetsova, I. V., & Rafikov, R. R. 1998, MNRAS, 299, 341
Best, P. N., Bailer, D. M., Longair, M. S., & Riley, J. M. 1995, MNRAS, 275, 1171
Best, P. N., & Heckman, T. M. 2012a, MNRAS, 421, 1569
—. 2012b, MNRAS, 421, 1569
Best, P. N., Kauffmann, G., Heckman, T. M., et al. 2005, MNRAS, 362, 25
Best, P. N., Röttgering, H. J. A., & Lehnert, M. D. 1999, MNRAS, 310, 223
Best, P. N., von der Linden, A., Kauffmann, G., Heckman, T. M., & Kaiser, C. R. 2007, MNRAS, 379, 894
Bhatnagar, S., Gopal-Krishna, & Wisotzki, L. 1998, MNRAS, 299, L25
Bianchi, L., & GALEX Team. 1999, Mem. Soc. Astron. Italiana, 70
Bigiel, F., Leroy, A., Walter, F., et al. 2008, AJ, 136, 2846
Birkinshaw, M. 1991, MNRAS, 252, 505
Bîrzan, L., McNamara, B. R., Nulsen, P. E. J., Carilli, C. L., & Wise, M. W. 2008, ApJ, 686, 859
Bîrzan, L., Rafferty, D. A., McNamara, B. R., Wise, M. W., & Nulsen, P. E. J. 2004, ApJ, 607, 800
Blandford, R., & Eichler, D. 1987, Phys. Rep., 154, 1
Blandford, R., Meier, D., & Readhead, A. 2019, ARA&A, 57, 467
Blandford, R. D. 1990, in Active Galactic Nuclei, ed. R. D. Blandford, H. Netzer,

L. Woltjer, T. J. L. Courvoisier, & M. Mayor, 161–275
Blandford, R. D., & Payne, D. G. 1982, MNRAS, 199, 883
Blandford, R. D., & Rees, M. J. 1974, MNRAS, 169, 395
Blandford, R. D., & Znajek, R. L. 1977, MNRAS, 179, 433
Blanton, M. R., & Roweis, S. 2007, AJ, 133, 734
Blundell, K. M., & Rawlings, S. 1999, Nature, 399, 330
Blundell, K. M., Rawlings, S., & Willott, C. J. 1999, AJ, 117, 677
Boccardi, B., Krichbaum, T. P., Ros, E., & Zensus, J. A. 2017, A&A Rev., 25, 4
Bock, D. C.-J., Large, M. I., & Sadler, E. M. 1999, AJ, 117, 1578
Bolatto, A. D., Wolfire, M., & Leroy, A. K. 2013, ARA&A, 51, 207
Bolton, A. S., Schlegel, D. J., Aubourg, É., et al. 2012, AJ, 144, 144
Bouwens, R. J., Illingworth, G. D., Oesch, P. A., et al. 2015, ApJ, 803, 34
Bregman, J. N., Anderson, M. E., Miller, M. J., et al. 2018, ApJ, 862, 3
Bridle, A. H., Davis, M. M., Fomalont, E. B., & Lequeux, J. 1972, AJ, 77, 405
Bridle, A. H., Davis, M. M., Meloy, D. A., et al. 1976, Nature, 262, 179
Brüggen, M., & Kaiser, C. R. 2002, Nature, 418, 301
Bruni, G., Panessa, F., Bassani, L., et al. 2019, ApJ, 875, 88
—. 2020, arXiv e-prints, arXiv:2003.09183
Burbidge, G. R. 1956, ApJ, 124, 416
Calzetti, D., Kennicutt, R. C., Engelbracht, C. W., et al. 2007, ApJ, 666, 870
Cantwell, T. M., Bray, J. D., Croston, J. H., et al. 2020, MNRAS, 495, 143
Capetti, A., Massaro, F., & Baldi, R. D. 2017, A&A, 601, A81
Caretta, C. A., Maia, M. A. G., & Willmer, C. N. A. 2004, AJ, 128, 2642
Carilli, C. L., Perley, R. A., Dhawan, V., & Perley, D. A. 2019, ApJ, 874, L32
Catalán-Torrecilla, C., Gil de Paz, A., Castillo-Morales, A., et al. 2015, A&A, 584, A87
Cen, R., & Ostriker, J. P. 1999, ApJ, 514, 1
Chambers, K. C., Magnier, E. A., Metcalfe, N., et al. 2016, arXiv e-prints, arXiv:1612.05560
Chang, Y.-Y., van der Wel, A., da Cunha, E., & Rix, H.-W. 2015, ApJS, 219, 8
Chatterjee, R., Marscher, A. P., Jorstad, S. G., et al. 2009, ApJ, 704, 1689
Chen, R., Peng, B., Strom, R. G., & Wei, J. 2011, MNRAS, 412, 2433
Chilingarian, I. V., Melchior, A.-L., & Zolotukhin, I. Y. 2010, MNRAS, 405, 1409
Chiuderi, C., Pietrini, P., & Ciamponi, G. T. 1989, ApJ, 339, 70
Cicone, C., Maiolino, R., Sturm, E., et al. 2014, A&A, 562, A21
Clarke, A. O., Heald, G., Jarrett, T., et al. 2017, A&A, 601, A25
Cluver, M. E., Jarrett, T. H., Hopkins, A. M., et al. 2014, ApJ, 782, 90
Cohen, M. H., Meier, D. L., Arshakian, T. G., et al. 2015, ApJ, 803, 3
Colla, G., Fanti, C., Ficarra, A., et al. 1970, A&AS, 1, 281
Colless, M., Dalton, G., Maddox, S., et al. 2001, MNRAS, 328, 1039
Combes, F., García-Burillo, S., Braine, J., et al. 2011, A&A, 528, A124

Combes, F., García-Burillo, S., Audibert, A., et al. 2019, A&A, 623, A79
Condon, J. J. 1984, ApJ, 287, 461
Condon, J. J., Cotton, W. D., Greisen, E. W., et al. 1998, AJ, 115, 1693
Cotter, G., Rawlings, S., & Saunders, R. 1996, MNRAS, 281, 1081
Croston, J. H., Hardcastle, M. J., Harris, D. E., et al. 2005, ApJ, 626, 733
Croston, J. H., Hardcastle, M. J., Mingo, B., et al. 2019, A&A, 622, A10
Croton, D. J., Springel, V., White, S. D. M., et al. 2006, MNRAS, 365, 11
Dabhade, P., Combes, F., Salomé, P., Bagchi, J., & Mahato, M. 2020a, A&A, 643, A111
Dabhade, P., Gaikwad, M., Bagchi, J., et al. 2017, MNRAS, 469, 2886
Dabhade, P., Röttgering, H. J. A., Bagchi, J., et al. 2020b, A&A, 635, A5
Dabhade, P., Mahato, M., Bagchi, J., et al. 2020c, A&A, 642, A153
Daly, R. A. 1994a, ApJ, 426, 38
—. 1994b, ApJ, 426, 38
—. 2011, MNRAS, 414, 1253
Daly, R. A., Djorgovski, S. G., Freeman, K. A., et al. 2008, ApJ, 677, 1
Danziger, I. J., & Goss, W. M. 1983, MNRAS, 202, 703
Davé, R., Cen, R., Ostriker, J. P., et al. 2001, ApJ, 552, 473
De Breuck, C., Neri, R., & Omont, A. 2003, New A Rev., 47, 285
de Bruyn, A. G. 1989, A&A, 226, L13
de Gasperin, F., Dijkema, T. J., Drabent, A., et al. 2019, A&A, 622, A5
de Vaucouleurs, G. 1963, ApJS, 8, 31
Delli Veneri, M., Cavuoti, S., Brescia, M., Longo, G., & Riccio, G. 2019, MNRAS, 486, 1377
Dennett-Thorpe, J., Bridle, A. H., Laing, R. A., & Scheuer, P. A. G. 1999, MNRAS, 304, 271
Doeleman, S. S., Fish, V. L., Schenck, D. E., et al. 2012, Science, 338, 355
Donoso, E., Best, P. N., & Kauffmann, G. 2009, MNRAS, 392, 617
Drake, C. L., McGregor, P. J., & Dopita, M. A. 2004, AJ, 128, 955
Dressler, A., & Shectman, S. A. 1988, AJ, 95, 284
Duncan, K. J., Sabater, J., Röttgering, H. J. A., et al. 2019, A&A, 622, A3
Eatough, R. P., Falcke, H., Karuppusamy, R., et al. 2013, Nature, 501, 391
Eckert, D., Jauzac, M., Shan, H., et al. 2015, Nature, 528, 105
Ekers, R. D., Wall, J. V., Shaver, P. A., et al. 1989, MNRAS, 236, 737
Emonts, B. H. C., Morganti, R., Struve, C., et al. 2010, MNRAS, 406, 987
Emonts, B. H. C., Norris, R. P., Feain, I., et al. 2014, MNRAS, 438, 2898
Enßlin, T. A., & Gopal-Krishna. 2001, in Astronomical Society of the Pacific Conference Series, Vol. 250, Particles and Fields in Radio Galaxies Conference, ed. R. A. Laing & K. M. Blundell, 454
Evans, A. S., Mazzarella, J. M., Surace, J. A., et al. 2005a, ApJS, 159, 197
Evans, D. A., Hardcastle, M. J., Croston, J. H., Worrall, D. M., & Birkinshaw, M.

2005b, MNRAS, 359, 363
Event Horizon Telescope Collaboration, Akiyama, K., Alberdi, A., et al. 2019, ApJ, 875, L1
Fabian, A. C., Celotti, A., Blundell, K. M., Kassim, N. E., & Perley, R. A. 2002, MNRAS, 331, 369
Falle, S. A. E. G. 1991, MNRAS, 250, 581
Fanaroff, B. L., & Riley, J. M. 1974, MNRAS, 167, 31P
Fanidakis, N., Baugh, C. M., Benson, A. J., et al. 2011, MNRAS, 410, 53
Fanti, C., Fanti, R., de Ruiter, H. R., & Parma, P. 1987, A&AS, 69, 57
Feretti, L., Perley, R., Giovannini, G., & Andernach, H. 1999, A&A, 341, 29
Ferrarese, L., & Merritt, D. 2000, ApJ, 539, L9
Gabuzda, D. C., Murray, É., & Cronin, P. 2004, MNRAS, 351, L89
Galvin, T. J., Huynh, M. T., Norris, R. P., et al. 2020, MNRAS, 497, 2730
Gao, J., Zou, H., Zhou, X., & Kong, X. 2018, ApJ, 862, 12
Gaspari, M., Ruszkowski, M., & Oh, S. P. 2013, MNRAS, 432, 3401
Gawroński, M. P., Marecki, A., Kunert-Bajraszewska, M., & Kus, A. J. 2006, A&A, 447, 63
Gebhardt, K., Bender, R., Bower, G., et al. 2000, ApJ, 539, L13
Ginzburg, V. L., & Syrovatskii, S. I. 1965, ARA&A, 3, 297
—. 1969, ARA&A, 7, 375
Godfrey, L. E. H., & Shabala, S. S. 2013, ApJ, 767, 12
Gopal-Krishna, Mhaskey, M., & Mangalam, A. 2012, ApJ, 744, 31
Gopal-Krishna, & Wiita, P. J. 1987, MNRAS, 226, 531
—. 2000, A&A, 363, 507
—. 2002, New A Rev., 46, 357
Gopal-Krishna, Wiita, P. J., & Saripalli, L. 1989, MNRAS, 239, 173
Gorbunov, D. S., & Rubakov, V. A. 2011, Introduction to the Theory of the Early Universe: Cosmological Perturbations and Inflationary Theory
Govoni, F., Falomo, R., Fasano, G., & Scarpa, R. 2000, A&A, 353, 507
Govoni, F., & Feretti, L. 2004, International Journal of Modern Physics D, 13, 1549
Gower, A. C., Gregory, P. C., Unruh, W. G., & Hutchings, J. B. 1982, ApJ, 262, 478
Gower, A. C., & Hutchings, J. B. 1982, ApJ, 258, L63
Graham, A. W. 2007, MNRAS, 379, 711
Green, D. A. 2011, Bulletin of the Astronomical Society of India, 39, 289
Greenstein, J. L., & Schmidt, M. 1964, ApJ, 140, 1
Greisen, E. W. 2003, AIPS, the VLA, and the VLBA, ed. A. Heck, Vol. 285, 109
Griffin, A. J., Lacey, C. G., Gonzalez-Perez, V., et al. 2019, MNRAS, 487, 198
Grupe, D., Beuermann, K., Thomas, H.-C., Mannheim, K., & Fink, H. H. 1998, A&A, 330, 25

Gruppioni, C., Zamorani, G., de Ruiter, H. R., et al. 1997, MNRAS, 286, 470
Gültekin, K., Richstone, D. O., Gebhardt, K., et al. 2009, ApJ, 698, 198
Gürkan, G., Hardcastle, M. J., & Jarvis, M. J. 2014, MNRAS, 438, 1149
Gürkan, G., Hardcastle, M. J., Jarvis, M. J., et al. 2015, MNRAS, 452, 3776
Gurvits, L. I., Kellermann, K. I., & Frey, S. 1999, A&A, 342, 378
Hada, K. 2020, Galaxies, 8, 1
Hao, J., McKay, T. A., Koester, B. P., et al. 2010, ApJS, 191, 254
Hardcastle, M. 2018a, Nature Astronomy, 2, 273
Hardcastle, M. J. 2018b, MNRAS, 475, 2768
Hardcastle, M. J., Birkinshaw, M., Cameron, R. A., et al. 2002, ApJ, 581, 948
Hardcastle, M. J., Cheung, C. C., Feain, I. J., & Stawarz, Ł. 2009, MNRAS, 393, 1041
Hardcastle, M. J., Evans, D. A., & Croston, J. H. 2007, MNRAS, 376, 1849
Hardcastle, M. J., Gürkan, G., van Weeren, R. J., et al. 2016, MNRAS, 462, 1910
Hardcastle, M. J., Williams, W. L., Best, P. N., et al. 2019, A&A, 622, A12
Hardee, P. E. 2007, ApJ, 664, 26
Hargrave, P. J., & Ryle, M. 1974, MNRAS, 166, 305
Hart, R. E., Bamford, S. P., Willett, K. W., et al. 2016, MNRAS, 461, 3663
Harwood, J. J., Croston, J. H., Intema, H. T., et al. 2016, MNRAS, 458, 4443
Heald, G. H., Pizzo, R. F., Orrú, E., et al. 2015, A&A, 582, A123
Healey, S. E., Romani, R. W., Taylor, G. B., et al. 2007, ApJS, 171, 61
Heckman, T. M., & Best, P. N. 2014, ARA&A, 52, 589
Heckman, T. M., Kauffmann, G., Brinchmann, J., et al. 2004, ApJ, 613, 109
Heinz, S., Choi, Y.-Y., Reynolds, C. S., & Begelman, M. C. 2002, ApJ, 569, L79
Hernquist, L. 1990, ApJ, 356, 359
Hillas, A. M. 1984, ARA&A, 22, 425
Hinshaw, G., Larson, D., Komatsu, E., et al. 2013, ApJS, 208, 19
Ho, L. C. 2008, ARA&A, 46, 475
Ho, L. C., & Kim, M. 2009, ApJS, 184, 398
Hoang, D. N., Shimwell, T. W., Stroe, A., et al. 2017, MNRAS, 471, 1107
Hocuk, S., & Barthel, P. D. 2010, A&A, 523, A9
Hodgson, J. A., Krichbaum, T. P., Marscher, A. P., et al. 2017, A&A, 597, A80
Hogan, M. T., Edge, A. C., Hlavacek-Larrondo, J., et al. 2015, MNRAS, 453, 1201
Hogbom, J. A., & Brouw, W. N. 1974, A&A, 33, 289
Hooper, D. 2016, ArXiv e-prints
Hopkins, P. F., Hernquist, L., Cox, T. J., & Kereš, D. 2008, ApJS, 175, 356
Hopkins, P. F., & Quataert, E. 2010, MNRAS, 407, 1529
Hörandel, J. R. 2008, in Reviews in Modern Astronomy, Vol. 20, Reviews in Modern Astronomy, ed. S. Röser, 198
Hota, A., Sirothia, S. K., Ohyama, Y., et al. 2011, MNRAS, 417, L36
Hubble, E. P. 1926, ApJ, 64, 321

Huchra, J. P., Macri, L. M., Masters, K. L., et al. 2012, ApJS, 199, 26
Hughes, D. H., Dunlop, J. S., & Rawlings, S. 1997, MNRAS, 289, 766
Hughes, S. A., & Blandford, R. D. 2003, ApJ, 585, L101
Hummel, C. A., Schalinski, C. J., Krichbaum, T. P., et al. 1992, A&A, 257, 489
Hurley-Walker, N., Callingham, J. R., Hancock, P. J., et al. 2017, MNRAS, 464, 1146
Huynh, M. T., Jackson, C. A., & Norris, R. P. 2007, AJ, 133, 1331
Ineson, J., Croston, J. H., Hardcastle, M. J., & Mingo, B. 2017, MNRAS, 467, 1586
Intema, H. T., Jagannathan, P., Mooley, K. P., & Frail, D. A. 2017, A&A, 598, A78
Intema, H. T., van der Tol, S., Cotton, W. D., et al. 2009, A&A, 501, 1185
Ishwara-Chandra, C. H., & Saikia, D. J. 1999, MNRAS, 309, 100
—. 2000, MNRAS, 317, 658
Ishwara-Chandra, C. H., Sirothia, S. K., Wadadekar, Y., Pal, S., & Windhorst, R. 2010, MNRAS, 405, 436
Isobe, N., & Koyama, S. 2015, PASJ, 67, 77
Ito, H., Kino, M., Kawakatu, N., Isobe, N., & Yamada, a. 2008, The Astrophysical Journal, 685, 828
Ivezić, Ž., Kahn, S. M., Tyson, J. A., et al. 2019, ApJ, 873, 111
Jaegers, W. J. 1987, A&AS, 71, 75
Jafelice, L. C., & Opher, R. 1992, MNRAS, 257, 135
Jaffe, W., Meisenheimer, K., Röttgering, H. J. A., et al. 2004, Nature, 429, 47
Jaffe, W. J., & Perola, G. C. 1973, A&A, 26, 423
Jamrozy, M., Konar, C., Machalski, J., & Saikia, D. J. 2008, MNRAS, 385, 1286
Jansky, K. G. 1933, Nature, 132, 66
Jennison, R. C., & Das Gupta, M. K. 1953, Nature, 172, 996
Jones, D. H., Read, M. A., Saunders, W., et al. 2009, MNRAS, 399, 683
Jones, D. L., & Wehrle, A. E. 2002, ApJ, 580, 114
Jones, P. A. 1989, Proceedings of the Astronomical Society of Australia, 8, 81
Junor, W., Biretta, J. A., & Livio, M. 1999, Nature, 401, 891
Kaiser, C. R., & Alexander, P. 1997, MNRAS, 286, 215
Kaiser, C. R., Dennett-Thorpe, J., & Alexander, P. 1997, MNRAS, 292, 723
Kaiser, N., Aussel, H., Burke, B. E., et al. 2002, in Society of Photo-Optical Instrumentation Engineers (SPIE) Conference Series, Vol. 4836, Survey and Other Telescope Technologies and Discoveries, ed. J. A. Tyson & S. Wolff, 154–164
Kaiser, N., Burgett, W., Chambers, K., et al. 2010, in Society of Photo-Optical Instrumentation Engineers (SPIE) Conference Series, Vol. 7733, Ground-based and Airborne Telescopes III, ed. L. M. Stepp, R. Gilmozzi, & H. J. Hall, 77330E
Kaldare, R., Colless, M., Raychaudhury, S., & Peterson, B. A. 2003, MNRAS, 339, 652

Kapahi, V. K. 1975, MNRAS, 172, 513
Kapahi, V. K., Athreya, R. M., van Breugel, W., McCarthy, P. J., & Subrahmanya, C. R. 1998, ApJS, 118, 275
Kapahi, V. K., & Saikia, D. J. 1981, Bulletin of the Astronomical Society of India, 9, 77
—. 1982, Journal of Astrophysics and Astronomy, 3, 465
Kapinska, A. D., Hardcastle, M., Jackson, C., et al. 2015, Advancing Astrophysics with the Square Kilometre Array (AASKA14), 173
Kapińska, A. D., Terentev, I., Wong, O. I., et al. 2017, AJ, 154, 253
Kardashev, N. S. 1962, Soviet Ast., 6, 317
Kauffmann, G., & Haehnelt, M. 2000, MNRAS, 311, 576
Kellermann, K. I., Pauliny-Toth, I. I. K., & Williams, P. J. S. 1969, ApJ, 157, 1
Kellermann, K. I., & Verschuur, G. L. 1988, Galactic and extragalactic radio astronomy (2nd edition)
Kennicutt, Robert C., J. 1998, ARA&A, 36, 189
Kettenis, M., van Langevelde, H. J., Reynolds, C., & Cotton, B. 2006, in Astronomical Society of the Pacific Conference Series, Vol. 351, Astronomical Data Analysis Software and Systems XV, ed. C. Gabriel, C. Arviset, D. Ponz, & S. Enrique, 497
King, A. R., & Pringle, J. E. 2006, MNRAS, 373, L90
King, A. R., Pringle, J. E., & Hofmann, J. A. 2008, Monthly Notices of the Royal Astronomical Society, 385, 1621–1627
Kirk, J. G., & Schneider, P. 1987, ApJ, 315, 425
Klamer, I. J., Ekers, R. D., Bryant, J. J., et al. 2006, MNRAS, 371, 852
Klein, U., Mack, K.-H., Gregorini, L., & Vigotti, M. 2003, A&A, 406, 579
Koester, B. P., McKay, T. A., Annis, J., et al. 2007, ApJ, 660, 239
Kolmogorov, A. 1933, Inst. Ital. Attuari, Giorn., 4, 83
Komberg, B. V., & Pashchenko, I. N. 2009, Astronomy Reports, 53, 1086
Konar, C., Hardcastle, M. J., Croston, J. H., & Saikia, D. J. 2009, MNRAS, 400, 480
Konar, C., Jamrozy, M., Saikia, D. J., & Machalski, J. 2008, MNRAS, 383, 525
Konar, C., Saikia, D. J., Ishwara-Chandra, C. H., & Kulkarni, V. K. 2004, MNRAS, 355, 845
Kormendy, J., & Ho, L. C. 2013, Annual Review of Astronomy and Astrophysics, 51, 511–653
Kormendy, J., & Richstone, D. 1995, ARA&A, 33, 581
Koshida, S., Minezaki, T., Yoshii, Y., et al. 2014, ApJ, 788, 159
Kozieł-Wierzbowska, D., Goyal, A., & Żywucka, N. 2020, ApJS, 247, 53
Koziel-Wierzbowska, D., & Stasinska, G. 2012, VizieR Online Data Catalog, 741
Krolik, J. H., & Chen, W. 1991, AJ, 102, 1659
Kronberg, P. P. 1994, Reports on Progress in Physics, 57, 325
—. 2004, Journal of Korean Astronomical Society, 37, 343

Kronberg, P. P., Colgate, S. A., Li, H., & Dufton, Q. W. 2004, ApJ, 604, L77
Kronberg, P. P., Dufton, Q. W., Li, H., & Colgate, S. A. 2001a, ApJ, 560, 178
—. 2001b, ApJ, 560, 178
Kronberg, P. P., Wielebinski, R., & Graham, D. A. 1986, A&A, 169, 63
Kuligowska, E., & Kuźmicz, A. 2018, in XXXVIII Polish Astronomical Society Meeting, ed. A. Ró&żańska, Vol. 7, 82–87
Kuźmicz, A., Czerny, B., & Wildy, C. 2019, A&A, 624, A91
Kuźmicz, A., & Jamrozy, M. 2012, MNRAS, 426, 851
Kuźmicz, A., Jamrozy, M., Bronarska, K., Janda-Boczar, K., & Saikia, D. J. 2018, ApJS, 238, 9
Kuźmicz, A., Jamrozy, M., Kozieł-Wierzbowska, D., & Weżgowiec, M. 2017, MNRAS, 471, 3806
Labiano, A., García-Burillo, S., Combes, F., et al. 2013, A&A, 549, A58
—. 2014, A&A, 564, A128
Lacy, M., Rawlings, S., Saunders, R., & Warner, P. J. 1993, MNRAS, 264, 721
Lacy, M., Storrie-Lombardi, L. J., Sajina, A., et al. 2004, ApJS, 154, 166
Lacy, M., Baum, S. A., Chandler, C. J., et al. 2019, arXiv e-prints, arXiv:1907.01981
Laing, R. A., & Peacock, J. A. 1980, MNRAS, 190, 903
Laing, R. A., Riley, J. M., & Longair, M. S. 1983, MNRAS, 204, 151
Lake, S. E., Wright, E. L., Petty, S., et al. 2012, AJ, 143, 7
Lanz, L., Ogle, P. M., Alatalo, K., & Appleton, P. N. 2016, ApJ, 826, 29
Laor, A. 2000, ApJ, 543, L111
Lara, L., Cotton, W. D., Feretti, L., et al. 2001a, A&A, 370, 409
Lara, L., Giovannini, G., Cotton, W. D., et al. 2004, A&A, 421, 899
Lara, L., Márquez, I., Cotton, W. D., et al. 2001b, A&A, 378, 826
Law-Green, J. D. B., Eales, S. A., Leahy, J. P., Rawlings, S., & Lacy, M. 1995, MNRAS, 277, 995
Leahy, J. P., Bridle, A. H., & Strom, R. G. 1996, in IAU Symposium, Vol. 175, Extragalactic Radio Sources, ed. R. D. Ekers, C. Fanti, & L. Padrielli, 157
Ledlow, M. J., & Owen, F. N. 1996, AJ, 112, 9
Ledlow, M. J., Owen, F. N., Yun, M. S., & Hill, J. M. 2001, ApJ, 552, 120
Letawe, G., Courbin, F., Magain, P., et al. 2004, A&A, 424, 455
Lin, Y.-T., Huang, H.-J., & Chen, Y.-C. 2018, AJ, 155, 188
Lintott, C., Schawinski, K., Bamford, S., et al. 2011, MNRAS, 410, 166
Lisenfeld, U., Espada, D., Verdes-Montenegro, L., et al. 2011, A&A, 534, A102
Livio, M. 1999, Phys. Rep., 311, 225
Lobanov, A. P., & Zensus, J. A. 2001, Science, 294, 128
Loeb, A. 2010, How Did the First Stars and Galaxies Form?
Longair, M. S. 2011, High Energy Astrophysics
Longair, M. S., & Pooley, G. G. 1969, MNRAS, 145, 121

Longair, M. S., Ryle, M., & Scheuer, P. A. G. 1973, MNRAS, 164, 243
Lopes, P. A. A. 2007, MNRAS, 380, 1608
Lynden-Bell, D. 1969, Nature, 223, 690
Machalski, J. 1998, A&AS, 128, 153
—. 2011, MNRAS, 413, 2429
Machalski, J., Chyzy, K. T., & Jamrozy, M. 2004a, Acta Astron., 54, 249
—. 2004b, Acta Astron., 54, 249
—. 2004c, Acta Astron., 54, 391
Machalski, J., Chyży, K. T., Stawarz, Ł., & Kozieł, D. 2007a, A&A, 462, 43
—. 2007b, A&A, 462, 43
Machalski, J., & Condon, J. J. 1999, ApJS, 123, 41
Machalski, J., & Jamrozy, M. 2006, A&A, 454, 95
Machalski, J., Jamrozy, M., & Saikia, D. J. 2009, MNRAS, 395, 812
Machalski, J., Jamrozy, M., & Zola, S. 2001, A&A, 371, 445
Machalski, J., Jamrozy, M., Zola, S., & Koziel, D. 2006a, A&A, 454, 85
—. 2006b, A&A, 454, 85
Machalski, J., Koziel-Wierzbowska, D., & Jamrozy, M. 2007c, Acta Astron., 57, 227
Machalski, J., Kozieł-Wierzbowska, D., Jamrozy, M., & Saikia, D. J. 2008, ApJ, 679, 149
Mack, K. H., Klein, U., O'Dea, C. P., & Willis, A. G. 1997, A&AS, 123, 423
Mack, K. H., Klein, U., O'Dea, C. P., Willis, A. G., & Saripalli, L. 1998, A&A, 329, 431
Magorrian, J., Tremaine, S., Richstone, D., et al. 1998, AJ, 115, 2285
Mahatma, V. H., Hardcastle, M. J., Williams, W. L., et al. 2018, MNRAS, 475, 4557
—. 2019, A&A, 622, A13
Mahony, E. K., Morganti, R., Prandoni, I., et al. 2016, MNRAS, 463, 2997
Malarecki, J. M., Jones, D. H., Saripalli, L., Staveley-Smith, L., & Subrahmanyan, R. 2015, MNRAS, 449, 955
Malarecki, J. M., Staveley-Smith, L., Saripalli, L., et al. 2013, MNRAS, 432, 200
Mangalam, A. V., & Gopal-Krishna. 1995, MNRAS, 275, 976
Mann, H. B., & Whitney, D. R. 1947, The annals of mathematical statistics, 50
Manolakou, K., & Kirk, J. G. 2002, A&A, 391, 127
Mao, M. Y., Owen, F., Duffin, R., et al. 2015, MNRAS, 446, 4176
Marconi, A., & Hunt, L. K. 2003, ApJ, 589, L21
Marconi, A., Risaliti, G., Gilli, R., et al. 2004, MNRAS, 351, 169
Marscher, A. P., Jorstad, S. G., Gómez, J.-L., et al. 2002, Nature, 417, 625
Marshall, H. L., Harris, D. E., Grimes, J. P., et al. 2001, ApJ, 549, L167
Martí-Vidal, I., Muller, S., Vlemmings, W., Horellou, C., & Aalto, S. 2015, Science, 348, 311

Masters, K. L., Mosleh, M., Romer, A. K., et al. 2010, MNRAS, 405, 783
Mauch, T., Murphy, T., Buttery, H. J., et al. 2003, MNRAS, 342, 1117
McCarthy, P. J., Kapahi, V. K., van Breugel, W., et al. 1996, ApJS, 107, 19
McConnell, N. J., & Ma, C.-P. 2013, ApJ, 764, 184
McGilchrist, M. M., Baldwin, J. E., Riley, J. M., et al. 1990, MNRAS, 246, 110
McGreer, I. D., Helfand, D. J., & White, R. L. 2009, AJ, 138, 1925
McKinney, J. C., & Narayan, R. 2007, MNRAS, 375, 513
McLure, R. J., Willott, C. J., Jarvis, M. J., et al. 2004, MNRAS, 351, 347
McMullin, J. P., Waters, B., Schiebel, D., Young, W., & Golap, K. 2007, in Astronomical Society of the Pacific Conference Series, Vol. 376, Astronomical Data Analysis Software and Systems XVI, ed. R. A. Shaw, F. Hill, & D. J. Bell, 127
McNamara, B. R., & Nulsen, P. E. J. 2007, ARA&A, 45, 117
McNamara, B. R., Nulsen, P. E. J., Wise, M. W., et al. 2005, Nature, 433, 45
Meier, D. L. 1999, ApJ, 522, 753
Meier, D. L., Koide, S., & Uchida, Y. 2001, Science, 291, 84
Mertens, F., Lobanov, A. P., Walker, R. C., & Hardee, P. E. 2016, A&A, 595, A54
Meyer, M., Petropoulou, M., & Christie, I. 2020, arXiv e-prints, arXiv:2012.09944
Mikhailov, A. G., & Gnedin, Y. N. 2018, Astronomy Reports, 62, 1
Miley, G. 1980, ARA&A, 18, 165
Miley, G. K., & Wade, C. M. 1971, Astrophys. Lett., 8, 11
Mills, B. Y. 1981, Proceedings of the Astronomical Society of Australia, 4, 156
Mingo, B., Hardcastle, M. J., Croston, J. H., et al. 2014, MNRAS, 440, 269
Mingo, B., Watson, M. G., Rosen, S. R., et al. 2016, MNRAS, 462, 2631
Mingo, B., Croston, J. H., Hardcastle, M. J., et al. 2019, MNRAS, 488, 2701
Mirakhor, M. S., Walker, S. A., Bagchi, J., et al. 2021, MNRAS, 500, 2503
Mitton, S., & Ryle, M. 1969, MNRAS, 146, 221
Mizuno, Y., Hardee, P. E., & Nishikawa, K.-I. 2014, ApJ, 784, 167
Mizuno, Y., Lyubarsky, Y., Nishikawa, K.-I., & Hardee, P. E. 2009, ApJ, 700, 684
—. 2012, ApJ, 757, 16
Mohan, N., & Rafferty, D. 2015, PyBDSF: Python Blob Detection and Source Finder
Molina, M., Bassani, L., Malizia, A., et al. 2014, A&A, 565, A2
Morabito, L. K., & Harwood, J. J. 2018, MNRAS, 480, 2726
Morganti, R., Peck, A. B., Oosterloo, T. A., et al. 2009, A&A, 505, 559
Morganti, R., Tadhunter, C. N., & Oosterloo, T. A. 2005, A&A, 444, L9
Morton, D. C. 1991, ApJS, 77, 119
Mukherjee, D., Bicknell, G. V., Sutherland , R., & Wagner, A. 2016, MNRAS, 461, 967
Mukherjee, D., Bicknell, G. V., Wagner, A. e. Y., Sutherland, R. S., & Silk, J. 2018, MNRAS, 479, 5544
Mulcahy, D. D., Mao, M. Y., Mitsuishi, I., et al. 2016, A&A, 595, L8

Mullin, L. M., Riley, J. M., & Hardcastle, M. J. 2008, MNRAS, 390, 595
Nakamura, M., Li, H., & Li, S. 2007, ApJ, 656, 721
Nakamura, M., & Meier, D. L. 2004, ApJ, 617, 123
Nakamura, M., Uchida, Y., & Hirose, S. 2001, New A, 6, 61
Nandi, S., Pirya, A., Pal, S., et al. 2010, MNRAS, 404, 433
Nandi, S., & Saikia, D. J. 2012, Bulletin of the Astronomical Society of India, 40, 121
Nandi, S., Saikia, D. J., Roy, R., et al. 2019, MNRAS, 486, 5158
Napier, P. J., Thompson, A. R., & Ekers, R. D. 1983, IEEE Proceedings, 71, 1295
Narayan, R., Igumenshchev, I. V., & Abramowicz, M. A. 2003, PASJ, 55, L69
Narayan, R., & Yi, I. 1994, ApJ, 428, L13
Nesvadba, N. P. H., Drouart, G., De Breuck, C., et al. 2017, A&A, 600, A121
Nesvadba, N. P. H., Boulanger, F., Salomé, P., et al. 2010, A&A, 521, A65
Netzer, H. 2015, ARA&A, 53, 365
Nicastro, F., Mathur, S., & Elvis, M. 2008, Science, 319, 55
Nicastro, F., Kaastra, J., Krongold, Y., et al. 2018, Nature, 558, 406
Nieto, J. L., Coupinot, G., Lelievre, G., & Madsen, C. 1983, MNRAS, 203, 39P
Nilsson, K. 1998, A&AS, 132, 31
Noordam, J. E. 2004, in Society of Photo-Optical Instrumentation Engineers (SPIE) Conference Series, Vol. 5489, Ground-based Telescopes, ed. J. Oschmann, Jacobus M., 817–825
Northover, K. J. E. 1973, MNRAS, 165, 369
Ocaña Flaquer, B., Leon, S., Combes, F., & Lim, J. 2010, A&A, 518, A9
Oesch, P. A., Brammer, G., van Dokkum, P. G., et al. 2016, ApJ, 819, 129
Offringa, A. R., McKinley, B., Hurley-Walker, N., et al. 2014, MNRAS, 444, 606
Ogle, P., Antonucci, R., Appleton, P. N., & Whysong, D. 2007, ApJ, 668, 699
Oort, M. J. A., Steemers, W. J. G., & Windhorst, R. A. 1988, A&AS, 73, 103
Orr, M. J. L., & Browne, I. W. A. 1982, MNRAS, 200, 1067
O'Sullivan, E., Combes, F., Hamer, S., et al. 2015a, A&A, 573, A111
O'Sullivan, S., Reville, B., & Taylor, A. M. 2009, MNRAS, 400, 248
O'Sullivan, S. P., Gaensler, B. M., Lara-López, M. A., et al. 2015b, ApJ, 806, 83
O'Sullivan, S. P., Machalski, J., Van Eck, C. L., et al. 2019, A&A, 622, A16
Owen, F. N., Ledlow, M. J., & Keel, W. C. 1995, AJ, 109, 14
Pacholczyk, A. G. 1970, Radio astrophysics. Nonthermal processes in galactic and extragalactic sources
Pâris, I., Petitjean, P., Aubourg, É., et al. 2018, A&A, 613, A51
Park, S., Sohn, B. W., & Yi, S. K. 2013, A&A, 560, A80
Parma, P., Murgia, M., de Ruiter, H. R., et al. 2007, A&A, 470, 875
Paturel, G., Petit, C., Prugniel, P., et al. 2003, A&A, 412, 45
Paul, S., John, R. S., Gupta, P., & Kumar, H. 2017, MNRAS, 471, 2
Peacock, J. A. 1983, MNRAS, 202, 615

Peebles, P. J. E. 1993, Principles of Physical Cosmology
—. 2012, ARA&A, 50, 1
—. 2017, Nature Astronomy, 1, 0057
Peng, B., Chen, R. R., & Strom, R. 2015, in Advancing Astrophysics with the Square Kilometre Array (AASKA14), 109
Perley, R. A., Bridle, A. H., & Willis, A. G. 1984, ApJS, 54, 291
Perley, R. A., & Erickson, W. C. 1979, ApJS, 41, 131
Perucho, M., Hanasz, M., Martí, J.-M., & Miralles, J.-A. 2007, Phys. Rev. E, 75, 056312
Pirya, A., Saikia, D. J., Singh, M., & Chandola, H. C. 2012, MNRAS, 426, 758
Planck Collaboration, Ade, P. A. R., Aghanim, N., et al. 2016, A&A, 594, A13
Prandoni, I., Laing, R. A., de Ruiter, H. R., & Parma, P. 2010, A&A, 523, A38
Prescott, M., Whittam, I. H., Jarvis, M. J., et al. 2018, MNRAS, 480, 707
Proctor, D. D. 2016, ApJS, 224, 18
Quilis, V., Bower, R. G., & Balogh, M. L. 2001, MNRAS, 328, 1091
Ratcliffe, A., Shanks, T., Parker, Q. A., et al. 1998, MNRAS, 300, 417
Rawlings, S., Saunders, R., Miller, P., Jones, M. E., & Eales, S. A. 1990, MNRAS, 246, 21P
Reber, G. 1940, ApJ, 91, 621
—. 1944, ApJ, 100, 279
—. 1946, Nature, 158, 945
—. 1949, Scientific American, 181, 34
Rees, M. J. 1971, Nature, 229, 312
—. 1984, ARA&A, 22, 471
—. 1987, QJRAS, 28, 197
—. 1993, QJRAS, 34, 279
Rees, M. J., Begelman, M. C., Blandford, R. D., & Phinney, E. S. 1982, Nature, 295, 17
Rengelink, R. B., Tang, Y., de Bruyn, A. G., et al. 1997, A&AS, 124
Rentería Macario, J., & Andernach, H. 2017, arXiv e-prints, arXiv:1710.10731
Reynolds, C. S. 2019, Nature Astronomy, 3, 41
Richards, G. T., Myers, A. D., Gray, A. G., et al. 2009, ApJS, 180, 67
Richards, G. T., Myers, A. D., Peters, C. M., et al. 2015, ApJS, 219, 39
Romanova, M. M., & Lovelace, R. V. E. 1992, A&A, 262, 26
Rottgering, H. J. A., Wieringa, M. H., Hunstead, R. W., & Ekers, R. D. 1997, MNRAS, 290, 577
Rowan-Robinson, M. 1967, Nature, 216, 1289
Ruffa, I., Prandoni, I., Laing, R. A., et al. 2019, MNRAS, 484, 4239
Ruzmaikin, A., Sokolov, D., & Shukurov, A. 1989, MNRAS, 241, 1
Rybicki, G. B., & Lightman, A. P. 1986, Radiative Processes in Astrophysics
Ryle, M. 1952, Proceedings of the Royal Society of London Series A, 211, 351

Sadler, E. M., Jackson, C. A., Cannon, R. D., et al. 2002, MNRAS, 329, 227
Sadler, E. M., Cannon, R. D., Mauch, T., et al. 2007, MNRAS, 381, 211
Safouris, V., Subrahmanyan, R., Bicknell, G. V., & Saripalli, L. 2009, MNRAS, 393, 2
Sahni, V., & Starobinsky, A. 2000, International Journal of Modern Physics D, 9, 373
Saikia, D. J., & Jamrozy, M. 2009, Bulletin of the Astronomical Society of India, 37, 63
Saikia, D. J., Junor, W., Cornwell, T. J., Muxlow, T. W. B., & Shastri, P. 1990, MNRAS, 245, 408
Saikia, D. J., Konar, C., & Kulkarni, V. K. 2006, MNRAS, 366, 1391
Saikia, D. J., Thomasson, P., Jackson, N., Salter, C. J., & Junor, W. 1996, MNRAS, 282, 837
Saintonge, A., Catinella, B., Tacconi, L. J., et al. 2017, ApJS, 233, 22
Salim, S., Boquien, M., & Lee, J. C. 2018, ApJ, 859, 11
Salomé, Q., Salomé, P., & Combes, F. 2015, A&A, 574, A34
Salpeter, E. E. 1964, ApJ, 140, 796
Sandage, A. 1965, ApJ, 141, 1560
Saripalli, L., Gopal-Krishna, Reich, W., & Kuehr, H. 1986, A&A, 170, 20
Saripalli, L., Hunstead, R. W., Subrahmanyan, R., & Boyce, E. 2005, AJ, 130, 896
Saripalli, L., & Mack, K. H. 2007, MNRAS, 376, 1385
Saripalli, L., & Malarecki, J. M. 2015, in Proceedings of "The many facets of extragalactic radio surveys: towards new scientific challenges" (EXTRARADSUR2015). 20-23 October 2015. Bologna, 44
Saripalli, L., Malarecki, J. M., Subrahmanyan, R., Jones, D. H., & Staveley-Smith, L. 2013, MNRAS, 436, 690
Saxena, A., Röttgering, H. J. A., Duncan, K. J., et al. 2019, MNRAS, 489, 5053
Scaife, A. M. M., & Heald, G. H. 2012, MNRAS, 423, L30
Scheuer, P. A. G. 1974, MNRAS, 166, 513
Scheuer, P. A. G. 1987, in Superluminal Radio Sources, ed. J. A. Zensus & T. J. Pearson, 104–113
—. 1995, MNRAS, 277, 331
Scheuer, P. A. G., & Readhead, A. C. S. 1979, Nature, 277, 182
Scheuer, P. A. G., & Williams, P. J. S. 1968, ARA&A, 6, 321
Schmidt, M. 1963, Nature, 197, 1040
Schoenmakers, A. P., de Bruyn, A. G., Röttgering, H. J. A., & van der Laan, H. 2001, A&A, 374, 861
Schoenmakers, A. P., de Bruyn, A. G., Röttgering, H. J. A., van der Laan, H., & Kaiser, C. R. 2000a, MNRAS, 315, 371
Schoenmakers, A. P., Mack, K. H., de Bruyn, A. G., et al. 2000b, A&AS, 146, 293
Schoenmakers, A. P., Mack, K. H., Lara, L., et al. 1998, A&A, 336, 455
Sebastian, B., Ishwara-Chandra, C. H., Joshi, R., & Wadadekar, Y. 2018, MNRAS,

473, 4926
Seyfert, C. K. 1943, ApJ, 97, 28
Shankar, F., Weinberg, D. H., & Miralda-Escudé, J. 2009, ApJ, 690, 20
Sheth, R. K., Mo, H. J., & Tormen, G. 2001, MNRAS, 323, 1
Shimwell, T. W., Röttgering, H. J. A., Best, P. N., et al. 2017, A&A, 598, A104
Shimwell, T. W., Tasse, C., Hardcastle, M. J., et al. 2019, A&A, 622, A1
Shklovskii, I. S. 1955, AZh, 32, 215
Shu, F. H. 1991, The physics of astrophysics. Volume 1: Radiation.
Shukla, A., & Mannheim, K. 2020, Nature Communications, 11, 4176
Shulevski, A., Barthel, P. D., Morganti, R., et al. 2019, A&A, 628, A69
Sikora, M., & Begelman, M. C. 2013, ApJ, 764, L24
Sikora, M., Stawarz, Ł., & Lasota, J.-P. 2007, ApJ, 658, 815
Silk, J., & Rees, M. J. 1998, A&A, 331, L1
Singh, V., Ishwara-Chandra, C. H., Sievers, J., et al. 2015, MNRAS, 454, 1556
Sironi, L., Petropoulou, M., & Giannios, D. 2015, MNRAS, 450, 183
Sironi, L., Spitkovsky, A., & Arons, J. 2013, ApJ, 771, 54
Sirothia, S. K., Saikia, D. J., Ishwara-Chandra, C. H., & Kantharia, N. G. 2009, MNRAS, 392, 1403
Skrutskie, M. F., Cutri, R. M., Stiening, R., et al. 2006, AJ, 131, 1163
Smirnov, N. 1948, The Annals of Mathematical Statistics, 19, 279
Smirnov, O. M., & Tasse, C. 2015, MNRAS, 449, 2668
Smith, D. J. B., Best, P. N., Duncan, K. J., et al. 2016, in SF2A-2016: Proceedings of the Annual meeting of the French Society of Astronomy and Astrophysics, ed. C. Reylé, J. Richard, L. Cambrésy, M. Deleuil, E. Pécontal, L. Tresse, & I. Vauglin, 271–280
Smith, F. G. 1951, Nature, 168, 555
Smolčić, V. 2009, ApJ, 699, L43
Smolčić, V., & Riechers, D. A. 2011, ApJ, 730, 64
Solomon, P. M., & Vanden Bout, P. A. 2005, ARA&A, 43, 677
Solovyov, D. I., & Verkhodanov, O. V. 2011, Astrophysical Bulletin, 66, 416
—. 2014, Astrophysical Bulletin, 69, 141
Soltan, A. 1982, MNRAS, 200, 115
Springel, V., White, S. D. M., Jenkins, A., et al. 2005, Nature, 435, 629
Stanghellini, C., O'Dea, C. P., Dallacasa, D., et al. 2005, A&A, 443, 891
Stern, D., Eisenhardt, P., Gorjian, V., et al. 2005, ApJ, 631, 163
Stern, D., Assef, R. J., Benford, D. J., et al. 2012, ApJ, 753, 30
Strom, R. G., & Willis, A. G. 1980, A&A, 85, 36
Subrahmanyan, R., Hunstead, R. W., Cox, N. L. J., & McIntyre, V. 2006, ApJ, 636, 172
Subrahmanyan, R., & Saripalli, L. 1993, MNRAS, 260, 908
Subrahmanyan, R., Saripalli, L., & Hunstead, R. W. 1996, MNRAS, 279, 257

Subrahmanyan, R., Saripalli, L., Safouris, V., & Hunstead, R. W. 2008, ApJ, 677, 63

Swarup, G. 1984, Journal of Astrophysics and Astronomy, 5, 139

Swarup, G. 1991, in Astronomical Society of the Pacific Conference Series, Vol. 19, IAU Colloq. 131: Radio Interferometry. Theory, Techniques, and Applications, ed. T. J. Cornwell & R. A. Perley, 376–380

Swarup, G., Ananthakrishnan, S., Kapahi, V. K., et al. 1991, Current Science, 60, 95

Tacconi, L. J., Genzel, R., Saintonge, A., et al. 2018, ApJ, 853, 179

Tamhane, P., Wadadekar, Y., Basu, A., et al. 2015, MNRAS, 453, 2438

Tasse, C. 2014, A&A, 566, A127

Tasse, C., Hugo, B., Mirmont, M., et al. 2018, A&A, 611, A87

Tasse, C., Shimwell, T., Hardcastle, M. J., et al. 2020, arXiv e-prints, arXiv:2011.08328

Taylor, G. L., Dunlop, J. S., Hughes, D. H., & Robson, E. I. 1996, MNRAS, 283, 930

Tchekhovskoy, A., Narayan, R., & McKinney, J. C. 2011, MNRAS, 418, L79

Thompson, A. R., Clark, B. G., Wade, C. M., & Napier, P. J. 1980, ApJS, 44, 151

Thorne, K. S. 1974, ApJ, 191, 507

Thwala, S. A., Shafi, N., Colafrancesco, S., Govoni, F., & Murgia, M. 2019, MNRAS, 485, 1938

Tingay, S. J., Goeke, R., Bowman, J. D., et al. 2013, PASA, 30, e007

Tomimatsu, A. 1994, PASJ, 46, 123

Toomre, A. 1964, ApJ, 139, 1217

Tremblay, G. R., O'Dea, C. P., Baum, S. A., et al. 2010, ApJ, 715, 172

Turland, B. D. 1975, MNRAS, 172, 181

Turner, R. J., & Shabala, S. S. 2019, MNRAS, 486, 1225

Urry, C. M., & Padovani, P. 1995, PASP, 107, 803

Ursini, F., Bassani, L., Panessa, F., et al. 2018, MNRAS, 481, 4250

Valentijn, E. A., & Bijleveld, W. 1983, A&A, 125, 223

van Breugel, W. J. M., & Miley, G. K. 1977, Nature, 265, 315

van den Bosch, R. C. E., Gebhardt, K., Gültekin, K., et al. 2012, Nature, 491, 729

van Diepen, G., Dijkema, T. J., & Offringa, A. 2018, Astrophysics Source Code Library, ascl:1804.003

van Haarlem, M. P., Wise, M. W., Gunst, A. W., et al. 2013, A&A, 556, A2

van Ojik, R., Roettgering, H. J. A., van der Werf, P. P., et al. 1997, A&A, 321, 389

van Weeren, R. J., Brüggen, M., Röttgering, H. J. A., et al. 2011, A&A, 533, A35

van Weeren, R. J., de Gasperin, F., Akamatsu, H., et al. 2019, Space Sci. Rev., 215, 16

van Weeren, R. J., Röttgering, H. J. A., Brüggen, M., & Hoeft, M. 2010, Science, 330, 347

van Weeren, R. J., Williams, W. L., Hardcastle, M. J., et al. 2016, ApJS, 223, 2
van Weeren, R. J., Shimwell, T. W., Botteon, A., et al. 2020, arXiv e-prints, arXiv:2011.02387
Véron-Cetty, M. P., & Véron, P. 2006, A&A, 455, 773
Volonteri, M., Haardt, F., & Madau, P. 2003, ApJ, 582, 559
Volonteri, M., Madau, P., Quataert, E., & Rees, M. J. 2005, ApJ, 620, 69
Volonteri, M., Sikora, M., & Lasota, J. 2007, The Astrophysical Journal, 667, 704–713
Volonteri, M., Sikora, M., Lasota, J. P., & Merloni, A. 2013, ApJ, 775, 94
Waggett, P. C., Warner, P. J., & Baldwin, J. E. 1977, MNRAS, 181, 465
Walker, S. A., Bagchi, J., & Fabian, A. C. 2015, MNRAS, 449, 3527
Wei, J.-Y., Xu, D.-W., Cao, L., et al. 1998, A&A, 329, 511
Weinberg, D. H., Mortonson, M. J., Eisenstein, D. J., et al. 2013, Phys. Rep., 530, 87
Wen, Z. L., Han, J. L., & Liu, F. S. 2012, ApJS, 199, 34
Whitaker, K. E., van Dokkum, P. G., Brammer, G., & Franx, M. 2012, ApJ, 754, L29
Whitaker, K. E., Franx, M., Bezanson, R., et al. 2015, ApJ, 811, L12
Whittam, I. H., Prescott, M., McAlpine, K., Jarvis, M. J., & Heywood, I. 2018, MNRAS, 480, 358
Wiita, P. J., Rosen, A., Gopal-Krishna, & Saripalli, L. 1989, Giant Radio Galaxies via Inverse Compton Weakened Jets, ed. K. Meisenheimer & H.-J. Roeser, Vol. 327, 173
Wiklind, T., Combes, F., Henkel, C., & Wyrowski, F. 1997, A&A, 323, 727
Wilcoxon, F. 1945, Biometrics Bulletin, 1, 80
Williams, W. L., van Weeren, R. J., Röttgering, H. J. A., et al. 2016, MNRAS, 460, 2385
Williams, W. L., Hardcastle, M. J., Best, P. N., et al. 2019, A&A, 622, A2
Willis, A. G., Strom, R. G., & Wilson, A. S. 1974, Nature, 250, 625
Willott, C. J., Rawlings, S., Blundell, K. M., & Lacy, M. 1999, MNRAS, 309, 1017
Winter, L. M., Mushotzky, R. F., Tueller, J., & Markwardt, C. 2008, ApJ, 674, 686
Wright, E. L. 2006, PASP, 118, 1711
Wright, E. L., Eisenhardt, P. R. M., Mainzer, A. K., et al. 2010, AJ, 140, 1868
Wu, X.-B., Hao, G., Jia, Z., Zhang, Y., & Peng, N. 2012, AJ, 144, 49
Wuyts, S., Förster Schreiber, N. M., van der Wel, A., et al. 2011, ApJ, 742, 96
Xu, Y., Kronberg, P. P., Habib, S., & Dufton, Q. W. 2006, ApJ, 637, 19
Yang, X.-h., Chen, P.-s., & Huang, Y. 2015, MNRAS, 449, 3191
York, D. G., Adelman, J., Anderson, Jr., J. E., et al. 2000, AJ, 120, 1579
Young, L. M., Bureau, M., Davis, T. A., et al. 2011, MNRAS, 414, 940
Yuan, F., & Narayan, R. 2014, ARA&A, 52, 529
Zamaninasab, M., & ., et al. 2014, Nature, 510, 126

Summary

Giant radio galaxies

Our current understanding of Active Galactic Nuclei (AGNs) tells us that they are broadly divided into two distinct physical classes, namely the AGNs dominantly radiating at radio wavelengths with radio jets, called as radio-loud AGNs or jetted AGNs and others without radio jets called as radio-quiet or non-jetted AGNs. Radio-loud AGN are also referred to as radio galaxies (RGs) or radio quasars (RQs), which exhibit radio jets-lobes system extending beyond the galactic scales. Their formation and evolution have been studied for nearly six decades with the help of large sky radio and optical surveys along with theory and numerical simulations. This has resulted in models that explain most of their observed properties. However, some outstanding problems related to radio-loud AGNs are still under active investigation, like what are the conditions under which an AGN becomes radio-loud and why do only a small fraction of RG population grow to megaparsec (Mpc) size. RGs or RQs growing more than 0.7 Mpc in size are defined as GRGs, which were found almost two decades (1974) after RGs were discovered in the early 1950s.

Until the advent of large sky area radio surveys in the 1990s, discovering exceptional radio objects depended on the dedicated observations of bright sources selected from radio catalogues (e.g. 3CRR), containing hundreds of radio sources. The arrival of sensitive large area surveys likes NVSS, WENSS, FIRST and SUMSS in the 1990s led to discoveries of interesting radio objects ranging from galactic to extragalactic; stars to AGNs to galaxy clusters. This consequently led to the possibility of carrying out studies of large samples, unveil the trends in their respective properties and also discovery of GRGs. However, most of the studies on GRGs were restricted to radio wavelengths and focused on their large scale radio properties. Therefore, the unexplored AGN properties of GRGs provides an opportunity to understand them by comparing with normal-sized RGs. The comparison will allow us to determine the distinguishing factors between them and thereby the reasons for the giant nature of some RGs/RQs. In this thesis, the work has been

carried to address the questions (see section 1.5 of Chapter 1) pertaining to the giant nature of GRGs and to fill the remaining gaps in our understanding of their properties.

This thesis

Until the year 2016 only about 300 GRGs were known and the studies of their properties were very limited. In order to understand the possible causes for the giant nature of GRGs and their rarity, it is essential to study their AGN as well as environmental properties. In order to carry out such a study, there is a need for a statistically large GRG sample. Hence the main focus of this thesis was to carry out large scale search in radio surveys complemented by new optical data to create large samples of GRGs to study their properties and respective trends. The studies carried out with the new samples have answered some key questions about their properties which are described in the chapter wise summary below.
Chapter 2 presents the pilot results of the project called SAGAN, which stands for 'Search and Analysis of Giant radio galaxies with Associated Nuclei'. The aim of this project is to carry out systematic search for GRGs from available radio surveys combined with new optical surveys. As a result, new 25 GRGs were discovered from the NRAO VLA Sky Survey (NVSS) in the redshift range of $0.07 < z < 0.67$. Using publicly available data we studied their radio, optical and mid-infrared properties. Combining the newly discovered 25 GRGs with the known ones from literature, we created a sample of 137 GRGs and for the first time classified their AGN excitation type using mid-infrared colours. This allowed us to show that AGNs of the GRGs do not have preferred excitation state (high or low accretion rate). Also, using our 25 new GRGs and other GRG data from literature we created a sample of 82 GRGs (largest sample then) to study them with respect to Power (P) - Size (D) or P-D diagram along with a sample of smaller sized radio sources from literature (3CRR). Our analysis revealed that at 1.4 GHz the GRGs tend to be less luminous compared to RGs, which could be due to higher adiabatic expansion and radiative losses in GRGs. RG models have suggested that RGs with age evolve towards larger sizes and lower luminosities. We also found the lower right corner region of the P-D diagram to be empty, or in other words we did not find sources with very large sizes and low luminosities. These are mostly faded sources with very low surface brightness and beyond the detection capabilities of surveys like NVSS. Also, our findings suggests that GRGs with sizes greater than 2 Mpc are more rare.

In Chapter 3, results of an extensive search of GRGs from the LOFAR Two-metre Sky Survey (LoTSS) data release 1 is presented. The LoTSS covers a sky area of 424 deg^2 in the northern sky at 144 MHz with a sensitivity of $\sim 100\,\mu$Jy with images available at two resolutions of $6''$ and $20''$. The low-frequency nature of the survey makes it ideal to map diffuse and steep spectrum radio emission from

sources. LoTSS with its high sensitivity and high resolution is able to resolve intricate details of the sources, allowing us to study their morphologies in great details. As a result of a hybrid method of manual and semi-automated search, a record 239 GRGs were found in the redshift range of $0.1 < z < 2.3$, of which 225 were new discoveries. This is the single largest sample of GRGs found to date from any survey and has almost doubled the known population of GRGs. Our new sample also has three giant radio quasars (GRQs) with $z > 2$, which are difficult to detect owing to the high redshift nature and rarity. Several GRGs have a very steep spectrum and are not visible in high-frequency surveys like the 1.4 GHz NVSS. About seven sources in our sample have projected linear sizes greater than 2 Mpc. We combined the LoTSS low-frequency data with NVSS high-frequency data to determine the spectral index (α) and found that the average α for GRGs is 0.78 which is similar to that of normal-sized RGs. Contradictory to the prevailing assumptions, this study shows that old GRGs with diffuse relic (older) emission do not dominate the GRG population, since the spectral index distribution is similar to that RGs. Owing to our large sample size and availability of good observational data, we were able to identify GRGs with unique characteristics. Our sample has 40 GRGs hosted by quasars (GRQs), 14 with restarted AGN activity- called the double-double radio galaxies (DDRGs), 6 GRGs with hybrid radio morphology, and 20 GRGs hosted by the brightest-cluster galaxies (BCG) residing in the dense cluster environment. The large sample of GRGs also allowed us to establish that at least 16% GRGs at $z < 0.55$ are residing in the dense cluster or group environment. This result highlights that despite the dense environment, given enough jet power combined with ongoing AGN fueling (possibly), RGs can grow to megaparsec scales.

Chapter 4 presents the first results of project SAGAN, where we report the finding of 162 new GRGs based on our search from the NVSS. The new sample of GRGs are found in the redshift range of $0.03 < z < 0.95$ with sizes up to $\sim$2.8 Mpc and 23 sources powered by quasars. Combining all the GRGs reported (till March 2020) in literature since 1974 with our samples from SAGAN and LoTSS, we defined and created the largest GRG catalogue of 820 sources. To create the GRG-catalogue, all the papers reporting GRGs since its discovery in 1974 were searched from the various database and all the sources were manually inspected with updated radio survey data like NVSS, TGSS, FIRST, SUMSS, and WENSS. The optical host galaxies of each reported GRG were also re-examined using the latest optical database like SDSS, 6dF, 2MASS, 2dF, and PanSTARRS. In the absence of high-resolution maps showing entire structures, angular sizes of sources were remeasured uniformly using the NVSS. Uniform cosmology was used by adopting the latest Hubble constant value from the Planck mission to compute the projected linear sizes of GRGs. Our GRG-catalogue allowed us to create statistically significant sub samples (matched in redshift) to study its AGN and environmental properties in comparison with samples of normal-sized RGs. We carried out a multi-wavelength analysis of the AGNs of the GRGs using optical, mid-infrared and radio data. Our results show that black hole mass and radio

spectral index distribution of GRGs and RGs are similar. In contrast to the above, the average accretion rate of GRGs was found to be lower than that of RGs. We also show with larger samples that GRG AGNs do not have a preferred excitation state (low or high), which confirms the findings presented in Chapter 2. We observe GRGs in high excitation state tend to have larger sizes, radio power and accretion rate. Using the multi-wavelength data we also estimated the kinetic jet power, total radio power, magnetic field and total sizes and compared it with high and low excitation classes. Furthermore, we find that 10% GRGs reside in centres of galaxy clusters, i.e., in the dense environment and yet grow to megaparsec scales. Hence environment alone cannot be the only governing factor for the large sizes of GRGs. Using all the above results we discuss the possible factors governing the formation and growth of GRGs in detail.

Chapter 5 presents the results of our millimetre-wave study of host galaxies of GRGs. The study was carried out to understand the molecular gas content of the host galaxies of GRGs and its role in the AGN fueling. Such sample studies of GRGs are scarce and important to understand their working mechanism. Most GRGs are hosted by elliptical galaxies (with a few exceptions), which generally lack high star formation. A total of 12 GRGs were selected based on their mid-infrared colours for this study which show signs of heated dust and are likely to be in gas-accretion and star formation phase. Using our observations we report the molecular gas content and star formation efficiency. Our observations with IRAM-30m millimetre wave telescope show detection in three of the twelve selected target GRGs and report upper limits for the rest of the sample. We find two of the GRGs deficient in molecular gas content and with a short depletion time of ~ 200 Myr. Two detections from our sample belong to GRGs hosted by giant gas-rich spiral galaxies which are extremely rare. We use the information available in the literature for other four GRGs in addition to our sample to discuss the observed results and trends. We find the host galaxies of the GRGs follow the main sequence of galaxies with most of them being passive galaxies. Also, GRGs with detection of molecular gas either show signs of restarted AGN activity or are a part of galaxy groups. This sheds more light on the role of environment on refuelling of the AGN. Hence, our millimetre-wave study of GRGs shows that a complex cycle of AGN fueling along with environmental factors are involved in the growth of GRGs.

In Chapter 6 the first study a peculiar 'Barbell' shaped GRG (GRG-J2233+1315) is presented using observations from GMRT, LOFAR and optical 4.2m William Herschel Telescope (WHT). This object was found under project SAGAN and reported for the first time in Dabhade et al. 2017 (Chapter 2), where the size was estimated using photometric redshift from SDSS. In this chapter, we present its spectroscopic redshift from our optical observation with the WHT. The multi-frequency radio data was obtained at 144 MHz (LOFAR), 323 MHz, 612 MHz, and 1300 MHz (GMRT), which led to the finding of peculiar ~100 kpc 'kink' structure in the western jet of the GRG. We discuss the possible reason for this peculiar structure using available results, models from Magneto-hydrodynamical (MHD)

simulations along with its comparison with other similar examples from literature. Such features in extragalactic radio objects provide the ideal laboratory for studying large scale MHD effects. We also observe a long counter-jet on the eastern side which is rare in FR-II type of GRGs. Using the radio data we have estimated the classical and revised estimates of the magnetic field of both lobes ($\sim 5\,\mu$G), which is consistent with the estimates of other GRGs from literature. This also allowed us to estimate the spectral ages and found them to be greater than ~ 110 Myr, which shows the longevity of the AGN activity as well. Interestingly, the GRG resides in a dense cluster environment hosted by the brightest cluster galaxy (BCG) and yet has been able to grow to 1.88 Mpc in size. Using the information from the cluster catalogues, we present the galaxy cluster's virial mass (M_{200} of $\sim 1.1 \times 10^{14}$ $M_\odot$, virial radius ((R_{200}) of ~ 1.02 Mpc, and has expected X-ray luminosity of 0.29 $\times 10^{44}$ erg s^{-1}. It is most likely that the environment of this GRG surely has had an effect on its growth and morphology.

Future Scope

The work in this thesis has established that the GRGs are not as rare as previously thought to be. Now, with more than 800 GRGs catalogued, the next step would be to create subsamples (matched in redshift) of GRGs and study their properties also in comparison with normal-sized RGs using high resolution optical and infrared spectrographs or integral spectral unit (IFU) along with X-ray data. This will help determine the accretion state and overall AGN power of the GRG. Similarly, using optical and X-ray data, the effect of environmental densities and inhomogeneities on the GRG structure and growth will be probed.

With the rapid development in hardware and software in radio astronomy, the speed of carrying out large scale radio surveys has increased and hence surveys with LOFAR, uGMRT, MeerKAT, JVLA, and ASKAP are going to discover 100s of GRGs, which can be used for constraining RG growth and evolutionary models. Also, a large sample of GRGs can possibly be used to probe the warm-hot intergalactic medium (WHIM as described in section 1.5 of Chapter 1, by comparing their pressure balance using GRG radio observations and WHIM simulations. This particular aspect can be explored for GRGs hosted by brightest cluster galaxies or GRGs residing in a cluster environment and with the release of X-ray data from eROSITA mission in the near future it will be possible to carry out such studies.

Samenvatting in het Nederlands

Gigantische radiostelsels

Ons huidige begrip van actieve sterrenstelsels vertelt ons dat ze grofweg zijn onderverdeeld in twee verschillende fysische klassen, namelijk stelsels die gedomineerd worden door hun actieve kern en radio-jets die straling uitzenden op radiogolflengten, genaamd radio-luide actieve sterrenstelsels, en stelsels zonder radio-jets, genaamd radio-zwakke actieve sterrenstelsels. Radio-luide actieve sterrenstelsels worden ook wel radiostelsels genoemd. De radio-jets en lobben die ze vertonen reiken verder dan het optische sterrenstelsel. Hun vorming, groei en evolutie wordt al bijna zes decennia lang onderzocht en bestudeert met behulp van grootschalige radio- en optische observaties, samen met theoretisch onderzoek en numerieke simulaties. Dit heeft geresulteerd in de ontwikkeling van modellen die de meeste waargenomen eigenschappen verklaren en bijdragen aan ons huidige begrip ervan. Enkele openstaande problemen met betrekking tot radio-luide actieve sterrenstelsels of radiostelsels worden echter nog actief onderzocht, zoals wat de omstandigheden zijn waaronder een actief sterrenstelsel radio-luid wordt en waarom alleen een klein deel van de radiostelsel-populatie tot megaparsec-grootte groeit. Radiostelsels of radio-luide quasars die meer dan 0,7 megaparsec groot worden, worden gedefinieerd als gigantische radiostelsels (GRGs), die bijna twee decennia (1974) na de ontdekking van radiostelsels rond 1950 werden gevonden.

Tot de komst van grote observatie campagnes met radio telescopen in de jaren negentig, hing het ontdekken van uitzonderlijke radio objecten af van de toegewijde observaties van heldere bronnen die waren geselecteerd uit verfijnde radio catalogi (bijv. 3CRR), die honderden radio bronnen bevatten. De komst van gevoelige grote observatie campagnes zoals NVSS, WENSS, FIRST en SUMSS in de jaren negentig luidde het tijdperk in van snelle ontdekkingen van interessante radio objecten, variërend van galactisch tot extragalactisch; sterren tot actieve stelsels tot clusters van sterrenstelsels. Dit gaf de mogelijkheid om grote groepen radio bronnen te bestuderen, die de trends in hun respectievelijke eigenschappen aan het licht brachten en leidde tot de ontdekking van GRGs. De meeste onderzoeken naar GRG's waren echter beperkt tot radio golflengten en waren gericht op hun eigenschappen op grote schaal. De actieve kern eigenschappen van GRG's biedt

ons daarom de mogelijkheid om ze te vergelijken met normale radiostelsels. Deze vergelijking stelt ons in staat om de onderscheidende factoren tussen de twee groepen te bepalen en te leren hoe sommige radio stelsels zo groot zijn geworden. In dit proefschrift is gewerkt aan de bovengenoemde vragen (zie sectie 1.5 van hoofdstuk 1) over de gigantische aard van GRGs om ons begrip over hun eigenschappen te verbeteren.

Dit proefschrift

Tot het jaar 2016 waren slechts ongeveer 300 GRG's bekend en de studies van hun actieve kernen waren zeer beperkt. Om de mogelijke oorzaken van de gigantische aard van GRG's en de zeldzaamheid ervan te begrijpen, is het essentieel om zowel hun actieve kernen als hun omgevings eigenschappen te bestuderen en grootschalige onderzoeken uit te voeren. Om dit te bereiken is er behoefte aan een statistisch grote hoeveelheid GRGs. Daarom was de belangrijkste focus van dit proefschrift het uitvoeren van grootschalige zoektochten in radio observaties, aangevuld met nieuwe optische data om grote groepen GRGs te maken voor het bestuderen van hun eigenschappen en trends. Het onderzoek wat is uitgevoerd met deze nieuwe groepen GRGs heeft een aantal belangrijke vragen beantwoord over de zeldzaamheid en eigenschappen van de actieve sterrenstelsels die worden beschreven in de hoofdstuksgewijze samenvatting hieronder.

Hoofdstuk 2 presenteert de resultaten van het project genaamd SAGAN, wat staat voor 'Search and Analysis of Giant radio Galaxies with Associated Nuclei'. Het doel van dit project is om een specifieke studie van GRG's uit te voeren om open vragen die ermee verband houden te beantwoorden. In het kader van dit project hebben we systematisch gezocht naar GRG's uit beschikbare radio data aangevuld met optische observaties. Als resultaat werden 25 GRG's ontdekt in de NRAO VLA Sky Survey (NVSS) met een roodverschuiving van $0{,}07 < z < 0{,}67$. Met behulp van openbaar beschikbare gegevens hebben we hun radio-, optische en middel-infrarood eigenschappen bestudeerd. Door de nieuw ontdekte 25 GRG's te combineren met de bekende GRG's uit de literatuur, hebben we een groep van 137 GRG's gemaakt en voor het eerst hun actieve stelsel excitatie type geclassificeerd met behulp van infrarood kleuren. Hierdoor konden we aantonen dat actieve stelsels van de GRG's geen geprefereerde excitatie toestand hebben (hoog of laag). Ten slotte hebben we met behulp van onze 25 nieuwe GRG's en andere GRG-gegevens uit de literatuur een groep van 82 GRG's gemaakt om ze te bestuderen met betrekking tot hun lichtkracht en grootte (met behulp van een P-D-diagram), samen met een groep kleinere radio bronnen uit de literatuur. Onze analyse heeft onthuld dat de GRGs een lagere helderheid hebben vergeleken met de radiostelsels op een frequentie van 1.4 GHz. Dit zou mogelijk kunnen komen door de hogere adiabatische uitzetting en verlies van straling in GRGs. Radiostelsel modellen hebben laten zien dat radiostelsels met leeftijd evolueren naar grotere formaten en lagere helderheden. Daarnaast hebben we ook gevonden dat er zich geen bronnen

bevinden in de rechter onder hoek van het P-D diagram, wat betekent dat we geen bronnen hebben gevonden met heel grote formaten en lage helderheden. Deze bronnen hebben een lage oppervlaktehelderheid en zijn te zwak om gedetecteerd te worden door observatie campagnes zoals NVSS. Ook tonen onze resultaten aan dat GRGs met formaten groter dan 2 Mpc zeldzaam zijn.

In hoofdstuk 3 worden de resultaten gepresenteerd van een uitgebreide zoektocht naar GRG's in de LOFAR Two-meter Sky Survey (LoTSS). De eerste LoTSS data release bestreek een gebied van 424 graden ^{2} aan de noordelijke hemel op 144 MHz met een gevoeligheid van $\sim 100\,\mu$Jy en met resoluties van $6''$ en $20''$. De lage frequentie van de observaties is ideaal voor het in kaart brengen van de diffuse en steil-spectrum radiostraling van de bronnen. Verder is LoTSS met zijn hoge gevoeligheid en hoge resolutie is in staat om kleinere details van de bronnen te zien, waardoor we hun morfologieën in meer detail kunnen bestuderen. Als resultaat van een hybride methode van handmatig en semi-automatisch zoeken, werd een recordaantal van 239 GRG's gevonden met roodverschuivingen in het bereik van $0{,}1 < z < 2{,}3$, waarvan 225 nieuwe ontdekkingen. Dit is het grootste aantal van GRG's die tot nu toe is gevonden in radio data en daarmee bijna een verdubbeling van de bekende populatie GRG's. Onze nieuwe catalogus bevat ook drie gigantische radio quasars (GRQ's) met $z > 2$, waarvan wordt aangenomen dat ze moeilijk te detecteren zijn vanwege de hoge roodverschuiving en zeldzaamheid. Een aantal van de GRG's hebben een zeer steil radio spectrum en zijn daarom niet zichtbaar in observaties op hogere frequenties, zoals de 1.4 GHz NVSS, waarvan zeven met geprojecteerde lineaire groottes groter dan 2 Mpc. We hebben de lage frequentie LoTSS gegevens gecombineerd met hoge frequentie NVSS gegevens om voor het eerst de spectrale index (α) van een groot aantal GRGs te bepalen en ontdekten dat de gemiddelde α van GRG's 0,78 is, wat vergelijkbaar is met die van radiostelsels. In tegenstelling tot de eerdere opvattingen, toont deze studie aan dat oude GRG's met diffuse relikwie-emissie de GRG-populatie niet domineren, aangezien de spectrale index verdeling vergelijkbaar is met die RG's. Door de grootte van onze groep GRGs en beschikbaarheid van goede observaties, konden we GRGs identificeren met bijzondere kenmerken. Zo bevat onze groep 40 GRG's die worden gehost door quasars (GRQ's), 14 met herstartte actieve kern activiteit - de zogenaamde dubbele-dubbele radiostelsels. (DDRG's), 6 GRG's met hybride radio morfologie en 20 GRG's die worden gehost door de helderste cluster stelsels (BCG's) die zich in de cluster omgeving bevinden. Ten slotte stelde de grote hoeveelheid GRG's ons ook in staat om vast te stellen dat ten minste 16% van de GRG's van $z < 0{,}55$ zich in de hoge dichtheid cluster- of groepsomgeving bevinden. Dit resultaat benadrukt dat ondanks de hoge dichtheid van de omgeving, onder voorbehoud van voldoende jet vermogen in combinatie met voortdurende actieve kern brandstof, RG's kunnen uitgroeien tot megaparsec-schalen.

Hoofdstuk 4 presenteert de eerste resultaten van project SAGAN, waar we de vondst van 162 nieuwe GRG's rapporteren op basis van onze zoektocht in NVSS. De nieuwe groep van GRG's is gevonden in het roodverschuivings bereik van 0,03

$< z <$ 0,95 met groottes tot $\sim$ 2,8 Mpc, waarvan 23 bronnen een quasar bevatten. Door de GRG's die in de literatuur sinds 1974 (tot maart 2020) zijn gerapporteerd te combineren met onze samples van SAGAN en LoTSS, hebben we de grootste GRG-catalogus van 820 bronnen tot nu toe gedefinieerd en gemaakt. Om de GRG-catalogus te maken, werden alle artikelen die GRG's rapporteerden sinds de ontdekking in 1974 doorzocht in de verschillende databanken en alle gerapporteerde GRG's werden handmatig geïnspecteerd met nieuwe radio data zoals NVSS, TGSS, FIRST, SUMSS en WENSS. De optische sterrenstelsels van elke gerapporteerde GRG werden ook opnieuw onderzocht met behulp van de nieuwste optische databanken zoals SDSS, 6dF, 2MASS, 2dF en PANSTARRS. Bij gebrek aan kaarten met hoge resolutie die volledige structuren tonen, werden de afmetingen van bronnen opnieuw gemeten met behulp van NVSS. Een uniforme kosmologie werd gebruikt door de nieuwste Hubble-constante waarden van de Planck-missie over te nemen om de geprojecteerde lineaire afmetingen van GRG's te berekenen. Onze GRG-catalogus heeft ons in staat gesteld om statistisch significante groepen samen te stellen om de actieve kernen en omgevings eigenschappen te onderzoeken van GRGs in vergelijking met normale radiostelsels. We hebben een analyse uitgevoerd met observaties van verschillende golflengtes van de actieve kernen van de GRG's met behulp van optische, middel-infrarood en radio data. Onze resultaten tonen aan dat de massa van het zwarte gat en de radio spectrale index verdeling van GRG's en radiostelsels vergelijkbaar zijn. In tegenstelling tot het bovenstaande bleek de gemiddelde Eddington-ratio (ER) van GRG's lager te zijn dan die van RG's. We laten ook zien met grote groepen GRGs dat actieve kernen geen geprefereerde excitatie toestand hebben (laag of hoog), wat de resultaten gepresenteerd in Hoofdstuk 2 bevestigt. We zien dat GRG's in hoge excitatie toestand de neiging hebben om grotere afmetingen, hogere radio vermogens en snellere accreties te hebben. Met behulp van de data over meerdere golflengten hebben we ook het kinetische jet vermogen, het totale radio vermogen, het magnetische veld en de totale afmetingen geschat en vergeleken met hoge en lage excitatie klassen. Bovendien vinden we dat 10% van de GRG's zich in centra van clusters van sterrenstelsels bevinden, d.w.z. in een hoge dichtheid omgeving en toch uitgroeien tot megaparsec-schalen. De omgeving kan dus niet de enige factor zijn in het grote formaat van de GRGs. Met behulp van alle bovenstaande resultaten bespreken we in detail de mogelijke factoren die de vorming en groei van GRG's beïnvloeden.

Hoofdstuk 5 presenteert de resultaten van onze studie op millimeter golflengte van de optische sterrenstelsels van GRG's. Het doel van deze studie was het begrijpen van het moleculaire gasgehalte van de sterrenstelsels van GRG's en hun rol in de actieve kern brandstofvoorziening. Dergelijke studies van GRG's zijn schaars en zijn zeer essentieel om uit te voeren om hun werking te begrijpen. De meeste GRG's bevinden zich in elliptische sterrenstelsels (op een paar uitzonderingen na), die over het algemeen geen grote hoeveelheid stervorming hebben. Voor deze studie werden in totaal 12 GRG's geselecteerd op basis van hun middel-infrarood kleuren, die tekenen van verhit stof vertonen en zich waarschijnlijk in de fase van gas accretie en sterformatie bevinden. Met behulp van onze waarnemingen rapporteren

we het moleculaire gasgehalte en de efficiëntie van stervorming met betrekking tot hun melkwegstelsel morfologie. Onze waarnemingen met IRAM-30M millimeter golflengte telescoop tonen detecties aan in drie van de twaalf geselecteerde GRG's en rapporteren bovengrenzen voor de rest van de bronnen in de groep. We vinden twee van de GRG's met een tekort aan moleculair gasgehalte en met een korte uitputtingstijd van ∼200 Myr. Twee detecties uit onze groep behoren tot GRG's die worden gehost door gigantische gasrijke spiraalstelsels die uiterst zeldzaam zijn. We gebruiken de informatie die beschikbaar is in de literatuur voor vier andere GRG's naast onze groep om de waargenomen resultaten en trends te bespreken. We zien dat de sterrenstelsels van de GRGs de hoofdreeks volgen en dat de meeste passieve sterrenstelsels zijn. GRG's met detectie van moleculair gas vertonen ook tekenen van herstartende actieve kern activiteit of maken deel uit van melkwegstelsels. Dit werpt meer licht op de rol van de omgeving bij het voorzien van brandstof aan de actieve kern. Vandaar dat onze millimeter golflengte studie van GRG's laat zien dat een complexe cyclus van brandstof voorzien aan de actieve kern samen met omgevingsfactoren betrokken is bij de groei van GRG's, die verder onderzoek vereisen met behulp van een grotere groepen van GRG's.

In Hoofdstuk 6 wordt de eerste studie van een eigenaardige "Barbell" -vormige GRG (GRG-J2233+1315) gepresenteerd met behulp van waarnemingen van GMRT, LOFAR en optische 2m Himalayan Chandra Telescope (HCT). Dit object werd gevonden in het SAGAN project en voor het eerst gerapporteerd in Dabhade et al. 2017 (Hoofdstuk 2), waar het formaat geschat werd met behulp van de fotometrische roodverschuiving van SDSS. In dit hoofdstuk rapporteren we de spectroscopische roodverschuiving van onze optische waarneming met HCT en schatten we de stellaire snelheidsverspreiding van het sterrenstelsel, waardoor we de massa van het zwarte gat konden schatten op $7{,}7 \pm 2{,}9 \times 10^9$ $M_\odot$. De radio data werden verkregen op golflengtes van 144 MHz (LOFAR), 323 MHz, 612 MHz en 1300 MHz (GMRT) en leidden tot de vondst van eigenaardige ∼100 kpc 'kink ' structuur in de westelijke jet van de GRG. We bespreken de mogelijke reden voor de zeldzame en eigenaardige 'knik'-structuur met behulp van beschikbare resultaten en modellen van magnetohydrodynamische (MHD) simulaties, samen met de vergelijking met andere vergelijkbare voorbeelden uit de literatuur. Dergelijke kenmerken in extragalactische radio objecten vormen het ideale laboratorium voor het bestuderen van grootschalige MHD-effecten. We zien ook een lange tegengestelde jet aan de oostkant, wat zeldzaam is in FR-II-type GRG's. Met behulp van de radiogegevens hebben we de klassieke en herziene schattingen van het magnetische veld van beide lobben (∼5 μG) geschat, die consistent zijn met de schattingen van andere GRG's uit de literatuur. Hierdoor konden we ook de spectrale leeftijden schatten en ontdekken dat ze ouder waren dan ∼ 110 Myr, wat ook de levensduur van de activiteit van de sterrenstelsel kern aangeeft. Het is belangrijk op te merken dat tot op heden schattingen van het magnetische veld en de spectrale leeftijd zijn gemaakt voor minder dan 40 GRG's. Interessant is dat de GRG zich in een cluster omgeving met hoge dichtheid bevindt en het helderste sterrenstelsel in de cluster als optische tegenhanger heeft, de zogenoemde 'brightest cluster galaxy' (BCG), en toch

is uitgegroeid tot 1,88 Mpc in grootte. Met behulp van de informatie uit de cluster catalogus presenteren we de virale massa van het cluster van sterrenstelsels (M_{200} ~ 1.1 $\times 10^{14}$ M_{odot}, virale straal ((R_{200}) van ~ 1,02 Mpc, en verwachtte röntgen lichtsterkte van $0{,}29 \times 10^{44}$ erg s^{-1} Het is zeer waarschijnlijk dat de omgeving van deze GRG een effect heeft gehad op zijn groei en morfologie en daarom zullen toekomstige röntgen- en optische studies van dit object ons nieuwe antwoorden geven.

Toekomstig onderzoek

Het werk in dit proefschrift heeft aangetoond dat de GRG's niet zo zeldzaam zijn als eerder werd gedacht, dankzij onze vondst van grote aantallen GRGs in LoTSS en NVSS. Nu, met meer dan 800 GRG's gecatalogiseerd, zou de volgende stap zijn om subgroepen (op verschillende roodverschuivingen) van GRG's te maken en hun actieve kern eigenschappen te bestuderen in vergelijking met hun radiostelsel met behulp van optische en infrarood spectrografen met hoge resolutie of integrale spectrale eenheid (IFU) samen met röntgen data. Dit zal helpen bij het bepalen van de accretie toestand en de algehele actieve kern sterkte van de GRG. Evenzo is het met behulp van optische en röntgen data essentieel om de omgevingen van GRG's te bestuderen om het effect van omgevings dichtheid en inhomogeniteiten op de GRG-structuur en groei te onderzoeken. Met de snelle ontwikkeling van hardware en software in de radioastronomie is de snelheid waarmee grootschalige radio onderzoeken worden uitgevoerd toegenomen en daarom zullen onderzoeken met LOFAR, uGMRT, MeerKAT, JVLA en ASKAP honderden nieuwe GRG's ontdekken, die kunnen worden gebruikt voor het onderzoek naar de groei van radio sterrenstelsels en evolutionaire modellen. Ook kan een groot aantal GRG's worden gebruikt om het warm-hete intergalactische medium te onderzoeken (WHIM) zoals beschreven in paragraaf 1.5 van Hoofdstuk 1, door de drukbalans van GRGs uit observaties te vergelijken met WHIM simulaties. Dit specifieke aspect kan worden onderzocht voor GRGs gehost door de helderste cluster sterrenstelsels of GRGs die zich in een cluster omgeving bevinden en met de komst van röntgen data van de eROSITA-missie in de nabije toekomst zal het mogelijk zijn om dergelijke studies uit te voeren.

List of publications

First author publications

1. 'Discovery of giant radio galaxies from NVSS: radio and infrared properties', Dabhade, P., Gaikwad, M., Bagchi, J., Pandey-Pommier, M., Sankhyayan, S., & Raychaudhury, S. (2017), MNRAS, 469, 2886. DOI:10.1093/mnras/stx860

2. 'Giant radio galaxies in the LOFAR Two-metre Sky Survey. I. Radio and environmental properties', Dabhade, P., Röttgering, H. J. A., Bagchi, J., Shimwell, T. W., Hardcastle, M. J., Sankhyayan, S., Morganti, R., Jamrozy, M., Shulevski, A., & Duncan, K. J. (2020), A&A, 635, A5. DOI:10.1051/0004-6361/201935589

3. 'Search and analysis of giant radio galaxies with associated nuclei (SAGAN). I. New sample and multi-wavelength studies', Dabhade, P., Mahato, M., Bagchi, J., Saikia, D. J., Combes, F., Sankhyayan, S., Röttgering, H. J. A., Ho, L. C., Gaikwad, M., Raychaudhury, S., Vaidya, B., & Guiderdoni, B. (2020), A&A, 642, A153. DOI:10.1051/0004-6361/202038344

4. 'Search and analysis of giant radio galaxies with associated nuclei (SAGAN). II. Molecular gas content of giant radio galaxies', Dabhade, P., Combes, F., Salomé, P., Bagchi, J., & Mahato, M. (2020), A&A, 643, A111. DOI:10.1051/0004-6361/202038676

5. 'Barbell shaped giant radio galaxy with ∼100 kpc kink in jet', Dabhade, P et al. 2021- In preparation.

Co-authored publications

1. 'Tracking Galaxy Evolution Through Low-Frequency Radio Continuum Observations using SKA and Citizen-Science Research using Multi-Wavelength Data', Hota, A., Konar, C., Stalin, C. S., Vaddi, S., Mohanty, P. K., Dabhade, P., Dharmik Bhoga, S. A., Rajoria, M., & Sethi, S. (2016), Journal of Astrophysics and Astronomy, 37, 41.
DOI:10.1007/s12036-016-9415-8

2. 'Saraswati: An Extremely Massive 200 Megaparsec Scale Supercluster', Bagchi, J., Sankhyayan, S., Sarkar, P., Raychaudhury, S., Jacob, J., & Dabhade, P. (2017), ApJ, 844, 25.
DOI:10.3847/1538-4357/aa7949

3. ' 'Zwicky's Nonet': a compact merging ensemble of nine galaxies and 4C 35.06, a peculiar radio galaxy with dancing radio jets', Biju, K. G., Bagchi, J., Ishwara-Chandra, C. H., Pandey-Pommier, M., Jacob, J., Patil, M. K., Kumar, P. S., Pandge, M., Dabhade, P., Gaikwad, M., Dhurde, S., Abraham, S., Vivek, M., Mahabal, A. A., & Djorgovski, S. G. (2017), MNRAS, 471, 617.
DOI:10.1093/mnras/stx1476

4. 'MACS J0553.4-3342: a young merging galaxy cluster caught through the eyes of Chandra and HST', Pandge, M. B., Bagchi, J., Sonkamble, S. S., Parekh, V., Patil, M. K., Dabhade, P., Navale, N. R., Raychaudhury, S., & Jacob, J. (2017), MNRAS, 472, 2042.
DOI:10.1093/mnras/stx2028

5. 'AGN Feedback in Galaxy Groups: A Detailed Study of X-Ray Features and Diffuse Radio Emission in IC 1262', Pandge, M. B., Sonkamble, S. S., Parekh, V., Dabhade, P., Parmar, A., Patil, M. K., & Raychaudhury, S. (2019), ApJ, 870, 62.
DOI:10.3847/1538-4357/aaf105

6. 'GMRT observations of extragalactic radio sources with steeply inverted spectra', Mhaskey, M., Gopal-Krishna, Dabhade, P., Paul, S., Salunkhe, S., & Sirothia, S. K. (2019), MNRAS, 485, 2447.
DOI:10.1093/mnras/stz335

7. 'A low-frequency study of recently identified double-double radio galaxies', Nandi, S., Saikia, D. J., Roy, R., Dabhade, P., Wadadekar, Y., Larsson, J., Baes, M., Chandola, H. C., & Singh, M. (2019), MNRAS, 486, 5158.
DOI:10.1093/mnras/stz1184

8. 'GMRT observations of a first sample of 'Extremely Inverted Spectrum Extragalactic Radio Sources (EISERS)' candidates in the Northern sky', Mhaskey, M., Gopal-Krishna, Paul, S., Dabhade, P., Salunkhe, S., Bhagat, S., & Bendre, A. (2019), MNRAS, 489, 3506.
DOI:10.1093/mnras/stz2379

9. 'The LOFAR view of intergalactic magnetic fields with giant radio galaxies', Stuardi, C., O'Sullivan, S. P., Bonafede, A., Brüggen, M., Dabhade, P., Horellou, C., Morganti, R., Carretti, E., Heald, G., Iacobelli, M., & Vacca, V. (2020), A&A, 638, A48.
DOI:10.1051/0004-6361/202037635

10. 'Exploring the hot gaseous halo around an extremely massive and relativistic jet launching spiral galaxy with XMM-Newton', Mirakhor, M. S., Walker, S. A., Bagchi, J., Fabian, A. C., Barth, A. J., Combes, F., Dabhade, P., Ho, L. C., & Pandge, M. B. (2020), MNRAS,.
DOI:10.1093/mnras/staa3404

* List in NASA-ADS *

Conference Proceedings

- 'New results on the exotic galaxy 'Speca' and discovering many more Specas with RAD@home network', Hota, A., Croston, J. H., Ohyama, Y., Stalin, C. S., Hardcastle, M. J., Konar, C., Aravind, R. P., Agarwal, S. M., Dharmik Bhoga, S. A., Dabhade, P., et al. (2014), Astronomical Society of India Conference Series, 13, 141.

News articles / highlights

- 'Giant radio galaxies: the cosmic behemoths', P. Dabhade and M. Mahato, Nature Astronomy Community, Sept 10, 2020.
- 'Large sample of giant radio galaxies discovered', P. Dabhade, MNRAS OUP blog, July 2, 2017.
- 'LoTSS of giants', Nature Astronomy (Research Highlights), Feb 03, 2020.

Curriculum Vitae

I was born on 13th June 1989 in a town located in central part of Maharashtra state of India, called Jalna ($\sim$400 km from Mumbai). Most of my childhood summer time was spent at my maternal grandparent's house in Jalna, where there was hardly any light pollution, allowing me to gaze at the majestic star filled night sky. However, this privilege was not granted in the ever growing skylines of Mumbai, where I have spent most of my life under the loving care of my parents, Anand Sampatrao Dabhade and Bharati Anand Dabhade along with my sister Dr. Rachana Dabhade (Ophthalmologist). I also spent six formative years of my childhood in the lovely city of Indore, located in central Indian state of Madhya Pradesh, where I became proficient in the Hindi language and was exposed to the north Indian culture. Growing up I had huge interest in science-fiction and sports like cricket, football and table-tennis. I managed to play district level football league in Mumbai, which I discontinued after joining for bachelors studies.

I completed my schooling from Lok Puram Public school, followed by junior college from Saraswati Education Society College in Thane, Maharashtra state. In 2009, I joined the D.G.Ruparel College in Mumbai for my bachelors in physics, where I came in contact with inspiring and encouraging teachers. Fortunately in the same year of 2009 I was introduced to the fascinating field of Astrophysics via public talks at the Nehru planetarium as part of the IAU's International year of Astronomy program.

Towards the end of my first years of bachelors I got the opportunity to attend a summer school at IUCAA in Pune, which is one the premier institutes of astronomy in India. This summer school in 2010 opened altogether a new exciting world for me, where I decided to be an astronomer exploring the secrets of the Universe. I will forever be indebt to IUCAA for providing me this opportunity and changing the course of my life. During my second year of bachelors in 2010 I was generously offered a project by Prof Joydeep Bagchi to work on construction of Cosmic ray muon detector at IUCAA. This allowed me to grasp concepts of special theory relativity, particle and astro-particle physics. I completed the construction and calibration of the muon detector by summer of 2011 with the help of my friend and project partner. Consequently, we have been collecting muon data ever since in the radio physics lab of IUCAA and the experiments with this setup where included in the master's astrophysics lab course of Pune University (now Savitribai Phule Pune University).

The topic for master's thesis at Pune University was search for spiral host

radio galaxies and giant radio galaxies, which involved checking thousands of objects manually along with cross checking with several catalogs of radio and optical bands. The project really helped me several key concepts of radio astronomy as well as programming. In 2013, I also became the part of RAD@home Astronomy Collaboratory, which is India's first citizen science research platform in astronomy. Based on the work done on searches from TIFR-GMRT Sky Survey data as part of their camps I presented my research work for the first time at the annual Astronomical society of India's meeting in Mohali in 2014.

Having completed my masters in Physics from Pune University in 2015, I was selected for the position of 'junior research fellow' at IUCAA to work on a Indo-French CEFIPRA project with Prof Joydeep Bagchi and collaborators. Under this position I started to work on giant radio galaxies exclusively and in 2016 I was given opportunity by Prof Huub Röttgering to work with the LOFAR collaboration and consequently registered in University of Leiden as a PhD student. In the last five years I have spent time in Europe (Leiden and Paris) and at IUCAA working in a joint collaboration.

I have been associated with the radio physics lab of IUCAA for nearly a decade now, during which I have participated in various lab activities initially and later on organised them as well (e.g. winter school, science day, public talks, conducting masters practicals and projects students).

I will continue my journey in research career as a post-doctoral fellow in Paris working with Prof Francoise Combes at the Observatoire de Paris.

Acknowledgements

“ There is no such thing as a self-made man/woman. We are made up of thousands of others. Every one who has ever done a kind deed for us, or spoken one word of encouragement to us, has entered into the make-up of our character and of our thoughts, as well as our success. "

- George Matthew Adams

Here, I attempt to acknowledge a long list of people who have helped me in various stages of life so far and have knowingly or unknowingly contributed to whom I am today. I shall be forever grateful to all of them.

I begin by acknowledging my parents (Anand Dabhade and Bharati Dabhade) for their eternal support, limitless love and for believing in me. I thank my sister (Dr. Rachana Dabhade) for always leading by example when it came to academics and career, as growing up with her I always learnt to aim higher.

I thank Prof. Joydeep Bagchi for kick-starting my journey into the research field by generously offering projects to work on since my bachelors and for his teaching, guidance and support in the past decade. More importantly, thank you for inculcating and encouraging independent working.

This thesis would not have been possible without the financial and logistical support from the Indo-French CEFIPRA project, IUCAA, and Leiden University. I am thankful to all the people involved. I would like to thank Prof. Somak Raychaudhury, the director of IUCAA, for his support, guidance and encouragement during my tenure at IUCAA. I must mention the important role of Dr. V Chellathurai, who allowed me to attend IUCAA summer school back in 2010, which paved way for my research career.

As an observational astronomer, I had the wonderful opportunities of visiting various observatories in India and Europe for observations, where I met very kind people who made the observations and my stay memorable. Hence, I thank the hardworking staff of GMRT, ASTRON (LOFAR), HCT (IIA), IRAM, and DOT (ARIES).

I was fortunate to interact with the late Prof. Govind Swarup on several occasions, where he inspired me with his ideas and enthusiasm. He was quite pleased to know that my work has resulted in the finding hundreds of GRGs and they are being followed up by GMRT, one of the great telescopes he built.

As a CEFIPRA (Indo-French project) junior research fellow, I was able to travel to Paris and Lyon in France a couple of times for collaborative work, where I learnt a lot about millimetre-wave astronomy from Prof. Francoise Combes. She has been very instrumental in my research career.

I was quite fortunate to get Prof. D.J. Saikia in my neighbouring office at IUCAA, nearly three years back. This led to our interaction and eventual fruitful collaboration. His vast knowledge of radio galaxies and his humble nature combined with his patience has been very inspiring and helpful for me.

I am thankful to Prof. Ishwar Chandra (NCRA radio astronomy schools) for introducing me to AIPS and for fruitful discussions on radio galaxies and imaging. I thank Dr Huib Intema for creating and teaching me SPAM (radio imaging made simple). The project with the LoTSS data would not have been possible without great help from Dr Timothy Shimwell for which I am very grateful. I thank and appreciate Prof. Ananda Hota for creating and making me part of RAD@home Astronomy Collaboratory (citizen-science research platform) early on during my masters. It was very exciting to learn new techniques to find objects from TGSS.

I would also like to thank Prof. Madkaikar and Prof. Londhe from D.G. Ruparel college (Bachelors) for encouragement and guidance to take up research. They both introduced me to Prof. S Prabhu (TIFR), who was instrumental in providing me timely advice and direction with respect to higher education and research.

Tejas Kale, thank you for supporting and guiding me at my low points of life. I have always looked up to you. Your suggestion to take up basic sciences has done wonders for me. Madhuri Gaikwad, thank you for making the time in our bachelors and masters so great with all discussions and projects. Thank you for always being supportive of my ideas in our joint projects, for your patience, and for always being there for me.

The turning point in my life was attending IUCAA summer school in 2010, which would not have happened without my cousin Pravin Maghade who very graciously hosted me in Pune for a month and introduced me to the lifestyle of Pune. I will forever be thankful to him.

A major part of my PhD was spent at IUCAA, where numerous people made this journey very memorable. The hardships of PhD were made quite bearable by my friend and collaborator Shishir Sankhyayan who stood by me throughout. It was great working with you and thank you for being the brother I never had before. It is very crucial to understand the telescopes very well in radio astronomy especially if you are an observational astronomer. Over the years Ashish Mhaske not only has been a great friend but also has cleared my numerous technical doubts about radio telescopes which lead to some epic discussions for future projects. Junior turned collaborator turned friend- Mousumi Mahato- you have been of exceptional help to me during my crucial second half of my PhD. It has been an absolute pleasure working with you and thank you for being patient with me.

Radio physics lab at IUCAA was the place where I spent most of my time joyfully working alongside Shishir, Ashish, Mousumi, and Jameer Manur. It was great to have Jameer as a friend and colleague who always ensured smooth working of the lab and providing us all with amazing home-cooked food.

It was amazing to see Ajay Vibhute's computing and managerial skills at work. I learned a lot about Linux and computing from him, and he always had a solution

to my computing problems.

On my first visit to IUCAA during my bachelors, Dr Prashant Samantray showed me that being PhD student does not demand you to be nerdy all the time. Thank you for your timely guidance and for inspiring me with your work and fitness ethics.

I am grateful to Dr Biju K.G and Dr Joe Jacob for their support and inspiring me with their zeal to learn. It was refreshing to attend conferences with you both and spend joyful time at IUCAA during your visits.

From being my seniors at Pune University (masters) to great friends, Bhooshan Gadre and Shabbir Shaikh made times at IUCAA more joyous and always had sound advice for me. From trying new food with Bhooshan to taking late-night walks with Shabbir, there was always scope to have discussions on any topic with both of them.

Sharmad Navelkar always ensured that I had enough outings in the month so that I didn't burn out, thank you for a great time. Those outings were made epic by the company of Reju Sam John, Swagat Mishra, Sorabh Chhabra and many more (apologies for forgetting some names). Physics discussions and admiring rock music with Swagat Mishra were always gratifying, who always impressed me with his endearing passion for physics. A very essential skill that I developed during my PhD is cooking (my mother would be equally proud about this) and much of the credit goes to Sangeetha CR and Vidushi Sharma. I am grateful to them for always pushing to cook new dishes, which ensured I get the needed break from work. Vidushi's impromptu plans for cooking or outing or work discussions always broke the monotonous routine. In the past few years, I had some very scintillating discussions with Sayak Datta and Siddharth Maharana, which often gave me an interesting perspective on certain matters.

I am grateful to Prof. Sanjit Mitra and Prof. Varun Sahni for their amazing courses on general relativity and cosmology along with their cool parties and guidance over the years at IUCAA.

I am very grateful to Alexandra Schouten-Voskamp and Evelijn Gerstel for always ensuring that I am well taken care of at Leiden during my extended stay and during the course of my PhD project. It was very nice to have the company of Kimberly Emig, Soumyajit Mandal and Andrea Botteon who made my stays at Leiden pleasant.

Shruthi and Rashmi have always been supporting pillars for me who have encouraged and cheered me always. Thank you to both as it made the journey smoother.